On the maintenance of weak meridional temperature gradients during warm climates

Robert Lindsay Korty

B.A. Physics and Environmental Sciences
University of Virginia, 1999

Submitted to the
Department of Earth, Atmospheric and Planetary Sciences
in partial fulfillment of the requirements for the degree of

Doctor of Philosophy in Climate Physics and Chemistry

at the

MASSACHUSETTS INSTITUTE OF TECHNOLOGY

June 2005

Author .....
Robert Lindsay Korty
Department of Earth, Atmospheric and Planetary Sciences
May 9, 2005

Certified by .....
Kerry A. Emanuel
Professor of Atmospheric Sciences
Thesis Supervisor

Accepted by .....
Maria T. Zuber
E.A. Griswold Professor of Geophysics
Department Head

On the maintenance of weak meridional temperature gradients during warm climates

Robert Lindsay Korty

Submitted to the Department of Earth, Atmospheric and Planetary Sciences on May 9, 2005, in partial fulfillment of the requirements for the degree of Doctor of Philosophy in Climate Physics and Chemistry

Abstract

This thesis examines the dynamics of equable climates. The underlying physics of two mechanisms by which weak meridional temperature gradients might be maintained are studied. First, I examine the evolution of stratospheric dynamics and winter temperatures when the surface temperature gradient and tropospheric eddy energy decrease in order to assess whether large-scale conditions are more favorable for polar stratospheric cloud formation. Second, I examine whether the combination of high carbon dioxide and interactive, tropical cyclone dependent ocean mixing is sufficient to maintain a weak temperature gradient.

I examine planetary wave generation, the energetics of the general circulation, and vertical wave propagation in a general circulation model with a resolved stratosphere forced with a weak surface temperature gradient. Compared to the present climate, transient eddy energy decreases, but stationary eddy energy does not. The polar tropopause rises, which supports a weaker temperature gradient in the lower stratosphere, a weaker stratospheric jet, and an increase in the wave activity vertically propagating into the stratosphere. As a result, the residual mean circulation strengthens and temperatures in the polar stratosphere change little even when the surface temperature gradient is quite weak. Temperatures in the Arctic polar vortex remain much warmer than radiative equilibrium, inhibiting large-scale polar stratospheric cloud formation. The height of the extratropical tropopause rises and the tropospheric lapse rate follows a moist adiabat when surface temperatures are warm, suggesting convection plays a significant role in setting extratropical tropospheric stratification during warm climates.

The second part of the thesis addresses the role of tropical cyclone induced mixing in the oceans' general circulation. I examine the sensitivity of the oceans' meridional overturning circulation and heat flux to the locations at which mixing occurs. When confined to the tropical Atlantic, a robust single-basin circulation can be maintained, but the Indian and Pacific become quiescent, cut off from the dynamics occurring in the Atlantic. Mixing isolated in the tropical Pacific, however, can support a global circulation by mechanically lifting deep fluid parcels formed in the Atlantic, raising their potential energy. The oceans' total heat flux is found to be sensitive to mixing in the tropics, in both the Atlantic and the Pacific, and in the upper 400 meters of the ocean. Coupling mixing with a measure of tropical cyclone intensity and frequency creates

a positive feedback between climate and the poleward energy flux. When combined with a parameterization of the background mixing that evolves with stratification, a warmer, less stratified ocean can support a stronger diapycnal mixing during warm climates with high loads of carbon dioxide. In these simulations, tropical cyclones are stronger and more frequent, providing an increased energy source for more vigorous mixing in the tropical oceans. Combined with a stratification-dependent mixing scheme, such mixing provides a sufficiently strong heat flux that is able to maintain weak sea surface temperature gradients.

Thesis Supervisor: Kerry A. Emanuel
Title: Professor of Atmospheric Sciences

Acknowledgments

"Forsan et haec olim meminisse iuvabit."

—Vergil, *The Aeneid* (I, 203)

In 1845, William Barton Rogers, then chairman of the faculty of the University of Virginia, reported to the Virginia General Assembly that Thomas Jefferson's prohibition on honorary degrees should be continued. Granting a university's highest degree as an honorarium was "literary almsgiving...of spurious merit and noisy popularity," he wrote. Professor Rogers carried this tradition with him to Boston when he founded MIT. To this day, neither the University nor MIT has granted an honorary degree. I am proud to have earned one from each.

So many people have helped me during my studies at MIT, and I owe each of them an immense amount of gratitude. I thank my advisor, Kerry Emanuel, for his guidance, insight, and hospitality. He granted me a degree of independence to which I was unaccustomed previously. This confidence in his students was both stimulating and challenging, but ultimately he has steered me to become a better and more confident scientist than I would have been otherwise. I have been honored to work with him.

I am very grateful for all of the advice and help given to me by Jeff Scott, who served as a friend and mentor. He patiently explained diapycnal mixing and generously offered his time, helping me with technical and scientific questions related to this work. His interest in my progress and research rescued me from the doldrums during the semesters that followed my general exam. Perhaps more than any other person, he helped me focus the questions my work addressed and provided guidance and advice that kept me moving and on track.

My studies were enhanced by the input of each of my thesis committee members. I thank Julian Sachs for teaching me much about proxies of prehistoric temperatures; I have benefited immensely from the perspective he provided on my work. I am grateful for the patience he offered as this research progressed and for the amount of time he devoted to learning about the background of this material. My thesis improved directly as a result of many of our conversations.

I thank Alan Plumb for helping me focus the questions this thesis addresses and for helping to develop my research. He encouraged me to think critically about how the questions I posed could be addressed with the tools at my disposal. He is an excellent teacher, and I have learned much from him.

I thank Peter Stone for his interest in my work and for reviewing it with constructive insight. His careful attention to detail and thorough understanding of climate dynamics helped me to achieve an enriched appreciation for the way the atmosphere and oceans operate. He gave generously of his time and helped me hone both my research and presentation skills.

One of the greatest benefits of attending MIT is the ability to interact with gifted students from around the world. Greg Lawson and Pablo Zurita gave generously of their time, and they helped me settle here. They both possess great minds, and they explained difficult processes, papers, and subjects to me with remarkable clarity. They are excellent teachers, and I was fortunate to share an office with such talented people upon my arrival at MIT. I learned much from my fellow classmates, Nikki Privé and Peter Huybers; I shall carry fond memories of working together on problem sets for years to come. Many of my conversations with Donnan Steele, Bill Boos, Masa Sugiyama, and Mike Ring helped clarify my thinking as this work progressed. I am thankful for all of the friendships formed here.

I am very grateful for the opportunity to have spent a summer at the National Center for Atmospheric Research in Boulder, Colorado. The time off of the East Coast was simultaneously restful and productive. I am indebted to Phil Rasch for his gracious hospitality and support of my time at NCAR. He introduced me to many of the scientists in the Climate and Global Dynamics Division, and he gave a fresh perspective on my work. Jeff Kiehl, Byron Boville, and Jim McCaa all provided guidance and helpful suggestions. My time in the West rejuvenated my interest in science, and it helped solidify my post-graduate school plans at a critical moment in my studies.

Most importantly, I wish to thank my family. My grandparents, parents, and brother continually voiced an incredible confidence in my abilities. The pride they expressed in me carried and sustained me through these years. My father helped me with computer programming, and my brother helped me with mathematics I had forgotten quickly after college. My mother and grandparents offered sage advice and effusive praise that reminded me weekly how richly blessed I have been. Truly, I could not have earned this degree were it not for the support these three generations provided to me.

Success at a place like MIT requires an element of faith. Someone must believe you will succeed—if not yourself or a teacher then a spouse, a parent, a friend. You can call this faith a confidence or merely an expectation, but the word assigned to it is less important than its presence. I have been blessed by the presence of many who have believed in me with unwavering confidence through these years. Without their faith, I doubt I would have made it to the end.

Cambridge, Massachusetts Robert Lindsay Korty
May 2005

Contents

Chapter 1

The warm climate problem

1.1 Early Cenozoic climate dynamics

Around the rim of the Arctic Ocean, fossilized remains of ancient conifer forests, plants, and animals intolerant of frost lie scattered across the barren tundra. A rich variety of Eocene epoch fossils of flora from Spitsbergen (Schweitzer, 1980), of flying lemurs (McKenna, 1980) and alligators (Dawson et al., 1976) from Ellesmere Island, and of a *Meta sequoia* forest from Axel Heiberg Island (Eberle and Storer, 1999) prove that the climate of high latitudes during the early Cenozoic was mild enough to support a remarkable diversity of life. In Patagonia, New Zealand, and even Antarctica, high latitudes of the Southern Hemisphere were similarly warm during the early Cenozoic (Greenwood and Wing, 1995; K. Johnson, personal communication).

Compounding this evidence, geochemical proxies of ocean bottom water temperatures show that the deep waters were as mild as 10°C during the Paleocene and Eocene epochs (e.g., Zachos et al., 2001). After reaching a thermal maximum fifty-two million years ago, the climate began a long-term cooling trend; the first Cenozoic glaciation marks the end of the Eocene epoch (e.g., see figure 1-1).

Yet while polar temperatures varied substantially through the Cenozoic, tropical values were stable. Schrag (1999) estimated that Eocene tropical temperatures were similar to today's readings, while Pearson et al. (2001) suggest they were slightly warmer. Taken together, there is persuasive evidence that the equator-to-pole temperature gradient was much weaker fifty million years ago than it is presently.

Herein lies the paradox: the atmosphere transports the bulk of the energy exported to high latitudes (Trenberth and Caron, 2001), and it accomplishes this principally by eddies, whose growth is predicated, in part, on a meridional temperature gradient at the surface (e.g., Charney, 1947; Eady, 1949). With a reduced equator-to-pole temperature gradient, how does the atmosphere or the ocean sustain the poleward flux of energy necessary to maintain such a weak gradient? The proxy data suggest that the efficiency with which the climate system transports enthalpy poleward should itself vary with the temperature gradient.

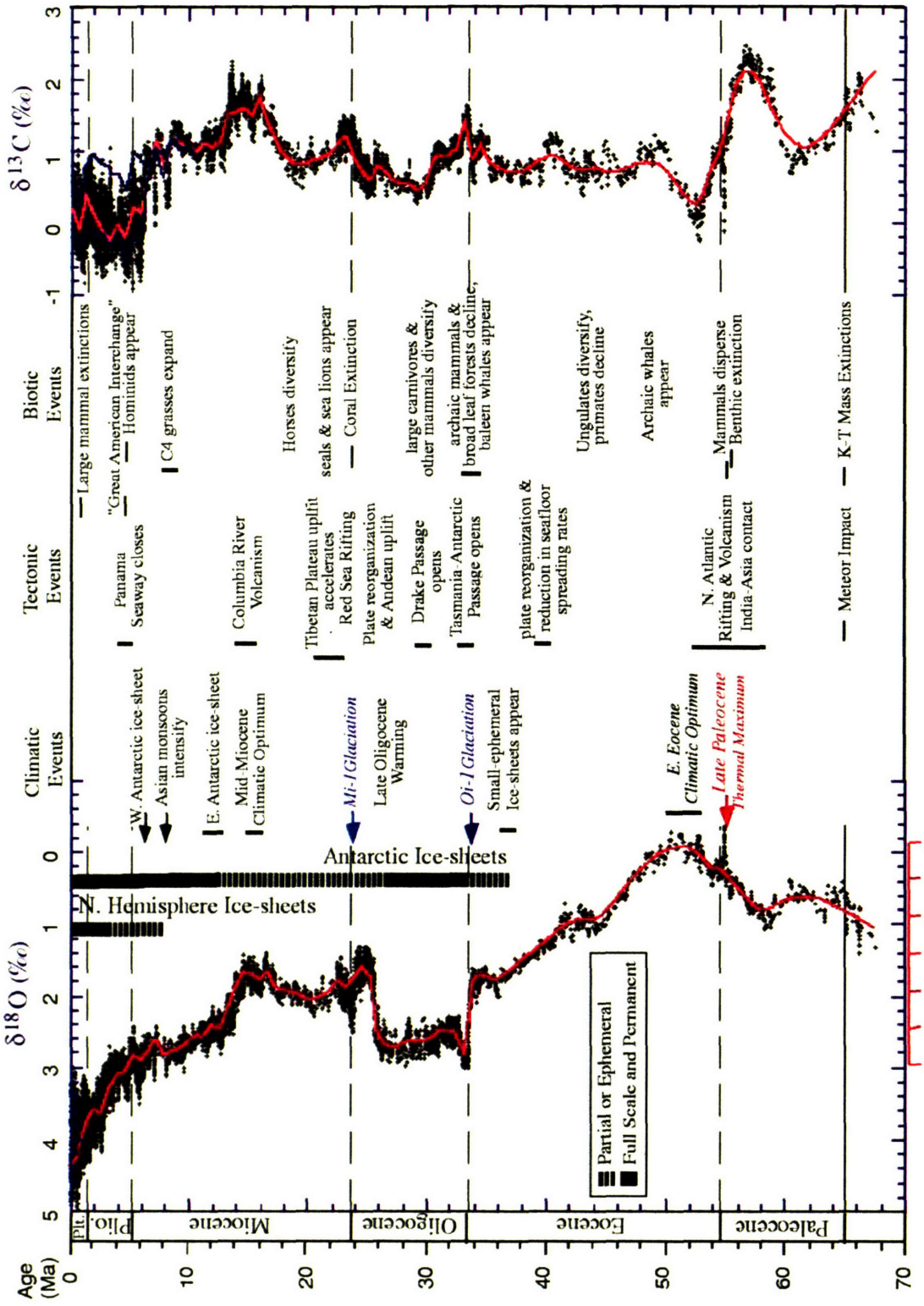

Figure 1-1: Major Cenozoic climate events; figure from Zachos et al. (2001). Note the warm bottom water temperatures inferred from low $\delta^{18}O$ values during the Paleocene and Eocene epochs.

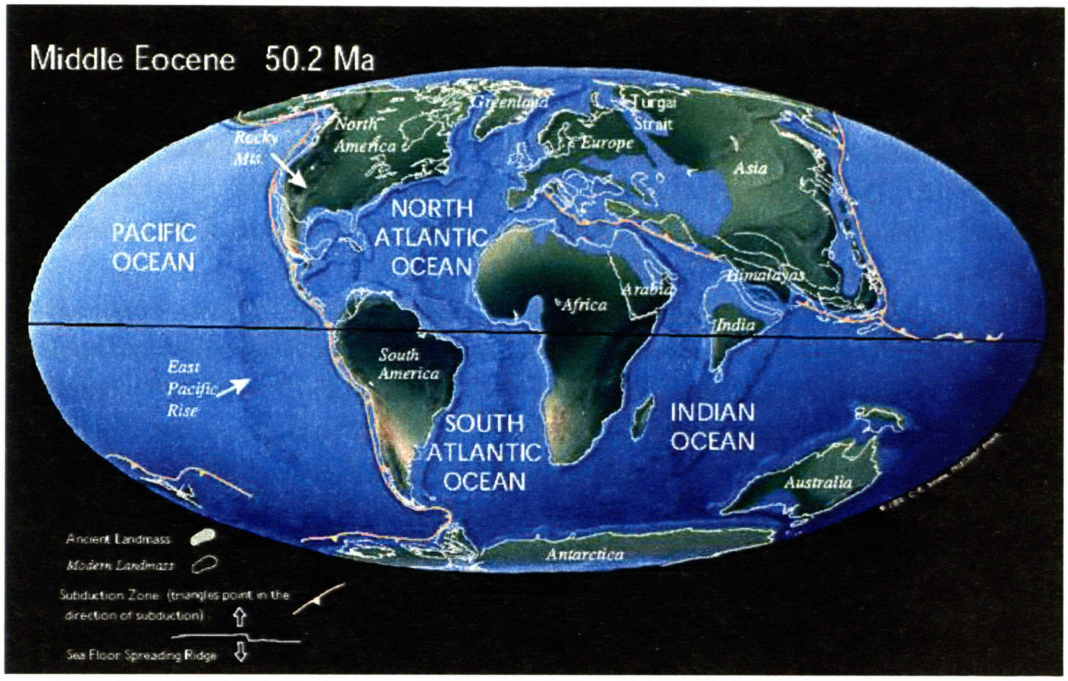

Figure 1-2: Chris Scotese's reconstruction of continental geography during the middle Eocene epoch. A deep Drake passage might not have opened until later in the Eocene, perhaps coinciding with the onset of Antarctic glaciation (Toggweiler and Bjornsson, 2000).

These conditions were not unique to the early Cenozoic. There is strong evidence that as much as three quarters of the Phanerozoic eon (the most recent 540 million years) was characterized by global warmth and a weak equator-to-pole temperature gradient (e.g., Huber et al., 2000). But over such tectonic time-scales, the location, configuration, and shape of the planet's landmasses become important factors in determining global climate (e.g., Barron, 1983). Continents located at high latitudes are more susceptible to seasonal variability than are high latitude oceans since land has a lower thermal capacity than water. For this reason, global ice can accumulate more easily when there is land in polar latitudes than when oceans are present there. Periods such as the Paleocene and Eocene epochs, which remained ice-free even while land stretched to high latitudes, are puzzling to understand. (See figure 1-2 for a map of the middle Eocene.)

Barron (1983) was among the first researchers to study the warm climate problem.[1] He found that paleogeography and efficient ocean transport were insufficient by themselves to explain mid-Cretaceous warmth (Barron and Washington, 1982;

[1] In the early literature on this subject, the term "equable climate" was used frequently to describe warm periods such as the Cretaceous and Paleogene. This phrase emerged during a time when proxy data suggested tropical temperatures were cooler than today (see Zachos et al., 1994, and references therein); combined with warmer high latitudes, it suggests a slight or absent temperature gradient. In light of more recent estimates that show tropical temperatures were not any cooler than they are today (e.g., Pearson et al., 2001), I use the phrase "warm climate" to refer to this state.

Schneider et al., 1985). In a separate simulation, elevating carbon dioxide created a new problem: predicted tropical temperatures exceeded the range suggested by proxy data (Barron and Washington, 1985). [Early proxies suggested the tropics were cooler than they are today, placing a particularly strong constraint on tropical temperatures (see Zachos et al., 1994, and references therein).] More recent studies have confirmed that elevated carbon dioxide alone does not produce a weak surface temperature gradient (e.g., Shellito et al., 2003).

The rise in tropical temperatures with high levels of carbon dioxide led some researchers to doubt that radiative forcing could be a viable mechanism for the Cretaceous or Eocene climate (e.g., Sloan et al., 1995). It is a bit curious, however, that this forcing has been considered only in isolation from other mechanisms, such as enhanced ocean heat transport [compare Sloan and Rea (1995) with Sloan et al. (1995)], even though fully coupled simulations of past climates are now feasible.

This thesis presents a new view of the dynamics of warm climates. The flora and fauna that populated the Arctic coastline are dramatic, but perhaps they have led us to ask the wrong question. Rather than ask why high latitudes were so warm, perhaps the question should be, why were the tropics so cool? If carbon dioxide (Pearson and Palmer, 2000), methane, and water vapor were abundant enough to raise temperatures around the globe, preclude ice even at high latitudes, and keep continental interiors from freezing during winter, the proper question for the Eocene and Cretaceous is why were tropical temperatures so similar to today?

In this thesis, we first analyze the atmospheric transport in the presence of a weak temperature gradient and assess whether existing theories regarding polar stratospheric clouds are tenable. In the second half of the thesis, we show that ocean models are quite sensitive to diffusion of heat in locations that are vigorously mixed by the passage of tropical cyclones. We then examine whether a parameterization of diapycnal diffusion that includes the effects of tropical cyclone-induced mixing is able to produce an elevated ocean heat transport. Combined with higher concentrations of greenhouse gasses, this has the potential to eliminate the gap between proxy data and climate model predictions.

Below, some background to the main problems studied in this thesis is presented, followed by an outline of the questions considered.

1.2 Existing theories

Early paleoclimate modeling studies (e.g., Barron and Washington, 1982; Schneider et al., 1985; Barron and Washington, 1985) illustrated the challenges that modeling warm climates present. When forced with isothermal sea surface temperatures and contemporary concentrations of carbon dioxide, continental interiors fall well below freezing during winter months (Schneider et al., 1985). While high latitudes warm when carbon dioxide is elevated sufficiently, the tropics do too (Barron and Washing-

ton, 1985), violating the constraint imposed by proxy data (Pearson et al., 2001).

Surprisingly little progress has been made since these early studies. Some researchers were discouraged by the inability of models to produce a weak temperature gradient, and questioned the veracity of the proxy data (see the exchange between Sloan and Barron, 1990; Archibald, 1991; Wing, 1991; and Sloan and Barron, 1991). Other work investigated radiative forcing and ocean heat transport separately (Sloan and Rea, 1995; Sloan et al., 1995), but to date no one has considered the mechanisms in combination, in spite of the availability of coupled models (e.g., Huber and Sloan, 2001; Shellito et al., 2003).

One of the limitations pointed out by the early work is that the meridional transport of enthalpy to high latitudes requires a vigorous general circulation to carry energy poleward; when forced with a weak gradient, atmospheric general circulation models produce a comparatively sluggish circulation incapable of sustaining the sea surface temperature gradient with which they were forced (Barron, 1983). There is a large implied ocean heat flux in such simulations, but no mechanisms were identified to produce a stronger ocean transport until recently (see Lyle, 1997; Emanuel, 2001; Nilsson et al., 2003; and discussion in the next section).

Farrell (1990) advanced the idea that if the Hadley circulation extended further poleward, an equable climate could be achieved. The difficulty with such an idea, however, is that the Earth rotates rapidly (the slow rotation of Venus permits a global Hadley circulation there), and fairly significant changes to the structure of the atmosphere would be necessary to achieve such a state. Lindzen and Hou (1988) show that a weaker pole-to-equator temperature contrast should result in a narrower Hadley cell. Absent any evidence to support Farrell's idea, little further work has been done on the topic.

To reconcile evidence of high-latitude, continental warmth during the polar nights of the Eocene epoch with general circulation models' inability to simulate such conditions, several authors have argued that elevated stratospheric water vapor in the polar nights of warm climates could lead to omnipresent polar stratospheric clouds, constituting an omitted feedback (Sloan et al., 1992; Sloan and Pollard, 1998; Sloan et al., 1999; Kirk-Davidoff et al., 2002). These authors note that polar stratospheric clouds are treated poorly, if at all, by general circulation models and postulate that optically thick, pervasive clouds could have insulated the Arctic during warm climates.

This idea has recurred unchecked in recent literature, and a careful review of the physics and dynamics necessary for this feedback has been lacking. Undoubtedly, the ubiquitous, seasonally persistent, optically thick polar stratospheric clouds Sloan et al. (1999) imposed would provide the surface warming they found, but the conditions they test are bizarre, and there is no evidence that the real atmosphere has ever behaved in such a manner. For example, polar stratospheric clouds that form over the Antarctic presently have an optical thickness of $O(10^{-2})$ (e.g., Rosenfield, 1992; Rosenfield, 1993), which makes them too thin to have an effect on Antarctic temperatures, but Sloan and Pollard (1998) impose stratospheric clouds with an optical

thickness that is 100 times greater than observed.

Regardless of its merits, this idea recently prompted some intriguing research. Noting that changes in planetary wave activity and in the refractive index for vertical propagation affect the meridional overturning of the stratosphere, Kirk-Davidoff et al. (2002) proposed that the state of the stratosphere will vary with the surface planetary temperature gradient. The stratosphere's overturning is a residual circulation driven by upwardly propagating Rossby and gravity waves. This overturning drives the tropical lower stratosphere colder than radiative equilibrium, and it dynamically heats the winter polar stratosphere. Kirk-Davidoff et al. (2002) argued that a weaker temperature gradient at the surface would reduce wave generation and ultimately lead to a weaker diabatic circulation in the stratosphere. These changes would warm temperatures near the tropical tropopause, which in turn raises the concentration of water vapor that can cross into the stratosphere. Additionally, a weaker overturning circulation would lessen the dynamical heating of the polar vortex, permitting temperatures to fall to colder values during the polar night. Such changes would bring temperatures in the Arctic vortex closer to radiative equilibrium and the local frost point of water. Their idea prompts an interesting question: is the state of the stratosphere a function of surface climate?

Previous modeling studies provide evidence that this mechanism may operate in unexpected ways. Rind et al. (1998) found that the residual circulation strengthened in a doubled carbon dioxide experiment as more energy became concentrated in the longest planetary-scale waves. The reasons why this occurs in this modeling study are somewhat less clear, but the wave-mean flow interaction presented in Kirk-Davidoff et al. (2002) is clearly idealized. Rind (2001) attempted to model the Paleocene with early Cenozoic geography, reduced topography, and a weak temperature gradient. In this study, reduced stationary wave generation and propagation led to a weaker stratospheric circulation. Clearly, the stratospheric response requires further study.

While this thesis does not assess all aspects of polar stratospheric cloud formation directly, we do investigate the thermal state and dynamic response of the stratosphere to forcing by the surface climate. Naturally, this work will have implications for the stratosphere's water vapor budget and provide a necessary foundation for examining the cloud hypothesis more critically.

1.3 Ocean heat transport

In the present climate, the world's oceans transport at least a third of the total poleward flux of enthalpy (Trenberth and Caron, 2001); equatorward of 20°, the ocean flux is larger than the atmospheric one (Peixoto and Oort, 1992).

Sloan et al. (1995) catalog a variety of methods by which an Eocene climate might be achieved; they estimate that, excluding other factors, the ocean heat transport would need to be double the contemporary flux in order to redistribute energy

and produce a weak temperature gradient. They estimate that the entire climate system must transport 30% more heat, but they appear to have neglected an important feedback on high latitude albedo.[2] We shall see at the end of this chapter that the flux of enthalpy needed to maintain a weak temperature gradient is not much different than what the total climate system transports today (Stone, 1978b).

Blindly accepting the ramifications of atmosphere only studies, namely that the ocean is mostly responsible for changes in the planetary temperature gradient, implicitly assumes that a general circulation model's dynamics are correct. Assumptions such as this often prove limiting. Lindzen et al. (2001) have argued that changes in tropical cloudiness and radiative windows to space could change with climate, and this would strongly influence the surface response. Moreover, until the last few years no mechanism had been proposed for increasing the oceans' circulation in warm climates, which led some to question whether enhanced ocean heat transport occurred during the Eocene (see, e.g., Sloan et al., 1995; Huber and Sloan, 2001).

New ideas offer a way to interactively couple the oceans' heat transport with the surface temperature gradient (e.g., Lyle, 1997; Emanuel, 2001; Nilsson et al., 2003). Some of the strongest evidence of high latitude warmth comes from fossils found along the Arctic coast and of mild surface and benthic ocean temperatures. Given the lack of any convincing mechanisms allowing the atmosphere to transport additional heat in the presence of a weak surface temperature gradient, it is natural to examine the oceans' transport more carefully.

The prevailing view among many ocean and climate dynamicists is that the oceans' meridional overturning circulation (Berggren and Hollister, 1974) and heat transport should weaken when the planetary temperature gradient weakens (e.g., Welander, 1986; Huber and Sloan, 2001), though there is some evidence the ocean responds minimally to large changes in carbon dioxide (Manabe and Bryan, 1985). The combination of weaker winds and a reduced density gradient produces a weaker ocean heat transport in some coupled studies (e.g., Huber and Sloan, 2001).

Nilsson et al. (2003) show that replacing fixed mixing with a fixed amount of energy available for mixing causes the meridional overturning circulation to strengthen when the planetary temperature gradient weakens, but the heat transported by this circulation, which is proportional to the product of the circulation's intensity and the

[2]While they do note that an ice-free planet would have a lower albedo at high latitudes later in their paper, they do not address this when they estimate that the total climate system must have transported 30% more heat poleward during the Eocene in order to maintain the weak temperature gradient inferred from proxy data. Their presentation is descriptive only, and they give no indication that they considered changes in the albedo when they estimated what the top of the atmosphere radiative fluxes would have been during the Eocene. Stone (1978b) showed that there is an anticorrelation between thermal emissions and albedo; as temperatures warm, snow and ice melt and the albedo decreases, allowing more of the incident shortwave radiation to be absorbed. This compensation minimizes the change in the local imbalance between absorbed solar radiation and emitted terrestrial radiation; thus, while the amount of enthalpy that must be transported from low to high latitudes increases with a weaker temperature gradient, the albedo feedback limits the magnitude of the required increase.

pole-to-equator temperature difference, does not increase. If, however, mixing were substantially stronger during warm climates, it is conceivable that a vigorous circulation could transport more heat even when the temperature gradient decreases. When mixing evolves with stratification, as in Nilsson et al. (2003), bottom waters may be more efficiently lifted during warm climates because temperatures at high latitudes increase and bottom waters warm, weakening the global stratification. There is a paucity of data from which mixing in the present climate can be inferred, and there is no proxy to deduce how it might have varied in the geologic past (E. Boyle, personal communication).

What could cause ocean mixing to increase during warm climates? As we shall see later in this thesis, tropical cyclones mix regions of the ocean to which the heat transport is quite sensitive, and Emanuel (2001) has argued that the poleward heat flux required to compensate the mixing down of warm waters is large. In fact, a good deal of evidence already supports this claim. Scott (2000) showed that low-latitude mixing is important in a single-hemisphere model; Bugnion (2001) applied an adjoint to the MIT general circulation model and found that the oceans' heat transport was sensitive to mixing in the upper ocean near the equator. Boccaletti et al. (2005) have illustrated that the oceans' heat flux is carried almost exclusively in the upper 500 meters, a point alluded to earlier by Cummins et al. (1990) and Scott and Marotzke (2002).

Tropical storms, which to the oceans are nothing more than an intense, isolated burst of wind stress, induce strong mixing of thermocline water with the surface mixed-layer owing to a shear instability (Price, 1981); this mixing limits the intensity that a storm can achieve (Schade and Emanuel, 1999; Emanuel et al., 2004) in addition to leaving a rich structure of temperature and current anomalies in its wake (Price, 1983). Raymond et al. (2004) recently presented data showing that mixing in the thermocline of the eastern tropical Pacific occurs only when the shear in near-inertial waves is strong enough to cause the local Richardson number to fall below a critical value. As a result, oceanic mixing is a highly nonlinear process, with no mixing occurring when the shear does not cross the instability threshold. They conclude that the strongest atmospheric disturbances will be responsible for nearly all of the total mixing. Climate models, which do not consider this dependence, could accumulate large errors when extrapolated to different climates.

In this thesis, we shall investigate the climate response when mixing induced by tropical cyclones is considered. During the Eocene, these storms were likely much stronger because tropical sea surface temperatures were higher (Pearson et al., 2001) and the ocean stratification was weaker; Emanuel (1988a) and Schade and Emanuel (1999) demonstrate that these factors strongly regulate the intensity a storm can achieve. Recent calculations also suggest storms were likely to be more frequent (Emanuel and Nolan, 2004) and, perhaps, persist at their peak intensity for longer (e.g., Emanuel, 2005). Taken together, there may have been much more mixing in the upper tropical oceans during the Eocene than there is today.

1.4 Thesis overview

Figure 1-3 shows a calculation of the poleward energy transport required to sustain the present planetary temperature gradient and the transport necessary to produce a weaker temperature gradient like that of the Eocene epoch (with a 15°C pole-to-equator temperature difference). Recent estimates of the present climate from Trenberth and Caron (2001) are shown for reference.

One of the most vexing questions regarding warm climate states is how can the atmosphere or the ocean produce a robust heat flux when the planetary temperature gradient is weak? Figure 1-3 shows that the climate system must have produced a

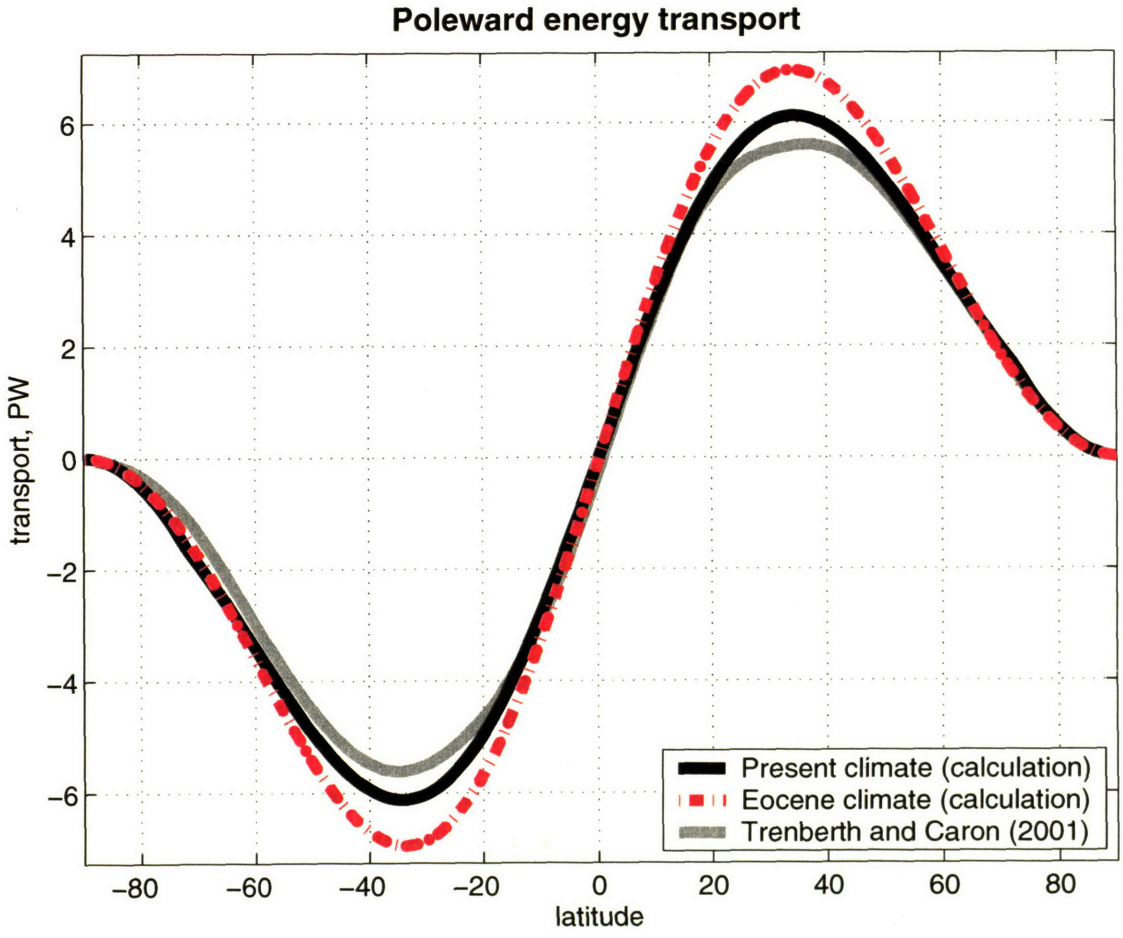

Figure 1-3: Calculations (see Appendix A for details) of the poleward energy transport needed to sustain the present climate (solid, black line) and a climate with a weak temperature gradient (dash-dotted, red line). The estimate of the real climate system's present energy transport from Trenberth and Caron (2001) is shown in solid gray for reference. This simple calculation suggests the present climate needs to transport a peak of 6.12 PW [Trenberth and Caron (2001) estimate the actual peak to be 5.61 PW], while in the Eocene it would peak at 6.94 PW. See Appendix A for further discussion.

modest 13% increase in the heat transport during the Eocene (relative to present), but both atmospheric (e.g., Shellito et al., 2003) and oceanic (e.g., Huber and Sloan, 2001) general circulation models suggest that the heat transport in each media should decrease when the temperature gradient is weak. The small increase in the total heat transport may appear a bit surprising at first, but Stone (1978b) showed that the leading term in the expansion of the poleward flux is completely independent of the structure of the system; aside from the global mean albedo, no external parameters affect the leading term. Thus, the geometry of the planet tightly constrains the strength of the flux; additionally a compensation between increasing thermal emissions and decreasing albedo with warming high latitude temperatures further minimizes changes in the strength of the flux (Stone, 1978b). Still, it is not obvious how the system could sustain the present flux, much less increase in the presence of a weak temperature gradient.

As discussed earlier, it is well known that atmospheric general circulation models fail to transport sufficient heat in order to reduce the planetary temperature gradient to the levels proxy data insist were present during the early Cenozoic. We shall see an example of this in the simulations presented in Chapter 3. In the first half of the thesis, we confine our focus to how temperatures in the winter stratosphere were likely to evolve in the presence of a weak temperature gradient. Sloan et al. (1992) hypothesized that high altitude clouds were responsible for mild polar conditions; this remains a largely untested proposition. While we shall not address the presence of polar stratospheric clouds directly, we do examine whether dynamics were likely to evolve into a state conducive for large-scale, abundant cloud formation.

We pursue a novel view of warm climates in the second part of this thesis. Barron and Washington (1985) found that elevated concentrations of greenhouse gases could warm the planet and create ice-free conditions at the poles, but many paleoclimate modelers have been reluctant to accept this idea because tropical temperatures were not much warmer than they are today. But if the tropical oceans were more vigorously mixed during such times, the tropical climate may have been stabilized by mixing down warm surface waters and transporting heat poleward. We shall see that tropical cyclones mix in regions that could accomplish this feat.

The thesis is organized as follows. Chapter 2 contains a review of stratospheric dynamics, polar stratospheric clouds, and a problem that demonstrates how the thermal structure of the stratosphere is set. The feasibility of reaching polar night temperatures cold enough to support synoptic-scale stratospheric cloud formation is examined with a two-dimensional model. Simulations from a three-dimensional atmospheric general circulation model are presented in Chapter 3. The stratospheric structure, atmospheric energy cycle, and atmospheric enthalpy transport in warm climates are discussed and compared with simulations of the present climate.

We examine where vertical mixing matters most to the oceans' heat transport in Chapter 4. This work extends the progress begun in single-hemisphere models, and the sensitivity to mixing in the upper tropical oceans around the world is ex-

plored. We demonstrate that the coupling of ocean mixing to the climate state has profound implications for the Cretaceous and Eocene epochs at the beginning of Chapter 5. Parameterizations of vertical mixing that incorporate a dependence on the local stratification and the power put into the ocean by tropical cyclones are tested using a simple coupled model. The combination of elevated greenhouse gasses and vigorous upper ocean mixing that evolves with tropical cyclone statistics are able to produce conditions that look similar to the proxy evidence from warm climates of the geologic past. The results of these tests are promising.

Before proceeding, a word of caution. As noted earlier, general circulation models have had great difficulty sustaining weak temperature gradients. This immediately suggests that such tools have limitations when pushed to states far from the present climate. I emphasize that the questions in this thesis focus on processes and examine the behavior of the climate system. No attempt is made to simulate fully any specific periods in the geologic past. Our present, limited understanding renders that task a difficult feat, but the results and conclusions of this thesis should prove useful in understanding some of the more enigmatic problems of warm climates.

Chapter 2

The stratosphere in warm climates

2.1 Motivation

The stratosphere is dry. Water vapor in this layer comes from two principal sources: transport across the tropical tropopause and the oxidation of methane. Temperatures near the tropical tropopause are colder than in nearly every other region of the troposphere and stratosphere, though temperatures can drop to lower levels in the stratospheric Antarctic vortex during the Southern Hemisphere winter. The cold temperatures at the tropical tropopause prohibit the transport of large amounts of water vapor into the stratosphere and limit the region's saturation specific humidity over ice ($q^{\#}$), the maximum value of water vapor that an air parcel can hold. This quantity is a state variable, a function of temperature and pressure alone.

In spite of the paucity of research on middle atmosphere dynamics in climate states very different from present conditions, speculation that polar stratospheric clouds contributed substantially to high-latitude warmth during the early Cenozoic grew during the last decade (Sloan et al., 1992; Sloan and Pollard, 1998; Sloan et al., 1999; Kirk-Davidoff et al., 2002). In some respects, manipulating cloud parameterizations offers an easy route by which models can be forced to reproduce warm climate states. Clouds are poorly represented in models, heavily parameterized, and have a strong impact on the climate. The initial work on this problem imposed thick polar stratospheric clouds to quantify the magnitude of the induced surface warming. It is large, but such clouds and the dynamics necessary for their formation may not be viable for reasons best summarized by the phrase, occasionally heard when seeking directions in New England, "You can't get there from here." This state may be unreachable for many reasons, including radiative-cloud feedbacks on the temperature of the polar stratosphere.

To begin to understand why seasonally persistent, large-scale polar stratospheric clouds are not viable presently, consider figure 2-1. Temperatures in the Arctic vortex may drop to 200 K, but this is far warmer than the temperatures required for condensation of a parcel of air containing 5 ppmv water vapor, a common estimate of

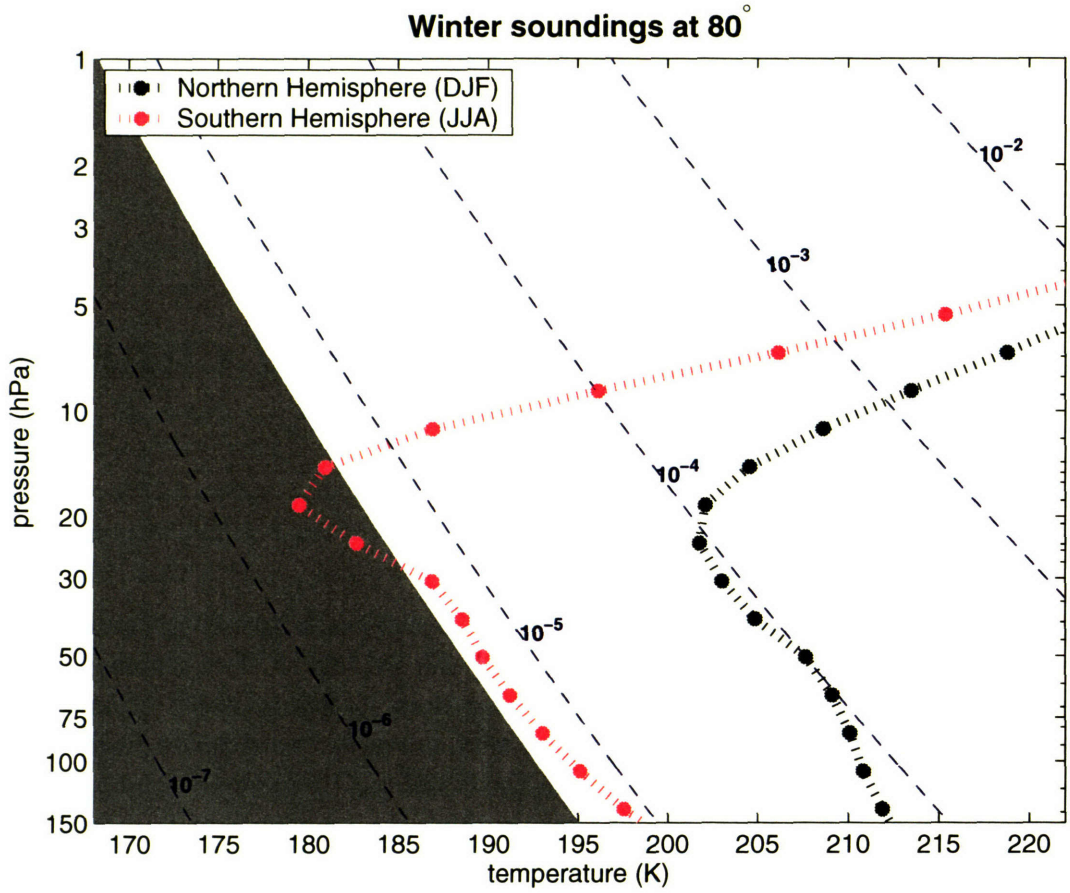

Figure 2-1: Vertical structure of zonally averaged temperatures at 80°N (black) and 80°S (red) during the winter months. Saturation vapor curves are plotted in dashed blue lines; these are labeled with the maximum amount of vapor a parcel at this (T, p) can hold in units of parts by volume (e.g., 10^{-6} represents a concentration of 1 ppmv water vapor). The shaded area represents the (T, p) values in which $q^{\#}$ is less than or equal to 5 ppmv, the ambient concentration of water vapor in the polar winter stratosphere. The relative warmth precludes large-scale, persistent polar stratospheric clouds in the Arctic in the present climate.

winter polar stratospheric water concentrations (e.g., Remsberg et al., 1984; Kent et al., 1986; MacKenzie et al., 1995). In fact, were temperatures to remain fixed, water vapor concentrations would have to increase by more than an order of magnitude over present values in order for this condition to be met. Even then, research by Jeff Kiehl (personal communication) shows that the formation of a thickening polar stratospheric cloud pushes the local temperature higher owing to the radiative forcing of the cloud itself. This warming is intense enough to push the area enveloping the cloud above the saturation point of water, causing the cloud to equilibrate with a small optical thickness and a thin depth. This is consistent with the observational findings of Rosenfield (1992).

Temperatures in the Antarctic during July are much nearer to the frost point of a parcel of air holding 5 ppmv water vapor; these temperatures are low enough to permit widespread polar stratospheric cloud formation. As will be discussed in section 2.2, polar stratospheric clouds begin to form when the temperature falls to within $\sim$3 K of the frost point temperature. Winter temperatures in the Southern Hemisphere are cold enough for polar stratospheric clouds, and they are more abundant than in the Northern Hemisphere. Still, these clouds are not optically thick, and any surface warming effects of these clouds are insufficient to keep Antarctica from reaching extremely cold temperatures (e.g., Kinne and Toon, 1990; Rosenfield, 1992).

Winter stratospheric temperatures limit cloud formation, but since dynamics govern the large departures from radiative equilibrium (e.g., Andrews et al., 1987), any thorough study of the prerequisites for cloud formation must include an assessment of the dynamical state of the layer. During winter, planetary-scale waves propagate into the stratosphere and deposit momentum, which decelerates the jet and drives a residual mean meridional overturning circulation. This circulation drives the tropical lower stratosphere colder than radiative equilibrium and dynamically warms the polar stratosphere.

Kirk-Davidoff et al. (2002) argue that changes to the overturning circulation would affect the temperatures near the tropical tropopause, which in turn would affect stratospheric concentrations of water vapor. Additionally, a weaker overturning circulation would permit temperatures in the polar vortex to fall to colder levels during the polar night, bringing these temperatures closer to radiative equilibrium and to the local frost point of water. Such a mechanism may be complicated, however; increased longwave cooling to space as water vapor concentrations rise in the tropics places an upper bound on the temperature, and thus the frost point, that the tropical lower stratosphere can achieve.

In this thesis, we shall examine the way in which dynamics and radiative forcing in warm climates alter the stratosphere's large-scale circulation, thermal structure, and energetics. The dynamic response governs how the temperature field will evolve, thus altering the ease with which polar stratospheric clouds form. Understanding this response is a prerequisite to critically assessing the merits of the polar stratospheric cloud hypothesis, but this information is valuable in its own right.

As noted earlier, we shall not assess directly whether or not polar stratospheric clouds were more abundant or thicker during warm climates in the past. Their presence is predicated on several thermal and chemical requirements; it is not possible to reconstruct all of the necessary parameters from the geologic record. Rather, in this chapter and the next I present the response of the stratosphere to different surface boundary conditions and to radiative forcings of elevated concentrations of greenhouse gasses. From this we can assess whether the thermal structure of the stratosphere becomes more or less conducive to the formation of polar stratospheric clouds in the Arctic during winter.

This chapter contains an introduction to polar stratospheric clouds and strato-

spheric dynamics. Following a review of related studies, I present the dynamical and radiative changes found in a simple two-dimensional model devoid of eddies. This work will lay the foundation for a discussion in the next chapter of results from a more comprehensive study using the Community Atmospheric Model developed at the National Center for Atmospheric Research. These chapters conclude with a discussion challenging the use of polar stratospheric clouds to close the gap between geologic evidence of warmth and general circulation model predictions. None of these results shows whether such clouds were more abundant. By diagnosing how the residual mean circulation varies with climate state, however, we can explore whether it is reasonable to expect more clouds and, to the extent possible, assess whether this mechanism constitutes a tenable theory.

2.2 Polar stratospheric clouds

Recorded observations of polar stratospheric clouds date at least to the nineteenth century; they were known first for their colorful glows filling the polar skies during winter and early spring (Stanford and Davis, 1974; Tabazadeh et al., 2001). In the decades following the seminal work of Molina and Rowland (1974), which predicted the destructive power of cholorofluorocarbons on stratospheric ozone, research on mechanisms by which ozone loss occurs accelerated. Solomon et al. (1986) hypothesized and Molina et al. (1987) and Tolbert et al. (1987) proved that polar stratospheric clouds promote the formation of active chlorine, which catalytically destroys ozone molecules. Largely owing to the importance of these clouds to stratospheric chemistry, there is a great body of work in which their microphysical structure and the dynamics governing their presence are examined.

Polar stratospheric clouds are classified into two groups: those that are composed of hydrated nitric acid particles (Type I) and those that are primarily composed of nonspherical, crystalline ice particles (Type II) (Seinfeld and Pandis, 1991). Type I clouds are subdivided into two additional groups: Type Ia, which are composed of crystals of nitric acid trihydrate ($HNO_3 \cdot 3H_2O$, abbreviated NAT), and Type Ib, which consist of supercooled ternary solutions of nitric acid (HNO_3), sulfuric acid (H_2SO_4), and water. Observations suggest that Type II clouds are rare in the Arctic, as the frost point is seldom reached.

The frost point temperature, T_f, is the temperature at which ice saturation occurs:

$$e^{\#}(T_f) = e, \tag{2.1}$$

where e is the partial pressure of water (vapor pressure), and $e^{\#}$, the saturation vapor pressure over ice, is defined empirically (e.g., Emanuel, 1994):

$$\ln e^{\#} = 23.33086 - \frac{6111.72784}{T} + 0.15215 \ln T; \tag{2.2}$$

the units of T are in Kelvin. The amount of water vapor a parcel of air can hold is additionally a function of pressure. The saturation specific humidity over ice, $q^{\#}$, is defined (e.g., Emanuel, 1994):

$$q^{\#} = \frac{\rho_v^{\#}}{\rho_d + \rho_v^{\#}} = \frac{\epsilon e^{\#}}{p - e^{\#}(1 - \epsilon)}, \tag{2.3}$$

where ρ_v is the density of water vapor, ρ_d is the density of dry air, ϵ is the ratio of the molecular weights of water and dry air (equivalently, $R_d/R_v \approx 0.622$), and the pound superscripts (#) denote saturation over ice. The specific humidity, q, may be calculated by substituting the vapor pressure, e, for the saturation vapor pressure, $e^{\#}$, in equation (2.3). Type II clouds are limited to forming when the temperature falls below the frost point temperature, a condition met rarely during winters in the Arctic (see figure 2-1). The temperatures at which Type I clouds can form are usually 3-4 K warmer than the frost point temperature, though this depends partially on concentrations of nitric acid (e.g., Carslaw et al., 1994).

The formation of Type I clouds is quite sensitive to both the local temperature and the rate of cooling. There is a narrow range of temperatures at which nitric acid dihydrate and NAT crystallization are maximized; in the present atmosphere, Type I cloud particle production rates peak at 191 ± 1 K (Tabazadeh et al., 2001). Below these temperatures, production rates decrease quickly (Tabazadeh et al., 2001); as a result, homogeneous freezing of solid polar stratospheric clouds occurs more readily when temperatures pass slowly through this range. Type II clouds form once the frost point is reached, usually at temperatures colder than 185-190 K, depending on altitude (Seinfeld and Pandis, 1991; see also figure 2-1). These temperatures are colder than the synoptic climatological temperatures in the Arctic winter. Local variations owing to meso-scale cooling can lower temperatures to the frost point, but such conditions are limited spatially and temporally, confining polar stratospheric clouds to a short period in mid-winter (Carslaw et al., 1994). Gravity waves may induce local cooling in which the temperature falls below the frost point temperature, but such deviations are limited in scale (Carslaw et al., 1994).

Airborne measurements taken during winter in the Antarctic suggest that polar stratospheric clouds impart a radiative feedback on stratospheric temperatures. These effects are complex because the clouds facilitate ozone depletion, the severity of which affects late winter and spring temperatures in the polar stratosphere. During the Antarctic polar night, observed clouds produced only small heating rates, ~ 0.1 K/day (Rosenfield, 1992). When the surface was relatively warm (such as over the Antarctic coast), the troposphere clear, and polar stratospheric clouds more abundant, ambient stratospheric temperatures rose ~ 6 K, though a more typical range was limited to ± 1-2 K (Rosenfield, 1993). Kiehl et al. (1988) found ozone depletion in the Antarctic spring leads to a 5-6 K drop in lower stratosphere temperatures during October. As stratospheric water vapor decreases when large ice particles form and sedimentation

continues, infrared cooling to space is reduced. This partially offsets the cooling by ozone loss and causes a net rise of 2-3 K in the polar night owing to the combined effects of dehydration and ozone depletion (Mancini et al., 1992). In regions where the temperatures are only marginally favorable for polar stratospheric cloud development, this slight warming could prove significant in warming adjacent regions above the threshold temperature. As noted earlier, Jeff Kiehl has done some work using a thermodynamic model that demonstrates the difficulty of achieving thick clouds owing to this feedback.

These studies show that the formation and maintenance of polar stratospheric clouds is complex, and that simple arguments regarding the conditions governing their formation are incomplete. Nevertheless, because some work in the literature addresses the role pervasive, seasonal clouds with extreme emissivity could have played during the Eocene epoch, we address whether the requisite thermal conditions for such extreme clouds are feasible.

Here we confine our interest to whether temperatures over long times and over large areas were favorable for the formation of such clouds; such information is necessary in order to evaluate whether or not it is reasonable to suspect polar stratospheric clouds played a significant role in the radiative balance of high-latitude winters. For this reason, we focus on synoptic-scale temperatures, recognizing that local deviations could produce more favorable conditions for cloud formation in smaller areas. To influence the surface climate strongly, polar stratospheric clouds must be rife, optically thick, and seasonally persistent (e.g., Sloan and Pollard, 1998; Kirk-Davidoff et al., 2002).

While Type I clouds represent the vast majority of polar stratospheric clouds that form in the Arctic presently (Stein et al., 1999), their formation is predicated on requisite chemical concentrations for which data are unavailable in past climates. For this reason, this chapter is devoted to assessing radiative and dynamical changes in the stratosphere and whether such alterations suggest that Type II (ice) clouds were more likely in past climates. While ozone destruction and radiative warming occur regardless of whether Type I or Type II clouds form, the absence of information about chemical concentrations limits my study to assessing the thermal requirements for polar stratospheric cloud formation, not the chemical ones. Both Type I and Type II clouds depend on concentrations of water vapor; Type I depend additionally on concentrations of nitric acid. Increased water vapor concentrations would raise the threshold temperature for cloud formation of either type (Carslaw et al., 1994).

2.3 Review of the stratosphere

Before examining whether polar stratospheric clouds were more likely to form in past climates, one must understand how the temperature and dynamics of the winter stratosphere evolve; radiation and dynamics control the large-scale temperature field.

Cold temperatures in the polar night, closer to those in radiative equilibrium than observed presently, are a necessary precursor to polar stratospheric cloud formation. Must increasing longwave absorption continuously cool the stratosphere? I examine a series of simple problems in the first subsection to address this.

This section contains a cursory review of the stratospheric temperature structure, overturning dynamics, and a review of research testing increased polar stratospheric clouds as a mechanism for sustaining high-latitude warmth during periods such as the Eocene epoch. Much of the material for the second subsection has been summarized from the review paper by Shepherd (2000) and from Alan Plumb's course notes on the middle atmosphere.

2.3.1 Radiation and the vertical temperature structure

At the dawn of the twentieth century, it was well known temperatures cooled away from the surface; the atmosphere was believed to cool continuously to the background coldness of space until Teisserenc de Bort (1902) published his conclusions from balloon data retrieved from 11-14 km altitude, which showed that a stably stratified layer exists (see also Hartmann, 1985).

Earth's atmosphere is largely transparent to solar radiation, but there are important exceptions. Clouds and surfaces reflect a portion of this radiation, and a small amount of it is absorbed in the atmosphere. Free and molecular oxygen in the thermosphere, ozone in the upper stratosphere, and the surface all absorb shortwave radiation, which heats these regions to local thermal maxima. Away from each of these the temperature decreases, and convection acts to redistribute heat vertically in the troposphere. Minimum temperatures in the lower atmosphere occur near the tropopause, the boundary between the troposphere and stratosphere.

From simple radiative equilibrium calculations, it is possible to make some important deductions about the atmosphere. Balancing the fraction of incoming solar radiation absorbed with the outgoing longwave radiation yields a predicted effective emissions temperature, T_e, of 255 K:

$$\frac{S_o}{4}(1-\alpha) = \sigma T_e^4. \tag{2.4}$$

The solar constant is S_o, α is the planetary albedo, and σ is the Stefan-Boltzmann constant. While T_e is sometimes mischaracterized as the temperature the surface would have if there were no atmosphere, such a label is unmeritorious. This calculation implicitly acknowledges the presence of an atmosphere on the left-hand-side by including the effects of water in the albedo. While water vapor warms the troposphere and surface by absorbing and re-radiating longwave radiation, clouds[1] and

[1] Clouds have a complicated impact; they both warm owing to absorption of longwave radiation by water vapor and cool by reflecting incoming shortwave radiation. High altitude clouds predominantly do the former while lower altitude clouds predominantly do the latter. If T_e were replaced with T_s, the

ice act to enhance the planet's albedo, giving it a value higher than it would have in their absence. If T_e were replaced with T_s, equation (2.4) would become incorrect: an atmosphere would be implicitly included on the left-hand-side, but neglected on the right, where the effect of returned longwave radiation from the atmosphere on the surface must be treated. The effective emissions temperature is the temperature at which the whole Earth system (the surface, the atmosphere, and all of its constituents) emits radiation to space. Interestingly, if α is set to zero in equation (2.4), T_e is 278 K, only ten degrees cooler than the observed surface temperature.

One-layer atmosphere

Now add an atmospheric layer that is transparent to incoming solar radiation but absorbs and emits longwave radiation with an emissivity of ε_1. Balancing radiation that is emitted (left-hand-side) with radiation that is absorbed (right-hand-side) at the surface yields:

$$\sigma T_s^4 = \frac{S_o}{4}(1-\alpha) + \varepsilon_1 \sigma T_1^4. \tag{2.5}$$

The first term on the right-hand-side is the incoming solar radiation; this can be substituted, using equation (2.4), with the effective emission temperature multiplied by the Stefan-Boltzmann constant (σT_e^4). The second term represents the radiation emitted by the atmospheric layer above the surface (layer 1). The balance at this level is:

$$2\varepsilon_1 \sigma T_1^4 = \varepsilon_1 \sigma T_s^4; \tag{2.6}$$

the factor of two on the left-hand-side arises because the atmospheric layer emits $\varepsilon_1 \sigma T_1^4$ both up and down. This system of equations can be solved directly; in the black-body limit ($\varepsilon_1 = 1$), T_s is 303 K and T_1 is 255 K, equal to the effective emissions temperature. For values of $\varepsilon_1 < 1$, both T_s and T_1 cool to lower values, and the effective emissions level (the altitude at which $T = T_e$) falls from the top of the atmosphere into the interior, here implicitly between layer 1 and the surface. Adding additional atmospheric layers (i), each of which with its own emissivity (ε_i), further raises the temperatures in the lower atmosphere and at the surface owing to the additional contribution of longwave radiation downwardly re-radiated by the new levels. See Appendix B for calculation details. Note that here and in a multi-layer problem without considering ozone heating (see section B.2), the maximum temperature at the top of the atmosphere is achieved in the blackbody limit. Thus, increasing the fraction of longwave radiation absorbed at the top layer has the effect of warming the layer by closing the window through which some longwave radiation escapes directly to space.

---

cooling effect of clouds would remain implicitly in α, but the warming effect of longwave absorption would be neglected.

Add a second, stratospheric layer

Next, make a small modification to the one-layer problem above by adding a second layer at the top. This layer is assumed to be thin enough so that its interactions with the lower atmosphere and the surface may be neglected. This new layer (layer 2) could represent a stratosphere in which an infinitesimal fraction of incoming solar radiation (A) is absorbed, and, since the layer is thin, an infinitesimal amount of radiation is absorbed and emitted in the longwave portion of the spectrum (emissivity $\varepsilon_2 \ll 1$). The temperature at this level (T_2) then may be calculated by:

$$\begin{aligned} 2\varepsilon_2\sigma T_2^4 &= A\sigma T_e^4 + \varepsilon_2\varepsilon_1\sigma T_1^4 + \varepsilon_2\left(1-\varepsilon_1\right)\sigma T_s^4 \\ \Longrightarrow T_2^4 &= \frac{A}{2\varepsilon_2}T_e^4 + \frac{\varepsilon_1}{2}T_1^4 + \frac{1-\varepsilon_1}{2}T_s^4. \end{aligned} \tag{2.7}$$

Note that the top of the atmosphere balance, which equates received solar radiation with outgoing longwave radiation, is:

$$T_e^4 = \varepsilon_2 T_2^4 + (1-\varepsilon_2)\varepsilon_1 T_1^4 + (1-\varepsilon_2)\left(1-\varepsilon_1\right)T_s^4,$$

but in the limit that $A \ll 1$ and $\varepsilon_2 \ll 1$ this reduces to the top of the atmosphere balance in the one-layer problem:

$$\sigma T_e^4 = \varepsilon_1 T_1^4 + (1-\varepsilon_1)T_s^4. \tag{2.8}$$

(This simplification is permissible as layer 2 is assumed to be thin enough so that it does not affect lower levels.) Substituting (2.8) into equation (2.7) yields:

$$T_2 = \left(\sqrt[4]{\frac{A}{2\varepsilon_2} + \frac{1}{2}}\right) T_e. \tag{2.9}$$

Note that for a fixed amount of solar heating, increasing the emissivity now has the effect of cooling this layer. This represents the stratosphere's balance between solar (ozone) heating and longwave cooling to space. For this reason, while elevated greenhouse gases warm the surface and troposphere, they cool the stratosphere. The fraction of longwave radiation absorbed by this layer will increase with increasing optical depth:

$$\varepsilon_2 \approx \rho_a k_a dz, \tag{2.10}$$

where ρ_a is the density of the longwave absorber (e.g., carbon dioxide), k_a is the absorption coefficient, and dz is the path length, here equal to the thin layer depth. Essentially, if A is fixed, as ρ_a increases so too does ε_2, which leads to a drop in T_2 according to equation (2.9). (Note that a proper radiative equilibrium calculation should be performed on a line-by-line basis, with each wavelength and each species having its own emissivity. Here the calculation is performed in a bulk fashion, treating

all longwave lines together in a semi-gray model.)

This problem is treated in most standard texts, and when coupled with a convective readjustment of the tropospheric layers, it demonstrates how the basic physics of radiative-convective equilibrium set, to a first approximation, the vertical temperature profile in the lower atmosphere (e.g., Hartmann, 1994). This predicts that increasing carbon dioxide or other longwave absorbers will lower the temperature of the stratosphere. But is this always true?

Does increasing CO_2 always cool the stratosphere?

Here I wish to extend this problem by explicitly allowing the second layer to interact with the ones below it. This relaxes the restriction imposed above that the layer must be thin. The behavior revealed is far more complex, and not all of it is relevant to planetary atmospheres. However, some intriguing questions arise from this relatively simple calculation.

Suppose now that the fraction of incoming solar radiation absorbed at the second layer and the longwave emissivity of that layer need not be negligibly small. This layer is now fully interactive with the lower atmospheric layer and with the surface as diagrammed in figure 2-2.

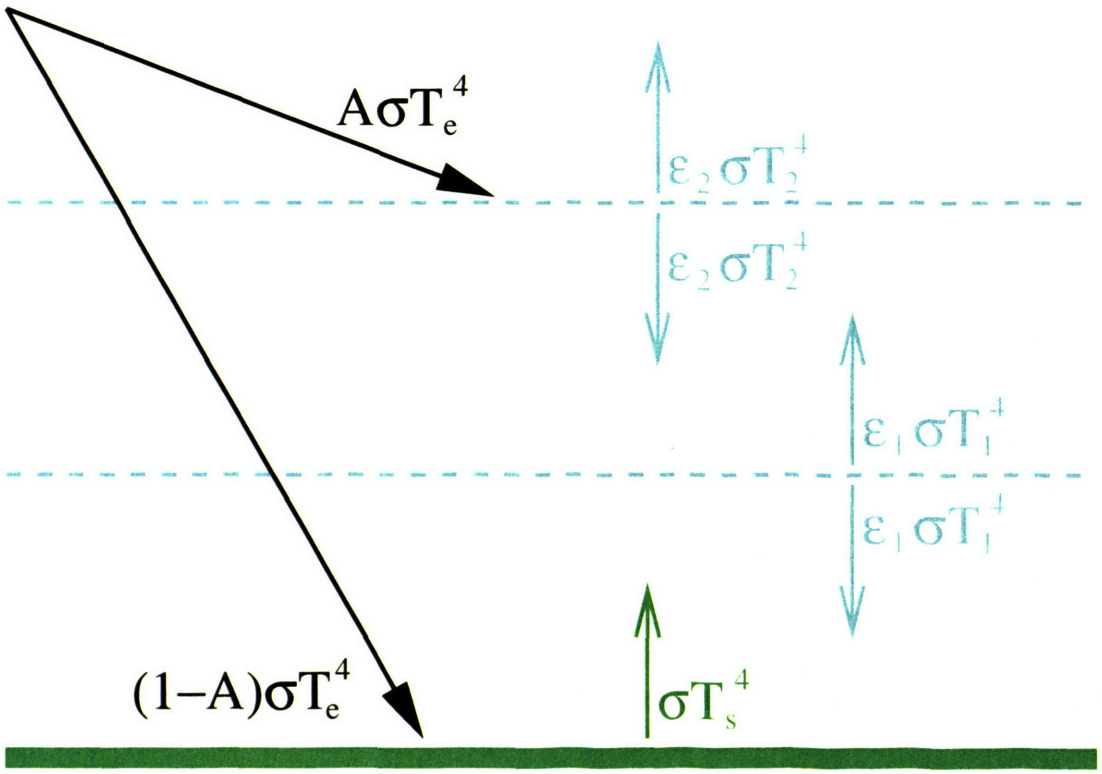

Figure 2-2: A two layer model in which a fraction (A) of the incoming solar radiation is absorbed at the top layer. Longwave emissivities of ε_1 and ε_2 govern the fraction of absorption and emissions at the two atmospheric levels.

The balances at the surface, first layer, and second layer are:

$$T_s^4 = (1-A)T_e^4 + \varepsilon_1 T_1^4 + \varepsilon_2 (1-\varepsilon_1) T_2^4 \quad (2.11)$$

$$2\varepsilon_1 T_1^4 = \varepsilon_1 T_s^4 + \varepsilon_2 \varepsilon_1 T_2^4 \quad (2.12)$$

$$2\varepsilon_2 T_2^4 = A T_e^4 + \varepsilon_2 \varepsilon_1 T_1^4 + \varepsilon_2 (1-\varepsilon_1) T_s^4. \quad (2.13)$$

Note that the balance at the top of the atmosphere now includes contributions from the second layer:

$$T_e^4 = \varepsilon_2 T_2^4 + (1-\varepsilon_2)\varepsilon_1 T_1^4 + (1-\varepsilon_2)(1-\varepsilon_1) T_s^4. \quad (2.14)$$

This system of equations can be solved, and the algebra is documented in Appendix B. The solutions for the second (top) layer are shown in figure 2-3. For values of $A \ll 1$ and $\varepsilon_2 \ll 1$, shown in panel (b), the traditional cooling with increases in ε_2 is shown. If it were possible for ε_2 to increase to non-negligible values, as in panel (c), a higher emissivity at the top layer higher first cools the layer, but then begins to warm as the emissivity increases further; when no shortwave heating is present, the increasing emissivity always causes a warming of the layer (see Appendix B for details of a two layer problem without ozone heating). The second layer starts to warm when the emissivity increases to the point that the local balance between longwave cooling and shortwave heating is disrupted: the longwave window to space closes as $\varepsilon_2 \to 1$.

It may be that the only portion of the parameter space relevant to the Earth is shown in panel (b) of figure 2-3. After all, carbon dioxide only absorbs at particular wavelengths, and there is a limit to the amount of radiation it can absorb. (After a particular wavelength has been entirely absorbed, it is said to be saturated, and further increasing the concentration of the responsible gas only broadens the amount of radiation absorbed to neighboring lines.) If, though, a larger range of values for ε_2 are achievable for the Earth, perhaps as in panel (c) of figure 2-3, our basic understanding of the stratosphere's response to increasing concentrations of longwave absorbers may be too simplistic.

2.3.2 Overturning dynamics

Interest in ozone drove a great deal of the research on stratospheric dynamics owing to the gas's critical importance in both atmospheric physics and chemistry. Brewer (1949) inferred that air entering the stratosphere must do so through the tropical tropopause from *in situ* measurements showing low amounts of stratospheric water vapor; in no other region are temperatures at the tropopause cold enough to provide sufficient dehydration. Dobson (1956) used ground-based measurements of total ozone to infer the existence of a stratospheric circulation, which transports ozone from its source region in the tropics to the extratropics. From these two studies, a picture of stratospheric overturning emerged and was named the Brewer-Dobson circulation; air

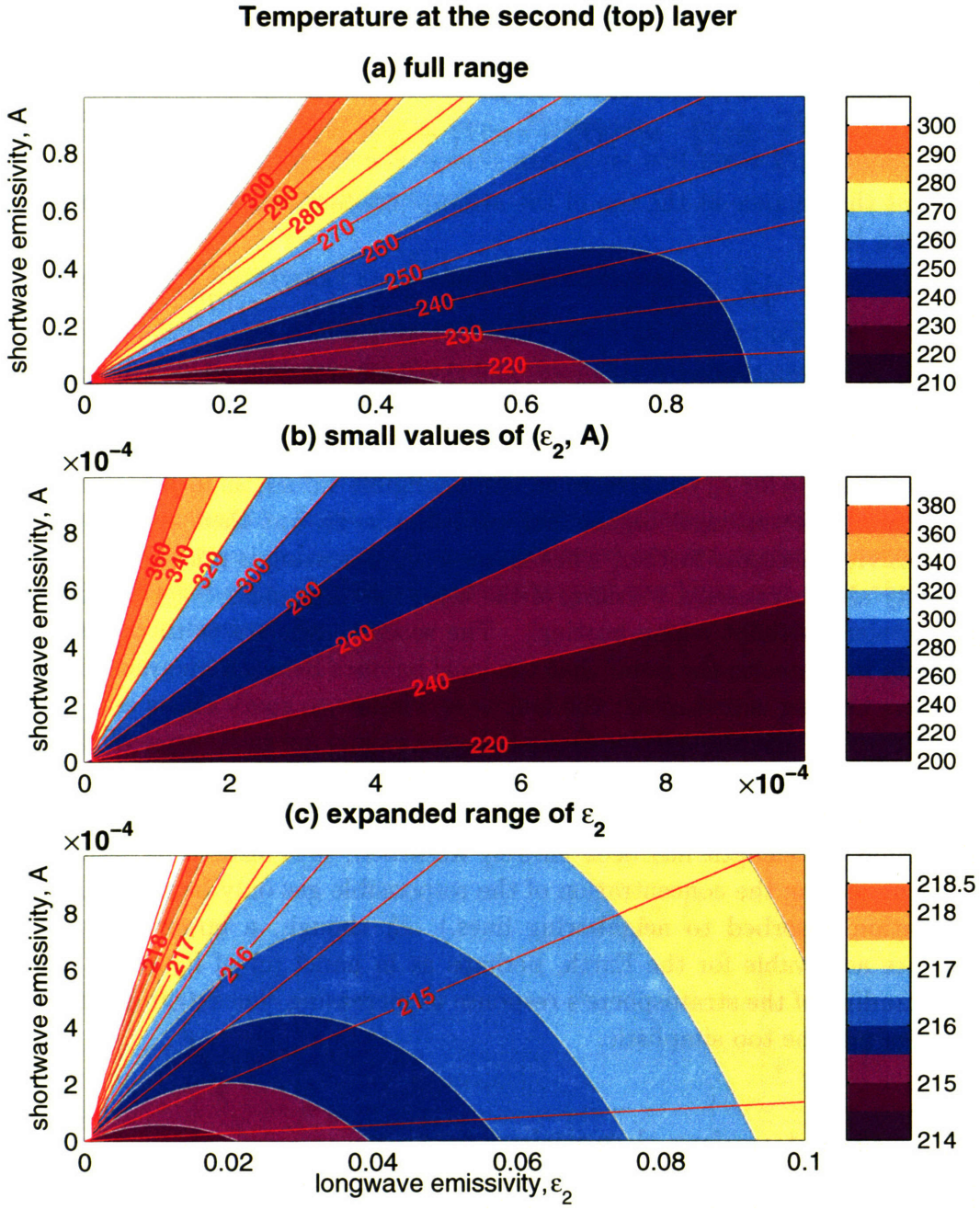

Figure 2-3: Temperatures at the second level when the values of A and ε_2 are permitted to influence the temperatures below. The labeled lines represent the estimate given by equation (2.9), which assumes that both A and ε_2 are small enough to be neglected at all levels beneath their layer. (a) Solution over the full range of A and ε_2. (b) Solution zoomed in on infinitesimal values of A and ε_2; note the good approximation by equation (2.9). (c) Solution expanded to view larger values of ε_2. In all three panels, the regions in white on the left side may greatly exceed the values on the color scale.

rises in the tropics, moves poleward in both hemispheres and sinks in the extratropics. Calculations of the radiative heating and cooling of the atmosphere are consistent with this view, with heating in the tropics and cooling at higher latitudes, particularly in the winter hemisphere (Murgatroyd and Singleton, 1961).

Once the amount of stratospheric wind data became sufficient to calculate the mean meridional circulation, discrepancies with the Brewer-Dobson picture emerged. Observational studies motivated many authors to conclude that eddies are able to influence both the magnitude and structure of the (Eulerian) mean meridional circulation in the winter stratosphere (Reed et al., 1963; Julian and Labitzke, 1965); in the Eulerian frame, these authors found a thermally indirect cell forced by waves with rising air over the winter pole and sinking in middle latitudes. The circulation inferred by Murgatroyd and Singleton's (1961) calculations, which used the radiative heating rates of Murgatroyd and Goody (1958), is in agreement with the Brewer-Dobson model. Dunkerton (1978) noted that the Lagrangian and Eulerian mean velocities need not coincide, and the circulation diagnosed from observations can be reconciled with the Brewer-Dobson cell by changing from an Eulerian to a Lagrangian viewpoint.

The Brewer-Dobson is easiest to view in isentropic coordinates where the thermodynamic equation is quite simple: the vertical velocity (across an isentrope) equals the diabatic heating, and there are no eddy terms by definition (e.g., Andrews et al., 1987). In the zonal momentum equation, the Coriolis term involves the meridional mass flux, which is the meridional wind (v) multiplied by the isentropic density (σ). The meridional mass flux on each isentropic surface ($[\sigma v]$) is fundamental in the angular-momentum balance, not the mean meridional wind ($[v]$); these quantities need not be in the same direction. Thus the Brewer-Dobson circulation is a circulation of mass transport, and it can be deduced from the generalized Lagrangian mean equations. The transformed Eulerian mean equations, which absorb the eddy flux of heat into the definition of the residual circulation, provide a similarly clear picture of the large-scale dynamics. These equations, which were derived by Andrews and McIntyre (1976), constitute a system of four equations for zonal-mean wind, zonal-mean temperature, and the residual circulation, $([v\star], [w\star])$:

$$\frac{\partial [u]}{\partial t} - f_o [v\star] = G + \frac{1}{\rho} \nabla \cdot \mathbf{F} \tag{2.15}$$

$$\frac{\partial [T]}{\partial t} + S[w\star] = Q \tag{2.16}$$

$$\frac{\partial [v\star]}{\partial y} + \frac{1}{\rho} \frac{\partial (\rho [w\star])}{\partial z} = 0 \tag{2.17}$$

$$f_o \frac{\partial [u]}{\partial z} = -\frac{g}{T_s} \frac{\partial [T]}{\partial y}, \tag{2.18}$$

where G is friction, Q diabatic heating, T_s a reference surface temperature, S strat-

ification, and $\nabla \cdot \mathbf{F}$ is the divergence of the Eliassen-Palm Flux. This flux, denoted $\mathbf{F}$, has a meridional and vertical component:

$$F_y = \rho \left[\frac{\partial \psi^*}{\partial x} \frac{\partial \psi^*}{\partial y} \right] = -\rho \left[u^* v^* \right] \tag{2.19}$$

$$F_z = \frac{\rho f_o^2}{N^2} \left[\frac{\partial \psi^*}{\partial x} \frac{\partial \psi^*}{\partial z} \right] = \rho \frac{f_o}{S} \left[v^* T^* \right]. \tag{2.20}$$

The northward component of $\mathbf{F}$ takes the opposite sign to the northward flux of zonal momentum by the waves; the vertical component is proportional to the northward flux of heat. The residual streamfunction, $\chi\star$, may be calculated by:

$$\left([v\star], [w\star] \right) = \left(\frac{1}{\rho} \frac{\partial \left(\rho \chi\star \right)}{\partial z}, -\frac{\partial \chi\star}{\partial y} \right); \tag{2.21}$$

the residual streamfunction is the sum of the ageostrophic Eulerian mean circulation and the eddy flux of heat:

$$\chi\star = \chi_a + \frac{[v^* T^*]}{S}. \tag{2.22}$$

In the absence of friction in a time mean, the zonal-wind acceleration must vanish and the angular-momentum budget shown in equation (2.15) reduces to a balance between angular-momentum deposition by waves and a Coriolis torque associated with a meridional mass flux. Angular-momentum deposition is accommodated by moving air equatorward or poleward depending on the sign of the deposition. Rossby waves that propagate into the stratosphere carry westward angular-momentum, and the deposition of this momentum then causes a poleward mass flux in both hemispheres. The mass conservation shown in equation (2.17) links the meridional mass flux to a vertical mass flux: air must rise in the tropics and sink in higher latitudes. In a time mean, equation (2.16) shows that the vertical mass flux is balanced by diabatic heating (Q). If radiative heating acts to relax a temperature distribution towards radiative equilibrium, the sign of Q will take the opposite to that of the temperature perturbation ($T - T_{rad}$). Thus the temperature is driven colder than radiative equilibrium in the tropics, where there is ascent, and warmer than radiative equilibrium in regions of descent in higher latitudes; this is called "dynamical heating" (A. Plumb, course notes).

As summarized by Shepherd (2000), the stratosphere acts as a refrigerator: it is mechanically driven (by angular momentum deposition) and thermally damped. The causality of this circulation has been verified by Haynes et al. (1991), who also note that the induced circulation always extends downward from the region of wave forcing; this mechanism is called "downward control" (e.g., Holton et al., 1995).

Rossby waves propagate into the stratosphere only during winter when the

[2] Asteriks denote a departure from a zonal mean. Any spatially varying variable A may be decomposed into a zonal mean, $[A]$, plus a departure from the zonal mean, A^*.

winds are westerly (Charney and Drazin, 1961). The overturning circulation described above exists in the winter hemisphere and is driven by the divergence of the Eliassen-Palm Flux; as a result, the polar vortex warms and the tropical stratosphere cools. Planetary-wave generation is greater in the Northern Hemisphere than in the Southern Hemisphere; this accounts for the asymmetry between the hemispheres in the stratosphere. Relative to Southern winter, the Northern Hemisphere winter has greater negative angular-momentum deposition, a stronger poleward branch of the Brewer-Dobson circulation, stronger downwelling over the pole, warmer polar temperatures, and a weaker polar vortex. This makes polar stratospheric cloud formation much less likely in the Northern Hemisphere than in the Southern Hemisphere, where polar temperatures do not deviate as far above radiative equilibrium values.

2.3.3 Stratospheric changes during warm climates

Following little success simulating warm periods such as the Eocene epoch, Sloan et al. (1992) and Sloan and Pollard (1998) examined mechanisms absent in general circulation models that might preferentially warm winter high-latitude temperatures. These studies focused on the surface warming that would result if optically thick polar stratospheric clouds persisted during the winter months.

Sloan et al. (1992) proposed increased methane as the source of higher concentrations of stratospheric water vapor. They note that global wetlands might have occupied an area three times larger during the Eocene than they do now. They also point out that such a reservoir would sequester large quantities of organic, isotopically light carbon, which would produce a significant change in the global ^{13}C composition. Indeed, $\delta\,^{13}C$ values are depressed (Shackleton et al., 1984) concurrently with negative $\delta\,^{18}O$ values measured in benthic foraminifera (e.g., Miller et al., 1987) during the early Eocene epoch. Greater oxidation of methane to water vapor could increase water vapor concentrations in the stratosphere.

Kirk-Davidoff et al. (2002) suggested another route by which stratospheric water vapor could increase during warmer climates. As tropospheric eddy kinetic energy with weaker surface temperature gradients, Kirk-Davidoff et al. (2002) argued that the vertical propagation of energy to the stratosphere should decrease. This would lead in turn to a reduction of the stratosphere's residual circulation, and a reduction of the deviation from radiative equilibrium during winter. With higher temperatures at the tropical tropopause, a greater amount of water vapor would be able to rise into the stratosphere during warm climates. If true, this mechanism suggests water vapor in the stratosphere should increase with a weakening surface temperature gradient, providing an opportunity for polar stratospheric clouds to form throughout the warm Paleogene and Cretaceous, rather than just at the Paleocene-Eocene thermal maximum when methane likely spiked. This argument contradicts some unexpected findings from an earlier set of papers studying the middle atmosphere's response to an atmosphere in which carbon dioxide levels are increased to 630 ppm.

Until recently, the middle atmosphere's response to a weaker surface temperature gradient received scant attention. At the Goddard Institute for Space Studies (GISS), David Rind and his colleagues investigated the middle atmosphere's response to changes in the surface temperature and to a doubling of the atmosphere's carbon dioxide load (Rind et al., 1990; Rind et al., 1998). These authors used a version of the GISS global climate model extended through middle atmosphere altitudes (e.g., Rind et al., 1988a; Rind et al., 1988b). Their studies found that the model's troposphere warmed and its stratosphere cooled in response to increased carbon dioxide, as expected when more infra-red radiation is absorbed and re-radiated (Fels et al., 1980; see also section 2.3.1). Carbon dioxide molecules absorb longwave radiation emitted by the Earth and re-emit radiation nearly isotropically; this causes the surface to warm and stratosphere to cool.

But the model calculations revealed some interesting and unexpected behavior too. Tropospheric eddy energy decreased as the surface temperature gradient weakened, but it became more concentrated in longer planetary waves as the vertical stability of the troposphere decreased (Rind et al., 1990). As only wavenumbers one and two propagate into the stratosphere, the increase in these waves' energy is significant (e.g., Charney and Drazin, 1961).

Over the colder half of the year in the Northern Hemisphere, the polar stratosphere surprisingly warmed in the GISS middle atmosphere model when carbon dioxide loads were doubled. In a time-mean, statistically equilibrated atmosphere, the radiative balance in the stratosphere may be written:

$$J_{\mathrm{sw}} + Q_{\mathrm{lw}}(T) + Q_{\mathrm{dyn}} = 0, \tag{2.23}$$

where J_{sw} is solar heating; Q_{lw} is net longwave heating,[3] which is strongly temperature dependent; and Q_{dyn} is dynamical heating (Fels et al., 1980). This last term represents diabatic heating and is balanced by adiabatic cooling. The warming observed in the GISS studies occurred during a time of year in which $J_{\mathrm{sw}} \rightarrow 0$ in the polar stratosphere; with increased longwave cooling, the model warming must have resulted from an increase in the amount of dynamical heating. With increased longwave cooling from higher loads of carbon dioxide, a fixed amount of dynamical heating would lead to cooler temperatures given the decrease in radiative equilibrium temperatures.

With or without weaker surface temperature gradients, winter temperatures in the polar stratosphere warmed when carbon dioxide concentrations doubled, while the remainder of the stratosphere cooled, as expected from a higher load of greenhouse gas. When the surface temperature gradient was substantially weakened, the winter polar stratosphere temperatures did cool below the control run values, but not by as

[3]Gases such as carbon dioxide, methane, and water vapor absorb thermal longwave radiation and re-emit it; even in the polar night, when J_{sw} is zero, radiative equilibrium temperatures are above 0 K. At high altitudes, an increase in the concentration of these gases causes the longwave cooling to space to increase, resulting in cooler temperatures.

much as temperatures in the remainder of the stratosphere did. In all of these cases, the residual circulation increased in strength in the winter stratosphere, verifying that the changes made to the surface temperature gradient did not cause the dynamical heating in the polar vortex to weaken (Rind et al., 1990). The magnitude of the increases in dynamical heating did vary among runs with different lower boundary conditions, though.

This behavior is unexpected, as tropospheric eddy kinetic energy decreased when the surface temperature gradient was weakened (Rind et al., 1990). Yet in the middle atmosphere, eddy and gravity wave energy increased in nearly all cases and in nearly all months. As the surface temperature gradient weakened, baroclinicity (the conversion of eddy available potential energy to eddy kinetic energy) decreased. These authors argued that the warmer surface coupled with a cooler stratosphere led to a decrease in vertical stability, which tends to increase the amount of available potential energy accessible by planetary-scale waves. Indeed, the eddy energy of standing wavenumber one increased in the troposphere even as the total amount of eddy energy decreased. The longest planetary-scale waves are more strongly influenced by vertical stability than are the shorter ones (Rind et al., 1990). Upward fluxes of energy increase as the energy of wavenumbers one and two increases; these are the waves that are able to propagate into the winter hemisphere's stratospheric westerlies.

Rind et al. (1998) again found that tropical upper troposphere warming led to greater available potential energy of the mean flow; this warming also alters the refraction pattern for wave propagation, which helps to increase the Eliassen-Palm flux convergences that drive the increased residual circulation. These results are not expected and are affected by a model's ability to resolve the stratosphere (Rind et al., 1998).

These findings contradict the expectations of Kirk-Davidoff et al. (2002) and some related work. Rind et al. (2001) attempted to model the Paleocene with reduced topography and a weak temperature gradient; in these simulations, the stratospheric residual circulation weakened. Here energy in the standing eddies is also lower, suggesting that the reduced topography may play a significant role (e.g., see Held et al., 2002). Jessica Neu (personal communication) has completed some runs in which the stratosphere is allowed to deviate from a supplied radiative-equilibrium temperature distribution by upwardly propagating waves. She finds that a weaker surface temperature gradient reduces the upward Eliassen-Palm flux in some cases, but her results are dependent the formulation of topography and generation of stationary waves. It is also possible that these findings are due to the setup; the strong stratospheric meridional temperature gradient that results from the supplied initial conditions produces jet speeds that inhibit much of the tropospheric energy from propagating vertically.

The GISS studies show that the strongest effect on the temperature distribution made by doubling carbon dioxide came from the vertical differentiation of the radiative effects (Rind et al., 1990; Rind et al., 1998). That is, stratospheric altitudes cool from increased longwave cooling in the presence of elevated carbon dioxide. While

the GISS simulations were not run into radiative equilibrium, their results imply that the radiative equilibrium temperature field in a greenhouse atmosphere is likely to be uniformly lower than the present values. Dynamics affect the degree to which temperatures deviate from the radiative equilibrium field.

In the next chapter, I present the first simulations of the stratospheric circulation's response to a very weak surface temperature gradient. The general circulation and energetics will be examined to elucidate the salient physics.

2.4 Feasibility of dynamical changes

In section 2.3.2 I reviewed the dynamics governing the poleward transport of mass in the winter hemisphere of the stratosphere. During winter, upwardly propagating planetary-scale Rossby waves and gravity waves deposit westward angular momentum that damps the mean circulation; in the presence of the Coriolis torque, this deposition accounts for the poleward mass flow in the upper stratosphere.[4] Mass conservation links the meridional mass flux to the vertical mass flux, and thus to diabatic heating (parcels cross isentropes), as temperatures are driven away from radiative equilibrium. In this view, the stratosphere is a refrigerator, mechanically driven and thermally damped. The causality of this view was presented by Haynes et al. (1991) and is reviewed by Holton et al. (1995) and Shepherd (2000).

To first address the dynamical changes to which the stratosphere would be subjected in a warmer climate, I have used a zonally symmetric radiative-convective model; a precursor to the present version is described in Nilsson and Emanuel (1999). This model is devoid of relevant physics, namely eddies, but it has detailed physics in the vertical, including the convection scheme of Emanuel and Živković-Rothman (1999), the fractional cloudiness scheme of Bony and Emanuel (2001), and the radiative transfer code of Morcrette (1991). Dynamically, the system is rotating,[5] linear, and hydrostatic, which provides a crude coupling between each of the columns, but there are no eddies to transport enthalpy. This shortcoming, while limiting, allows me to study the response of the height and temperature of the tropopause to variations in the surface temperature gradient induced by convective adjustments and advective processes alone. In this sense, the model provides a background set of experiments with which results from more complicated models can be compared.

Rayleigh friction applied by a sponge layer near the model top provides a source of controllable damping. Like deposition of angular-momentum by breaking Rossby or gravity waves, this damping retards the jet and, by the Coriolis torque, induces a

[4]This is true in the winter of both hemispheres, as the sign of f and the Coriolis torque are opposite. During austral winter, deposition of westward angular momentum is turned southward in the Southern Hemisphere; during boreal winter, deposition is turned northward in the Northern Hemisphere.

[5]In the version described by Nilsson and Emanuel (1999), the system is non-rotating; in the version used here, a Coriolis torque is included in the momentum equation.

poleward flow. In the following section I present the model tropopause temperature and height response to different surface forcings, as well as the response to varying amounts of damping applied to the top model levels. These results will illuminate the magnitude of the changes necessary in these fields to reverse the inequality:

$$q^{\#}_{\mathrm{tt}} \leq q^{\#}_{\mathrm{at}}, \tag{2.24}$$

where $q^{\#}_{\mathrm{tt}}$ is the saturation specific humidity over ice at the tropical tropopause and $q^{\#}_{\mathrm{at}}$ is the same quantity calculated during the winter at the Arctic tropopause. This initial study shows the extent to which boundary conditions and momentum damping must change, in the absence of feedbacks from eddies and other dynamics, in order to allow more water vapor to come up through the tropical tropopause than is required to condense it in the Arctic vortex. In Appendix C, I show why there is a meridional overturning circulation in this two-dimensional model. In the process of this analysis, additional questions are raised: what role does the cold temperature anomaly at the top of the Hadley cell play in forcing tropical lower stratosphere temperatures below radiative equilibrium, and how does this affect the stratosphere's circulation? The principle of "downward control", first discussed by Haynes et al. (1991), suggests that the response can only extend below the level of forcing.

Given the absence of waves in this model, the stratospheric circulation is forced by the mechanism discussed above, not by upward propagating Rossby waves. Additionally, this model contains no ice, which surely has an impact on the quantities it calculates. The point of this exercise, therefore, is not to assess the arguments presented in Kirk-Davidoff et al. (2002) directly, but rather to assess their viability by testing whether the thermal structure of the stratosphere can be rearranged in a way such that $q^{\#}$ at the tropical tropopause exceeds $q^{\#}$ in the Arctic stratosphere during the winter months.

2.5 Experiments with the two-dimensional model

To assess the viability of attaining a stratospheric thermal structure conducive to the formation of polar stratospheric clouds, I have run a number of experiments with the two-dimensional model described in the last section. The model was forced with a varying sea surface temperature distributions. Temperatures were calculated by:

$$T(\phi, t) = \Delta\mathrm{T} \cos\left\{\frac{\pi}{2} \sin\left[\phi - \phi_m(t)\right]\right\} + \left(T_m - \Delta\mathrm{T}\right), \tag{2.25}$$

where ϕ is the latitude in degrees, t is day of the year, ΔT is the equator-to-pole temperature difference, $\phi_m(t)$ is the latitude at which the warmest sea surface temperature, T_m, can be found on day t. The latitude at which T_m resides oscillates on

an annual cycle:

$$\phi_m(t) = \frac{(\phi_n - \phi_s)}{2} \cos\left[2\pi \frac{(t - t_n)}{365}\right] + \frac{(\phi_n + \phi_s)}{2}. \tag{2.26}$$

Here ϕ_n is the northern most latitude at which T_m occurs, ϕ_s is the southern most latitude at which T_m occurs, and t_n is the day on which T_m reaches ϕ_n. By choosing t_n to be, say, August 1, the warmest sea surface temperatures will settle near ϕ_n during the Northern Hemisphere summer, and then will migrate south toward ϕ_s, reaching it six months later.

By choosing ϕ_n to be 8°N, ϕ_s to be 2°S, t_n to be August 1 (day 213), T_m to be 30°C, and allowing ΔT to vary, equations (2.25) and (2.26) produce tropical temperatures that peak at 30° and varying climates at high latitudes, depending on the amplitude of ΔT. Our choices for ϕ_n and ϕ_s closely mimic the present range of T_m (see, e.g., Lindzen, 1990). Note that this model has no ice.[6]

The model produces a robust overturning cell (Hadley circulation) in the tropical troposphere. At the top of this convective cell sits an anticyclone as ascending vertical motions diminish and air evacuates laterally at an outflow level between 150 and 100 mb, near the tropical tropopause. This anticyclone serves as a forcing on the stratospheric levels above it. It couples with a sponge layer that relaxes temperature, wind, and moisture perturbations to zero to produce a geostrophically balanced, upwardly decaying cold-core anticyclone in the tropics. The anticyclone decays in intensity as one moves poleward. The time scale over which the sponge layer acts is defined in the input to the model. Different time scales can be applied to the relaxation of zonal winds and to temperature and moisture perturbations; momentum damping forces the overturning circulation, so the momentum relaxation time scale controls the applied body force.

The temperature anomalies produced by these features are out of radiative-equilibrium. As the radiation code tries to restore the temperature profile to one radiatively determined (i.e., reduce the perturbations) and the sponge layer damps zonal wind near the model top, an ageostrophic overturning circulation is forced. To see this, review the Transformed Eulerian Mean equations (2.15)-(2.18). In the real stratosphere, the forcing term on the right-hand-side of (2.15), $(\nabla \cdot \mathbf{F})/\rho$, is nonzero, but in the two-dimensional model there are no Rossby waves to propagate, so this term is zero here. The friction near the model top drives the residual circulation in this model; additionally, heating that results from the relaxation of temperature perturbations can force an ageostrophic circulation. Where temperatures are colder than radiative equilibrium (i.e., the tropics), motion will be upward in a steady state. This forces a circulation that rises in the tropics, turns poleward with height, and settles in middle and high latitudes.

[6]The convection code treats ice and condensed water differently, but there is no surface ice to impact the albedo.

By lengthening the time scale over which the momentum damping relaxes zonal wind anomalies in the upper levels of the model, the stratospheric circulation is weakened. The stratosphere comes closer to being barotropic: the tropopause anticyclone penetrates into the stratosphere at higher altitudes, and temperature perturbations are increasingly nonexistent. Because of this, the intensity of the residual circulation weakens.

I have examined a number of runs in which the strength of the stratosphere's overturning circulation and the pole-to-equator temperature gradient are varied. I have run experiments in which either the pole-to-equator temperature gradient (ΔT) or the sponge layer momentum damping time scale (τ_m) varies. Much of the realistic (ΔT, τ_m) space has been sampled; these results are discussed in the subsections below.

First, the temperature gradient is varied while boundary conditions favoring a strong stratospheric overturning circulation are imposed. Next, an upper boundary condition forcing a weak overturning circulation is imposed while the temperature gradient is again varied. Finally, the temperature gradient is held fixed for a number of runs in which the strength of the overturning circulation is allowed to vary. Of course, none of these experiments is capable of examining a possible feedback between the intensity of the stratosphere's overturning circulation and the temperature gradient itself. This will be examined in the next chapter.

2.5.1 Strong stratospheric overturning

When the stratospheric overturning circulation is strong, the tropical lower stratosphere is driven colder than radiative equilibrium by the residual circulation. This region is where some of the coldest temperatures in all of the troposphere and stratosphere are found. High-latitudes are able to warm above radiative equilibrium even as the winter hemisphere lies in complete darkness; air is transported poleward and dynamical heating occurs during the polar night. Figure 2-4 shows the model's depiction of the temperature structure for a run in which the surface equator-to-pole temperature temperature difference is ΔT = 30°C and the sponge time scale is τ_m = 100 minutes.

In the runs presented in figure 2-5a, the pole-to-equator temperature difference was varied for a sponge time scale fixed at 100 minutes. For a fast time scale like this, temperature perturbations above 35 mb are damped quickly back to the radiative equilibrium temperature profile. When the temperature gradient is strong (ΔT = 50°C, for example), the temperature at the tropical tropopause is considerably lower than its radiative equilibrium value, while the Arctic lower stratosphere is much warmer than radiative equilibrium. As in the real atmosphere, this is because dynamical heating occurs in high-latitudes during the polar night and dynamical cooling occurs in the tropical stratosphere. Moving to the left in the figure, toward weaker temperature gradients closer to the present-day atmosphere, the curves first begin to pinch together; that is, the Arctic tropopause temperature cools and the tropi-

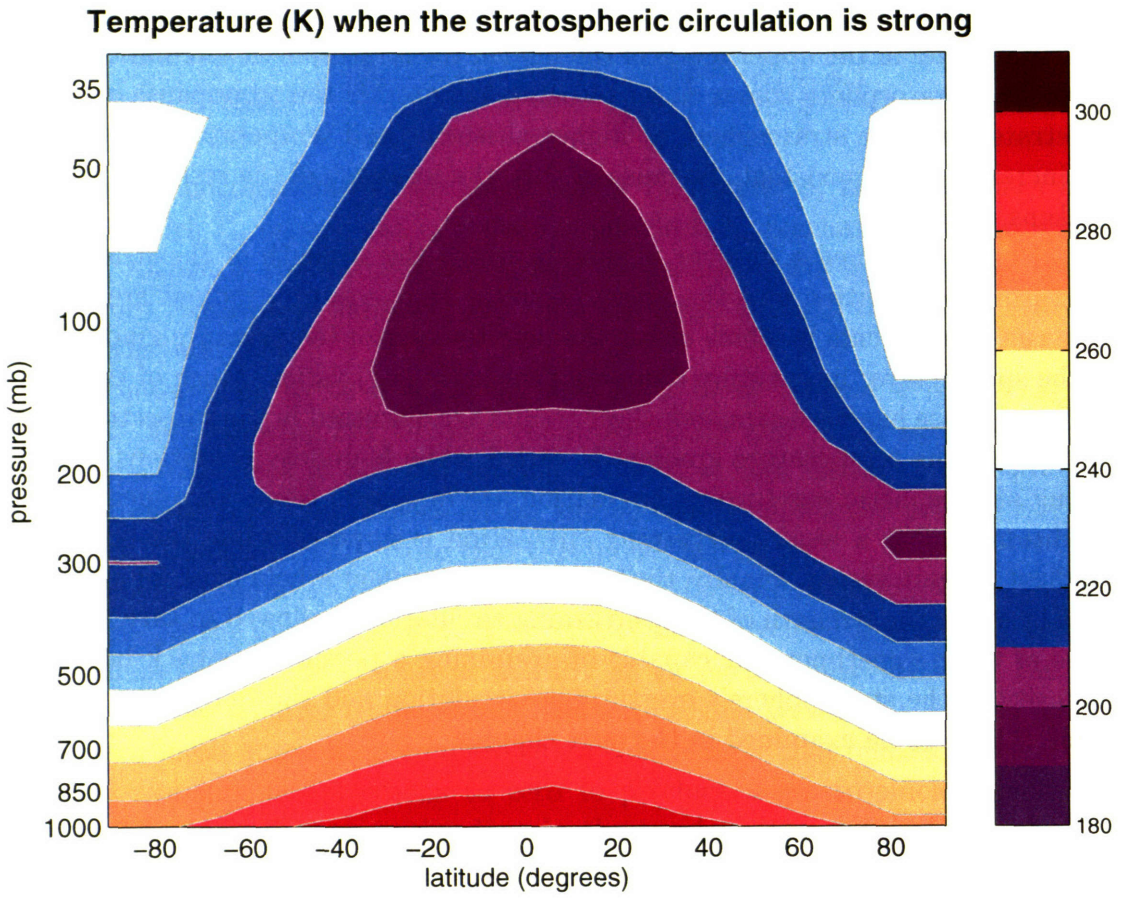

Figure 2-4: Temperature averaged over December through February for a run in which ΔT is 30°C and τ_m is 100 minutes, which produces a strong overturning circulation. The temperature structure deviates from radiative equilibrium as the tropical stratosphere cools and high latitude stratosphere warms. The minimum temperature in the tropical lower stratosphere is 191.6 K, and the minimum in the Arctic stratosphere is 198.7 K.

cal tropopause temperature warms as the degree of dynamical heating and cooling lessens. The tropical tropopause temperature continues this trend across the entire range of temperature differences examined. The intensity of tropical cooling weakens because the strength of the stratosphere's overturning circulation weakens with the temperature gradient, as shown in figure 2-6b. In the model, the strength of the circulation is controlled by two parameters: the intensity of the anticyclone at the top of the troposphere's Hadley circulation, and the rapidity with which momentum damping forces perturbations to zero at the top levels of the model. As the latter is fixed in the set of runs examined in figures 2-5 and 2-6, only the intensity of the anticyclone forcing the bottom of the stratosphere changes. Figure 2-6a shows that the intensity does indeed drop as the temperature gradient weakens, which explains why the stratosphere's overturning circulation is weaker and, in turn, why the dynamical cooling in the tropical stratosphere diminishes.

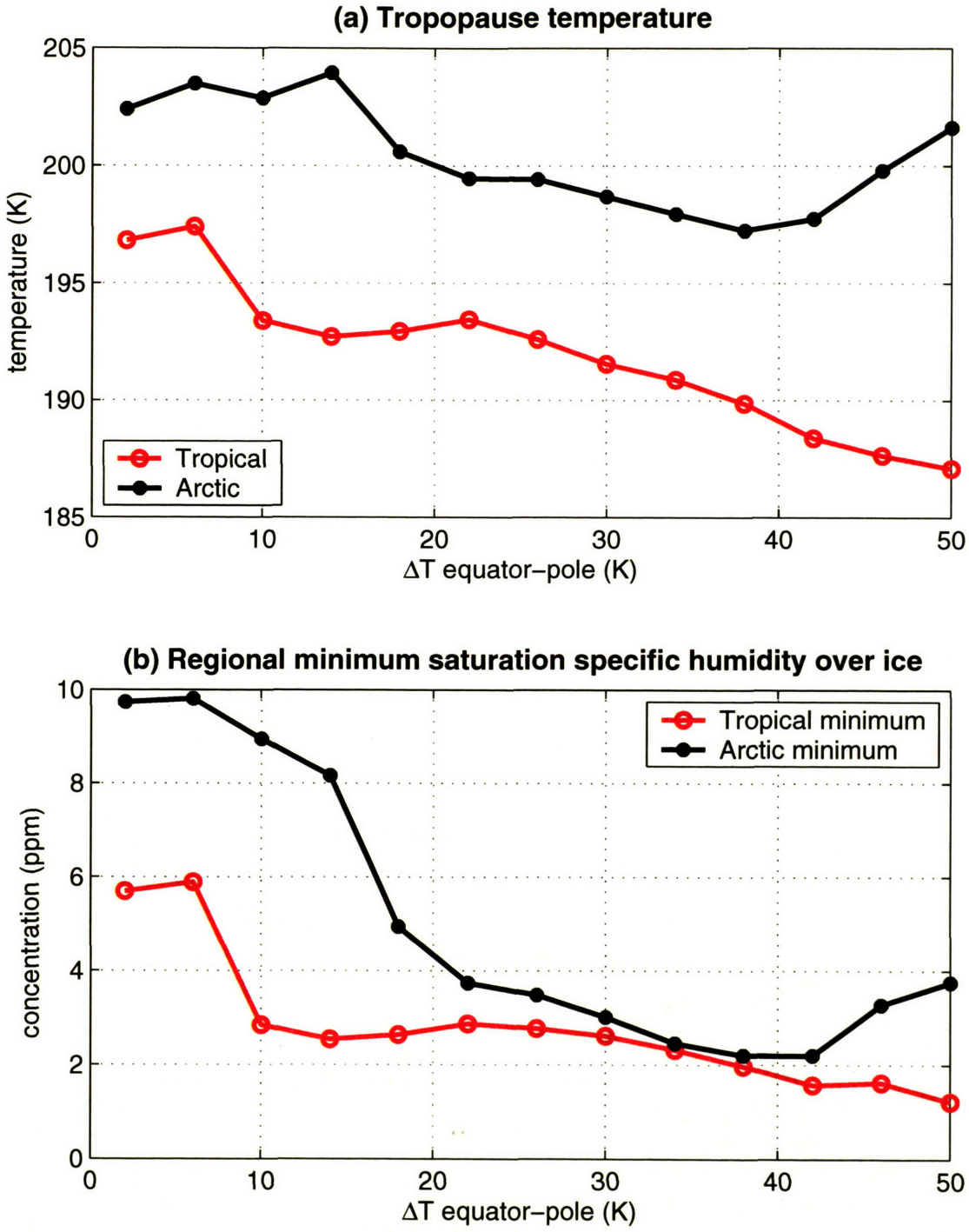

Figure 2-5: December-February averages from a run with τ_m set to 100 minutes. Short sponge time scales create a stronger overturning circulation in the stratosphere. (a) Coldest temperature at the tropopause in the tropics and in the Arctic. (b) Minimum saturation specific humidity over ice, $q^{\#}$.

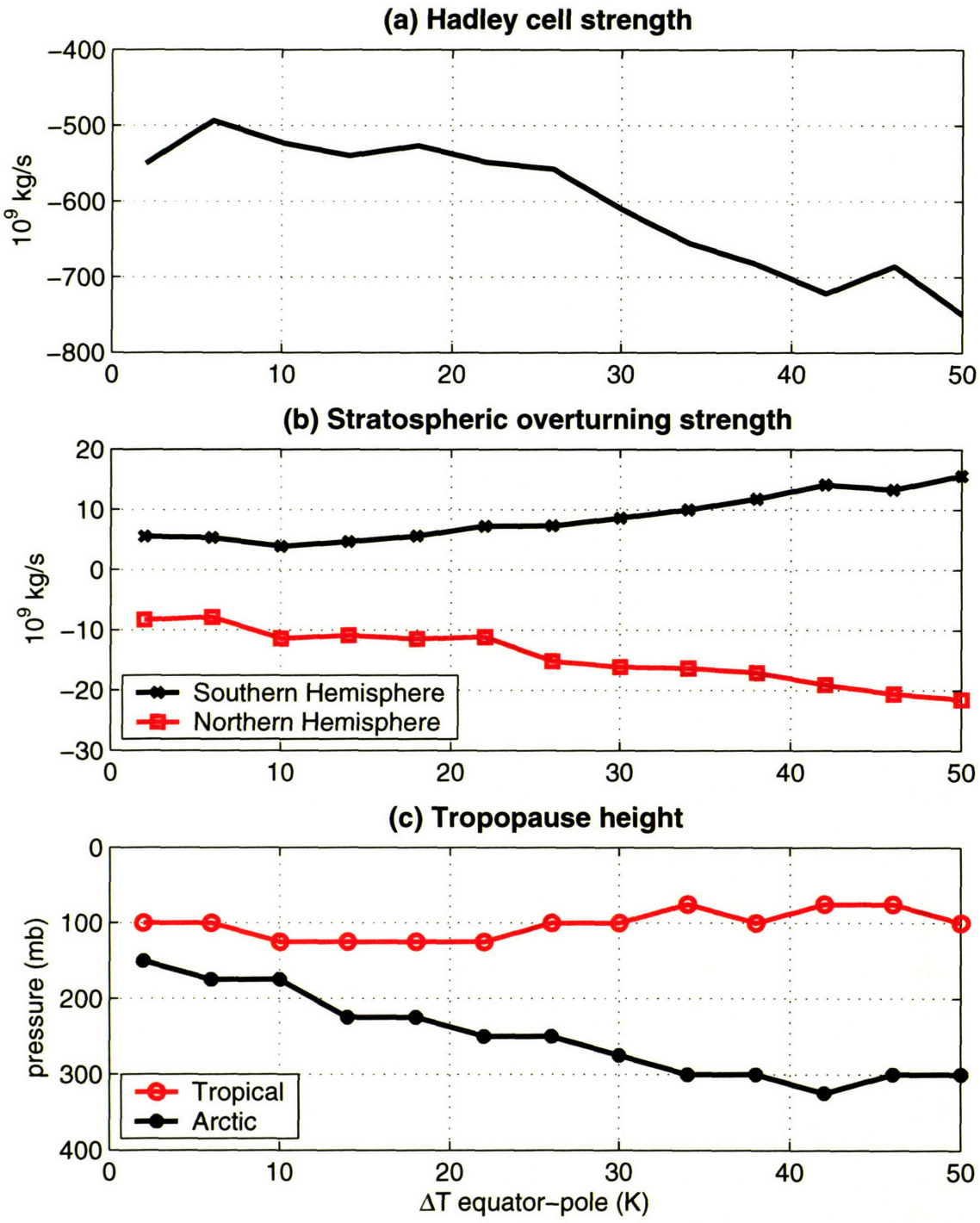

Figure 2-6: December-February averages from a run with a strong overturning circulation (τ_m is 100 minutes). (a) Maximum streamfunction in the Hadley cell. (b) Strongest streamfunctions found in the stratosphere. (c) Height of the model tropopause.

Note, however, that for temperature differences below about $\Delta T = 35°C$ the Arctic tropopause temperature actually begins to rise even while the intensity of the stratosphere's overturning circulation continues to weaken. This coincident change inhibits a decrease in Arctic tropopause temperatures. Figure 2-6c shows the height of the tropopause in tropical and Arctic latitudes. The tropopause is quite low when the temperature gradient is strong. But as the surface temperature gradient weakens, so too does the vertical lapse rate, and the height of the tropopause begins to rise once ΔT weakens below 35°C.

Recall that this model does not have any parameterization of eddies, so there is no lateral transport of heat aside from that done by large-scale circulations. The intensity of model convection, viewed in the mass updraft, vertical velocity, or stream-function fields is not particularly strong in runs forced with weak temperature gradients, but the difference between high-latitude and low-latitude convection is smaller in these cases.

The point of these experiments was to analyze differences between the saturation specific humidity over ice, $q^{\#}$, in high latitudes and the tropics. Ignoring oxidation of methane, only if the value of $q^{\#}$ in the tropics exceeds the value in the Arctic can the condensation necessary for the formation of polar stratospheric clouds be expected. This is because the amount of water that can rise into the stratosphere in the tropics is limited by the cold temperatures there. The minimum values of $q^{\#}$ found at the tropopause in both the tropics and in the Arctic are plotted in figure 2-5b.

Given both the higher temperatures and lower pressure of the Arctic tropopause in weak temperature gradients, $q^{\#}$ reverses its initial trend toward the value found in the tropics as the temperature difference weakens from $\Delta T = 50°C$. As the tropopause and temperatures rise in the Arctic with weakening gradients, the gap between $q^{\#}$ in the tropics and in the Arctic actually widens. The thermal structures at weak temperature gradients in these model runs are *less* conducive to the formation of polar stratospheric clouds. In fact, were these results to prove robust, one would expect polar stratospheric clouds to be most likely at temperature gradients slightly stronger than presently observed.

2.5.2 Weak stratospheric overturning circulation

In my second set of experiments, the momentum damping time scale was increased two orders of magnitude to 10^4 minutes. With this condition, the anticyclone at the tropical tropopause penetrates into the stratosphere, and temperature perturbations are of a much smaller order. The small departures from radiative equilibrium drive only a very weak residual circulation. Figure 2-7 shows the temperature structure (averaged over December to February) for a run with a weak overturning circulation and with a surface temperature difference of 30°C between the Equator and the poles.

With only weak amounts of dynamic heating and cooling in the stratosphere, the temperatures are coldest in the polar night, as they are in radiative equilibrium.

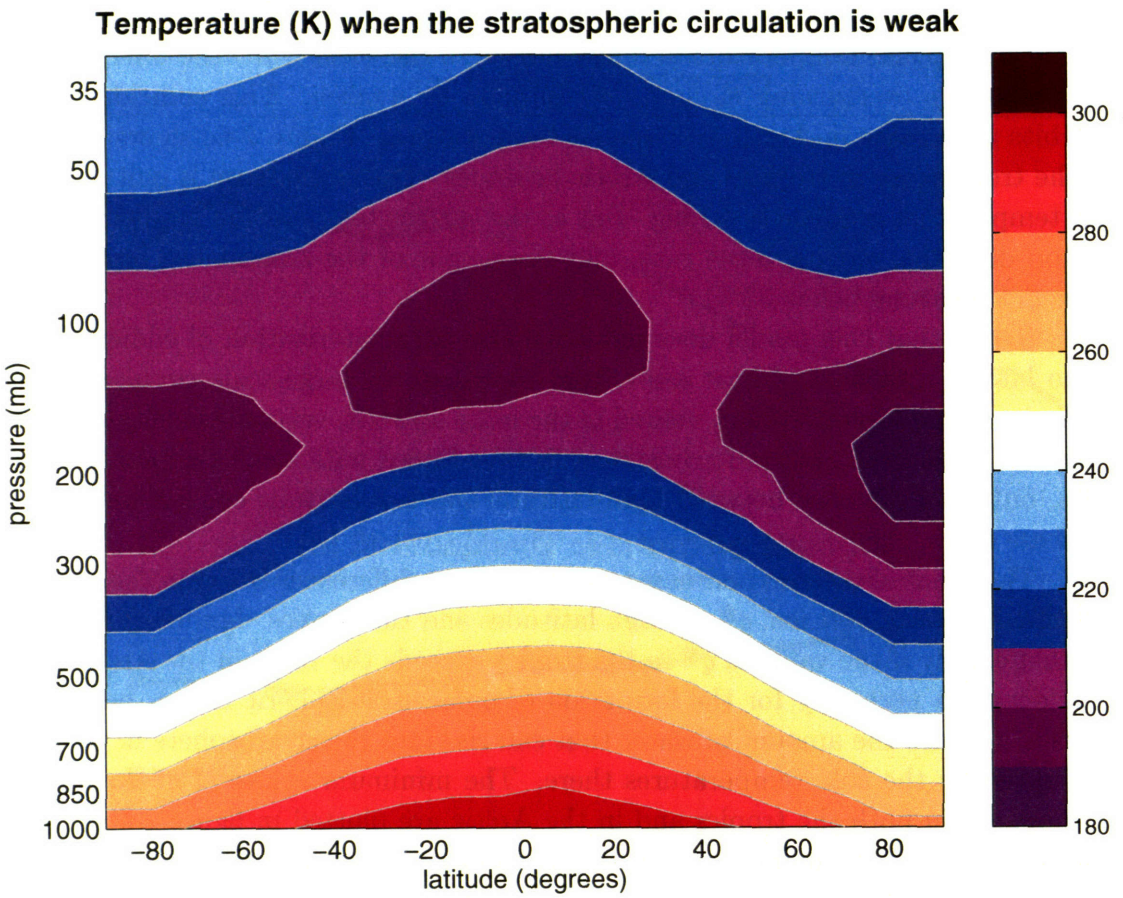

Figure 2-7: Temperature averaged over December through February for a run in which ΔT is 30°C and τ_m is 10^4 minutes, which produces a weak overturning circulation. The temperature structure through much of the model stratosphere does not deviate far from radiative equilibrium. The minimum stratospheric temperature in the tropics is 197.0 K; the minimum in the Arctic stratosphere is 186.8 K, which is now the coldest region in the model domain.

Figure 2-8a shows that the temperatures at the tropopause in the tropics are warmer than those at the Arctic tropopause for all values of ΔT when the residual circulation is weak. This is hardly surprising as the residual circulation is principally responsible for driving the stratosphere out of radiative-equilibrium.

As in figure 2-5a, the tropopause warms as the temperature gradient weakens, particularly in high-latitudes. This is because convection develops at all latitudes, and the model tropopause rises with weaker gradients. This can be seen in figure 2-9c, which shows that the Arctic tropopause is substantially higher when the temperature gradient is weaker. Note in figure 2-9b that while the overturning circulation weakens as the temperature gradient drops, its intensity is generally three to five times weaker than it was when the sponge time scale was shorter (compare with figure 2-6b, where τ_m was 100 minutes).

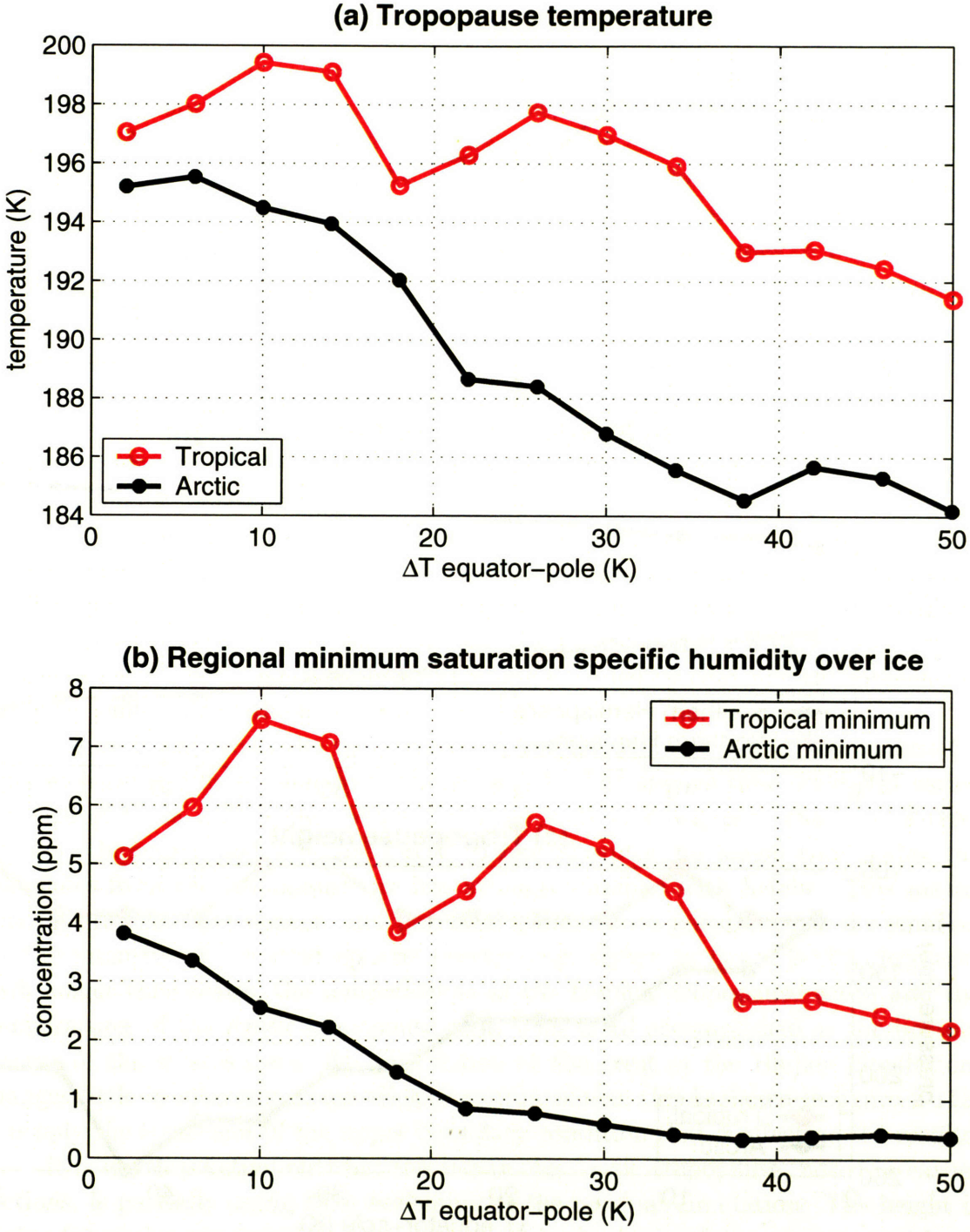

Figure 2-8: As in figure 2-5, but from runs with τ_m set to 10^4 minutes (approximately one week). Long sponge time scales create a weaker overturning circulation in the stratosphere. (a) Coldest temperature at the tropopause in the tropics and in the Arctic. (b) Minimum saturation specific humidity over ice, $q^{\#}$.

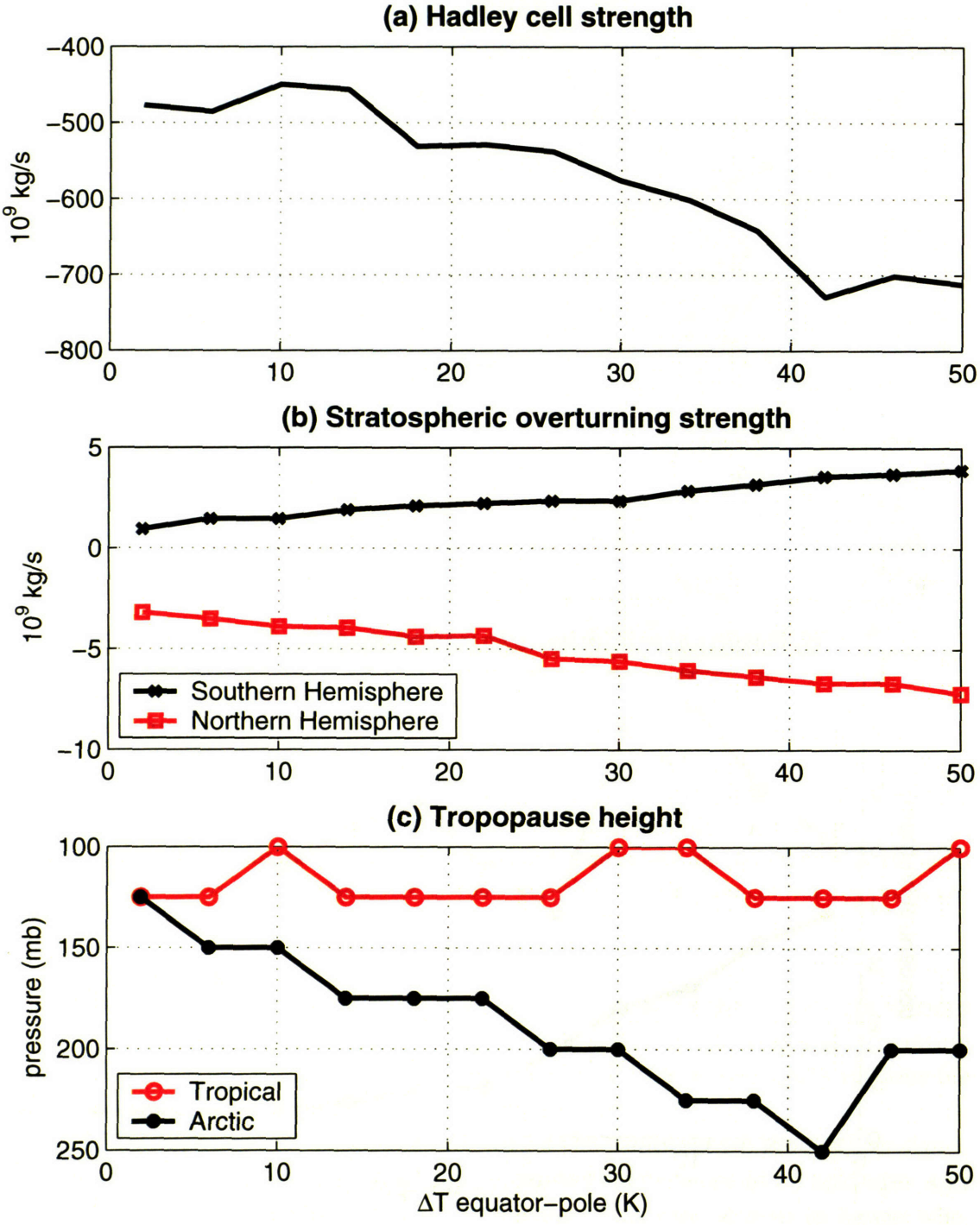

Figure 2-9: As in figure 2-6, but from runs with a a weak overturning (τ_m is 10^4 minutes). (a) Maximum streamfunction in the Hadley cell. (b) Strongest streamfunctions found in the stratosphere. (c) Height of the model tropopause.

Because the tropical tropopause is warmer than the Arctic for all gradients in this set, and is at least as high, the values of $q^{\#}$, which are shown in figure 2-8b, are higher in the tropics than in the Arctic. This means that more water vapor can enter the stratosphere than is required to reach condensation in the polar night.

One new obstacle to forming polar stratospheric clouds is the weak circulation itself. In order to sustain a thick polar stratospheric cloud, there must be a source (chemical or by advection) of water to compensate for the settling of ice crystals; if clouds are thick enough to precipitate, there must be a source to compensate for the sink of water. The same circulation that warms high-latitudes to temperatures unfavorable for polar stratospheric cloud formation is responsible for transporting water vapor poleward from the tropics.

2.5.3 Variations of the sponge time scale, τ_m

In the preceding two sections, we saw that if the momentum damping is weak enough, it is possible for more water vapor to enter the stratosphere in the tropics than is required for condensation at high latitudes. This is true for all values of ΔT examined. In this section, I present runs designed to examine how weak the stratospheric overturning circulation must be in order to permit an adequate amount of water vapor into the stratosphere for polar stratospheric clouds to form. For a variety of temperature gradients, the strength of the overturning is varied by changing the momentum damping time scale at the model top.

Figure 2-10a shows the temperature of the tropical and Arctic tropopause for runs with three different but fixed values of ΔT. The sponge time scale was varied for each of these ΔT values. When the time scale is short, perturbations of temperature, humidity, and wind are forced to zero abruptly; for longer time scales, the anomalies from the tropopause are less strongly damped with height. This means vertical gradients are weaker, and potential temperature perturbations are smaller. As the intensity of the stratospheric overturning, shown in figure 2-11b, decreases with longer time scales, the temperatures at the tropical tropopause warm and the temperatures of the Arctic tropopause cool. This is all accomplished as the bottom forcing of the stratosphere, the anticyclone at the crest of the Hadley circulation, changes little in intensity across all sponge time scales; this is shown in figure 2-11a. It is only the treatment of the upper boundary condition that is affecting the results.

It is worth pointing out that the rise in the Arctic tropopause, noted in earlier sections, is partially owing to a weakening of the residual circulation. The height is higher for weaker temperature gradients, but it is also higher for weaker stratospheric overturning circulations (see figure 2-11c).

Even with the rise in the height of the Arctic tropopause, the tropical and Arctic $q^{\#}$ lines all cross each other as shown in figure 2-10b. For all temperature gradients studied, the value of $q^{\#}$ is higher in the Arctic than in the tropics when the overturning is strong, but the situation reverses as the overturning diminishes in

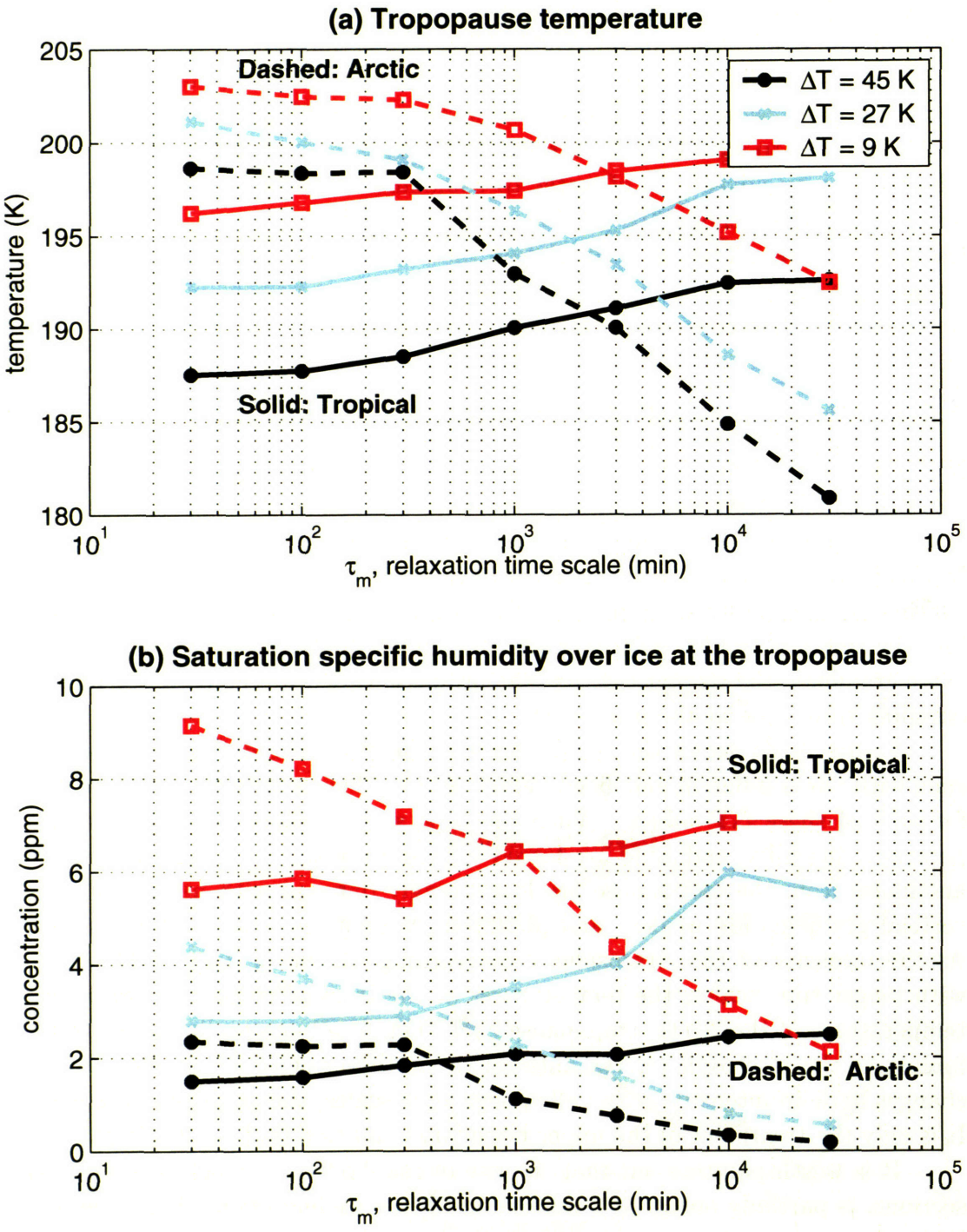

Figure 2-10: Runs of varying sponge layer time scales. Longer sponge time scales create a weaker stratospheric overturning circulation. (a) Coldest tropopause temperatures in the tropics (solid) and in the Arctic (dashed). (b) Minimum saturation specific humidity over ice, $q^{\#}$, at the tropical tropopause (solid) and at the Arctic tropopause (dashed).

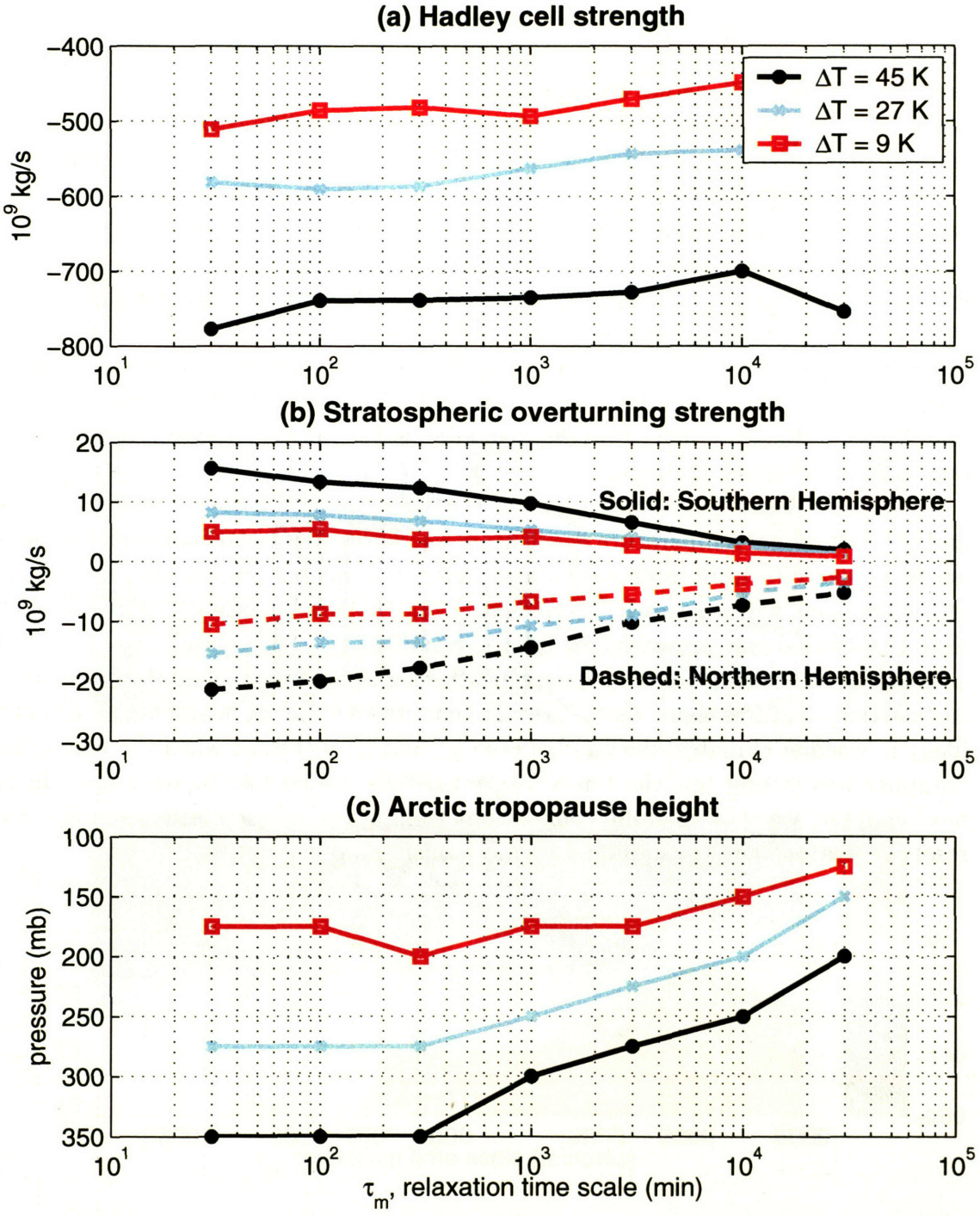

Figure 2-11: As in figures 2-6 and 2-9, but from runs with varying time scales for the sponge coefficient. (a) Maximum streamfunction in the Hadley cell. (b) Strongest streamfunctions found in the stratosphere. (c) Height of the model tropopause.

intensity. This phase-space is mapped in figure 2-12. Panel 2-12a shows the difference between values of $q^{\#}$ at the tropical and Arctic tropopause; positive values indicate regions where enough water vapor is permitted into the stratosphere to condense at high-latitudes. Saturation specific humidity is a function of both temperature and pressure. Panel 2-12b shows the difference between temperatures at the tropical and Arctic tropopause; positive values indicate regions where the tropical tropopause is warmer than the Arctic tropopause. Panel 2-12c shows the difference in pressure level between the tropical and Arctic tropopause. Note that the difference decreases as the temperature gradient weakens and sponge layer time scale increases.

The momentum damping sponge layer time scale is merely serving as a proxy for the strength of the momentum forcing. Figure 2-13a shows that the stratospheric circulation does weaken with increasing sponge layer time scales, but in a non-trivial manner. Figure 2-13b is a remapping of figure 2-12c onto a plot with the stratospheric overturning circulation on the x-axis. This shows that the difference between tropical and Arctic tropopause height becomes smaller as both the temperature gradient and overturning circulation weaken.

If there exists a feedback between the strength of the overturning circulation and the meridional temperature gradient, it is possible that polar stratospheric clouds are more likely to form in climate states different from our present one, but the size of the feedback will need to be significant. But this two-dimensional model indicates that the mechanism presented in Kirk-Davidoff et al. (2002) might be difficult to achieve. In this model, the tropopause height rises in middle and high-latitudes as the surface temperatures there warm. Rather than make polar stratospheric clouds more likely in warmer climates, the gap between $q^{\#}_{\mathrm{tt}}$ and $q^{\#}_{\mathrm{at}}$ increased when the momentum damping was strong but the temperature gradient varied (see figure 2-5b). In the next chapter, we shall examine simulations from a general circulation model with a resolved stratosphere to examine this mechanism more carefully.

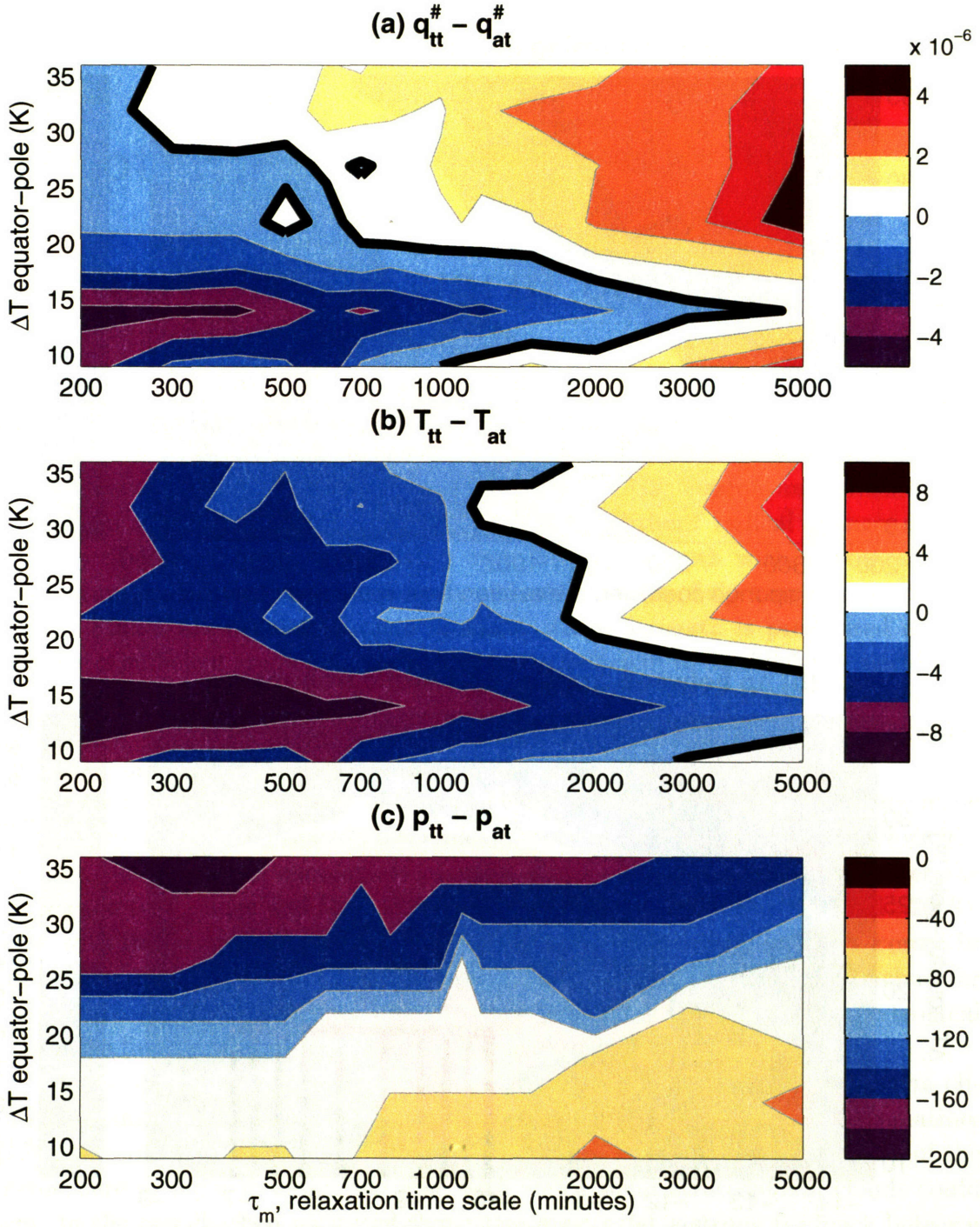

Figure 2-12: Maps of $(\Delta T, \tau_m)$ space. (a) The difference between tropical and Arctic tropopause values of $q^{\#}$. Positive values indicate enough water vapor is permitted into the stratosphere to condense again in high latitudes. (b) Temperature difference between the tropical and Arctic tropopause. (c) Difference in pressure level between the tropical and Arctic tropopause.

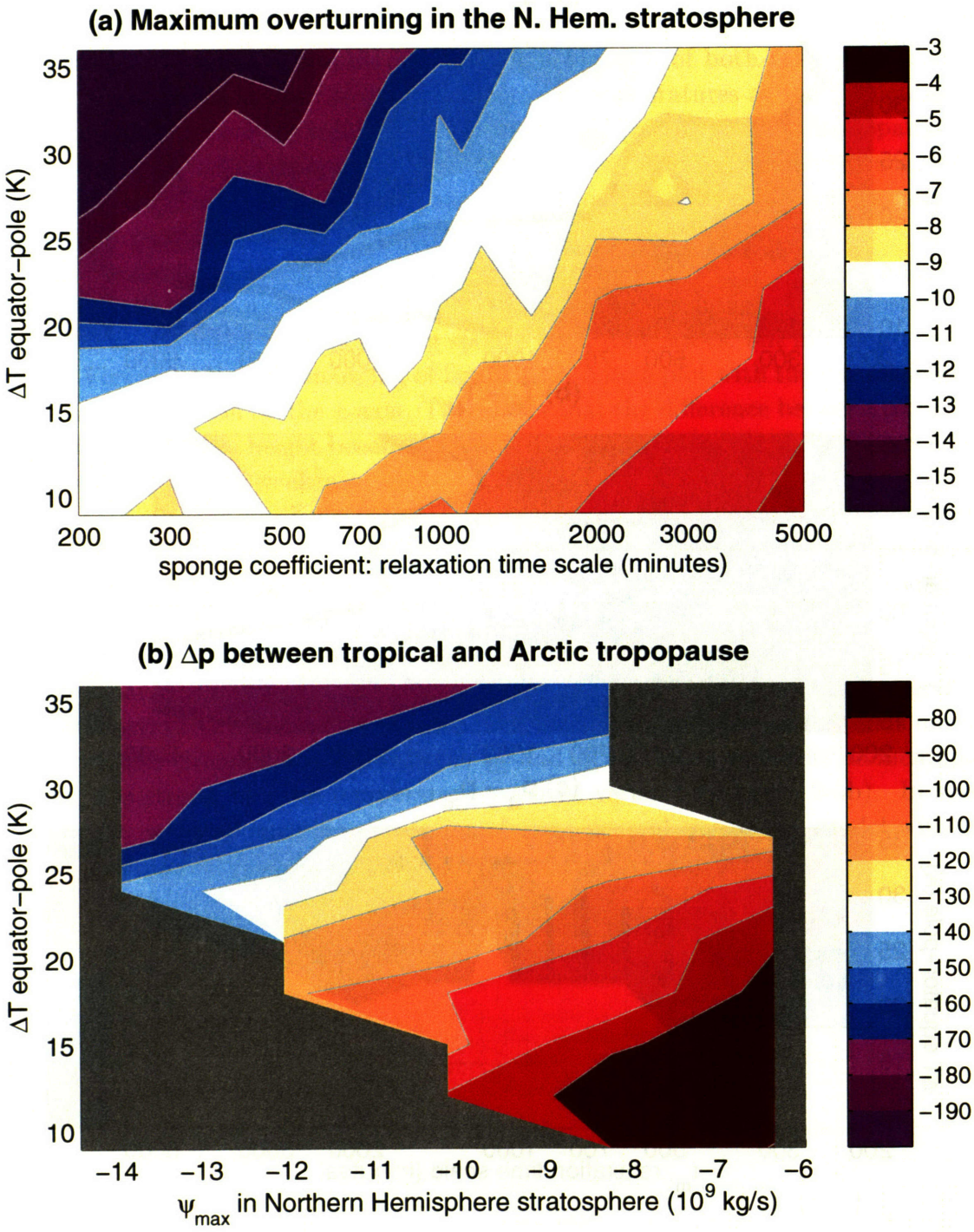

Figure 2-13: (a) Maximum strength of the stratospheric overturning circulation. (b) As in figure 2-12c, but mapped so that the maximum value of the stratospheric overturning circulation is the x-coordinate; gray areas are outside the data's domain.

Chapter 3

Simulations of warm climates

In the two decades following Eric Barron's pioneering modeling studies of the warm climates common in the geologic past, successful simulations of these periods have proved elusive (e.g., Barron 1983; Schneider et al., 1985; Barron and Washington, 1985; Sloan and Rea, 1995; Shellito et al., 2003). Without radical changes in the geometry of Earth's orbit, maintaining high latitude warmth with a weak surface temperature gradient requires a robust flux of enthalpy out of the tropics (e.g., Stone, 1978b). Fluxes are dependent upon motions, whose strength is predicated on the existence of sufficient gradients. Sustaining fluxes sufficient to diminish the meridional temperature gradient is difficult in the absence of a strong gradient. Theory and models have fallen equally behind in their ability to explain past warm periods, which dominate much of the Phanerozoic eon (Huber et al., 2000).

Aside from the early work of Barron (1983) and Farrell (1990), scant attention has been paid to the atmospheric dynamical theory of warm climate states. Notwithstanding, the number of simulations of warm climate states has multiplied over the past decade (e.g., Sloan and Rea, 1995; Huber and Sloan, 2001; Shellito et al., 2003). Along with these simulations, many explanations for their deficiencies have come. In atmosphere only studies, the ocean's implicit heat transport is large (e.g., Schneider et al., 1985). Kirk-Davidoff et al. (2002) suggest that poor resolution near the tropical tropopause limits stratospheric water vapor concentrations.

In this chapter, I add some new simulations to the growing batch of warm climate experiments, but I do this with an emphasis on analyzing the general circulation. Specifically, our goal will be to examine the evolution of the thermal structure of the stratosphere in order to assess the ease with which polar stratospheric clouds could form. In the last chapter, we noted that there must exist a strong feedback between the surface temperature gradient and the intensity of the stratospheric overturning in order for temperatures in the Arctic polar night to fall low enough to reach the frost point. The size of the necessary feedback increases owing to a rise in the height of the polar tropopause, which reduces both the meridional temperature gradient and westerly jet speeds in the lower stratosphere. In the simple model discussed in the last

chapter, there is no parameterization of eddy fluxes, so the height of the tropopause is determined by local radiative and convective processes alone.

Generating the planetary-scale Rossby waves that propagate into the stratosphere requires a three-dimensional model, and we used a modified version of the Community Atmosphere Model (CAM) developed at the National Center for Atmospheric Research for this work. This model is the atmospheric component of a suite of models coupled in the Community Climate Model package. The modifications made to the standard model are presented in the first section and a description of the simulations follows in the second section. Results are shown in section 3.3.

The energetics of the atmosphere were calculated for each simulation, and this work is presented in section 3.4. The energetics were computed for both the full atmosphere and the stratosphere alone so that a fuller comparison of each simulation can be made. This analysis enables us to quantify the strength of the various eddies, the cycling of energy through the atmosphere, and the strength of the eddies that propagate into the stratosphere in each simulated climate state. A summary of the main findings in this and the proceeding chapter is presented in the final section.

3.1 The Community Atmosphere Model

The standard version of CAM has twenty-six vertical levels, which extend to an altitude around 3 mb (approximately 40 km) (Collins et al., 2004). In order to separate the model top from the stratosphere, which is the principal region of interest in my experiments, the vertical resolution above 100 mb has been increased and the model top has been moved into the middle mesosphere, around 63 km. Additionally, Rayleigh friction has been added to the levels above 3 mb to dampen waves radiating out of the stratosphere. This reduces the reflection of these waves off of the model top and gives the energy passing through the stratopause a sink. These changes closely follow the techniques of Boville (1986).

The Rayleigh friction term added to the zonal momentum equation provides a crude parameterization of the effect of breaking gravity waves in the mesosphere in addition to reducing the reflection of waves off of the top boundary. The frictional damping coefficient is determined by:

$$K_R = \frac{2}{3}\left[1 + \tanh\left(\frac{z-63}{H}\right)\right] \text{days}^{-1}, \tag{3.1}$$

where z is the height in kilometers and H is the scale height (7.5 km). This form is identical to that used in Boville (1986), except that the amplitude has been increased by a factor of two. The addition of this friction damps the jet towards zero over the time-scales shown in figure 3-1.

Boville (1986) notes that the Rayleigh friction term should not be regarded as an accurate representation of mesospheric dynamics, which the model does not explic-

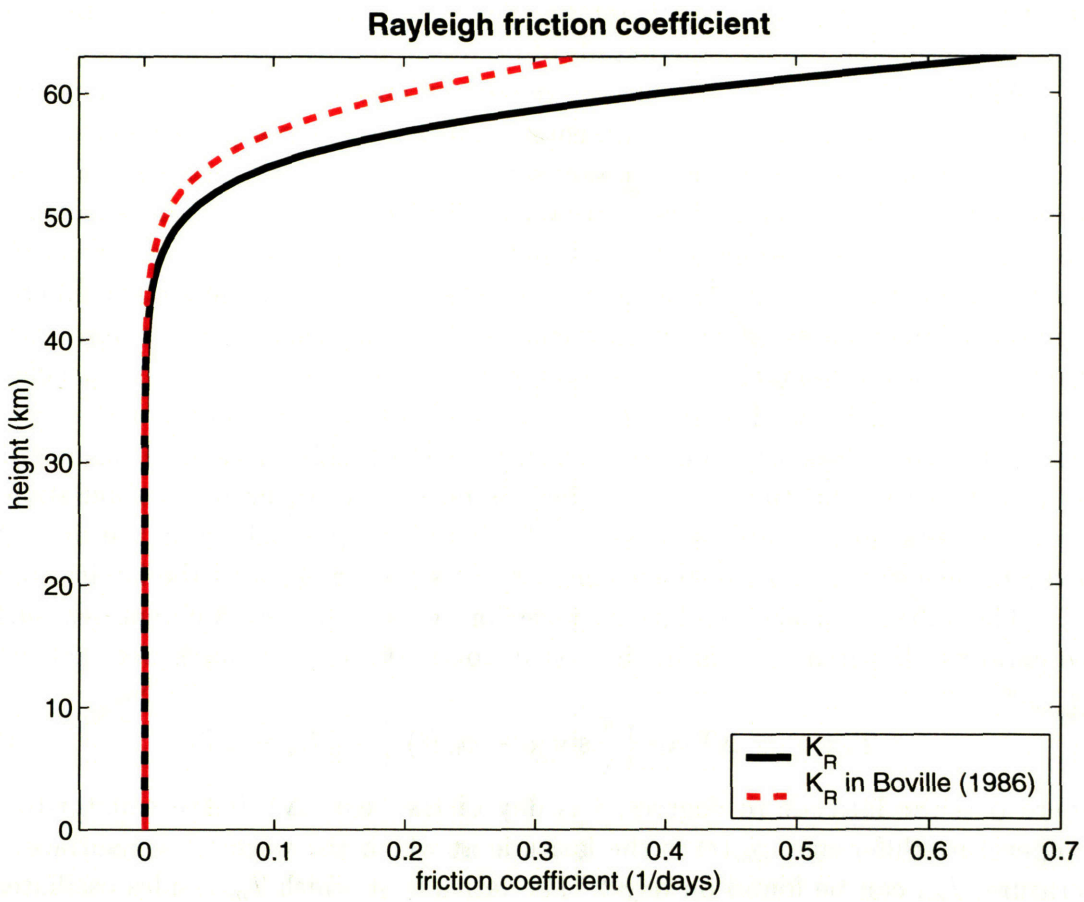

Figure 3-1: The Rayleigh friction coefficient, K_R, from equation (3.1) in solid black and from Boville (1986) in dashed red. Below 40 km, the damping is negligible.

itly resolve. The magnitude of K_R that Boville (1986) used was chosen to match the damping estimated from observations by Smith and Lyjak (1985) in the mesosphere and to be insignificant in the stratosphere. Following Byron Boville's suggestion, I have increased the amplitude in order to replicate more accurately the observed jet speeds near the stratopause (B. Boville, personal communication). Because the hyperbolic tangent term asymptotically approaches -1 as its argument becomes increasingly negative, K_R is negligible below about 3 mb (see figure 3-1).

For all runs presented here, the remainder of the model code was not altered.

3.2 Model simulations

I have done several experiments with the deeper version of CAM, but I shall focus primarily on a comparison of three simulations in this chapter. These are labeled Present, Eocene, and Greenhouse, but these titles are assigned only for reference; no attempt to simulate an ancient climate is made here. Rather, we investigate how the

stratosphere evolves with a weak temperature gradient and changes in the load of longwave absorbing gasses. The details of each run are discussed below.

All runs were forced with current geography and an imposed, monthly-varying sea surface temperature field. Continental temperatures are explicitly calculated by the land model. The control run was forced using Levitus data and the default parameters for the model; this simulation is called Present, as it attempts to replicate the contemporary atmosphere. The simulations of warm climates were forced with a zonally symmetric sea surface temperature profile. This is an important difference, but I regard the paucity of data from warm climates long ago as a critical limitation to forming a two-dimensional sea surface temperature field; it is simply too speculative. (For comparison, I forced a second simulation of the current climate with a zonally averaged Levitus data set; qualitatively, there were no differences in the stratosphere between this run and the control.) There is no sea ice in the warm simulations as ocean temperatures are always too warm for it to form (see below); in the simulation of the present climate, monthly varying sea ice is prescribed with the Levitus data.

The warm climate simulations were forced with a very different sea surface temperature distribution. As in the last chapter, the temperatures were calculated by:

$$T(\phi,t) = \Delta\mathrm{T}\cos\left\{\frac{\pi}{2}\sin\left[\phi-\phi_m(t)\right]\right\} + (T_m - \Delta\mathrm{T})\,, \tag{3.2}$$

where ϕ is the latitude in degrees, t is day of the year, ΔT is the equator-to-pole temperature difference, $\phi_m(t)$ is the latitude at which the warmest sea surface temperature, T_m, can be found on day t. The latitude at which T_m resides oscillates on an annual cycle:

$$\phi_m(t) = \frac{(\phi_n - \phi_s)}{2}\cos\left[2\pi\frac{(t-t_n)}{365}\right] + \frac{(\phi_n + \phi_s)}{2}. \tag{3.3}$$

Here ϕ_n is the northern most latitude at which T_m occurs, ϕ_s is the southern most latitude at which T_m occurs, and t_n is the day on which T_m reaches ϕ_n. By choosing t_n to be, say, August 1, the warmest sea surface temperatures will settle near ϕ_n during the Northern Hemisphere summer, and then will migrate south toward ϕ_s, reaching it six months later.

By choosing ϕ_n to be 8°N, ϕ_s to be 2°S, t_n to be noon on August 1 (day 213.5), T_m to be 30°C, and ΔT to be 10°C, equations (3.2) and (3.3) produce a warm profile over the entire planet. These choices for ϕ_n and ϕ_s closely mimic the present range of T_m (see, e.g., Lindzen, 1990). There is no reason to expect these to remain fixed through geologic time, but the small value of ΔT strongly limits the variability of temperatures in both space and time. Temperatures in the tropics are confined to 28-30°C, while high latitude temperatures are never colder than 20°C year round.

The seasonal extremes of the temperature profile produced by equations (3.2) and (3.3) are plotted in figure 3-2. Note that this profile is a function of latitude and month only; it is zonally symmetric. This warm temperature profile produces a

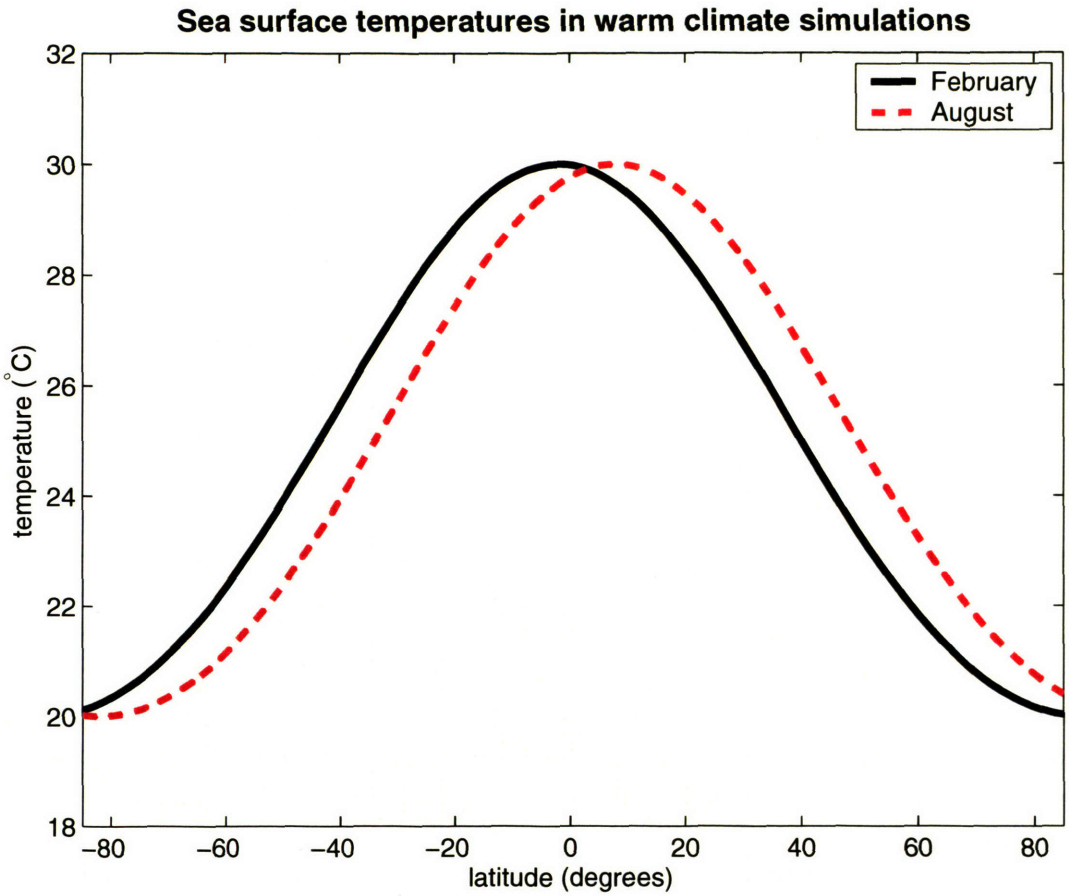

Figure 3-2: Zonally symmetric sea surface temperature profile that forces the two warm climate simulations (Eocene and Greenhouse). February and August, the seasonal extremes, are plotted.

meridional gradient that is more gradual than suggested by any of the paleo-climate proxy data, but I choose this for several reasons. First, the most striking features of warm climates are captured: tropical temperatures are near the values observed today (e.g., Schrag, 1999; Pearson, 2001) while high latitude temperatures are kept mild enough to inhibit sea ice. While my choice of 10°C for ΔT produces a temperature gradient closer to an isothermal one than can be justified by proxy data, my point is not to simulate conditions from the Eocene or any other time period directly. This study focuses on mechanisms, and I choose a temperature gradient weaker than any the Earth possessed throughout the Cenozoic in order to test the limits of the polar stratosphere cloud hypothesis. If the stratosphere does not evolve to conditions conducive to polar stratospheric cloud formation with a temperature gradient this weak, dynamics are unlikely to have led it to such a state at any point during the Cenozoic, when temperature gradients remained stronger than in the profile I created.

All warm climate simulations use this temperature profile, but they differ in

the concentrations of key longwave absorbers. The Eocene simulation retains the present concentrations of carbon dioxide (355 ppm) and methane (1.714 ppm) while using the warm sea surface temperature profile. The CO_2 simulation elevates carbon dioxide concentrations to 1500 ppm, uses present methane concentrations, and the warm temperature profile. Finally, the Greenhouse simulation elevates carbon dioxide to 1500 ppm, methane to 10 ppm, and uses the warm temperature profile. The presentation will focus on the contrast between Eocene and Greenhouse and the control run, Present; there is little difference between CO_2 and Greenhouse.

All experiments were integrated for twenty model years, and results presented in this chapter were averaged over the last five years of data.

3.3 Results

As discussed in the last chapter, contemporary synoptic-scale temperatures in the Arctic stratosphere are considerably warmer than the frost point. Temperatures must cool $15-20$ K, local water vapor concentrations must rise by a factor of ten to fifteen, or some combination of both must occur in order for widespread polar stratospheric cloud formation to occur (see figure 2-1).[1] As observations in the Antarctic show, reaching the local frost point of water on the synoptic-scale does not guarantee that any clouds will be thick enough to affect the surface climate, though this is at least a minimum requirement.

In figure 3-3 I update the winter soundings by including model predicted temperatures as well. The dashed black curve is actual data, which was also plotted in figure 2-1. The solid black curve is the simulation of the present climate using CAM; it attempts to replicate the observational data. Note that there is a cold bias in the model, which has occurred in all versions of CAM in this region of the atmosphere. Following improvements made to the radiation code, this continued bias is most likely attributable to an underestimated strength of the residual circulation and dynamical heating in the polar vortex (P. Rasch, personal communication).

The remaining curves come from various attempts to simulate warm climates. As introduced in the last section, the other three simulations were each forced with a warm sea surface temperature profile. The Eocene simulation, shown in solid red, shows little movement away from the Present sounding. The two simulations with higher concentrations of longwave absorbers have cooler temperatures in the upper stratosphere owing to increased longwave cooling to space, but they remain warmer than the frost point of water.

The dark gray area on the left side of the plot represents those temperatures and pressures at which a parcel of air containing 5 ppmv water vapor will be satu-

[1] Recall that the frost point serves as the threshold temperature for Type II clouds in the stratosphere, which are composed of ice crystals. Type I clouds, which are composed of a nitric acid-water compound, can form at temperatures about 3 K warmer than the frost point. See section 2.2 for more discussion and references.

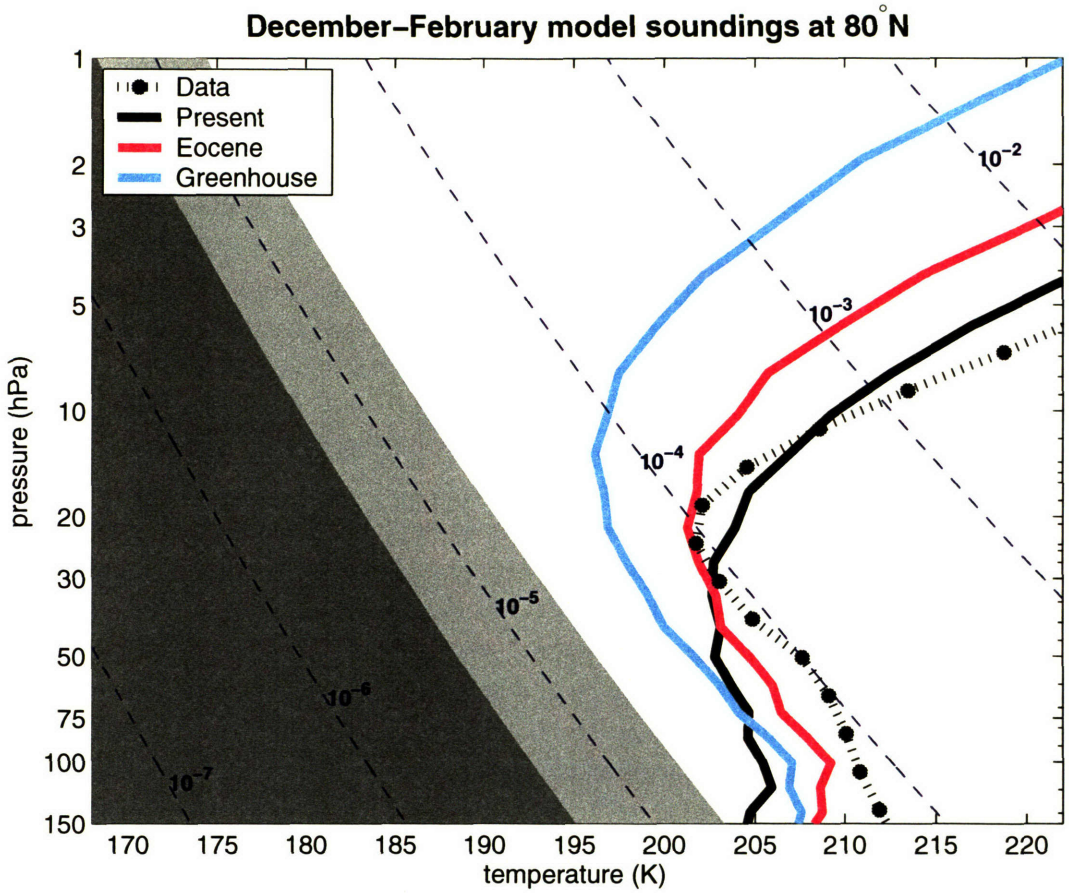

Figure 3-3: As in figure 2-1, but with model-predicted zonal mean temperatures at 80°N (averaged over the last five Decembers, Januaries, and Februaries) plotted too. The dotted starred black curve is the real present temperature sounding shown in figure 2-1. The solid black curve represents the model-predicted sounding of the present climate; note that there is a slight cold bias through much of the Arctic vortex. The colored curves both come from runs forced with a weak surface temperature gradient; the red (Eocene) has no other changes, but the blue (Greenhouse) has 1500 ppm of CO_2 and 7 ppm CH_4. The dark gray shading represents the region in which parcels containing 5 ppmv water vapor or less will be saturated; the light gray band expands this to 20 ppmv.

rated. If methane were higher in warm climates, there might be an increase in the stratospheric concentration of water vapor owing to this chemical source. Recently, Schmidt and Shindell (2003) found that a ten-fold increase in methane would triple the amounts of water vapor. Should this chemical source be combined with a rise in the temperature of the tropical tropopause, ambient water vapor concentrations in the winter stratosphere could be higher in warm climates. But a three-fold increase from methane oxidation (Schmidt and Shindell, 2003) and a warming of 5 K at cold trap in the equatorial lower stratosphere would increase water vapor concentrations only modestly. For reference, the temperatures and pressures that would be saturated

if 20 ppmv of water vapor were present in the winter stratosphere are highlighted in light gray in figure 3-3. Note that even a four-fold increase in water vapor concentrations is insufficient to bring the frost point up to average temperatures in the winter stratosphere.

Note that all simulations produce temperatures that are too warm for large-scale polar stratospheric cloud formation. The combination of a cooler stratosphere from increased longwave absorbers and more water vapor from higher concentrations of methane may bring the stratosphere closer to saturation, but the movement is not dramatic. There is no evidence that dynamics contributed to the slight movement, as the Eocene simulation[2] is actually warmer than the Present in the lower stratosphere. Were the residual circulation substantially weaker, less dynamical heating should cause temperatures to cool towards radiative equilibrium.

Similarly, simulated winter temperatures in the Antarctic show little change as a result of a weaker surface temperature gradient (see figure 3-4). The predicted temperature for the Present is again colder than observations, but all warm climate simulations predict temperatures will not be colder below 20 hPa.

While these soundings are cool enough to support polar stratospheric cloud formation on the large-scale, such clouds prove insufficient to affect surface climate in the real atmosphere. The Southern Hemisphere offers a nice place to test a broader question of the polar stratospheric cloud hypothesis. Observational studies suggest that the residual circulation in the Southern Hemisphere is weaker than in the Northern Hemisphere, most likely owing to the fact that there is less planetary-scale wave generation [land masses and topographic features are biased to the north of the equator, and this strongly affects planetary-wave formation (see, e.g., Held and Hoskins, 1985)]. In light of this, it is not surprising that Antarctic stratospheric winter temperatures change so little with a different surface gradient; the dynamical heating of the Antarctic vortex is already comparatively small. Still, Antarctica remains frozen presently; a viable mechanism to increase the thickness of polar stratospheric clouds is needed before this idea can gain any further credence. While a warmer tropical tropopause could permit more water vapor to enter the stratosphere, as we shall see below, temperatures change little there in these simulations.

Kirk-Davidoff et al. (2002) argue that poor resolution in the vicinity of the tropical tropopause is responsible for an underestimate of stratospheric water vapor. That may well be true, but regardless there is little support for their claim that a weaker surface temperature gradient will produce a weaker residual circulation. Surprisingly, temperatures in the lower stratosphere are warmer in the simulations of warm climate states.

[2]Recall that the Eocene simulation, like the Present simulation, contains contemporary amounts of longwave absorbers. Both Present and Eocene have concentrations of carbon dioxide that are fixed at 355 ppm, and concentrations of methane that are fixed at 1.714 ppm.

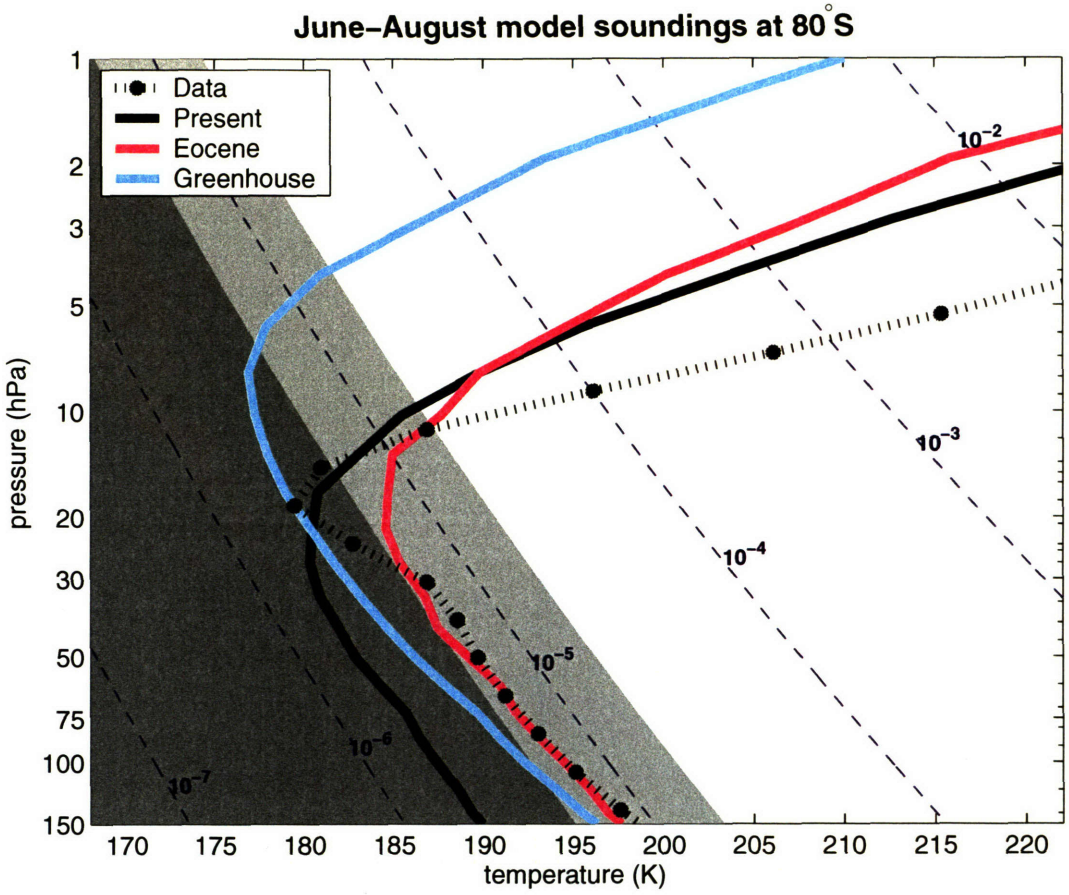

Figure 3-4: As in figure 3-3, but with model-predicted zonal mean temperatures at 80°S (averaged over the last five Junes, Julys, and Augusts) plotted. The dotted starred black curve is the actual contemporary temperature sounding shown in figure 2-1 for the Southern Hemisphere winter.

3.3.1 Thermal and dynamic structure

We now examine the zonally symmetric seasonal mean state of the stratosphere. Figure 3-5 shows the December-February mean zonal mean temperature between 100 and 1 mb. Note the coldest temperatures are, as in the real atmosphere, found at the tropical tropopause, where temperatures can fall below 190 K. Temperatures rise with altitude through the stratosphere, creating a strong stratification and vertical potential vorticity gradient. Temperatures in the winter stratosphere are cold, but not nearly as cold as radiative equilibrium values, which are as low as 140 K in the winter stratosphere (see, e.g., Fels, 1985).

In thermal wind balance with this temperature field are two jets: one easterly in the summer hemisphere, the other westerly in the winter one. The zonal mean zonal wind averaged over the last five Decembers, Januaries, and Februaries is plotted in figure 3-6. Note that the strong westerly winds in the winter hemisphere form the

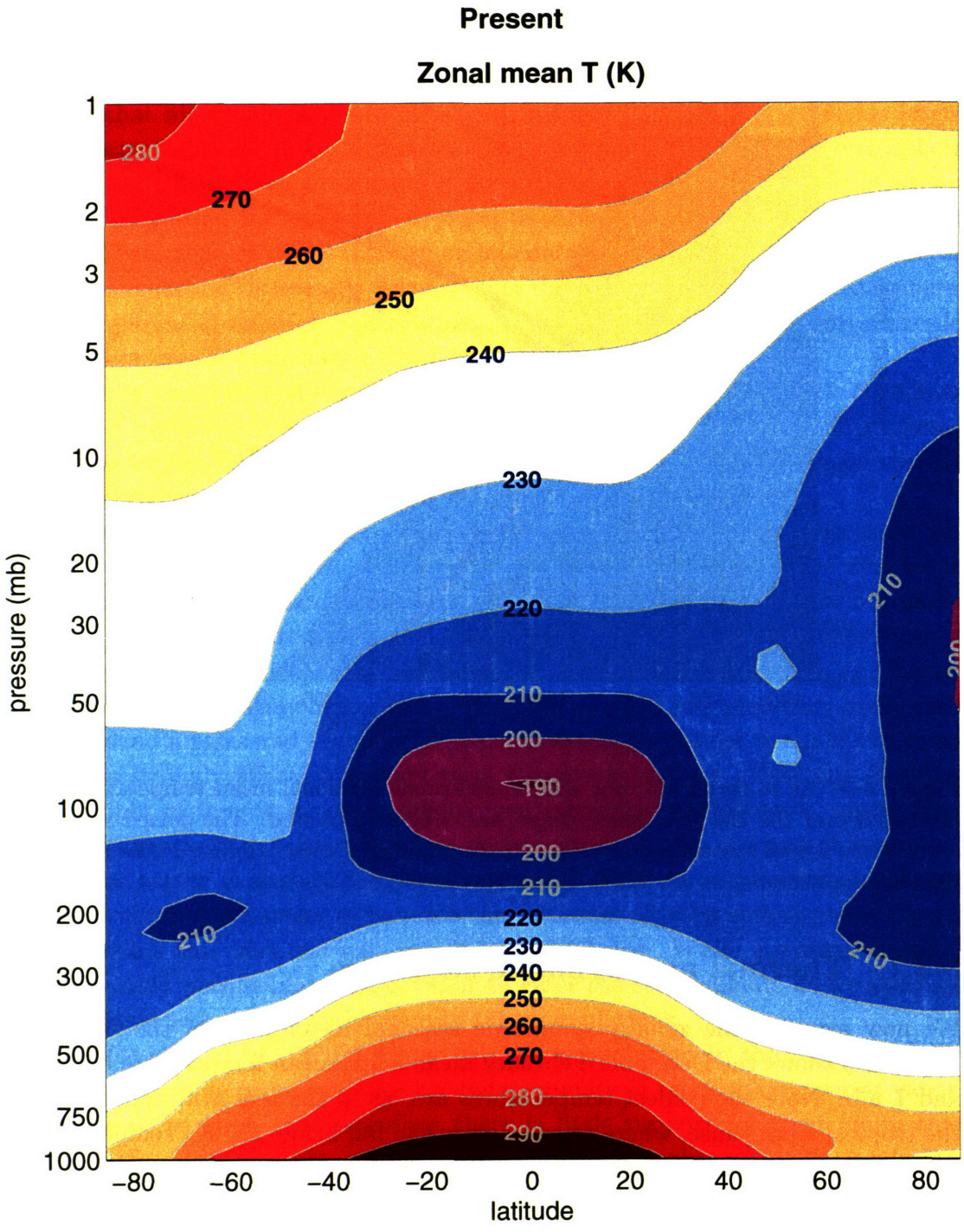

Figure 3-5: Zonally averaged temperatures averaged over the last five Decembers, Januaries, and Februaries of the Present simulation. Sea surface temperatures were specified from Levitus data. Note the low-level inversion of winter temperatures at high latitudes of the Northern Hemisphere.

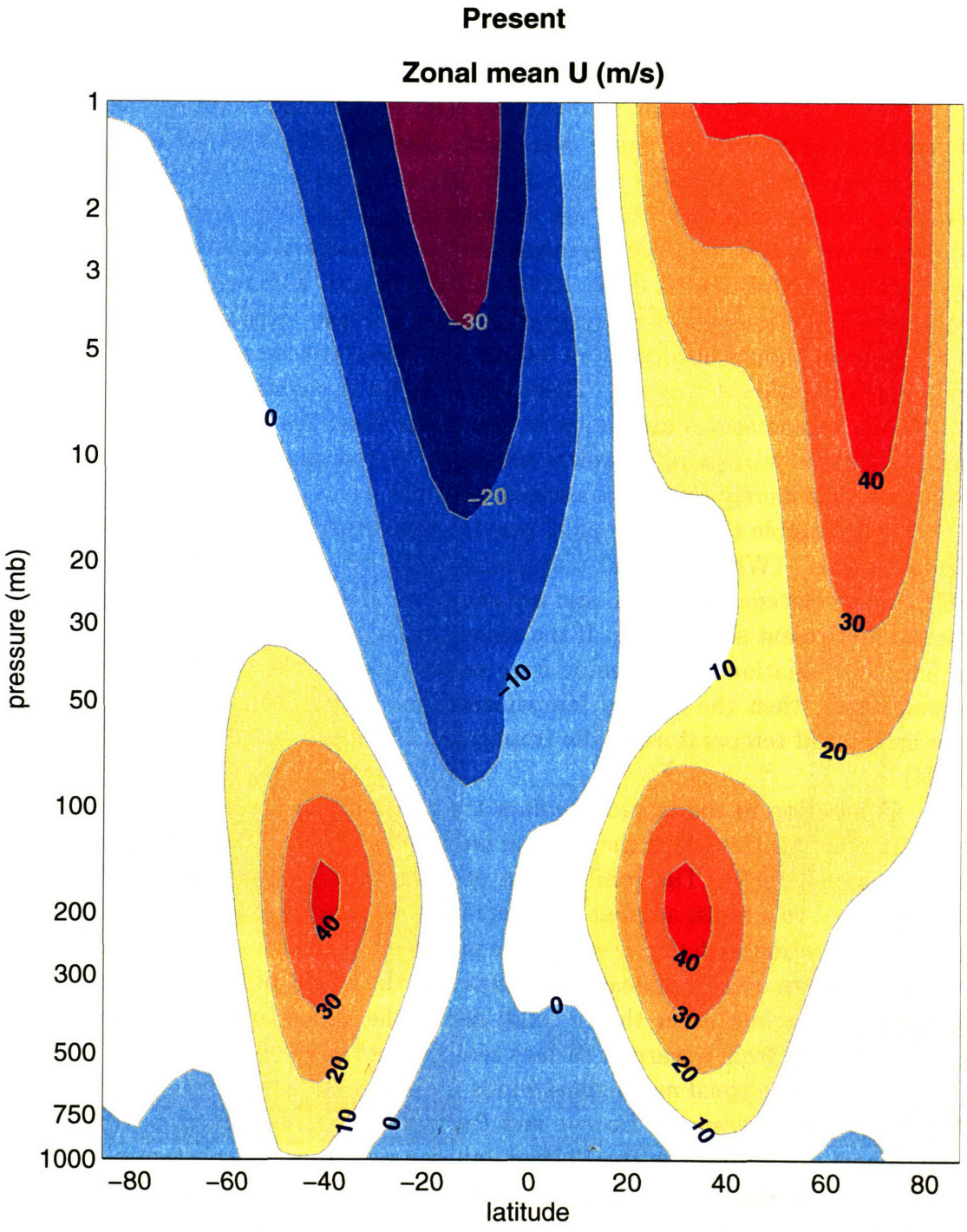

Figure 3-6: Zonally averaged zonal wind averaged over the last five Decembers, Januaries, and Februaries of the Present simulation. Note the strength of the westerly jets in the troposphere and winter stratosphere. Easterlies in the summer stratosphere prohibit vertical propagation of standing Rossby waves.

wall to the Arctic vortex. Winds increase with altitude, as predicted by thermal wind balance ($\partial_z u \propto -\partial_y T$). The top of the tropospheric jets can be seen in the mid-latitudes of each hemisphere at the bottom of the panel; they reach a maximum at the tropopause, between 200 and 250 mb.

The zonal mean December-February stratospheric temperatures for the Eocene simulation are plotted in figure 3-7a, with the difference between the Eocene and Present simulations shown in panel 3-7b. Broadly, the temperature fields are quite similar between runs, but there are notable exceptions. Temperatures near and just above the tropical tropopause are warmer in the Eocene simulation than in the Present one. While Kirk-Davidoff et al. (2002) expected such a change owing to a weaker residual circulation (and less dynamical cooling of the tropical stratosphere), such a mechanism should also cool the middle and high latitude stratosphere, where the residual circulation downwells. There is no change in middle latitude temperatures, and while temperatures are cooler in the upper most Arctic stratosphere, they are several degrees warmer in the lower stratosphere; this suggests that the temperature minimum has merely shifted to a higher altitude.

It is possible that the tropical tropopause warming is caused by higher surface temperatures. (While tropical temperatures do not change much, they are nearly 30°C in the Eocene simulation and are nearer to 27°C in the Levitus data set, which forces the Present simulation.) If the temperature profile in the tropical stratosphere is fixed by radiation (which, aside from water vapor, is the same between these two simulations), then the surface temperature and tropospheric lapse rate determine the height and temperature of the tropopause (Thuburn and Craig, 1997; Schneider, 2004).

Convection in the tropics confines the tropospheric lapse rate to closely follow a moist adiabat; this keeps the tropical troposphere neutral to moist convection (Xu and Emanuel, 1989). The combination of a higher surface temperature and a lapse rate confined to a moist adiabat dictates that the tropopause be higher in the tropics, as the intersection with the stratospheric profile occurs at a warmer[3] and higher point. While this is an oversimplification of what sets the height of the tropical tropopause, it illustrates to first order that a small rise in the upper tropospheric temperatures follows directly from a warmer surface temperature in the deep tropics.

The Eocene zonal mean zonal winds are shown in figure 3-8a; figure 3-8b shows the difference between the Eocene and Present cases. The easterlies in the summer hemisphere are stronger in the Eocene, but the westerlies are substantially weaker in the lower stratosphere. This is a critical point because the strength of the westerly jet determines which waves can propagate into the stratosphere (Charney and Drazin, 1961). The meridional temperature gradient at 100 mb is less steep in the winter hemisphere in the Eocene case by warming both the tropical and Arctic temperatures. In a later section, I argue that this results from a rise in the height of the extratropical

[3]Provided the stratospheric profile remains unchanged and increases with height.

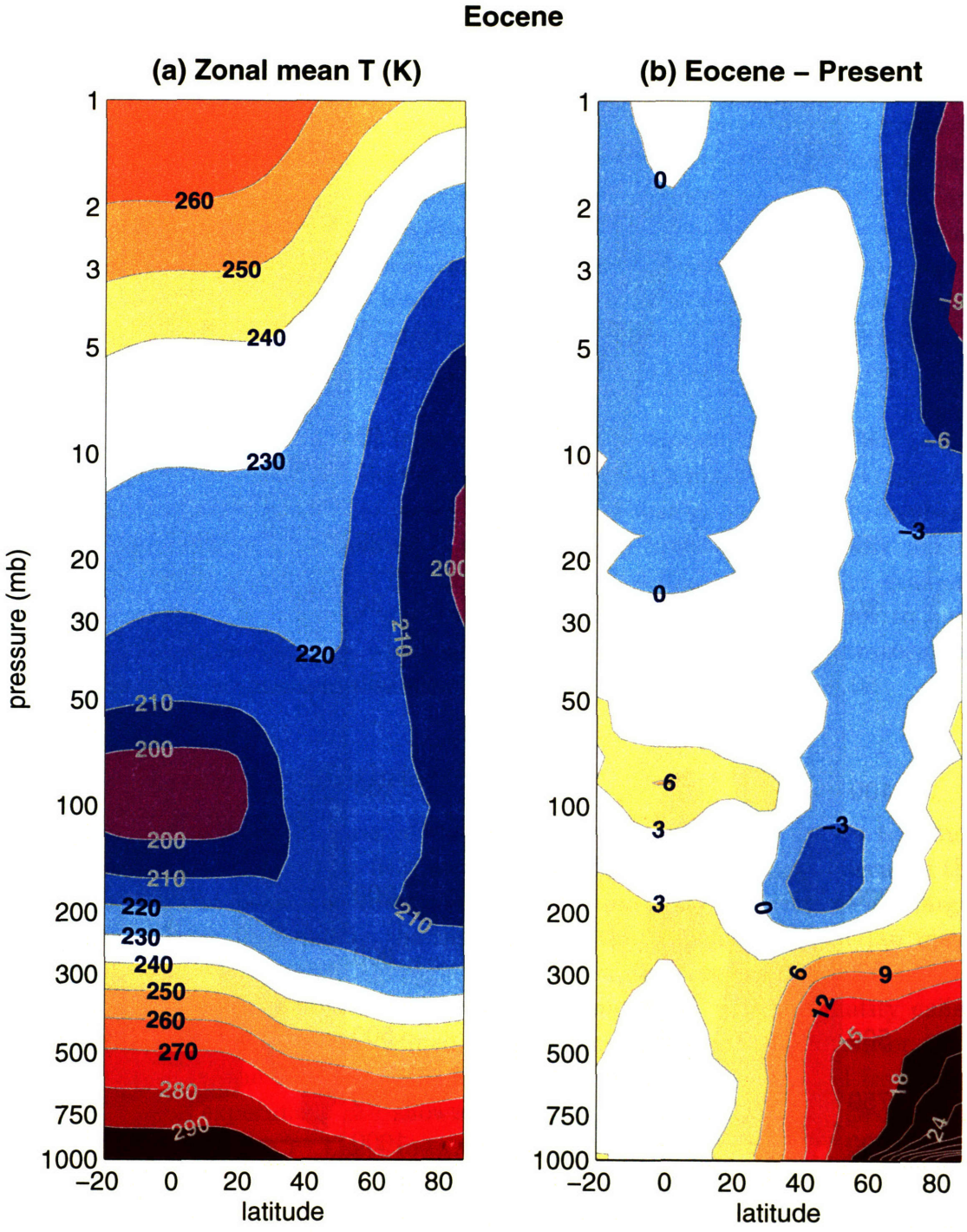

Figure 3-7: (a) As in figure 3-5, but for the Eocene simulation (for compactness, only latitudes north of 20°S are shown). (b) The difference in zonal mean December-February temperatures between the Eocene and Present simulations. Note that temperatures in the lower stratosphere are warmer in the tropics and Arctic. Temperatures are as much as ten degrees cooler in the Arctic upper stratosphere.

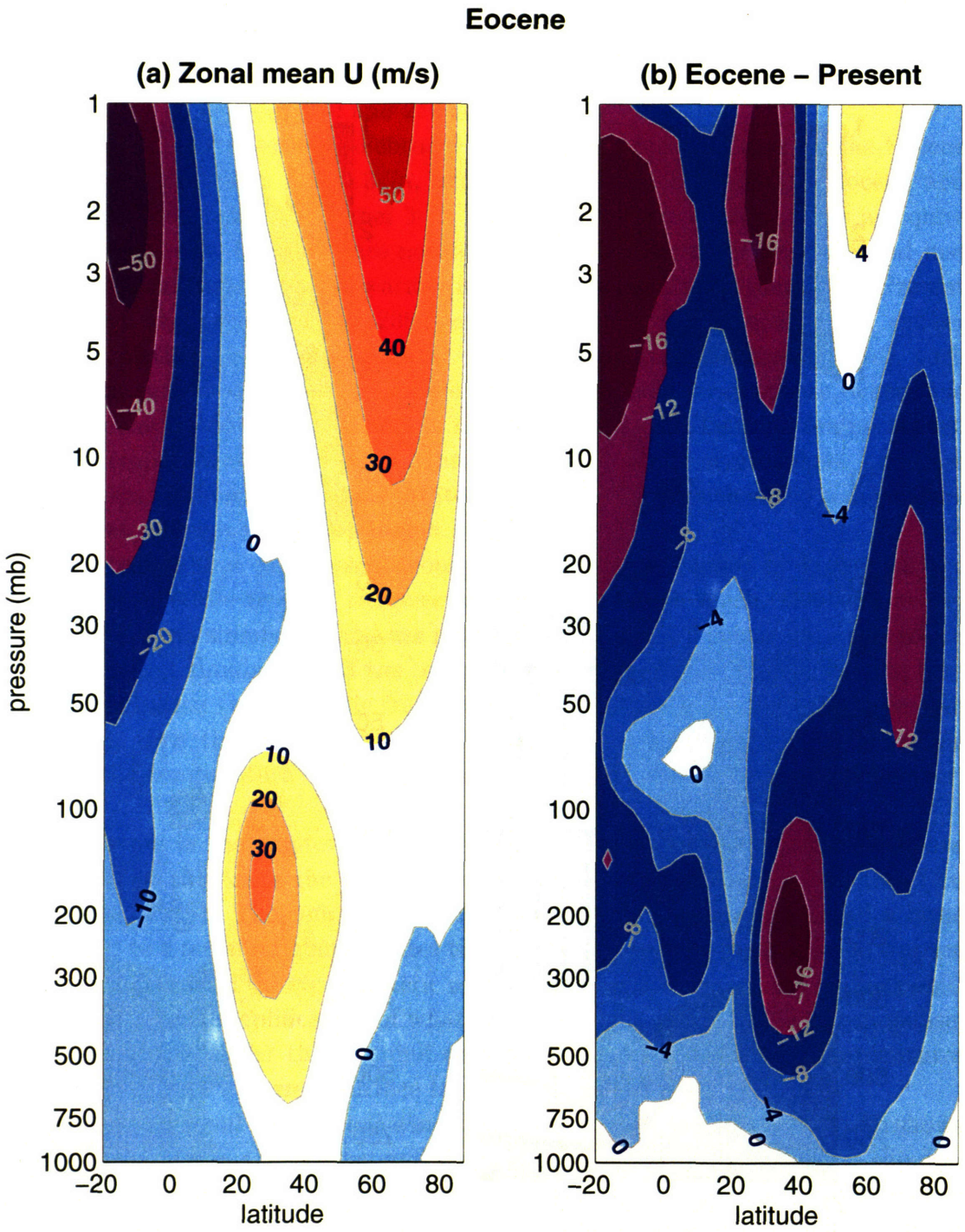

Figure 3-8: (a) As in figure 3-6, but for the Eocene simulation (for compactness, only latitudes north of 20°S are shown). (b) The difference in zonal mean December-February zonal wind. Note that the easterlies are stronger in the Southern Hemisphere stratosphere while the westerlies are weaker in the lower stratosphere of the winter hemisphere. The westerly jet is of comparable strength aloft, but winds in the lower stratospheric are less than 20 m/s everywhere below 30 mb, and often less than 10 m/s.

tropopause in high latitudes, thus lessening the planetary-scale gradient in tropopause height and causing winds in the lower stratosphere to weaken in thermal wind balance.

In the Greenhouse simulation, temperatures are much cooler throughout most of the stratosphere (see figure 3-9). Temperatures near the stratopause are as much as $25-30$K cooler in the Greenhouse simulation than in the Present (or in the Eocene); this is owing to the radiative cooling properties of increased concentrations of carbon dioxide, methane, and water vapor at such high altitudes (see section 2.3.1, appendix B, and references therein). Stratospheric longwave cooling to space increases with higher concentrations of carbon dioxide (e.g., Hartmann, 1994). Temperatures are again warmer in the tropical lower stratosphere and in the Arctic lower stratosphere by a couple of degrees. A reduction in the strength of the residual circulation should cause a warming of the tropical stratosphere but a cooling of the Arctic. This pattern is not observed here.

The zonal mean zonal winds from the Greenhouse simulation are shown in figure 3-10. Like the Eocene, the westerly jet is weaker through much of the stratosphere, and this has implications for what waves are able to propagate into the stratosphere.

The remainder of this chapter is devoted to an investigation of why winter stratosphere temperatures are so stable, even as the surface temperature gradient changes markedly. The thermal structure of the stratosphere appears not to have evolved with the surface climate, which suggests that the dynamics of the stratosphere are changing little in these simulations.

3.3.2 Residual circulation

Among the most striking features of the middle atmosphere is the degree to which dynamics alter the temperature field away from radiative equilibrium. Because the stratosphere is stably stratified to convection, radiation and dynamics set the large-scale structure. As discussed in the last chapter, the transformed Eulerian mean equations offer a proxy for the Lagrangian flow. By subtracting the derivatives of the eddy heat flux from the Eulerian mean velocities, one is left with a quantity called the residual circulation; this was defined by equation (2.21) in the last chapter.

In figure 3-11, the Eliassen-Palm flux and its divergence calculated from data from the Present experiment are shown. (The data are the last five Decembers, Januaries, and Februaries.) The arrows show an upward propagation of eddy activity in the middle latitudes of the winter hemisphere that turns poleward in the upper stratosphere. Here it converges (indicated by the negative shaded contours), and $\nabla \cdot \mathbf{F}$ acts as a body force on the winter stratosphere. The waves deposit angular momentum, damping the jet and driving a flow poleward in the upper stratosphere, in balance with the Coriolis torque. (Note that this balance must be true in a steady state, as $\partial_t \overline{u}$ is then zero.) This poleward flow is connected to vertical flow by mass continuity: the flow is upward in the tropics and downward at high latitudes. This will be illustrated in figure 3-17.

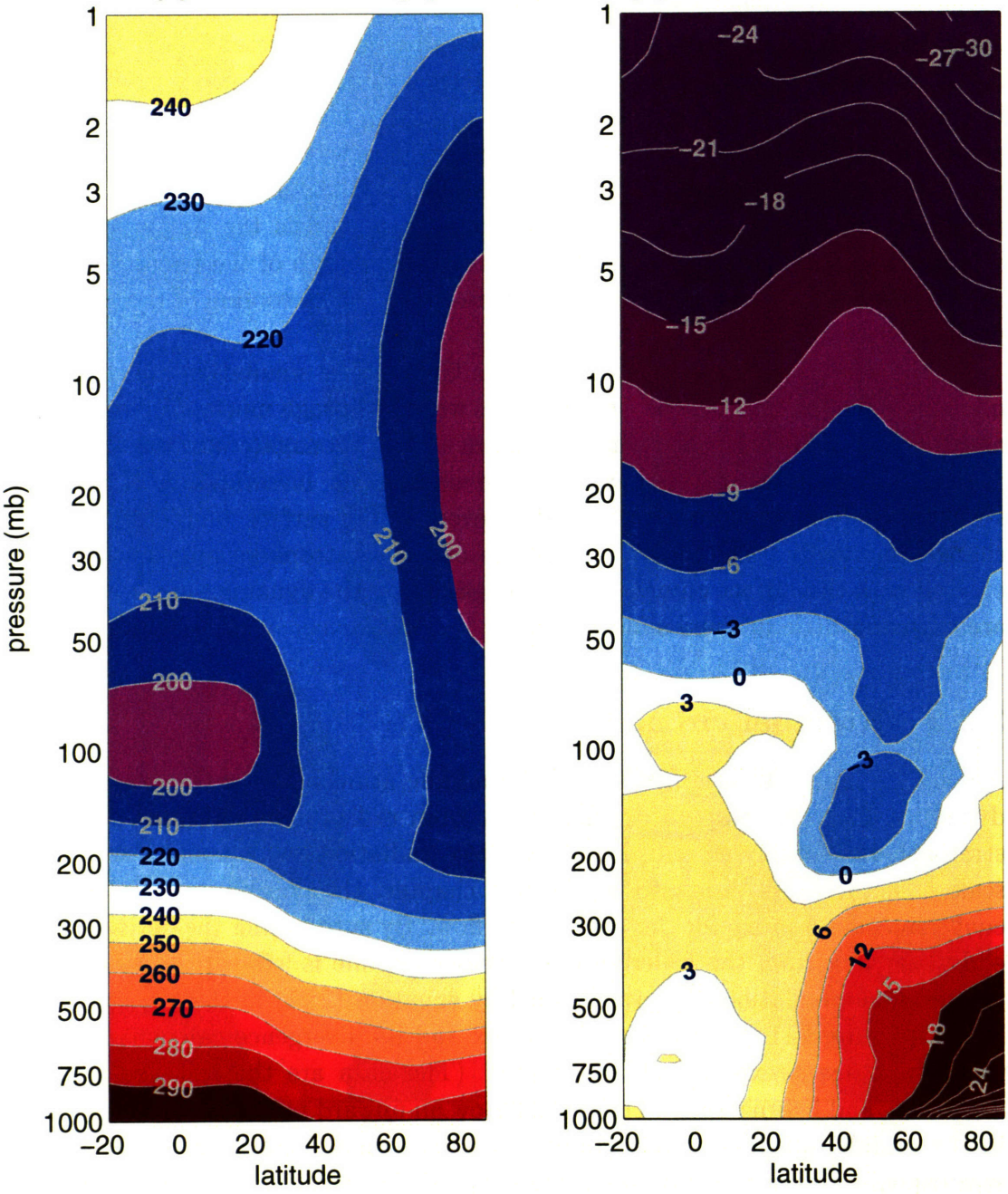

Figure 3-9: (a) As in figure 3-7, but for the Greenhouse simulation. (b) The difference in zonal mean December-February temperatures between the Greenhouse and Present simulations. The most striking feature is the uniform cooling of the stratosphere owing to increased longwave cooling to space. Temperatures are as much as 30 K colder near the stratopause, while they slightly warmer near the tropopause in the tropics and Arctic.

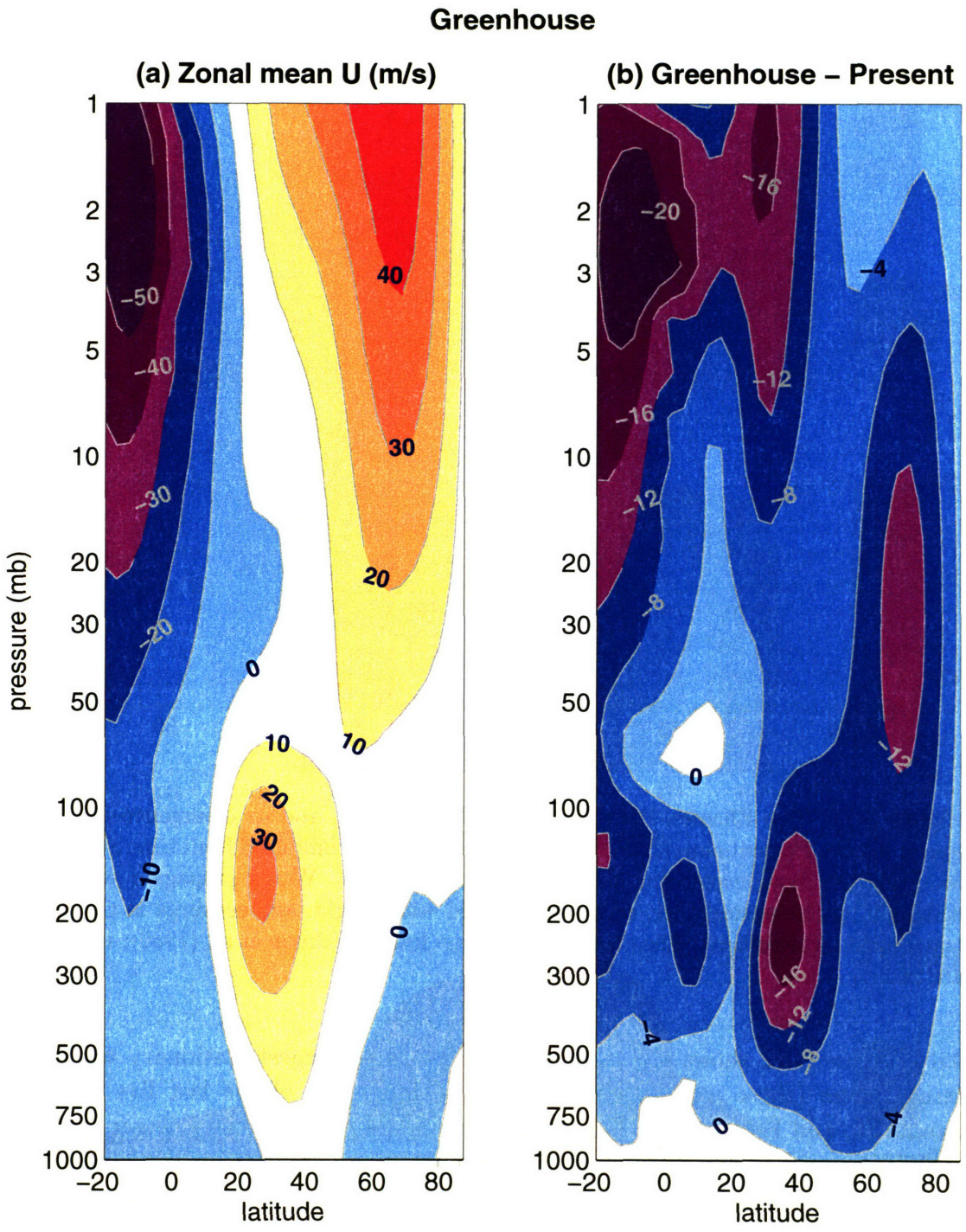

Figure 3-10: (a) As in figure 3-8, but for the Greenhouse simulation. (b) The difference in zonal mean December-February zonal wind. Note that the easterlies are stronger in the Southern Hemisphere stratosphere while the westerlies are weaker in the winter hemisphere. The westerly jet is more than 8 m/s weaker through much of the Northern Hemisphere extratropical stratosphere; jet speeds are below 20 m/s everywhere below 30 mb, and often less than 10 m/s.

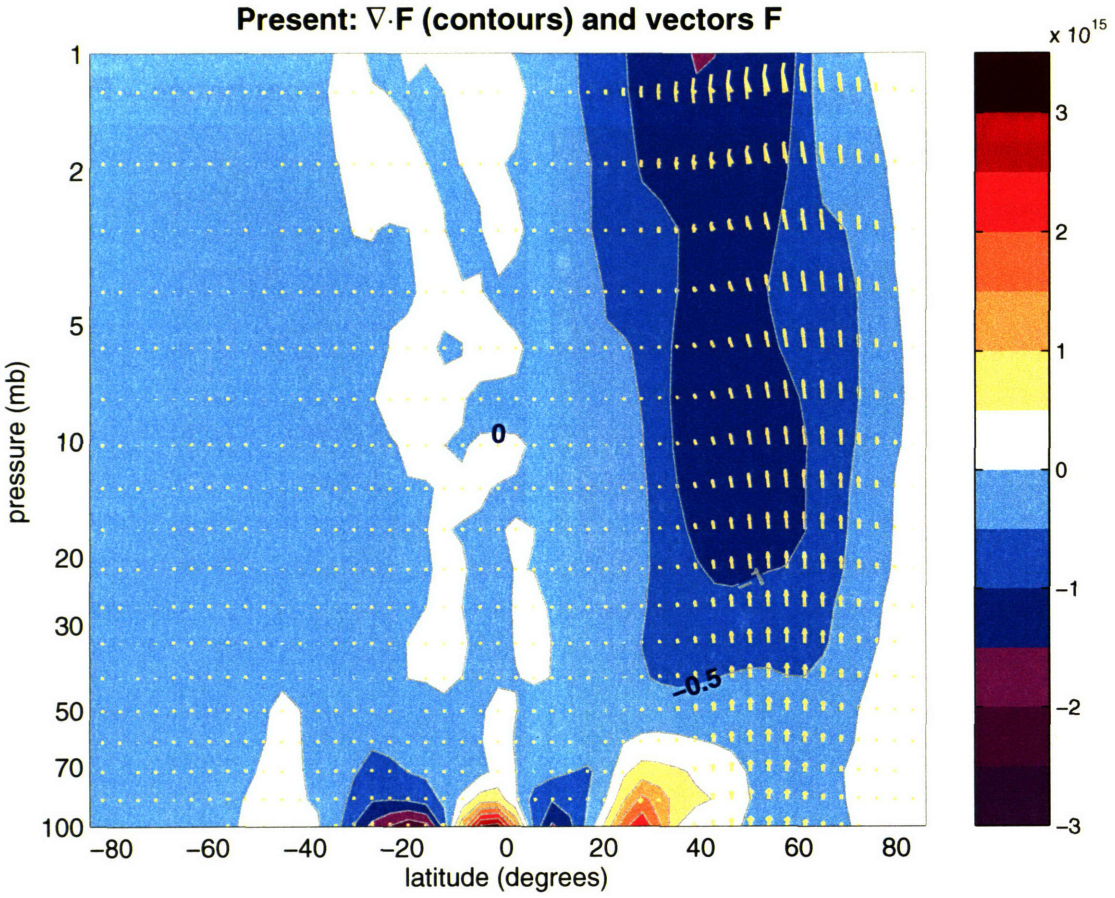

Figure 3-11: The Eliassen-Palm flux, **F** (yellow arrows), and its divergence (colored contours) for the Present simulation. These quantities were computed from time averaged data over the last five Decembers, Januaries, and Februaries. Waves propagate vertically, are deflected by the westerly jet, turn equatorward with height, and converge in the upper extratropical stratosphere. The plotting technique follows Edmon et al. (1980); units of $\nabla \cdot \mathbf{F}$ are in m^3.

Figure 3-12 shows the amplitude of the three longest stationary waves in the stratosphere (these were calculated from a time-mean of the last five Decembers, Januaries, and Februaries). Though real waves are not stationary, linear, or small in scale compared to the mean flow, the amplitudes are greatest for the longest waves, in agreement with the predictions of Charney and Drazin (1961). There is a strong presence of the two longest planetary waves, but wavenumber three is evanescent. This agrees well with observations (e.g., Andrews et al., 1987). Wavenumber three and shorter waves are largely prohibited from vertically propagating into the stratosphere by the strong winds at the tropospheric jet; the winds in the lower stratosphere, though weaker than the peak in the tropospheric jet, are also too strong to allow for propagation of these short waves.

The Eliassen-Palm flux and its divergence from the Eocene run are shown in

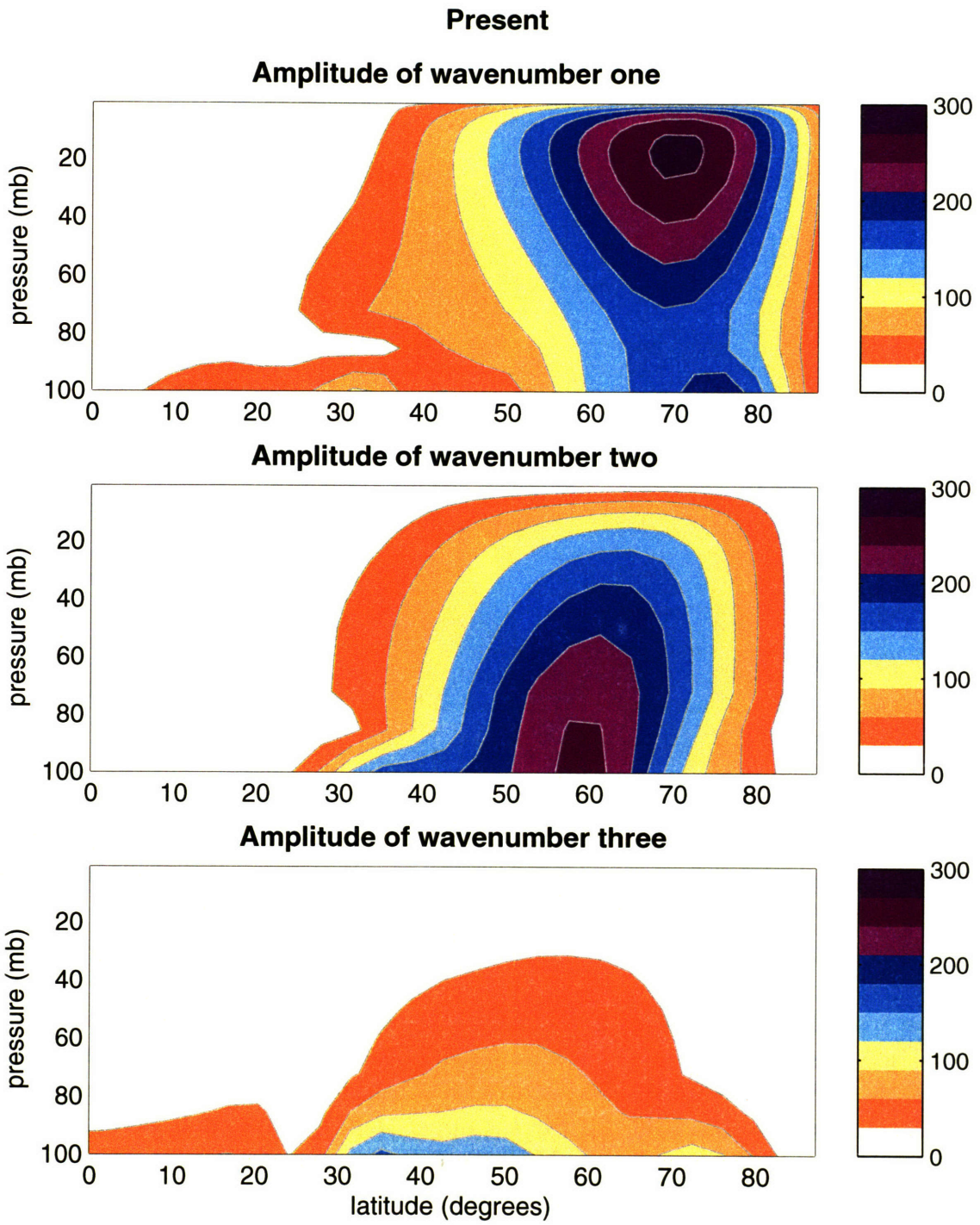

Figure 3-12: The amplitude of the three longest waves in the geopotential height field in the stratosphere in the Present simulation. The geopotential field was decomposed into Fourier components, and the amplitudes of waves 1, 2, and 3 are shown. Units are in meters, but the values have been normalized by $\sqrt{p/p_o}$ to compensate for the increase in amplitudes with decreasing density. These are from time averaged data over the last five Decembers, Januaries, and Februaries. (The amplitudes shown are $\sqrt{p/p_o}\sqrt{A \cdot A^\star}$, where A is the amplitude of each Fourier component and $A^\star$ is its complex conjugate.)

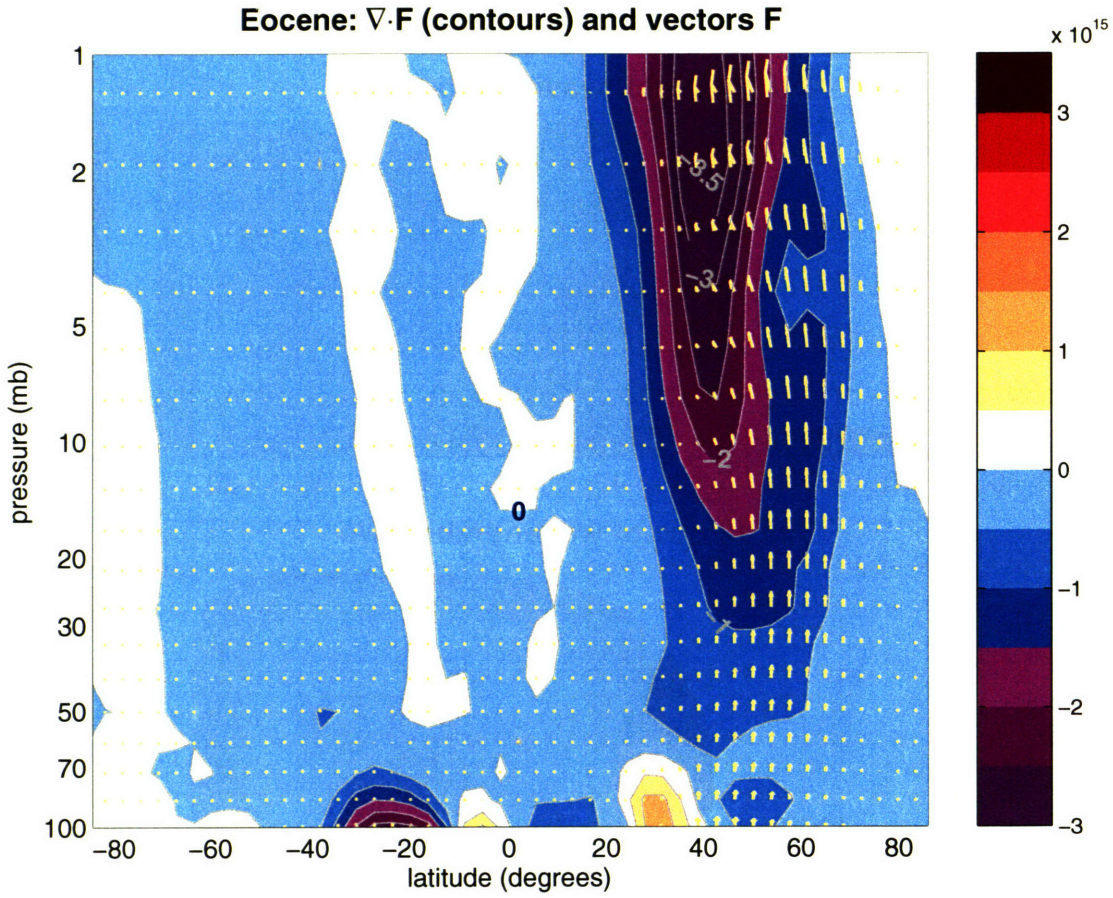

Figure 3-13: As in figure 3-11, but for the Eocene. The convergence of the Eliassen-Palm flux is stronger in this simulation than in Present. Waves propagate vertically, are deflected by the westerly jet, turn equatorward with height, and converge in the upper extratropical stratosphere. The plotting technique follows Edmon et al. (1980); units of $\nabla \cdot \mathbf{F}$ are in m^3.

figure 3-13. The convergence in the upper stratosphere is larger than in the Present case, which shows that the force driving the residual circulation has increased in intensity. Indeed, the flux of $\mathbf{F}$ across the 100 mb surface is larger in this case than in the Present simulation. It is larger in the upper troposphere as well, becoming equal between 400 and 500 mb. Below this level, $\mathbf{F}$ is larger in the Present case (this will be further discussed in section 3.4 and shown in figure 3-18).

One clear difference between the Present and Eocene cases is the decrease in upper tropospheric and lower stratospheric winds in the Eocene experiment. A plot of the amplitudes of the first six stationary waves shows that the tropospheric energy has decreased, particularly in some of the synoptic scale waves (not shown). The increase in the flux of $\mathbf{F}$ above all pressure levels above 400 mb, however, indicates that although the energy in the troposphere has decreased on the whole, the fraction that is propagating vertically into the upper troposphere and lower stratosphere has in-

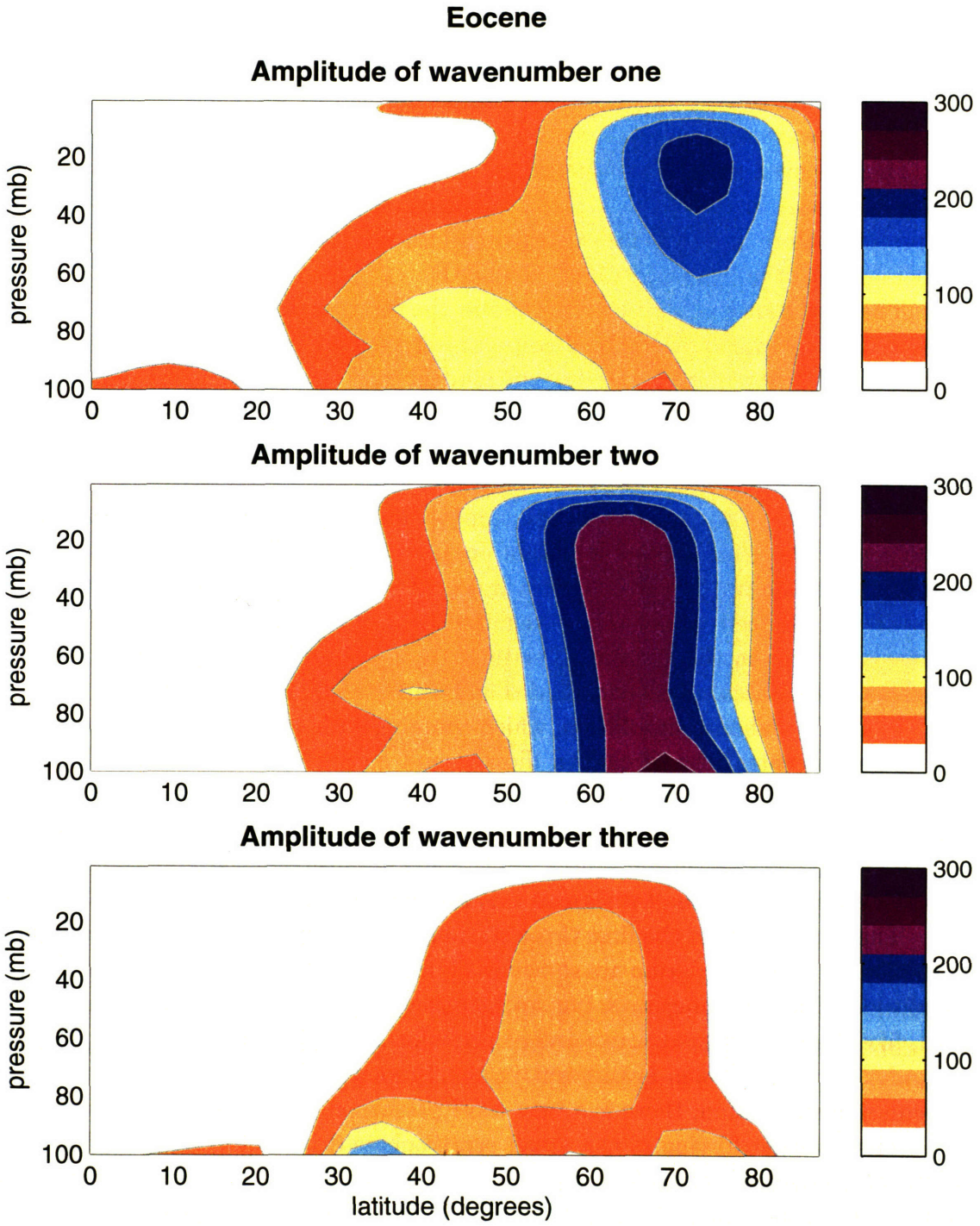

Figure 3-14: As in figure 3-12, but for the Eocene. The geopotential field was decomposed into Fourier components, and the amplitudes of waves 1, 2, and 3 are shown. Units are in meters, but the values have been normalized by $\sqrt{p/p_o}$ to compensate for the increase in amplitudes with decreasing density. These are from time averaged data over the last five Decembers, Januaries, and Februaries. (The amplitudes shown are $\sqrt{p/p_o}\sqrt{A \cdot A^\star}$, where A is the amplitude of each Fourier component and $A^\star$ is its complex conjugate.)

creased. Rind et al. (1988) found a similar result in a middle atmosphere model forced with a slightly weaker sea surface temperature gradient and higher concentration of carbon dioxide.

This point is also illustrated by comparing figures 3-12 and 3-14. While the amplitude of wavenumber one has decreased in the Eocene case, wavenumber two has not. There is even now a local maximum in wavenumber three; although weak, this peak was absent in the Present case. This suggests that a shorter wave, which was not present before, is vertically propagating into the stratosphere in the Eocene case, contributing to the increased forcing by $\nabla \cdot \mathbf{F}$.

The dominance of wavenumber two in the stratosphere is interesting. It is conceivable that the warm sea surface temperatures are arbitrarily increasing the thermal forcing of stationary waves. Because the model's land surface temperatures are calculated directly, they are cooler than the high sea surface temperatures imposed at the same latitude, and a parcel of air circumnavigating a latitude circle will pass over a warm ocean, then cool continent, then warm ocean again. However, the amplitude of wavenumber two is no stronger in the troposphere in the Eocene simulation than in the Present case. This casts some doubt on an arbitrary forcing, though it is possible that wavenumber two is stronger than it would be with a zonally symmetric surface temperature. Indeed, all of the wavenumbers have less tropospheric energy in the Eocene case than in the Present. The increase in the stratosphere is attributable to an increase in vertical propagation of this limited energy.

In the Greenhouse simulation, which contains both a weak temperature gradient and large concentrations of carbon dioxide and methane, the Eliassen-Palm flux is stronger still. Figure 3-15 shows the large convergence of $\mathbf{F}$ in the middle and upper winter stratosphere. As in the Eocene case, the flux of $\mathbf{F}$ across all pressure surfaces above 400 mb increases in the winter hemisphere, even though the tropospheric energy decreases slightly. We shall return to this point in section 3.4.

The amplitudes of the first three stationary waves for the boreal winter months of the Greenhouse simulation are shown in figure 3-16. There is a small decrease in the amplitude of wavenumber one, but an increase in the intensity of wavenumber two. And, like the Eocene case, wavenumber three has a closed maximum at stratospheric altitudes, whereas it was evanescent in the Present case. In both the Eocene and Greenhouse simulation, there is a new wave present in the winter stratosphere.

The stronger forcing in the upper stratosphere drives a stronger residual circulation in the winter hemisphere, as seen in figure 3-17. The downward flow extends all the way to the North Pole, and the strength of the circulation has increased at all stratospheric levels.

A few additional points are worth noting here. First, the residual circulation is strongest in middle latitudes, with little downward motion poleward of 60°N, especially in the Present simulation. This is especially true above 40 mb, where the circulation is actually closing off aloft; this difficulty has been observed in other models of the middle atmosphere, as the flow closes in the arbitrary frictional layer at the

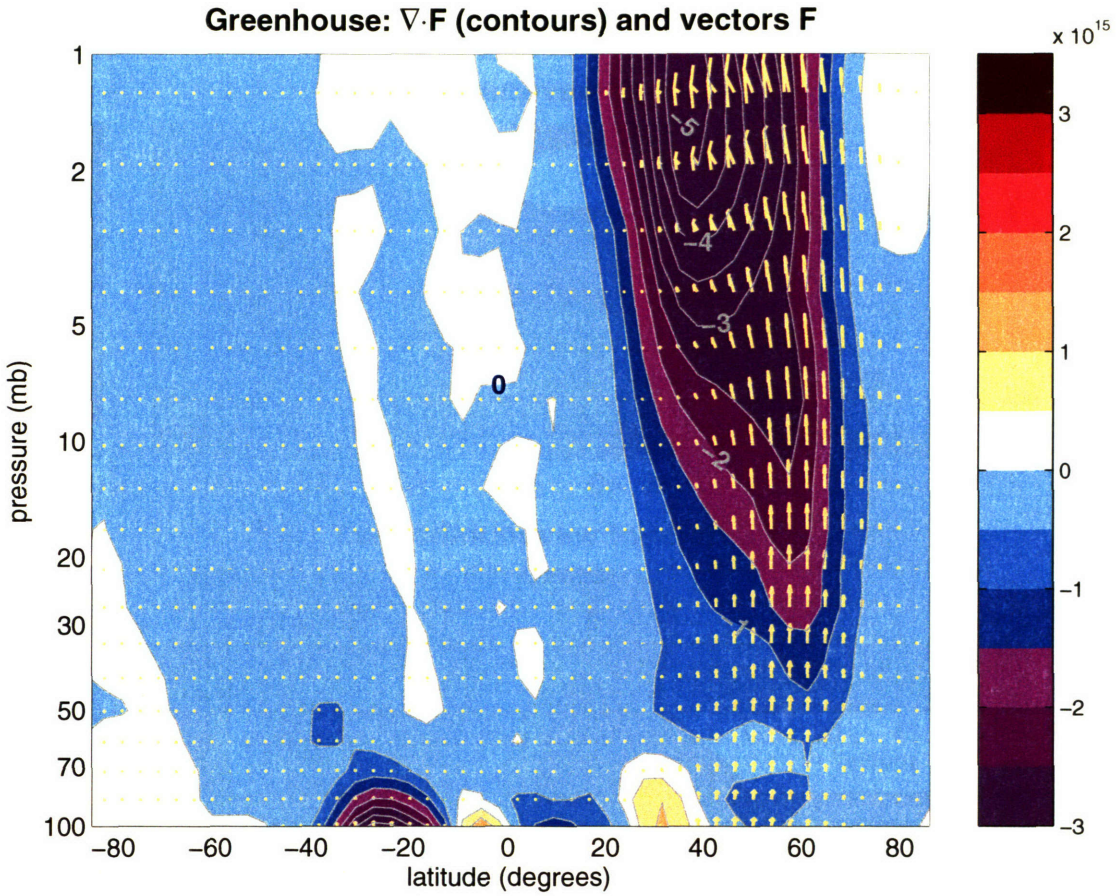

Figure 3-15: As in figure 3-11, but for Greenhouse. As in the simulation Eocene, the convergence of the Eliassen-Palm flux is stronger in this simulation than in Present. Waves propagate vertically, are deflected by the westerly jet, turn equatorward with height, and converge in the upper extratropical stratosphere. The plotting technique follows Edmon et al. (1980); units of $\nabla \cdot \mathbf{F}$ are in m^3.

model top rather than at the ground (Semeniuk and Shepherd, 2001). The simulated winter polar stratosphere has long been too cold in middle atmosphere models, and it is possible that poor resolution of the residual circulation is responsible, given the maturity of modern radiative codes.

Second, note that some of the streamlines that do reach the lower stratosphere in the highest latitudes must have traveled above 2 mb, a region in which the Rayleigh friction was imposed. We will examine to what extent, if any, this issue has on our results at the conclusion of this chapter. In spite of these deficiencies, our present focus is to investigate the model's response to a weakened surface temperature gradient, and we are comparing runs in which this alone is changed.

Because the intensity of the residual circulation did not decline in any of the warm climate simulations (there was a modest increase), the temperatures in the middle and high latitude stratosphere did not cool towards their radiative equilibrium

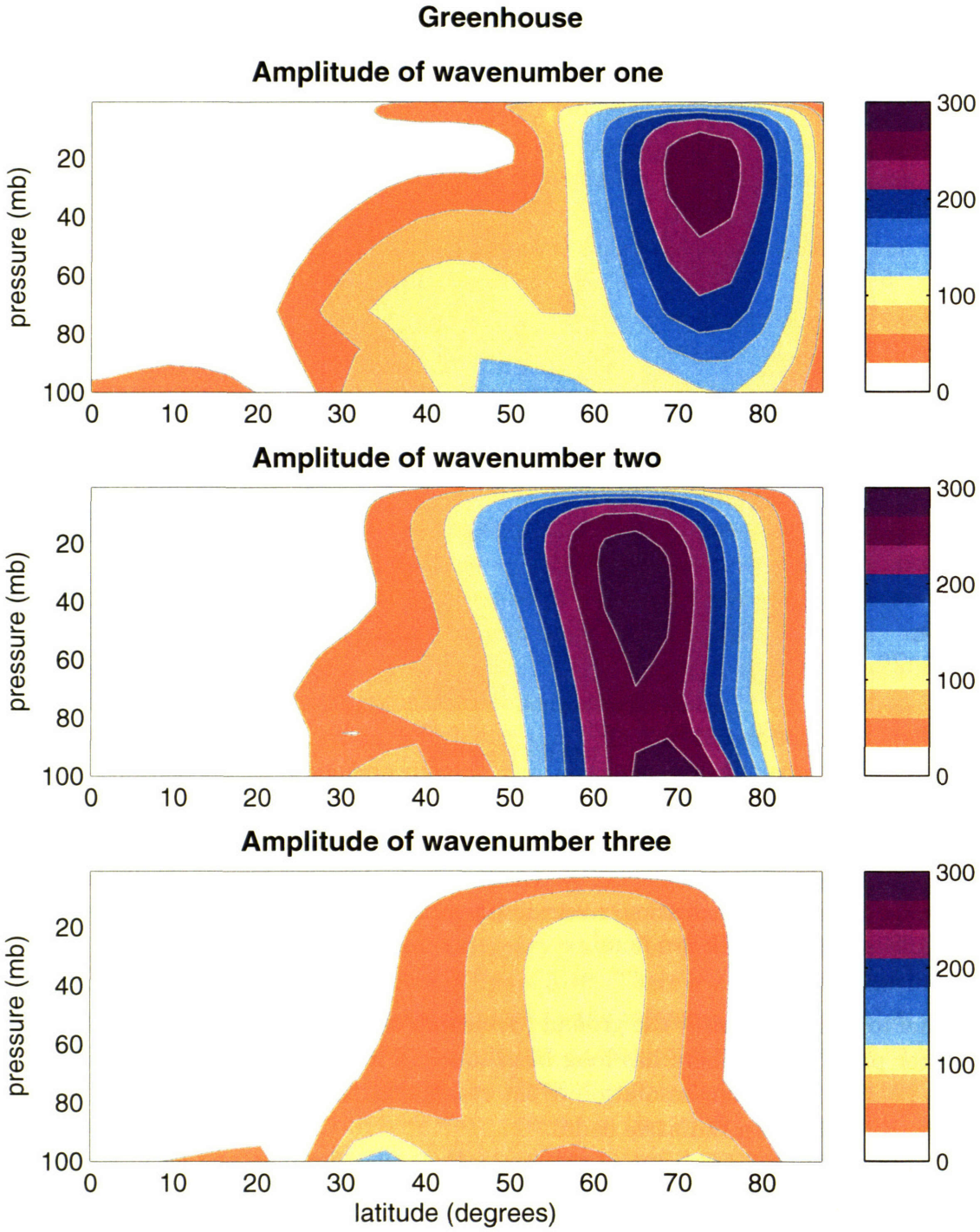

Figure 3-16: As in figure 3-12, but for the Greenhouse. The geopotential field was decomposed into Fourier components, and the amplitudes of waves 1, 2, and 3 are shown. Units are in meters, but the values have been normalized by $\sqrt{p/p_o}$ to compensate for the increase in amplitudes with decreasing density. These are from time averaged data over the last five Decembers, Januaries, and Februaries. (The amplitudes shown are $\sqrt{p/p_o}\sqrt{A \cdot A^\star}$, where A is the amplitude of each Fourier component and $A^\star$ is its complex conjugate.)

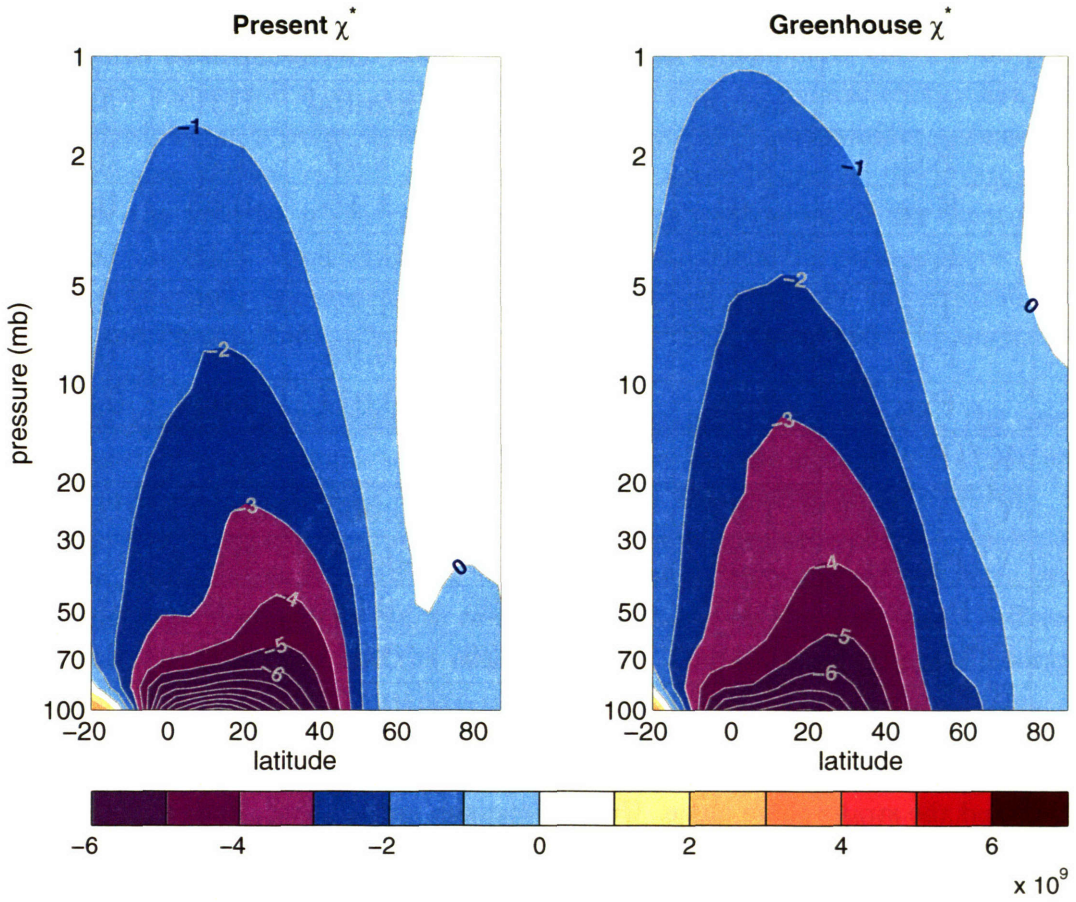

Figure 3-17: The residual mean circulation in the stratosphere for the Present (left panel) and Greenhouse (right panel) simulations. Negative values circulate clockwise in this figure, showing motion is upward in the tropics, poleward in the upper stratosphere, and down at middle and high latitudes. Units are kg/s.

values. Indeed the remarkable similarity in the zonal-mean, time-mean soundings presented in figure 3-3 seems consistent with the intensity of the dynamic forcing. In the next section, we more formally address the energy characteristics of the simulations.

3.4 Energetics

In this section we undertake an analysis of the energetics of the simulated atmospheric states in order to better understand the changes seen in the previous sections. Energy is just another diagnostic, a tool to establish consistency rather than an assignment of causality (Lindzen, 1990); it is not Galilean invariant, and we shall see a consequence of this limitation at the conclusion of this section. We proceed cautiously, therefore, and offer this analysis to understand how the energy is partitioned into its various forms and to note differences between the simulations. Ultimately, there must be

Present, global

	Full atmosphere			Stratosphere only		
	annual	DJF	JJA	annual	DJF	JJA
K_M	9.16	9.97	11.03	1.50	1.27	3.12
K_{TE}	7.61	6.07	5.58	1.15	0.63	0.51
K_{SE}	0.82	1.88	1.38	0.055	0.18	0.11
P_M	47.57	57.01	53.33	1.17	1.98	2.09
P_{TE}	8.43	3.98	4.40	0.93	0.29	0.20
P_{SE}	2.15	4.38	2.84	0.011	0.053	0.023
$K/(P+K)$	23	22	23			
$C(P_M, P_E)$	1.63	-1.49	1.03	0.0051	0.0071	0.0097
$C(P_E, K_E)$	2.33	2.25	2.16	-0.0067	-0.018	0.025
$C(P_M, K_M)$	-0.055	0.12	0.25	-0.065	-0.070	-0.065
$C(K_E, K_M)$	0.18	0.18	0.26	0.011	0.011	0.009
$B(K_E)$ evaluated at 100 mb				0.167	0.171	0.161

Table 3.1: Global energetics for the simulation of Present conditions in the full atmosphere and the stratosphere alone. Units of energies are $10^5 J/m^2$, units of the conversions are W/m^2, and the energy ratio, $K/(P+K)$, is expressed as a percent.

a balance between the generation of potential energy and dissipation by frictional forces; in the stratosphere, little energy is generated internally, so the local balance is between transfer of energy into the layer and dissipation. The energy equations are reviewed in Appendix D.

We begin by examining the energy budget for the Present simulation. The results of the calculations are presented in table 3.1. Note that in both the annual data and the seasonal extremes the kinetic energy is split between the mean flow and the eddies, with the transient eddies dominating the eddy kinetic energy. The available potential energy is weighted towards the mean flow; roughly a quarter of the total energy is in the kinetic form, a fraction similar to that found in observational studies (cf. table 14.1 of Peixoto and Oort, 1992).

The conversion terms show that energy cycles from available potential energy of the mean flow to the eddy available potential energy to the eddy kinetic energy to the kinetic energy of the mean flow, as in the real atmosphere. There is little direct conversion of available potential energy of the mean flow to the kinetic energy of the mean flow in the annual and global budget, but during particular months and at particular locations this term may be larger (Peixoto and Oort, 1992). Thus, as first suggested by Starr (1948), eddies play a crucial role in regulating the general circulation of the atmosphere.

The stratosphere has a much smaller amount of energy, but it also occupies only ten percent of the atmospheric mass. Unlike the full atmosphere, there is no period during which conversion from available potential energy to kinetic energy can offset frictional dissipation, a point first noted by Dopplick (1971). Boundary terms on the 100 mb pressure surface, which we take to be the lower bound of the stratosphere, account for the transfer of energy from the troposphere below to the stratosphere above. The boundary terms dominate the energy budget of the stratosphere: rather than being internally generated, energy is transported from the lower atmosphere (Charney and Drazin, 1961; Charney and Pedlosky, 1963; Oort, 1964; Muench, 1965; Dopplick, 1971).

When applied to the runs with the weak temperature gradients, the energy budget illuminates some important changes. For the Eocene simulation, whose energetics are presented in table 3.2, the full atmosphere loses energy in all its forms. The available potential energy is smaller because the isentropes are confined, at least at the surface, to be nearly flat; we saw in earlier sections that the temperature gradient remains weak through the depth of the troposphere, producing a small difference between the reference state and the modeled state. The available potential energy of the mean flow is only about one-third of what it was in the Present simulation.

The kinetic energy has also decreased considerably. The jets are weaker, leading to a weaker amount of energy in the mean flow, and the eddy kinetic energy has also fallen by about a factor of two. Interestingly, however, the kinetic energy of the stationary eddies has fallen by a smaller amount during the Northern Hemisphere winter, the only place and time that it makes a sizable contribution to the overall energy budget (Peixoto and Oort, 1992). The topography was unchanged in these simulations, and it appears that a strong forcing of the standing eddy energy remains.

While the energetics of the full atmosphere decrease by a sizable fraction, the decrease in the stratosphere is comparatively small. While most forms of energy decrease above 100 mb, the kinetic and available potential stationary eddy energy actually grows. This is consistent with the increase in the forcing of the residual mean circulation seen in section 3.3.2. While the entire atmosphere has become less energetic, the stratosphere has decreased by a much smaller fraction. The stratosphere is selective in what it accepts from the troposphere; only the longest planetary waves are able to propagate vertically (Charney and Drazin, 1961). The addition of wavenumber three seen in figure 3-14, coupled with the similar amplitude of wavenumbers one and two, has kept the energy of the stratosphere high, and the residual circulation strong.

Similarly, we see that the Greenhouse circulation has a much weakened circulation in the full atmosphere while retaining a large fraction of the energy in the stratosphere. The results of these calculations are presented in table 3.3. While the energetics of the full atmosphere have decreased by roughly a factor of two, the eddy energy in the stratosphere decreases by only a small amount (with a modest increase in the kinetic energy of the stationary eddies, especially during the Northern

Eocene, global

	Full atmosphere			Stratosphere only		
	annual	DJF	JJA	annual	DJF	JJA
K_M	3.08	4.35	5.27	0.97	1.20	2.21
$K_M/K_{M\,present}$	*34%*	*44%*	*48%*	*64%*	*94%*	*71%*
K_{TE}	4.13	2.75	2.16	0.89	0.44	0.23
$K_{TE}/K_{TE\,present}$	*54%*	*45%*	*39%*	*77%*	*70%*	*46%*
K_{SE}	0.43	1.38	0.78	0.059	0.18	0.077
$K_{SE}/K_{SE\,present}$	*52%*	*73%*	*57%*	*107%*	*105%*	*68%*
P_M	14.38	23.29	19.34	0.80	1.31	1.76
$P_M/P_{M\,present}$	*30%*	*41%*	*36%*	*68%*	*66%*	*84%*
P_{TE}	5.70	1.57	1.60	0.74	0.20	0.11
$P_{TE}/P_{TE\,present}$	*68%*	*39%*	*36%*	*79%*	*68%*	*55%*
P_{SE}	0.87	2.19	1.92	0.026	0.073	0.041
$P_{SE}/P_{SE\,present}$	*40%*	*50%*	*68%*	*237%*	*137%*	*179%*
$K/(P+K)$	27	24	26			
$C(P_M, P_E)$	0.25	-3.17	0.36	0.001	0.003	0.003
relative to present	*15%*	*214%*	*34%*	*28%*	*40%*	*29%*
$C(P_E, K_E)$	0.74	1.04	0.70	-0.003	-0.014	-0.008
relative to present	*32%*	*46%*	*32%*	*47%*	*-73%*	*-33%*
$C(P_M, K_M)$	-0.20	-0.18	-0.051	-0.029	-0.056	-0.002
relative to present	*369%*	*-152%*	*-21%*	*44%*	*81%*	*3%*
$C(K_E, K_M)$	0.009	0.003	0.009	0.005	0.005	0.007
relative to present	*5%*	*2%*	*3%*	*48%*	*47%*	*79%*
$B(K_E)$	evaluated at 100 mb				0.0755	
relative to present					*44%*	

Table 3.2: Global energetics for the simulation Eocene in the full atmosphere and the stratosphere alone. Units of energies are $10^5 J/m^2$, units of the conversions are W/m^2, and the energy ratio, $K/(P+K)$, is expressed as a percent. The second line of each entry gives a comparison of the strength between the Eocene and Present simulations.

Greenhouse, global

	Full atmosphere			Stratosphere only		
	annual	DJF	JJA	annual	DJF	JJA
K_M	3.12	4.52	5.55	1.02	1.22	2.40
$K_M/K_{M\,present}$	*34%*	*45%*	*50%*	*68%*	*96%*	*77%*
K_{TE}	4.26	2.63	2.21	0.97	0.48	0.26
$K_{TE}/K_{TE\,present}$	*56%*	*43%*	*36%*	*84%*	*75%*	*51%*
K_{SE}	0.45	1.53	0.85	0.062	0.25	0.085
$K_{SE}/K_{SE\,present}$	*55%*	*81%*	*62%*	*113%*	*145%*	*75%*
P_M	14.32	19.74	20.34	0.75	1.32	1.82
$P_M/P_{M\,present}$	*30%*	*35%*	*38%*	*64%*	*67%*	*87%*
P_{TE}	6.27	-1.28	1.53	0.82	0.21	0.12
$P_{TE}/P_{TE\,present}$	*74%*	*-32%*	*35%*	*89%*	*73%*	*57%*
P_{SE}	0.88	1.75	1.91	0.031	0.13	0.045
$P_{SE}/P_{SE\,present}$	*41%*	*40%*	*67%*	*291%*	*243%*	*195%*
$K/(P+K)$	27	30	27			
$C(P_M, P_E)$	0.24	0.011	0.34	0.0014	0.0049	0.0024
relative to present	*15%*	*-1%*	*33%*	*27%*	*69%*	*25%*
$C(P_E, K_E)$	0.67	1.01	0.47	-0.010	-0.013	-0.013
relative to present	*29%*	*45%*	*22%*	*147%*	*-72%*	*-52%*
$C(P_M, K_M)$	-0.26	-0.27	-0.090	-0.029	-0.071	-0.003
relative to present	*468%*	*-234%*	*-36%*	*45%*	*101%*	*5%*
$C(K_E, K_M)$	0.013	0.015	0.007	0.005	0.005	0.007
relative to present	*7%*	*8%*	*3%*	*44%*	*46%*	*81%*
$B(K_E)$	evaluated at 100 mb				0.0863	
relative to present					*50%*	

Table 3.3: Global energetics for the simulation Greenhouse in the full atmosphere and the stratosphere alone. Units of energies are $10^5 J/m^2$, units of the conversions are W/m^2, and the energy ratio, $K/(P+K)$, is expressed as a percent. The second line of each entry gives a comparison of the strength between the Eocene and Present simulations.

Hemisphere winter).

The boundary terms at the 100 mb surface continue to dominate the energy cycle of the stratosphere in the warm climate runs, but the size of their decrease seems surprising at first glance. This is an artifact of the decrease in the zonal mean wind, as we shall see below. Note that the dominant term in the boundary energy equations is the work performed by pressure forces on the boundary, which is the product of deviations of ω and ϕ (cf. figure 6 of Muench, 1965). By rearranging the steady-state linearized thermodynamic equation:

$$\begin{aligned} [u]\frac{\partial \theta^*}{\partial x} + \omega^* \frac{\partial [\theta]}{\partial p} &= 0 \\ \omega^* &= -[u]\frac{\partial_x \theta^*}{S}, \end{aligned}$$

multiplying by ϕ^*:

$$\omega^* \phi^* = -[u]\frac{\phi^* \partial_x \theta^*}{S}$$

and then zonally averaging:

$$[\omega^* \phi^*] = -[u]\frac{[\phi^* \partial_x \theta^*]}{S},$$

the equation becomes an approximation of $B(K_E)$ when integrated along an isobaric surface.[4] Note that $\phi^* \partial_x \theta^*$ may be rewritten as $\partial_x (\phi^* \theta^*) - \theta^* \partial_x \phi^*$, but the zonal average of $\partial_x (\phi^* \theta^*)$ is zero, so

$$[\omega^* \phi^*] = [u]\frac{[\theta^* \partial_x \phi^*]}{S}.$$

Using the zonal momentum equation to substitute fv^* for $\partial_x \phi^*$, we obtain:

$$-\int\int [\omega^* \phi^*]\, dA = -\int\int [u]\frac{f\,[v^* \theta^*]}{S} dA, \tag{3.4}$$

after integrating along an isobaric surface and multiplying by -1. This approximation shows that the boundary energy is a function of both the vertical component of the Eliassen-Palm flux and the zonal mean zonal wind. As we shall see below, the vertical component of the Eliassen-Palm flux across 100 mb increases in the warm climates, but the zonal mean zonal wind dropped by about a factor of two (see figures 3-8 and 3-10); thus, the decrease in the boundary energy terms is not representative of a change in wave activity.

In figure 3-18, the isobaric mean values of the vertical and horizontal components of the Eliassen-Palm flux, **F**, are shown for the three simulations. Note that the

[4] $S = \frac{d[\theta]}{dp}$, which is negative in a stably stratified fluid.

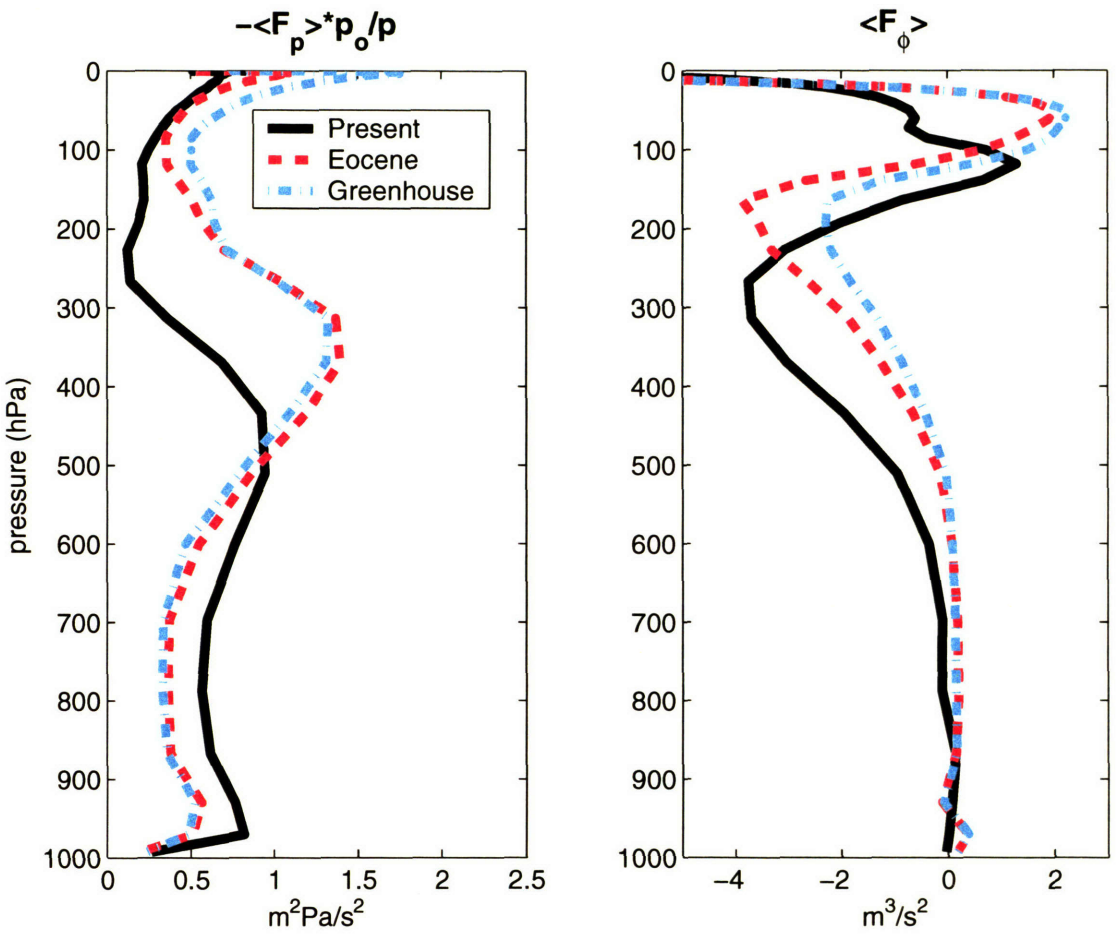

Figure 3-18: Isobaric mean values of the vertical component of **F** (left panel) and of the horizontal component (right panel). Note that the vertical component has been multiplied by -1, so that positive values correspond to an upward flux; negative values in the isobaric mean of F_ϕ are southward. Additionally, the vertical component is normalized by p_o/p for resolution at high altitudes. These values were from time-averaged data over the last five Decembers, Januaries, and Februaries.

vertical component, F_p, which is shown in the left panel, has been multiplied by -1 so that positive values correspond to an upward flux (towards decreasing pressure). The vertical component was also normalized by p_o/p in order to retain resolution above 100 mb in the figure.

The vertical component, which is proportional to the eddy flux of heat, is larger in the lower troposphere in the Present simulation than in the two warmer climate ones. This is consistent with stronger eddies and more generation in the present climate and a decrease in eddy energy during warm climates. By the middle troposphere, however, **F** acquires an equatorward tilt in the Present simulation as the strong tropospheric jet deflects eddy energy equatorward. In contrast, the vertical component of **F** in the warm climate states remains strong through the upper tropo-

sphere. This suggests that the weaker tropospheric jet in the warm climates, which is in balance with a weak meridional temperature gradient, permits more eddies to pass into the lower stratosphere in spite of the fact that fewer are generated in the lower troposphere.[5] This is consistent with the strong forcing of the residual mean circulation we saw in the last section.

3.5 Eddy transports

We now diagnose the model's meridional transport of energy to illuminate the model atmosphere's role in maintaining the sea surface temperature with which it was forced. While the atmosphere was examined in isolation, there is an implicit flux carried by the oceans.

Figure 3-19 presents the annual meridional energy transport for the Present simulation. The solid black line is the total flux that the climate system must carry to correct local radiative imbalances at the top of the atmosphere. The Earth receives and absorbs more solar radiation in the tropics than it emits there, and it emits more longwave radiation than it absorbs locally at high latitudes; this necessitates that heat be moved from the tropics to the poles by the atmosphere and ocean. This flux can be calculated by integrating the top of the atmosphere net radiation, F_{TA}, from a latitude circle, ϕ, northward:

$$T_A + T_{OC} = -\int_{\phi}^{\pi/2} F_{TA} 2\pi R^2 \cos\phi' \, d\phi'. \tag{3.5}$$

One must ensure that F_{TA} is balanced:

$$\int_{-\pi/2}^{\pi/2} [F_{TA}] \, R \cos\phi' \, d\phi' = 0; \tag{3.6}$$

otherwise, the errors will build with the integration in equation (3.5) and produce a spurious flux through the South Pole. Adding a small correction of 0.362 W/m^2 to F_{TA} at every point brings equation (3.6) into balance for the data from the Present simulation.[6]

Note that the corrected curve contains a slight asymmetry with respect to the equator, though Stone (1978b) has showed that the geometry of the planet constrains the real curve to be symmetric. This bias is similar in size to some older estimates with imperfect data, as shown by Oort and Vonder Haar (1976), Oort and Peixoto (1983), and later by Pexioto and Oort (1992).

[5]Note also that **F** acquires an equatorward tilt at a higher altitude in the upper troposphere of the warm climate states, which is consistent with a higher jet and extratropical tropopause.

[6]In the Eocene, shown in figure 3-20, a correction of 1.72 W/m^2 must be added to F_{TA} at each point; in the Greenhouse, shown in figure 3-21, a correction of -9.28 W/m^2 is required.

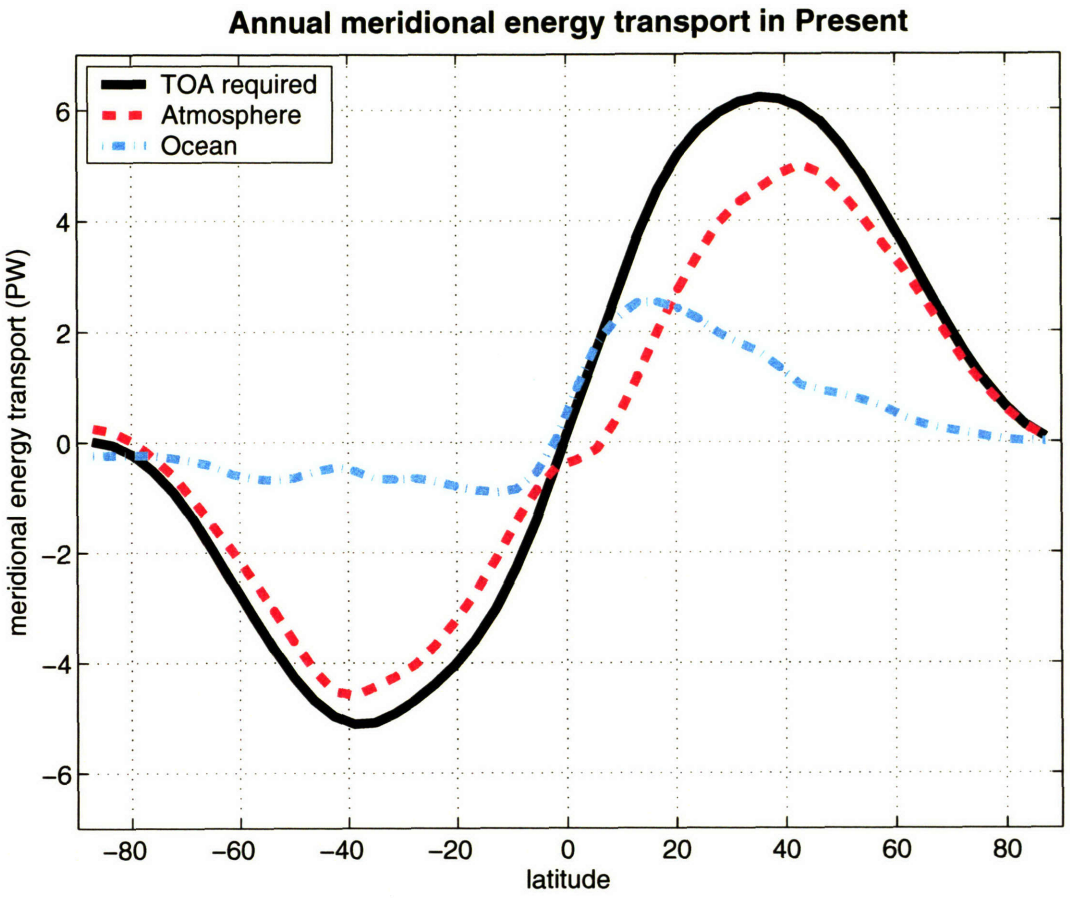

Figure 3-19: Total meridional transport of energy. The solid black line shows the flux required to balance top-of-the-atmosphere imbalances. The red dashed line shows the atmosphere's share, which is dominant in the present climate. The oceans' contribution is shown in dash-dotted light blue; the oceans dominate in the deep tropics.

One can quickly find the share of this total flux that is carried by the atmosphere by integrating the net downward radiative energy flux at the top of the atmosphere, as in Trenberth and Caron (2001):

$$T_A = \int_{\phi}^{\pi/2} (F_{TA} - F_{OA})\, 2\pi R^2 \cos\phi' d\phi', \tag{3.7}$$

where T_A is the atmospheric meridional energy flux, F_{TA} is the net upward radiative flux at the top of the atmosphere, and F_{OA} is the net upward enthalpy flux from the ocean to the atmosphere, which includes turbulent transport. Whatever column imbalances remain between the top and bottom of the atmosphere must be adjusted laterally. The surface fluxes are used to construct F_{OA}:

$$F_{OA} = F_{s_s} - F_{l_s} - SH - LH, \tag{3.8}$$

where F_{s_s} is the net shortwave (solar) flux at the surface, F_{l_s} is the net longwave (terrestrial) flux at the surface, SH is the surface sensible heat flux, and LH is the surface latent heat flux. The partitioning of the energy flux is shown in dotted red (atmosphere) and dash-dotted light blue (ocean) in figure 3-19.

One can use the model data to further partition the atmospheric heat flux into contributions from sensible heat, latent heat, and potential energy, and break each of these terms further into contributions from the mean circulation, transient eddies, and stationary eddies. The annual sensible and latent heat transports are actually equatorward in the tropics, as the low-level branch of the Hadley Cell flows equatorward. The poleward transport of potential energy in the upper branch of the Hadley circulation cancels this, resulting in a net atmospheric flux that is weak equatorward of 20°; the ocean dominates at these latitudes. In mid-latitudes, there is a peak in the poleward transport of latent and sensible heat, largely carried by transient eddies all year and by stationary eddies in the Northern Hemisphere winter. In middle latitudes, the atmosphere carries nearly all of the heat poleward required to keep the climate in equilibrium.

The energy transport estimates for the Eocene simulation are shown in figure 3-20. The total heat flux required to balance the top of the atmosphere fluxes has changed little, in agreement with the findings of Stone (1978b). The total flux carried by the atmosphere, however, is considerably smaller than in the Present simulation. We saw in the last section that the Eocene simulation was far less energetic, and here we see a major consequence: the atmosphere is unable to provide a heat flux to sustain the sea surface temperatures with which it was forced. The eddies in middle latitudes and a weaker Hadley circulation in the tropics are principally responsible for the decrease. The implied ocean transport has increased substantially; note that not only has its peak increased, but the latitudes over which the ocean must make an important contribution have expanded into the subtropics and middle latitudes. The magnitude of this ocean flux is likely untenable, but we forced this model with an unrealistically weak temperature gradient in order to provide a limiting case for the changes in the stratosphere. Nevertheless, these model results imply that the oceans' contribution to the poleward transport of heat must increase in order to sustain a weak temperature gradient.

Similarly, the atmospheric energy transport in the Greenhouse simulation is weak; the results are presented in figure 3-21. In both the Eocene and Greenhouse simulations, the latent heat flux decreases less strongly than do the sensible heat and potential energy fluxes. Though the eddies are considerably weaker in middle latitudes, the warmer climate permits a larger volume of water in the lower atmosphere. Lucarini (2002) found that the latent heat flux may increase in a doubled carbon dioxide atmosphere, and Pierrehumbert (2002) has also argued that the latent heat flux may have been larger in past warm climates.

Finally, we examine the partitioning of the eddy fluxes into transient and stationary components. In figure 3-22a, the sensible heat transport by both types of

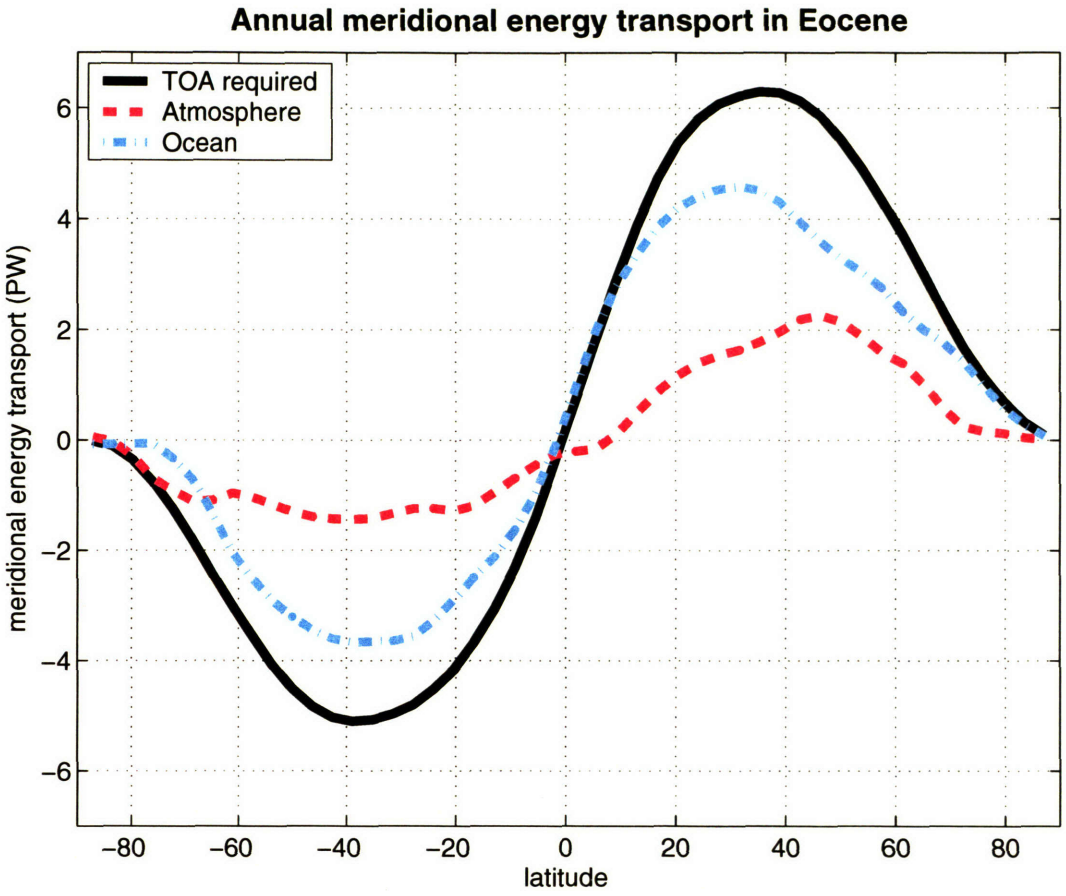

Figure 3-20: Total meridional transport of energy. The solid black line shows the flux required to balance top-of-the-atmosphere imbalances. The red dashed line shows the atmosphere's share, which is dominant in the present climate. The oceans' contribution is shown in dash-dotted light blue; the oceans dominate in the deep tropics.

eddies are shown for the Present and Eocene simulations. (Though not shown, the Greenhouse transports are quite similar to the Eocene ones.) Note that while there is a marked decrease in the transport by transient eddies between the Present and Eocene simulations, the amount of sensible heat carried by stationary eddies does not change. This is consistent with the findings in earlier sections, and suggests that the forcing of stationary waves has not been inhibited by the weak temperature gradient.

In figure 3-22b, the latent heat transport by transient and stationary eddies is shown. Again note that while the flux carried by the transient eddies falls markedly, the stationary eddy flux changes little. Stationary eddies transport a comparatively small fraction of the latent heat flux, so the decrease in atmospheric transports seen in figures 3-20 and 3-21 is largely owing to the drop in the transient eddies.

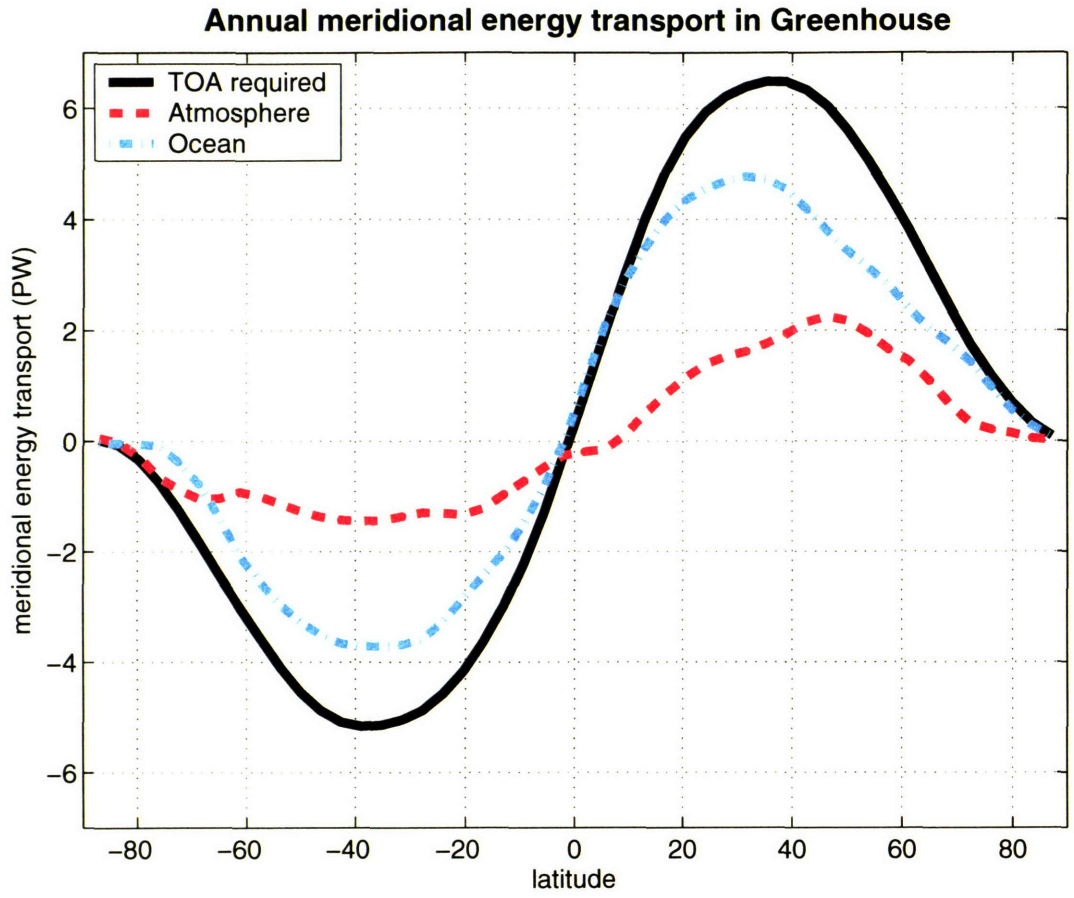

Figure 3-21: Total meridional transport of energy. The solid black line shows the flux required to balance top-of-the-atmosphere imbalances. The red dashed line shows the atmosphere's share, which is dominant in the present climate. The oceans' contribution is shown in dash-dotted light blue; the oceans dominate in the deep tropics.

3.6 Height of the extratropical tropopause

In this section, we briefly examine some model soundings. Many of the questions raised here will fall beyond the scope of this thesis, but the issues raise some interesting questions and motivate a proposal for some future work that is discussed in Chapter 6.

The soundings shown in figures 3-23–3-26 are averaged over the last five Decembers, Januaries, and Februaries from the Present (solid black), Eocene (dashed red), and Greenhouse (dash-dotted light blue). The thin gray curves are lines of constant equivalent potential temperature, θ_e, and represent moist adiabats (Emanuel, 1994). Note that the tropical soundings from Hawaii in figure 3-23 are confined to a moist adiabat through the depth of the troposphere; these soundings are neutral to moist convection and have been convectively adjusted (Xu and Emanuel, 1989).

In contrast, soundings at the North Pole (figure 3-24) and from Greenland (not shown) show vertical temperature profiles decidedly stable to upright moist convec-

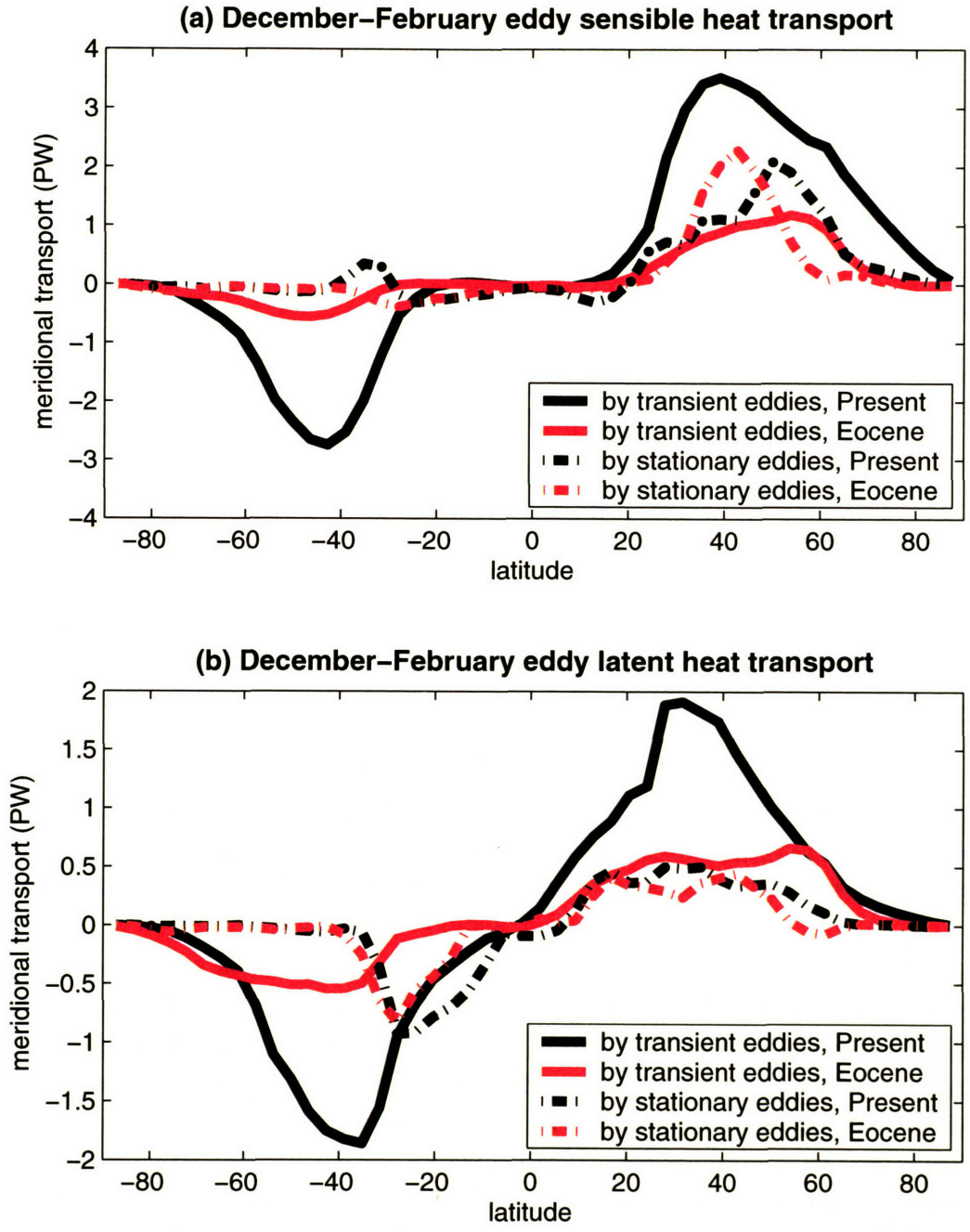

Figure 3-22: (a) The transport of sensible heat by transient and stationary eddies in December-February in the Present (black) and Eocene (lighter red) simulations. The transient eddy transports are plotted with solid lines, and the stationary eddy transports are plotted with dash-dotted lines. (b) As in (a), but for the latent heat transports. Though not shown, the transports in the Greenhouse simulation are quite similar to those in the Eocene.

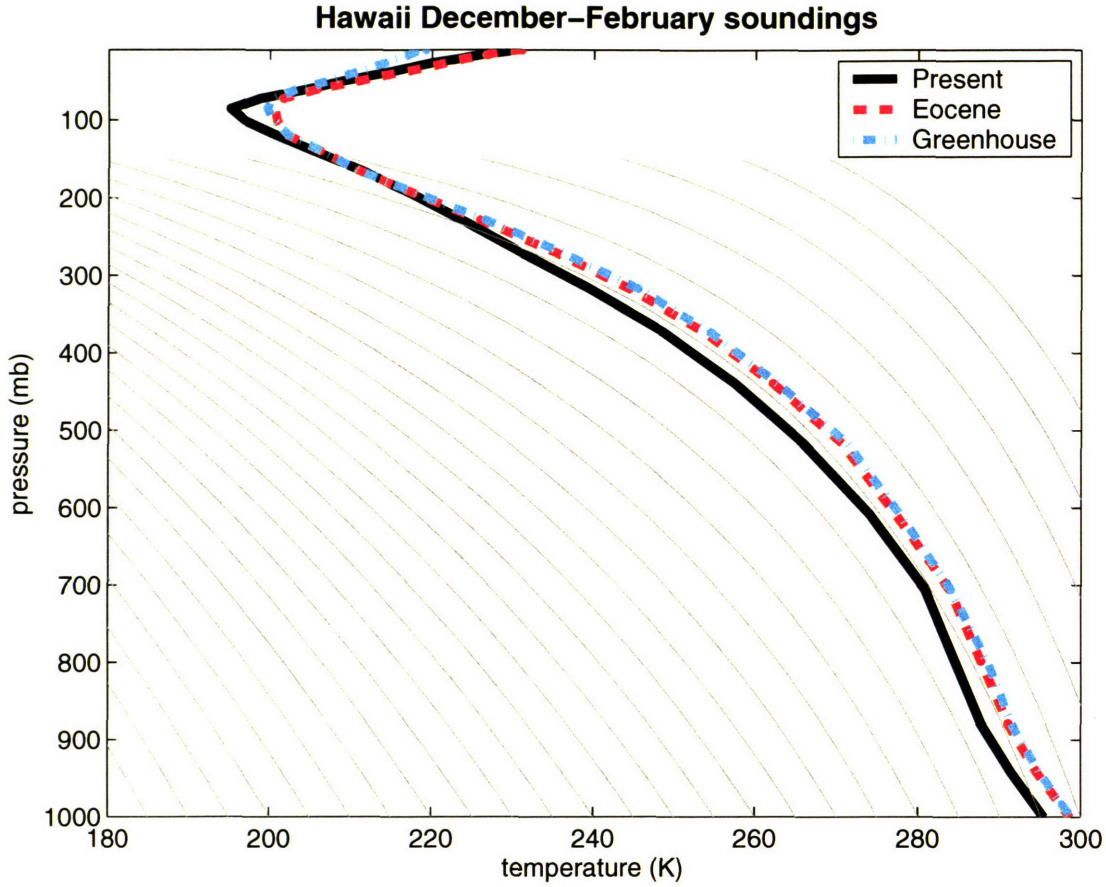

Figure 3-23: December-February soundings from Hawaii from the Present (solid black), Eocene (dashed red), and Greenhouse (dash-dotted light blue) simulations. The thin, light gray curves are moist adiabats. Actual model point is at 20.4°N, 157.5°W.

tion in the Present case; both of these also show a low-level inversion, a common feature of winter Arctic soundings. But the Eocene and Greenhouse simulations, which were forced with mild high latitude temperatures (near 20°C) appear to have been convectively adjusted, just as tropical soundings are today. Even on the interior of the continents, the lapse rate has gone from convectively stable to convectively neutral (see the soundings from North Dakota in figure 3-25). At high latitudes in the summer hemisphere, the same convectively neutral profiles can be found; profiles from McMurdo, Antarctica, are shown in figure 3-26. Note that the profile in the summer Antarctic is stable to deep convection in the Present simulation, though less so than the winter profiles from the North Pole.

It appears that convection is dominating the tropospheric stratification at all latitudes and in all seasons in these warm climate simulations. To some extent, this is not surprising as the eddies are weak and the imposed surface temperatures are warm and convectively unstable. But the nearly ubiquitous convective adjustment raises an interesting question: could moist convection or slantwise moist convection

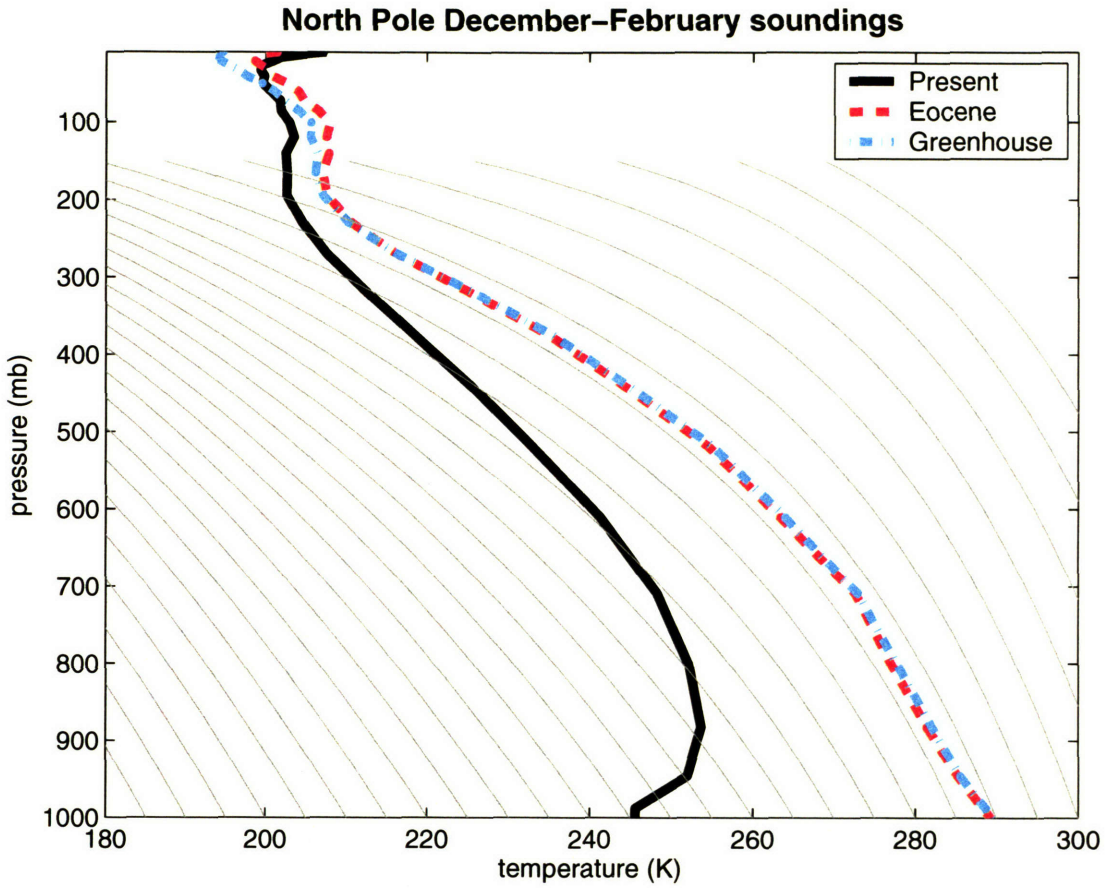

Figure 3-24: December-February soundings from the North Pole from Present (solid black), Eocene (dashed red), and Greenhouse (dash-dotted light blue) simulations. The thin, light gray curves are moist adiabats. These soundings were constructed from a zonal average around 87.2°N, the northern most model point.

set the tropospheric stratification during warm climates? If so, the consequences for the atmospheric heat flux are profound. Though it is hard to imagine that convection itself could ever control the meridional heat flux, it could strongly affect the eddies that do so through its control on the tropospheric stratification. This question lies beyond the scope of this thesis, but I shall revisit it in some proposed future work in Chapter 6.

3.7 Summary of the main findings

We have seen that winter stratospheric temperatures do not change significantly when the surface temperature gradient is greatly weakened. This surprising result comes from an increase in the vertical component of the Eliassen-Palm flux in the upper troposphere and lower stratosphere as the westerly jet speeds weaken. This is in spite

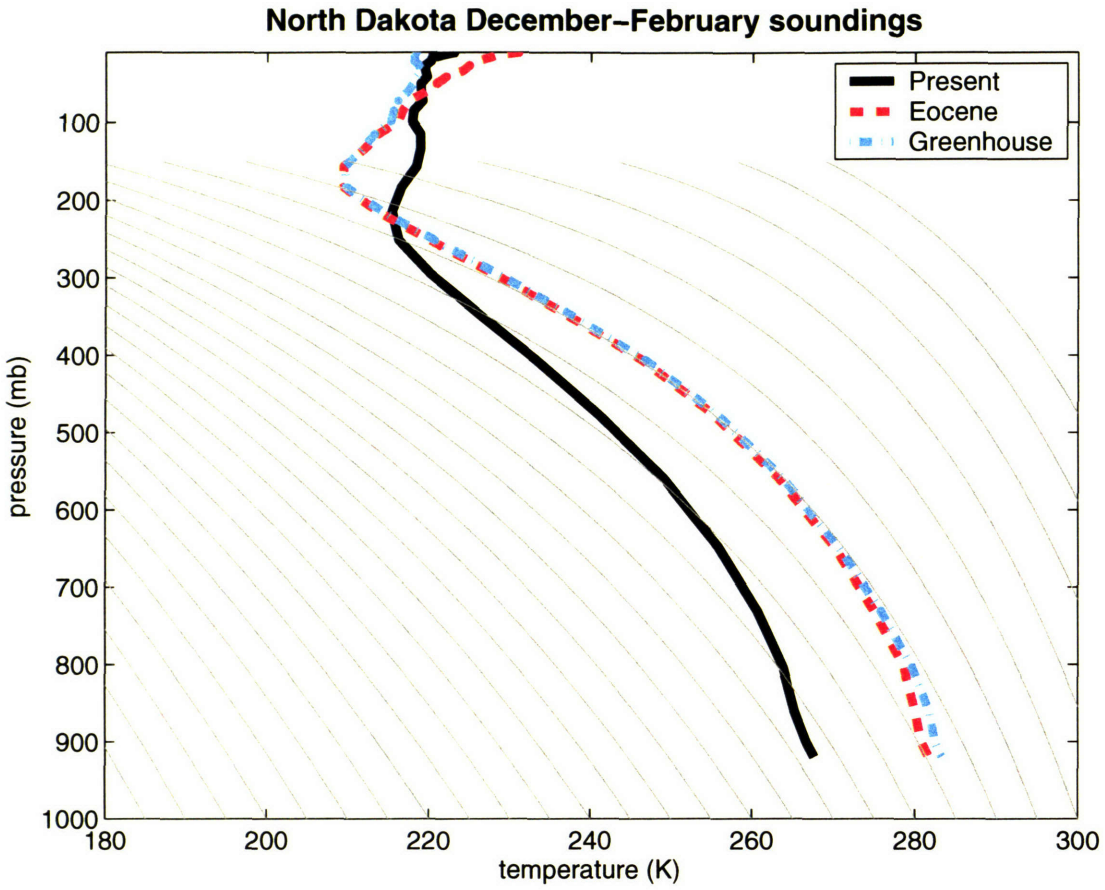

Figure 3-25: December-February soundings from North Dakota from the Present (solid black), Eocene (dashed red), and Greenhouse (dash-dotted light blue) simulations. The thin, light gray curves are moist adiabats. Actual model point is at 46.4°N, 101.2°W.

of the fact that the generation of eddies, particularly transient eddies, in the lower atmosphere falls with the temperature gradient. This flux of wave activity provides a constant damping of the stratospheric jet, a strong residual circulation, and winter stratospheric temperatures that are nearly constant in these simulations.

But what role did the imposed Rayleigh friction at the model top play? I ran a second simulation of the Greenhouse experiment, but with the amplitude of the imposed Rayleigh friction cut in half; soundings at 80°N averaged over the last five Decembers, Januaries, and Februaries are shown in figure 3-27.

The temperatures cooled by 0-4°C in the polar vortex below 15 mb, keeping the sounding above the saturation threshold if water vapor concentrations increase to 20 ppmv. The Rayleigh friction affects polar temperatures above 15 mb a bit more strongly, but here too temperatures remain too warm for saturation. The zonal mean wind are similar to within ~ 2 m/s below 15 mb; near the stratopause the summer and winter jets are 10-15 m/s stronger. As seen in figure 3-27, temperatures are cooler in the winter vortex, but they do not cool enough to change the results.

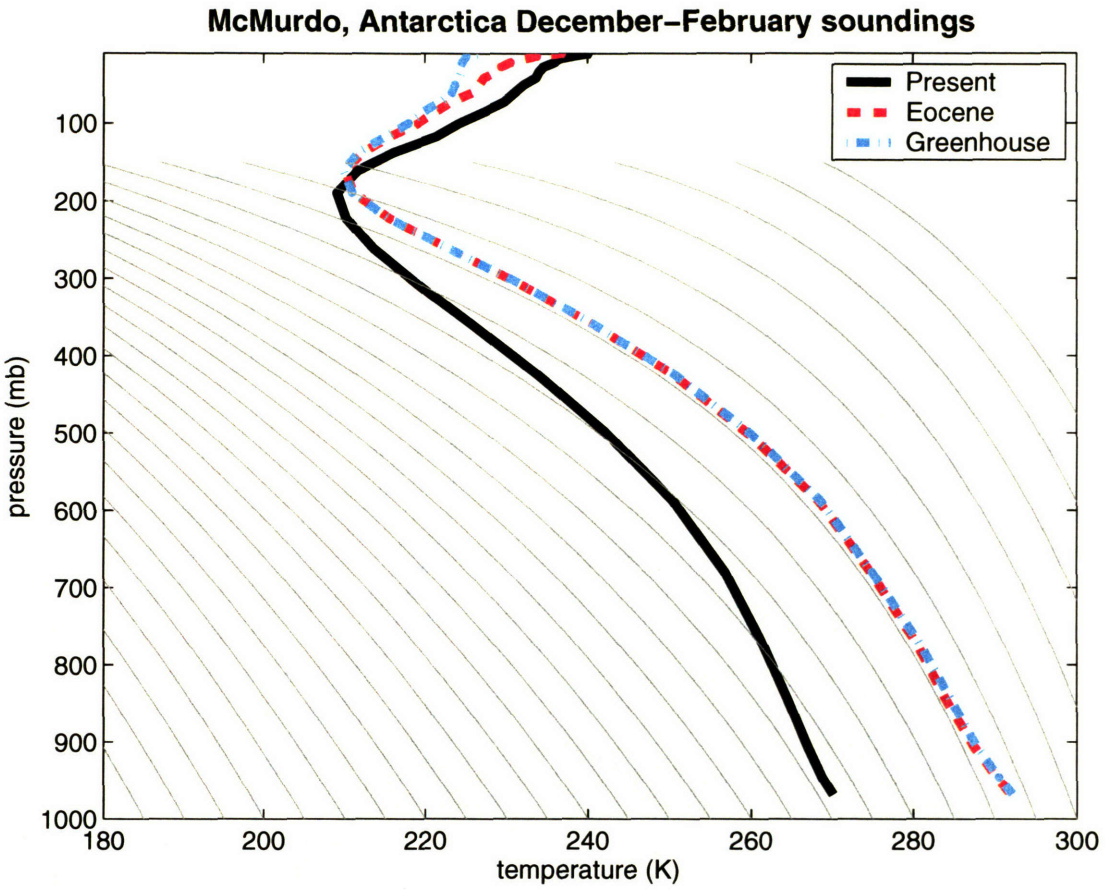

Figure 3-26: December-February (summer) soundings from Antarctica from the Present (solid black), Eocene (dashed red), and Greenhouse (dash-dotted light blue) simulations. The thin, light gray curves are moist adiabats. Actual model point is at 68.7°S, 168.8°E.

Byron Boville (personal communication) has conducted a test for the present climate in which all of the Rayleigh friction is replaced with some diffusion at the model top to control wave reflection. Without any friction, which qualitatively behaves like a gravity wave drag, jet speeds at the model top can exceed 200 m/s in the present climate. As a result, temperatures in the polar vortex fall. It is not possible to dampen the jet without affecting the temperatures below; one cannot have one without the other. This suggests that the evolution of gravity waves in the Eocene could have a significant role on the temperatures in the polar vortex, but little is known about the climatology of these waves in different climates. Nevertheless, we have seen that changes in the surface temperature gradient do not lead directly to a decrease in stratospheric winter temperatures.

The marked decrease in the atmospheric heat transport begs a question: could the oceans transport more heat during warm climates? In the second part of this thesis, we examine this possibility. What might increase the circulation and heat transport in the ocean? Proxy data strongly suggests that the horizontal buoyancy

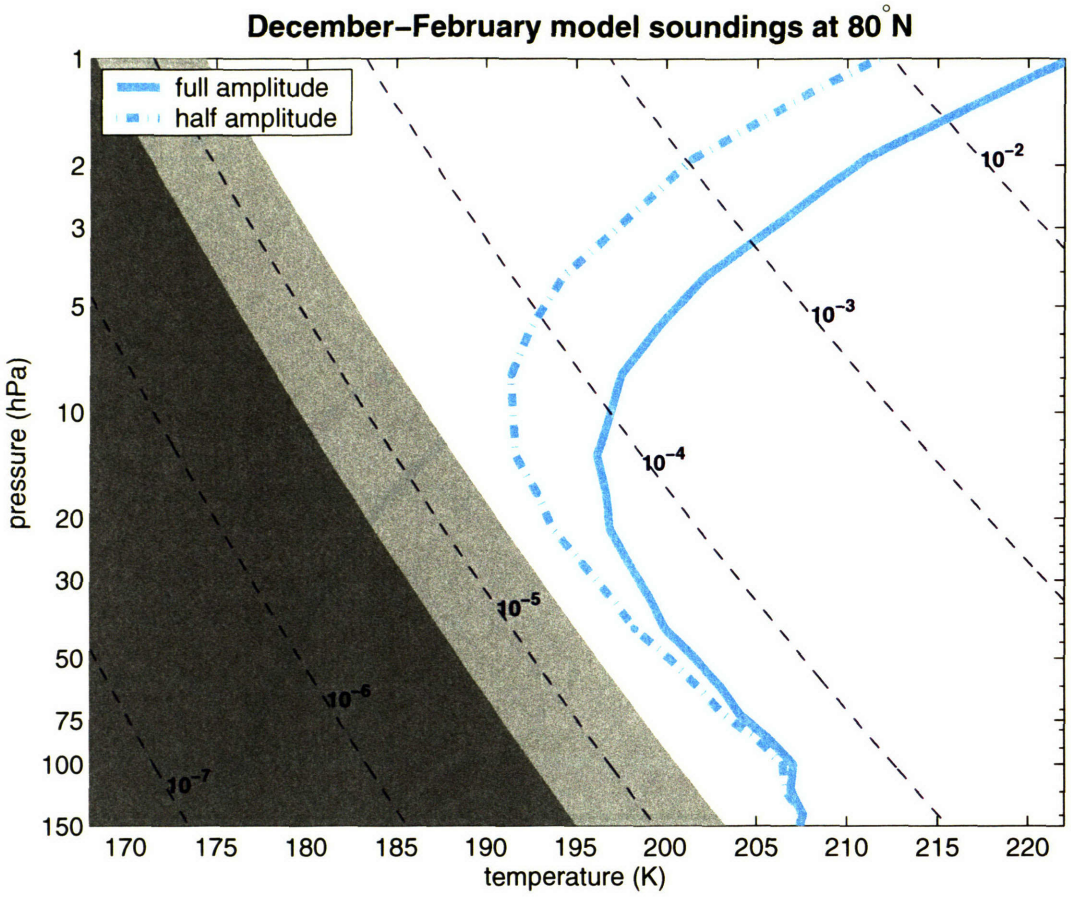

Figure 3-27: As in figure 3-3, but for two runs using the Greenhouse conditions (weak sea surface temperature gradient, and elevated carbon dioxide and methane). The solid light blue curve is from a run with the Rayleigh friction coefficient given by equation (3.1); this is the Greenhouse case examined in this chapter. The dash-dotted light blue curve is from a run with the Rayleigh friction cut in half. No other changes were made.

gradient, which would lead to a weaker circulation if mixing is fixed (Welander, 1986). But the vertical stratification was likely weaker during the Eocene, and if mixing increased during these climates, the oceans' heat transport might have risen. Tropical cyclones vigorously mix the upper tropical oceans, and there is reason to believe their frequency and intensity would have been higher during the warm climates. We investigate the sensitivity of the oceans' heat transport to mixing in the upper tropical oceans in Chapter 4, and then study some interactive parameterizations of mixing in Chapter 5.

Chapter 4

Where ocean mixing matters most

At the conclusion of the last chapter, I showed that the implied ocean heat transport in the atmosphere-only warm climate simulations is large. Thus far, this has been a ubiquitous feature of such simulations, and it dates to Eric Barron's early work on the Cretaceous (e.g., Schneider et al., 1985). In this second part of the thesis, our central question probes the role of the ocean during warm climates: Could the partitioning of the poleward heat flux shift to a larger contribution from the oceans? Held (2001) has argued that the atmospheric and oceanic fluxes in the deep tropics are coupled by the magnitude of the Ekman transport, which results from the same surface stress imposed on both media; under several assumptions, his calculations suggest that the atmosphere will dominate the poleward heat flux at the latitude of the Hadley cell's subtropical edge. Lindzen and Hou (1988) show that a weaker pole-to-equator temperature gradient should result in a narrower Hadley cell, but Farrell (1990) has argued that changes in the tropopause height and a loss of angular momentum in the poleward branch of the symmetric circulation may lead to the opposite during warm climates.

Our question immediately prompts another: By what means could the ocean heat transport increase? Given the need for an increase in the efficiency with which eddies transport heat in warm climates (Stone, 1978b) and the atmosphere general circulation models' inability to provide it (Barron and Washington, 1985; Sloan et al., 1995), the ocean has been invoked, not unlike a *deus ex machina*, to resolve the paradox posed by warm states. But until quite recently, no viable mechanisms by which the oceans could carry additional heat poleward during warm climates had been identified (e.g., see Lyle, 1997; Emanuel, 2001; Nilsson et al., 2003). Could stronger ocean mixing explain the previous deficiencies? Emanuel (2002) suggested that increases in tropical cyclone activity could elevate mixing, and he showed that the heat flux out of the tropical oceans must be about a petawatt in order to balance the net column heating that occurs in the wake of tropical cyclones (Emanuel, 2001).

I shall examine these issues in due course, but these questions imply still another, more fundamental one: Where does mixing matter most? Is the overturning

circulation most sensitive to mixing at locations different from those to which the heat flux is most sensitive? In order to later assess the feasibility of a sizable contribution from tropical cyclone mixing, we must first embark on a study of the essential physics of the ocean's general circulation. The material in this chapter might regarded as tangential to the central question of this thesis, but progress on the contribution of tropical cyclones to the oceans' heat flux first requires knowledge of what mixing in the upper tropical oceans accomplishes.

Additionally, a comprehensive theory for the oceans' general circulation remains elusive. While scaling analyses of the North Atlantic circulation have been performed in single hemisphere models (e.g., Park and Bryan, 2000; Scott, 2000), only Dalan et al. (2005) has examined scaling behavior in a global model. Marotzke (1997) developed a theory for the circulation of a single basin by considering boundary mixing. Gnanadesikan (1999) argues that the winds in the Southern Ocean, combined with mixing-induced upwelling, regulates the strength of the circulation. These ideas are not mutually exclusive. Before progressing further, we pause to investigate some of the fundamental characteristics of the circulation's response in a global model.

This chapter is framed around the role of mixing in different locations, examining the effects of both horizontal and vertical variations. The critical reader may question the relevance of some of the experiments presented in this chapter, particularly those testing concentrations of mixing that are clearly unphysical. Such objections are not unmeritorious, but they do miss the point: I caution that these simulations are strictly a test of model behavior, not all of which are motivated by observations. At the conclusion of this chapter, I summarize the salient findings and offer some applications from this exploration of model sensitivity to the real oceans.

The presentation is organized as follows: I review the relevant previous work in section 4.1; the model and control experiments are described in section 4.2; the effects of mixing at various latitudes, longitudes, and depths are discussed in sections 4.3–4.5; variations in the wind forcing are presented in section 4.6; different surface boundary conditions are discussed in section 4.7; the main findings are summarized in section 4.8. In Chapter 5, I build on these results and return to the question of what contribution tropical cyclones make to the oceans' heat transport.

4.1 Historical review

There are several review articles that nicely summarize the progress made in estimating mixing in the ocean. Wunsch and Ferrari (2004) describe the observational evidence in the context of theoretical developments, while Gregg (1987) reviews observations of thermocline mixing. Measurements by Ledwell et al. (1993), Polzin et al. (1997), and Ledwell et al. (2000) have contributed to a more complete picture of where mixing occurs in the ocean, and they have revealed some surprising structure.

Among the earliest modern contribution to understanding the oceans' general

circulation was the theoretical work of Sandström (1908). He considered the motion induced in a fluid by separated sources of heating and cooling, and analyzed a perfect fluid undergoing a Carnot cycle. By his arguments, the steady-state abyssal circulation should be motionless, as a circulation would be confined to a thin upper layer if surface heating occurs at a higher geopotential than cooling. Given heating in the tropics, the ocean should not be able to operate as a heat engine, extracting energy from the surface buoyancy forcing to maintain a vigorous overturning circulation.

Jeffreys (1925) noted that in a real fluid, as opposed to the perfect one discussed by Sandström, turbulent mixing could effectively lower the geopotential of the heating, creating horizontal temperature gradients at depth, which in turn could lead to an abyssal circulation. In the absence of diapycnal mixing, a strong circulation, perhaps driven by winds in the Southern Ocean (see Toggweiler and Samuels, 1998), would fill the ocean depths with dense water. Mixing is necessary to maintain a realistic vertical structure given upwelling of cold deep waters, with the stratification determined by vertical advective-diffusive balance. Munk (1966) examined this problem, and concluded that use of an eddy diffusivity was not inconsistent with the available data. Munk and Wunsch (1998) revisited this analysis and found a better fit with observations if the diapycnal diffusivity was allowed to vary with depth. This updated work also noted explicitly that the $O(10^{-4})$ m^2/s diffusivity should be considered a spatially averaged value, smoothing a quiescent background with localized regions of enhanced mixing.

Recent work by Scott (2000) and by Boos et al. (2004) has further illustrated this point. They found that mixing can be localized in space and/or isolated in time and still produce a vigorous overturning circulation, provided that the spatial and temporal average is conserved and that mixing occurs in the tropics.[1] Scott's (2000) work showed that the arguments of Sandström and Jeffreys are fundamental to the thermodynamics of the overturning circulation.

These developments have paralleled improved measurements of mixing in the real ocean. Bryan and Lewis (1979) suggested a vertical profile for mixing that broadly incorporates a physical dependence on the stratification. In the thermocline, where stratification is large, mixing is weak; the comparatively less stratified deep ocean has elevated values of mixing. Somewhat surprisingly, microstructure measurements have found that weak mixing of $O(10^{-5})$ m^2/s persists all the way to the sea floor over abyssal plains (Toole et al., 1994; Polzin et al., 1997), but greatly enhanced values occur over the mid-ocean ridges, generally increasing there with depth (Ledwell et al., 2000). These measurements present a picture of weak mixing through most of the ocean volume, from the base of the mixed-layer to the ocean floor, with greatly elevated values confined to small regions near rough terrain. Estimates by Ganachaud and Wunsch (2000) support a volume average value of $O(10^{-4})$ m^2/s or larger at

[1] The spatial average must be performed carefully, as mixing at high latitudes is ineffective at driving the overturning circulation. For example, one can conserve the spatial average of κ over the tropics, where mixing is most important (Scott, 2000; Bugnion, 2001).

depth, dominated by intense boundary processes rather than a spatially uniform value, which is often imposed in general circulation models. Data are too sparse to deduce a globally averaged vertical mixing profile (Wunsch and Ferrari, 2004).

Boccaletti et al. (2005) have revived the finding that most of the heat flux carried by the ocean is done so in the upper most 500 meters. This point has been known for some time (e.g., Haidvogel and Bryan, 1992; Held, 2001), but the diagnostic developed by Boccaletti et al. (2005) nicely illustrates this point. Perhaps, then, the degree of attention paid to the deep circulation in the context of climate has been somewhat unwarranted. The heat flux carried by the oceans is of paramount importance to the climate; much of this is accomplished in the surface Ekman layer cells, principally in the Pacific (Haidvogel and Bryan, 1992). The oceans dominate the heat flux equatorward of 20° latitude (Peixoto and Oort, 1992). The dependence of the heat flux on the vertical distribution of mixing will be examined later in this chapter.

4.2 Model and control run

We use the MIT general circulation model (Marshall et al., 1997a; Marshall et al., 1997b) for the experiments presented in this chapter. Our focus here is rather basic, and the experiments are idealized. The model geometry consists of two rectangular basins connected by a ribbon of grid points circumnavigating the southern end of the model domain; see figure 4-1.

Conceptually, the model construction consists of a long, narrow Atlantic basin connected to a broader Pacific-Indian basin (which terminates at 60°N) by a Southern Ocean circumnavigating the domain. Note that while the spacing is even in latitude, with a model node every 4°, the spacing is irregular in longitude, with a concentration of points along the eastern and western walls of each basin to better resolve the intense boundary circulations and Munk boundary layers (see Pedlosky, 1996). While this formulation is certainly idealized, it enables us to investigate a global circulation, rather than the more extensively studied North Atlantic component in isolation. Because these runs involve the ocean alone, boundary conditions at the upper surface must be specified. We begin with a simple construction, and discuss other boundary conditions in section 4.7.

For the runs presented through sections 4.6, the effects of salinity are neglected, and surface temperatures are rapidly restored on a time-scale of 30 days; this value was chosen so that the surface density gradient would be effectively prescribed. This simplicity allows us to approximate the equation of state as a linear function of temperature:

$$\rho(T) = \rho_o \left(1 - \alpha T\right), \tag{4.1}$$

where α is the coefficient of thermal expansion, equal to 2×10^{-4} °C^{-1}, and ρ_o is a reference density, taken here to be 1027 kg/m^3. As salt has been relegated to a passive

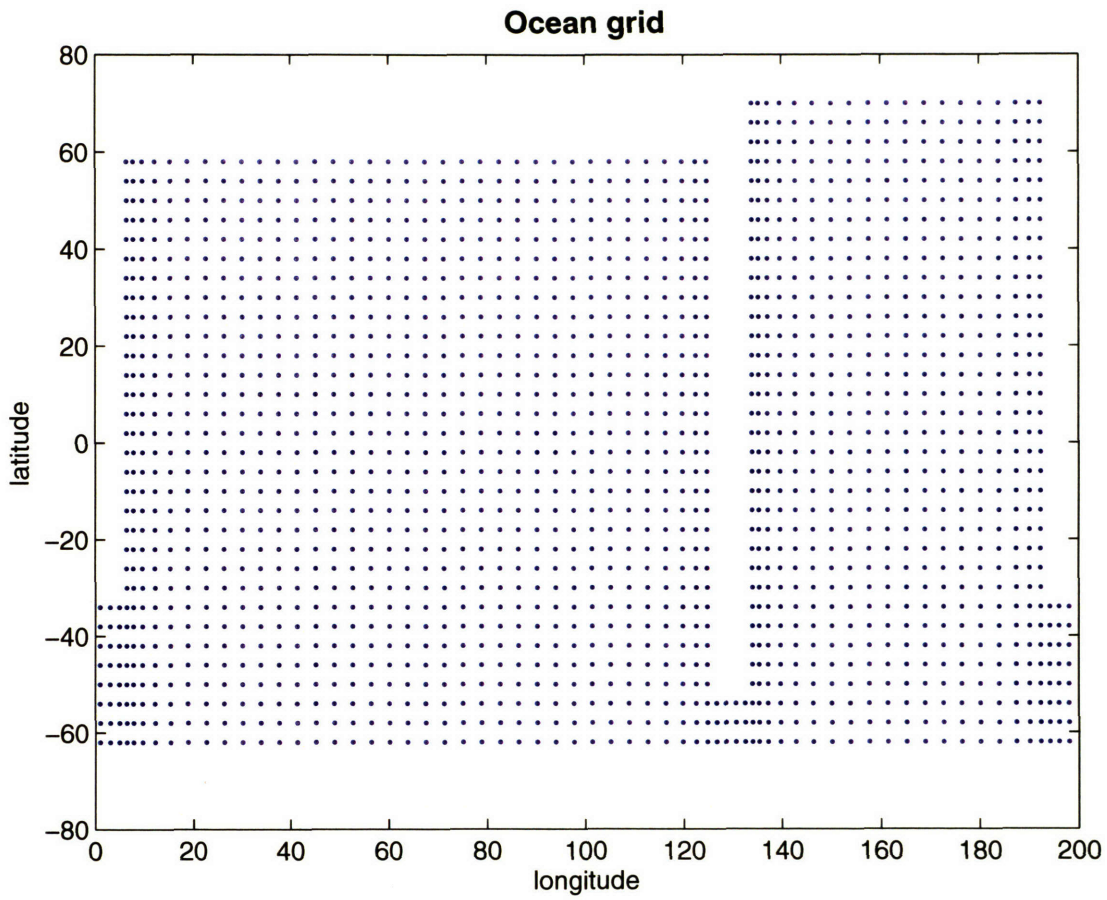

Figure 4-1: The ocean model grid. A Pacific-Indian basin, extending to 60°N (left), is connected to a long, narrow Atlantic basin (right) by a ribbon of points circumnavigating the globe in the Southern Ocean.

tracer, we run the model more rapidly by switching off its advection all together. The temperature and corresponding density profiles used to force the runs presented here are shown in figure 4-2. The temperatures were chosen so that the density gradient mirrors that observed in the present climate (e.g., see Peixoto and Oort, 1992, p. 193). This profile is zonally symmetric and does not vary in time. Note that the density is higher at the northern end of the Atlantic solely because it extends to a higher latitude than does the Pacific (see figure 4-1).

The model is also forced with an idealized wind profile, which is shown in figure 4-3. The profile is again zonally averaged and invariant in time. It is nearly symmetric about the equator, but the peak in Southern Hemisphere winds has been shifted south two grid points, or 8° latitude, to coincide with the location of the model's Drake Passage. The magnitude in the Southern Hemisphere closely mirrors the annually averaged wind stress; the Northern Hemisphere winds are stronger than observations support, but we retain the nearly-symmetric profile in these idealized

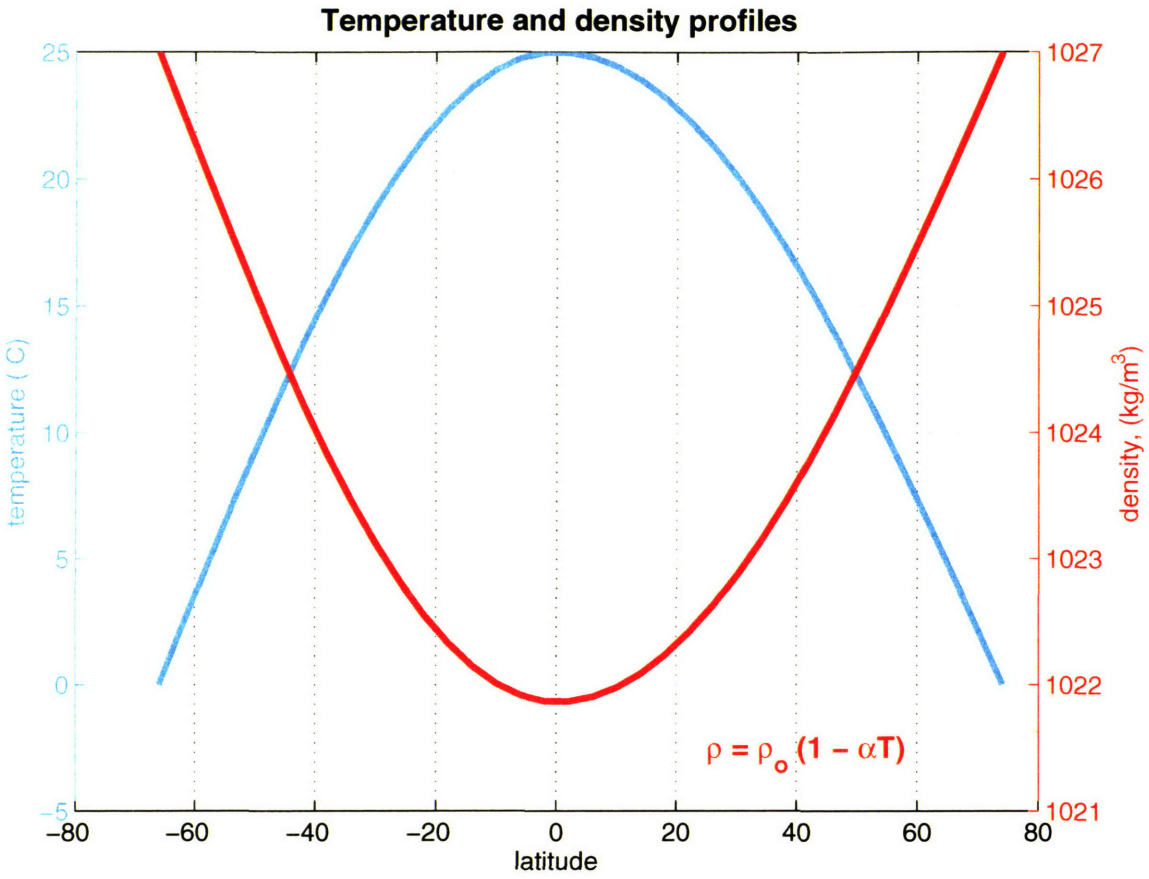

Figure 4-2: The temperature (blue, left axis) and corresponding density calculated from the linear equation of state (red, right axis) to which the surface temperature (density) field is restored. Given the rapidity with which the surface density is restored (here 30 days), the buoyancy gradient is effectively prescribed.

runs. The stronger Northern Hemisphere winds will force a stronger poleward heat flux in the Northern Hemisphere, but our focus in this chapter will be a comparison between runs rather than a comparison of these simulations with observations. We will examine simulations in which the magnitude of the wind stress is halved, doubled, and set to zero in section 4.6.

All simulations were run for at least 1000 model years, longer if they had yet to reach equilibrium (defined by a change in the global-mean ocean temperature of 0.02°C/100 years or less). All runs presented in this chapter are in equilibrium.

Our control runs force the model with a static, uniform value of the diapycnal (vertical) diffusion coefficient.[2] We begin with a review of the model's sensitivity to

[2]Given the flatness of the isopycnals (surfaces of constant density) through much of the ocean, especially in the tropics, and the large aspect ratio of the horizontal to vertical scales in the ocean, we take the diapycnal diffusivity to be represented by the model's vertical diffusivity. This amounts to a small error, particularly in the subtropics of the upper ocean where density surfaces outcrop.

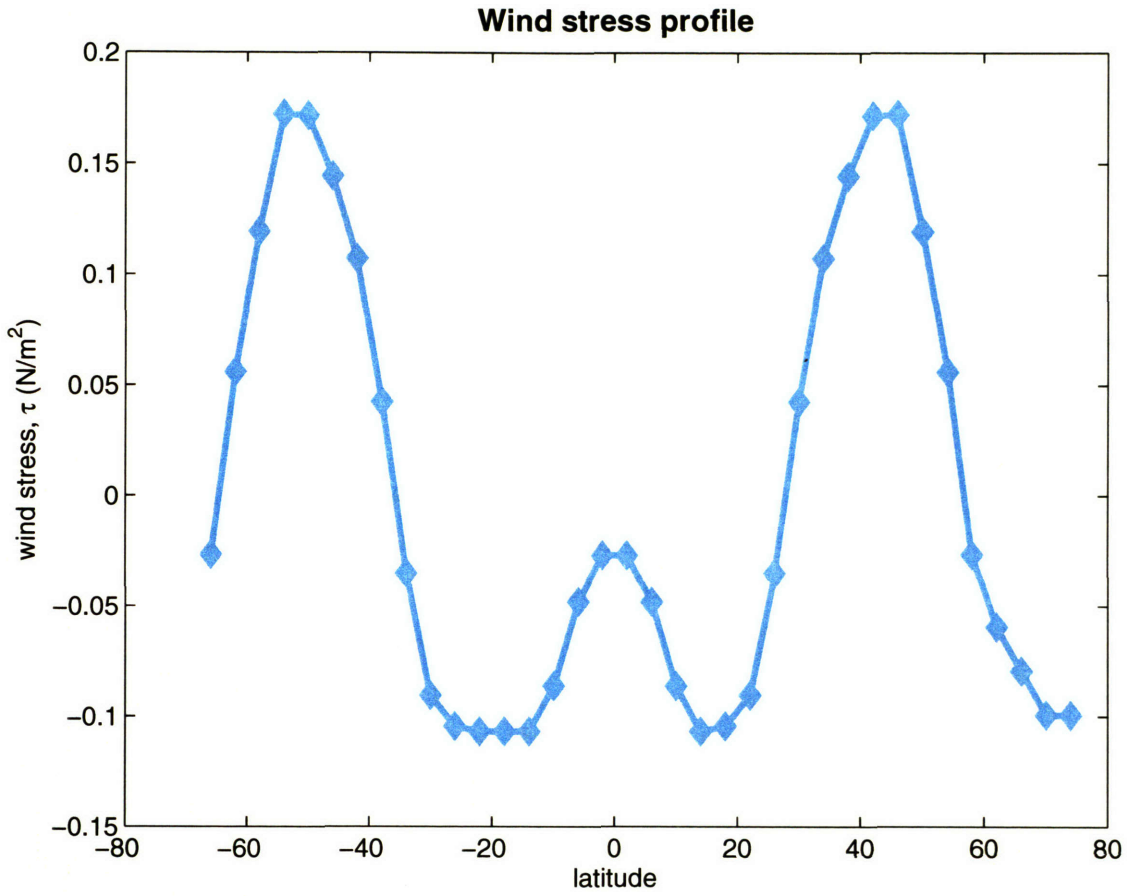

Figure 4-3: The wind stress profile applied to the model (diamonds are plotted at each actual grid point). The profile is nearly symmetric, but is offset 8° latitude (two grid points) in the Southern Hemisphere so that the peak westerly wind stress better corresponds with the location of the Drake Passage.

the specified values of the vertical diffusivity. Classic scaling arguments (Welander, 1986; Bryan and Cox, 1967) begin with a vertical-diffusive balance, and lead to the prediction that the strength of the overturning will scale with the 2/3 power of κ and the 1/3 power of the buoyancy gradient; see Scott (2000) for a nice review of these ideas. It is unclear, however, how the circulation should scale when both wind forcing and mixing contribute to the overturning, as is the case in our simulations.

The circulation that results from weak mixing of 0.1 cm^2/s is shown in figure 4-4. Panel (a) shows the overturning in the Atlantic; note that a 14 Sv circulation is forced even in the presence of weak mixing, suggesting a dominant role for wind forcing in this case; see Toggweiler and Samuels (1995) or Gnanadesikan (1999). The poleward heat flux in the North Atlantic is about a half a petawatt, and peaks in low latitudes. Note that 7 Sv flow into the Atlantic from the Southern Ocean, suggesting

The terms are used interchangeably in this chapter.

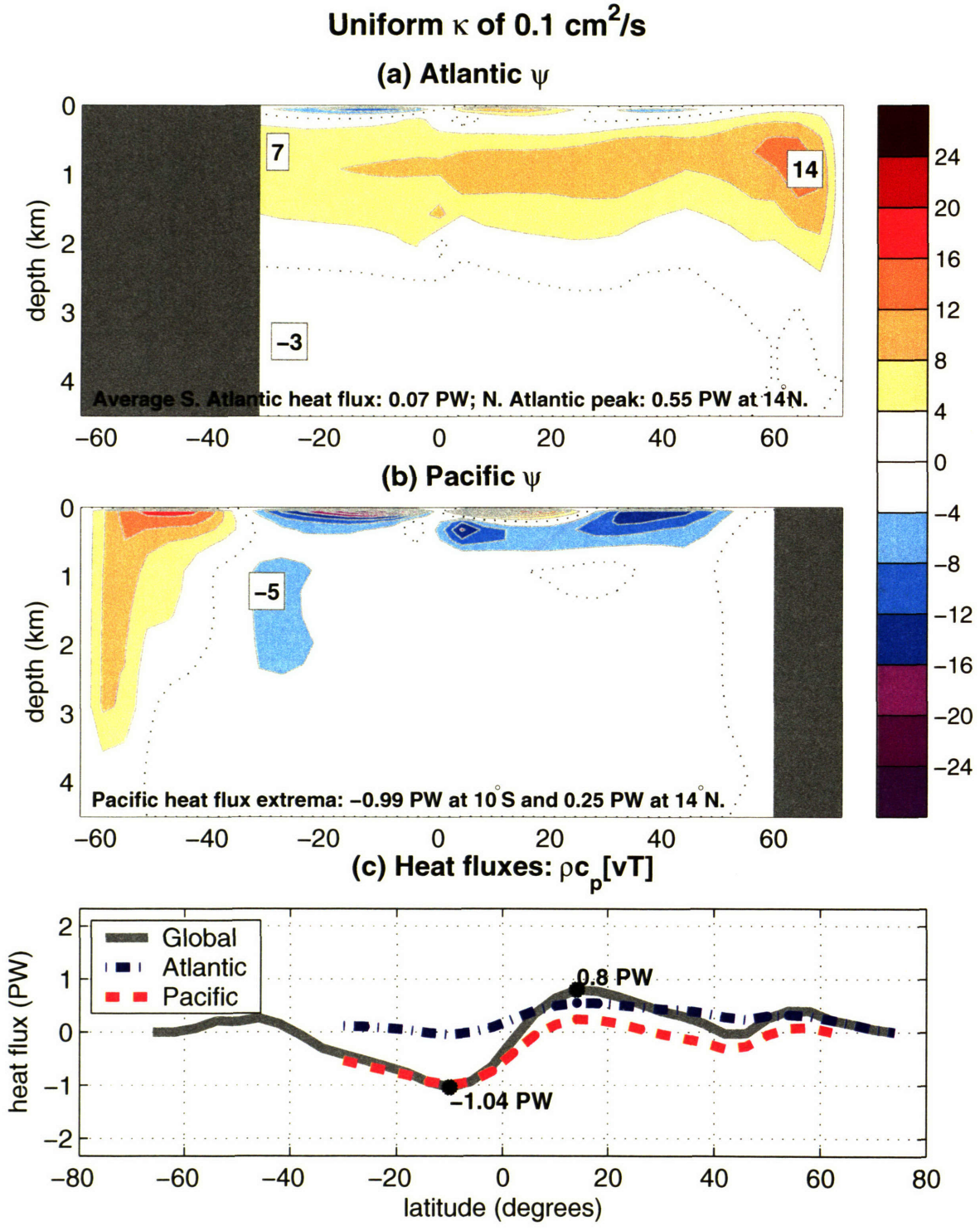

Figure 4-4: Overturning strength and heat fluxes when κ has a spatially uniform value of $0.1\,\mathrm{cm^2 s^{-1}}$. (a) Meridional overturning in the Atlantic (Sv). (b) Meridional overturning in the Pacific (north of 30°S) and in the entire Southern Ocean (south of 30°S). (c) Atlantic, Pacific, and global heat fluxes; extrema in global flux are noted.

that only half of the North Atlantic sinking upwells in low latitudes of that basin.

Panel (b) shows the circulation in the other basin; note that south of 30°S, the circulation is averaged around the entire globe and not just the longitudes south of the Pacific. While a Deacon cell, which is driven by Southern Ocean winds, can be seen in the southern latitudes, much of the Pacific is filled with a very weak circulation, always less than 5 Sv below the surface Ekman cells.[3]

Panel (c) shows the heat flux carried by the ocean. Given that surface density is nearly prescribed, the boundary conditions unrealistically constrain the heat flux; the rapid restoration at the surface effectively prescribes a surface flux to the atmosphere in middle latitudes, limiting the amount of heat that can be transported laterally. Estimates from observations suggest that the oceans carry a peak of about 2 PW (Trenberth and Caron, 2001). Note that the Southern Hemisphere heat flux is carried almost exclusively in the Pacific basin, as the heat flux in the southern Atlantic is equatorward. Both basins make a sizable contribution to the heat flux in the Northern Hemisphere.

When mixing is increased to a larger value, the circulation and heat fluxes increase. Figure 4-5 shows the results from a simulation with a static, uniform diffusion coefficient value of 0.9 cm^2/s. In panel (a), note that the intensity of the North Atlantic circulation has doubled, and this has been accomplished almost exclusively by stronger upwelling in the tropical Atlantic; 8 Sv flow into the Atlantic from the Southern Ocean, nearly identical to the 7 Sv seen in figure 4-4a. This stronger circulation drives an increased heat flux in the North Atlantic, peaking at 0.93 PW. In the Pacific, strong upwelling of deep waters occurs through the basin, and the Southern Hemisphere heat flux has been enhanced. The global heat fluxes have increased by about a third of a petawatt in both hemispheres.

Given the rapid restoration of surface density, winds in the Southern Ocean commingle with upwelling balanced by downward diffusion to affect the overturning circulation. It is not possible to partition the circulation into one equator-to-pole component driven by low latitude mixing and a second pole-to-pole component driven by Southern Ocean winds. The Welander scaling pertains to the mixing-induced part of the circulation, which is muddled by the role of wind forcing with fast restoration of surface density.[4]

---

[3]Although we use the Gent-McWilliams scheme (Gent and McWilliams, 1990), these figures show the Eulerian mean; bolus velocities have not been added. The main effect of the bolus velocities is to cancel much of the Deacon cell.

[4]Suppose that the the overturning circulation and heat transport temporarily weaken, perhaps by a weakening of Southern Ocean winds as discussed by Toggweiler and Samuels (1995). In a coupled model, or in one in which the restoration time-scale is sufficiently long, the reduced heat transport allows the ocean to cool in regions of deep water formation, elevating the density there and offsetting the decrease in the overturning circulation strength. This thermal feedback is absent in the presence of fast restoring, as used by Toggweiler and Samuels (1995); with rapid restoration, surface densities are clamped back to a prescribed value (Rahmstorf and England, 1997; Bugnion, 2001; J. Scott, personal communication.

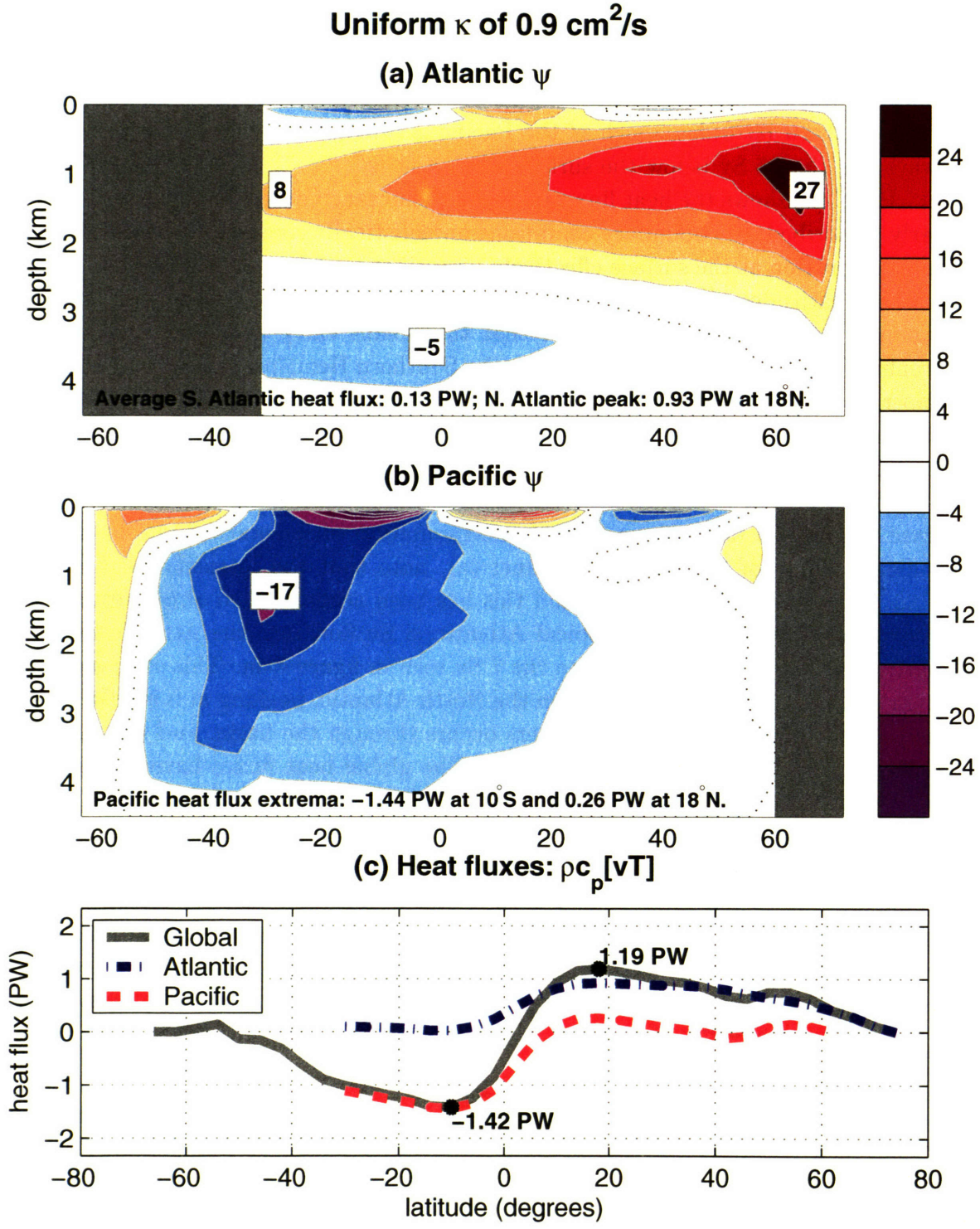

Figure 4-5: As in figure 4-4, but for a spatially uniform κ of $0.9\,\mathrm{cm^2 s^{-1}}$. (a) Meridional overturning in the Atlantic (Sv). (b) Meridional overturning in the Pacific (north of 30°S) and in the entire Southern Ocean (south of 30°S). (c) Atlantic, Pacific, and global heat fluxes; extrema in global flux are noted.

We employ the following technique to deduce the scaling: take the logarithm of both the maximum in the overturning, ψ, and the diffusion coefficient, κ, and then perform a linear regression. This least-squared method returns a slope, m, and an intercept, b. Thus,

$$\begin{aligned} \log(\psi - \psi_0) &= m \log \kappa + b \\ \log(\psi - \psi_0) &= \log \kappa^m + \log e^b \\ &= \log e^b \kappa^m \\ \psi &= \psi_0 + e^b \kappa^m. \end{aligned} \tag{4.2}$$

The parameter ψ_0 is an offset; when part of the circulation is wind-driven, the circulation can remain nonzero in the limit of no mixing (Samelson and Vallis, 1997). It may not be much better to assume that ψ_0 is a constant, but setting it to some fixed value is no worse than insisting it be zero. We shall choose ψ_0 such that the sum of the least squares is a minimum.

The scaling is plotted in figure 4-6. Clearly, the predicted dependence on κ falls short of the 2/3 power law suggested by Welander (1986) and found by Scott (2000) in a single basin model forced with no wind.[5] The scaling is closer to a 1/4 power law for the North Atlantic when ψ_0 is zero, but 1/3 when ψ_0 is 2.98, the value that minimizes the sum of the least squares. The overturning in the South Pacific follows a slightly stronger power law, between 1/2 and 3/5. Dalan (2003) used a similar idealized global ocean model and also found that the Pacific overturning scales with a higher power of κ then the Atlantic does, but his results were closer to the classic Welander (1986) scaling, finding a 1/2 dependence in the Atlantic and a 2/3 dependence in the Pacific.

The classic scaling also predicts a 2/3 power law for the heat fluxes with mixing (Welander, 1986), though Scott (2000) found this scaled closer to a 1/2 law in his work. Here the scaling is weaker still, closer to 1/4 (not shown), though the rapid restoration of surface density places a tight constraint on our model's ability to transport heat. Additionally, a large portion of the heat transport is accomplished in the wind-driven surface Ekman cells (Haidvogel and Bryan, 1992), which is held constant here. Scaling results depend on the relaxation time used, and coupling to an atmosphere model affects results too.

[5]Samelson and Vallis (1997) and Vallis (2000) argue that rather than the length of the gyre, the appropriate length scale to use in the advective-diffusive estimate of the horizontal temperature gradient is the horizontal distance across the sloping thermocline itself. Making this substitution in Welander's (1986) derivation leads to an overturning circulation that scales with $\kappa^{1/2}$, rather than with $\kappa^{2/3}$. The thermocline depth now scales with $\kappa^{1/2}$ in lieu of the conventional $\kappa^{1/3}$. In the limit of no wind, they argue that the slope of the isotherms flattens and the length scale returns to that of the domain.

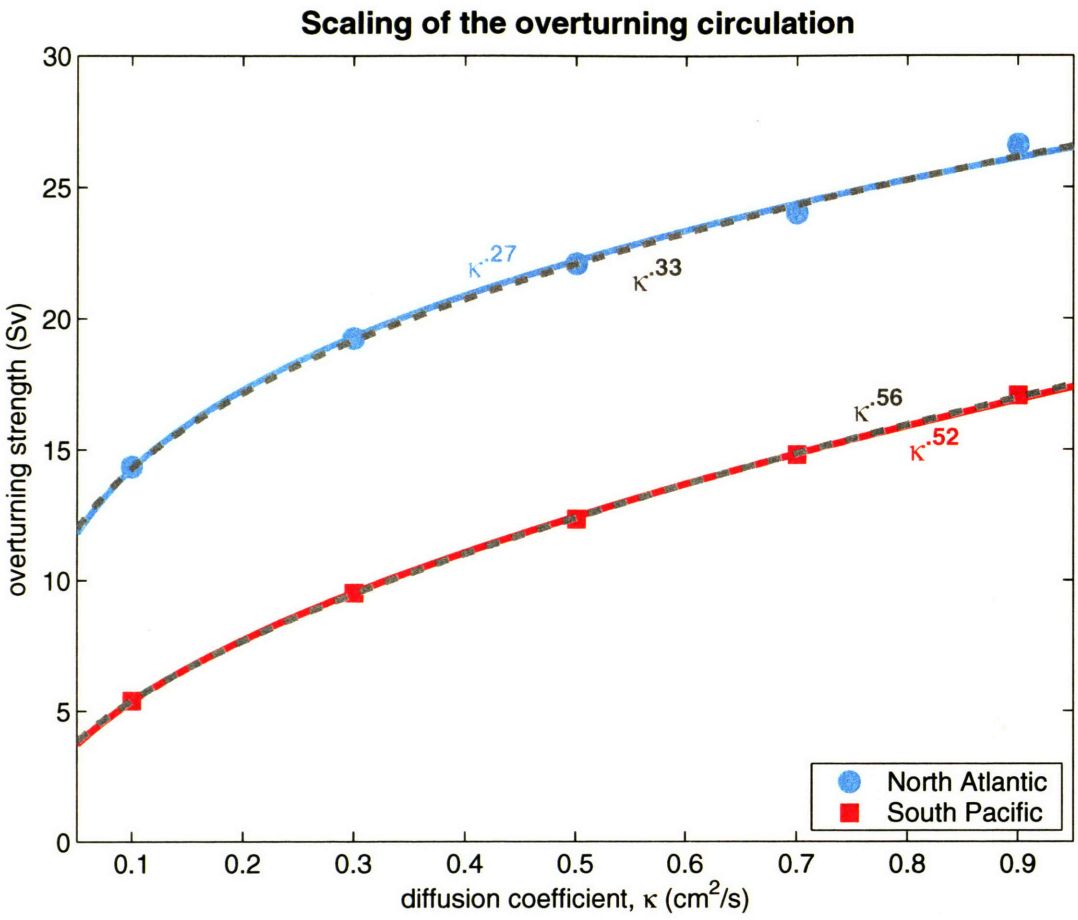

Figure 4-6: Maximum strength of the overturning in the North Atlantic (blue circles) and South Pacific (orange squares) across a decade of variation in κ, the diapycnal diffusion coefficient. The best fit curve estimated by equation (4.2) is shown running through the data with ψ_0 zero (solid, colored) and ψ_0 chosen so that the sum of the least squares is a minimum (dashed, gray). The labels κ^m are plotted next to their respective curves; the black labels go with the gray, dotted line.

4.3 Latitudinal dependence

We next examine the influence of κ at various latitudes. Much of the groundwork for this section has been laid by Scott (2000) and Bugnion (2001), who note that the North Atlantic overturning is most sensitive to mixing in tropical latitudes. Like Bugnion (2001), we consider the global circulation, but we extend her work to examine the influence of mixing on the circulation beyond the North Atlantic alone. Additionally, our work uses a fully nonlinear model, whereas Bugnion's (2001) study was linear.

In this section, we take a simulation in which the diapycnal diffusion coefficient is 0.5 cm^2/s everywhere as our control run; note that the wind forcing in all simulations

in this section is the standard profile shown in figure 4-3.

The control circulation is shown in figure 4-7. Panel (a) shows the Atlantic, where fluid flows into the southern part of the boundary, travels northward, sinks at high latitudes, and returns southward at depth. About 14 Sv is upwelled in low latitudes of the tropical Atlantic, while the remainder travels into the Southern Ocean where it upwells off of Antarctica or in the Pacific basin; the circulation transports 0.8 PW heat poleward in the Northern Hemisphere, and about 0.1 PW equatorward in the South Atlantic. Panel (b) shows the circulation in the Pacific north of 30°N and the global circulation south of this latitude. Note that a significant amount of deep water is upwelled throughout the Pacific. The surface Ekman cells carry a significant amount of heat poleward, dominating the global transport in the Southern Hemisphere (see figure 4-7c).

4.3.1 Tropical mixing

We now demonstrate that mixing in the tropics is almost entirely responsible for the diffusively driven portion of the global circulation. Figure 4-8 shows a simulation identical to that in figure 4-7, except that mixing has been decreased poleward of 30° latitude. The diffusion coefficient now takes a value of 0.5 cm^2/s equatorward of 30°, and a value of 0.05 cm^2/s poleward of this latitude; the high latitude value is only one order of magnitude larger than that for thermal diffusion by molecular processes, which is of $O(10^{-7})$ m^2/s.

The circulation shows only minor differences from the control run. Note that 7 Sv flow into the Atlantic, and that 20 Sv sink in the North Atlantic (compared to 8 Sv and 22 Sv before). Thus there is only a small difference (approximately 1 Sv) in the amount of North Atlantic Deep Water upwelled in the Atlantic when mixing is excluded north of 30°N. The heat flux carried poleward in the Atlantic also shows no change.

Likewise the Pacific circulation remains nearly unchanged. Both the overturning strength and the heat fluxes show only small changes. The peak heat transport in both hemispheres remains within 0.1 PW of the control run when mixing poleward of 30° is excluded.

Bugnion (2001) found that the strength of the North Atlantic overturning circulation is sensitive to mixing throughout the tropics, with a spike of sensitivity near the equator. Concentrating mixing in the latitudes between 4° and 30° or between 8° and 30° results in no changes if the area-weighted average value of κ is conserved (results not shown here). It is unclear to what extent the linearization inherent to the adjoint technique used by Bugnion (2001) affects the peaks in sensitivity.

The conclusion that the overturning circulation is highly sensitive to mixing in tropical latitudes appears robust. This has been shown by Scott (2000) in a single-basin, single-hemisphere model and confirmed by Bugnion (2001) and the results shown here. Thermodynamically, this must be true, as mixing lowers the geopo-

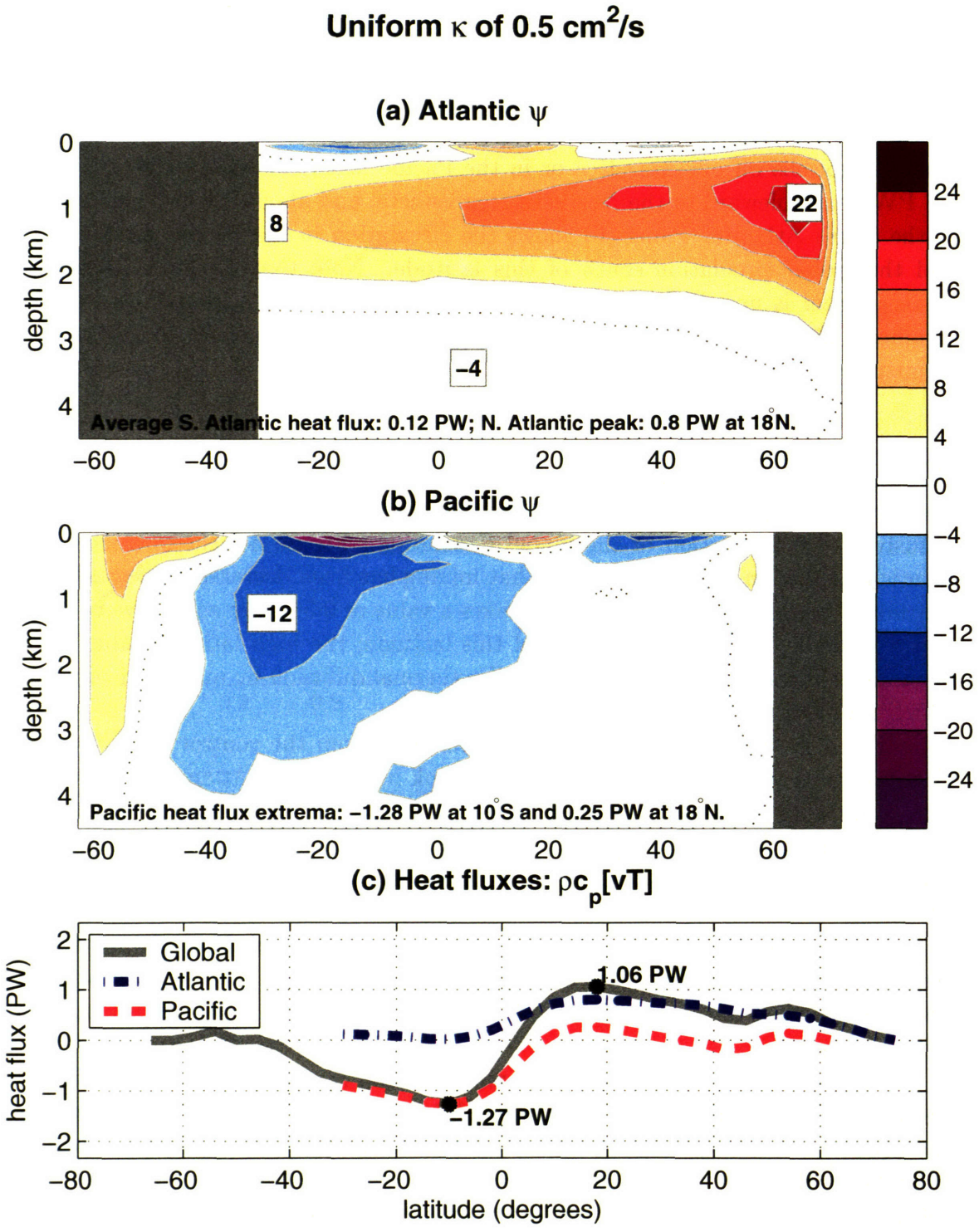

Figure 4-7: As in figure 4-4, but for a spatially uniform κ of $0.5\,\mathrm{cm^2 s^{-1}}$ (using the standard wind profile). (a) Meridional overturning in the Atlantic (Sv). (b) Meridional overturning in the Pacific (north of 30°S) and in the entire Southern Ocean (south of 30°S). (c) Atlantic, Pacific, and global heat fluxes; extrema in global flux are noted.

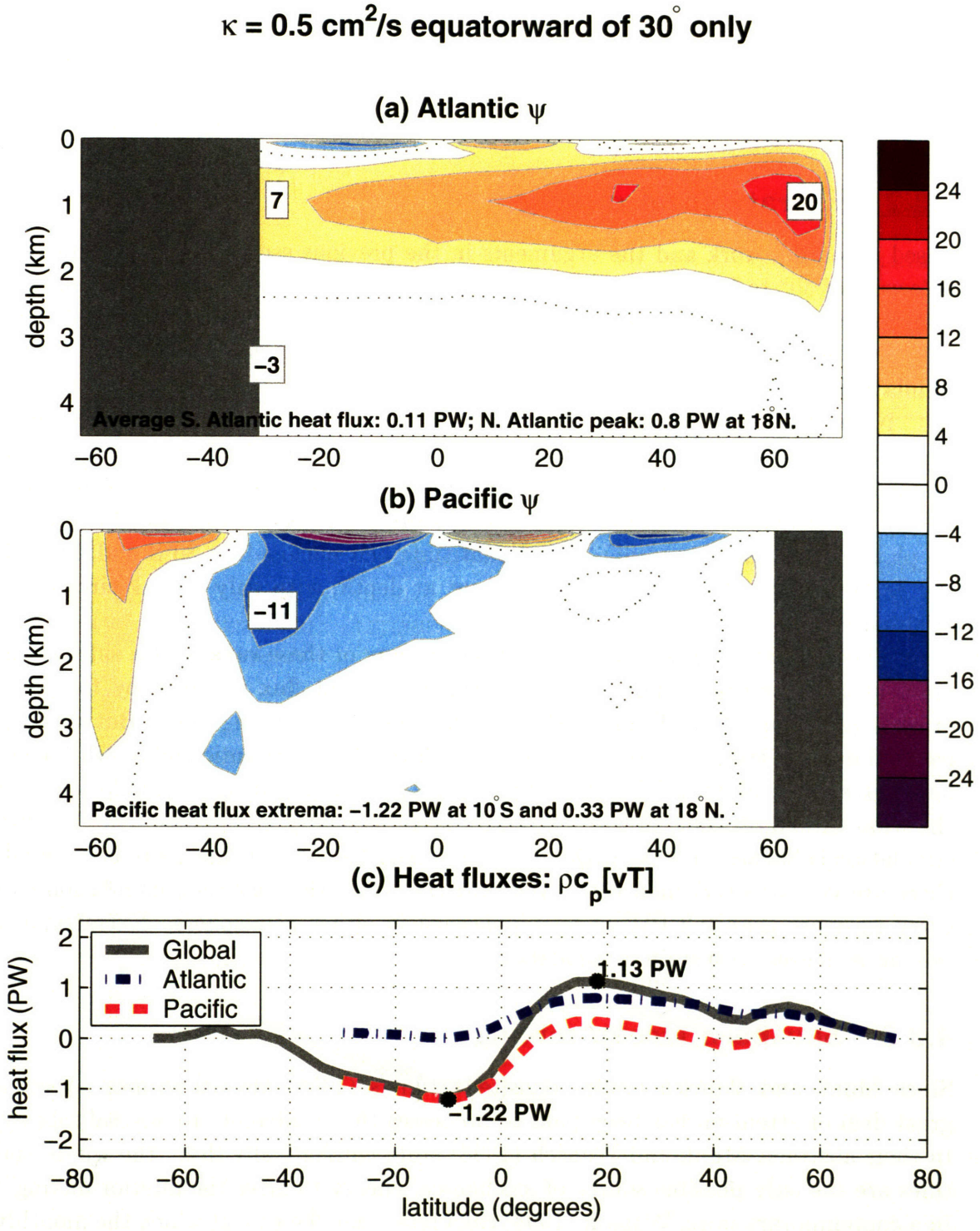

Figure 4-8: As in figure 4-4, but for a run in which κ is $0.5\,\mathrm{cm^2 s^{-1}}$ equatorward of 30° latitude only; poleward, it is $0.05\,\mathrm{cm^2 s^{-1}}$. (a) Meridional overturning in the Atlantic (Sv). (b) Meridional overturning in the Pacific (north of 30°S) and in the entire Southern Ocean (south of 30°S). (c) Atlantic, Pacific, and global heat fluxes.

tential at which tropical heating occurs by diffusing heat into the interior (Jeffreys, 1925). Were mixing concentrated at higher latitudes, mixing only cold surface waters with cold deep waters, Sandström's (1908) theorem would predict only a thin surface circulation with a quiescent abyss. This can be modified in the presence of wind forcing; the limitations of higher latitude mixing are explored in the next section.

4.3.2 Extratropical mixing

Based on earlier work and the arguments in the previous section, we expect mixing poleward of 30° to have little effect. To test this, we force a simulation in which the diffusion coefficient is 0.5 cm^2/s poleward of 30° latitude in both hemispheres, but only 0.05 cm^2/s equatorward, the inverse of the previous case. The results of this simulation are shown in figure 4-9.

Note that a vigorous North Atlantic overturning is maintained, but this is dominated by processes outside of the basin: while 15 Sv sink at the northern end of the basin, 7 Sv flow out through the southern end, suggesting that only 8 Sv is upwelled locally. Indeed, the mixing north of 30°N appears principally responsible for this, as no plotted streamline terminates in the latitude belt enclosed by 30°S and 20°N in the Atlantic. The Pacific is nearly quiescent at depth, with only a weak circulation of about 6 Sv.[6]

The wind stress has not changed between any of these runs, and a substantial portion of circulation responsible for carrying the heat flux is forced by the wind directly (i.e., the surface Ekman cells; see Haidvogel and Bryan, 1992). But without tropical mixing, the poleward transport in both the North Atlantic and South Pacific has decreased by about 0.3 PW from the control run. In a companion simulation with the wind turned off (not shown), the entire ocean is nearly motionless. The Atlantic circulation collapses to 9 Sv, with only 3 Sv in the Pacific; because there is no wind, there are no surface Ekman cells. Without the wind, the weakened circulation can carry no more than 0.2 PW of heat poleward in either hemisphere. Extratropical mixing is unable to sustain a circulation.

4.3.3 Southern Ocean mixing

Since Munk and Wunsch (1998) revisited Munk's (1966) abyssal recipes paper, a great deal of attention has been paid to processes that contribute to abyssal mixing. In their abstract, Munk and Wunsch (1998) state emphatically that "the winds and tides are the only possible source of mechanical energy to drive the interior mixing." In a contemporary note, Wunsch (1998) calculates that the rate at which the monthly

[6]The strong overturning near the equator that lies just below the surface Ekman cell in the Pacific seems to be a numeric problem that arises whenever mixing is weak near the equator. Here the diffusion coefficient is only 0.05 cm^2/s there, and a similar feature can be seen in other simulations with weak mixing in the equatorial Pacific. For example, review the runs that apply 0.1 cm^2/s everywhere; see figures 4-4, 4-23, and 4-26.

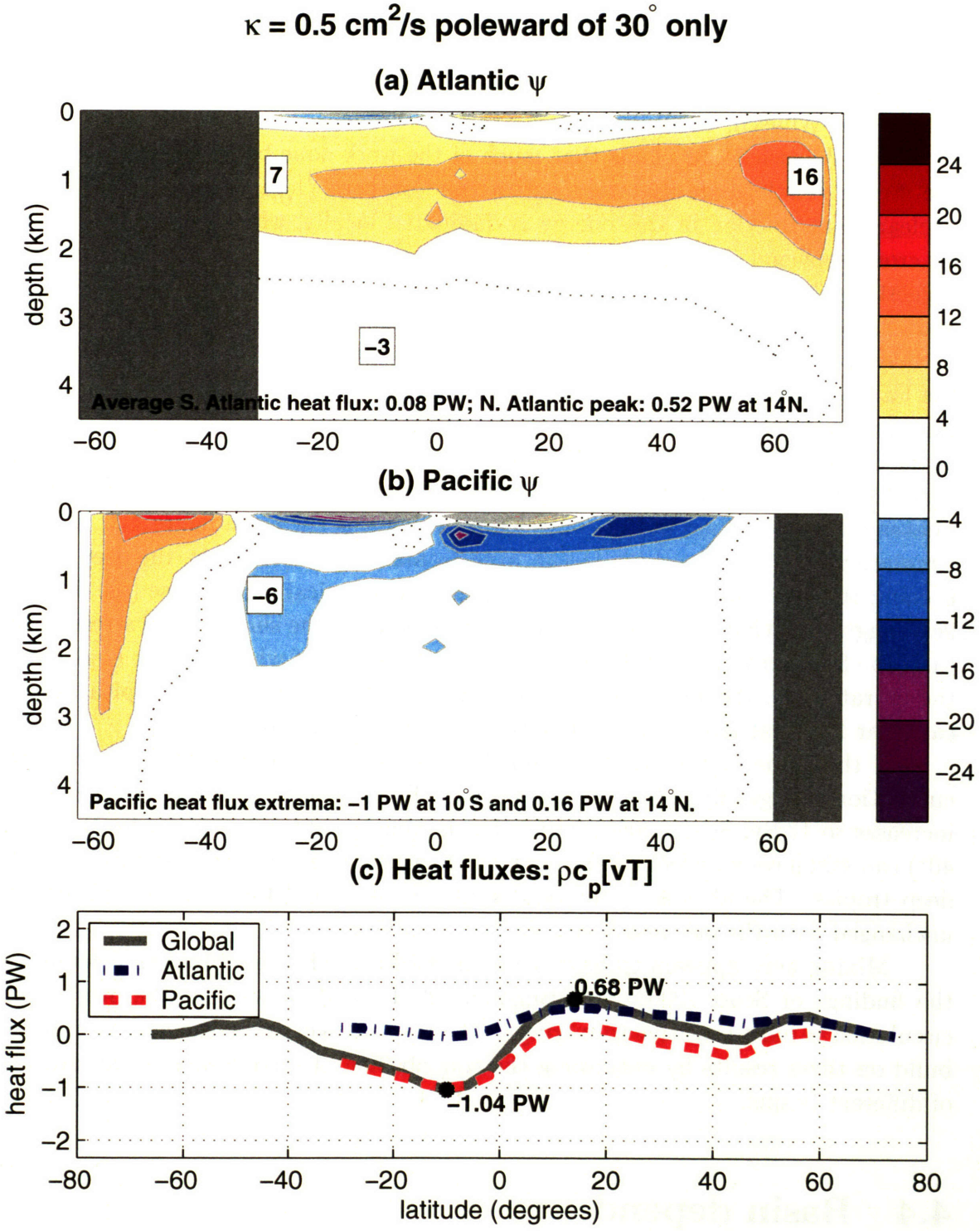

Figure 4-9: As in figure 4-4, but for a run in which κ is $0.5\,\mathrm{cm^2 s^{-1}}$ poleward of 30° latitude only; in the tropics, it is $0.05\,\mathrm{cm^2 s^{-1}}$. (a) Meridional overturning in the Atlantic (Sv). (b) Meridional overturning in the Pacific (north of 30°S) and in the entire Southern Ocean (south of 30°S). (c) Atlantic, Pacific, and global heat fluxes.

mean wind works on the oceanic general circulation is about 1 TW (one terrawatt is 10^{12} W), roughly the same amount of power that tides contribute. The combination of these estimates roughly accounts for the required 2 TW of power needed to return the downwelling dense water in the sinking branches of the overturning circulations (Munk and Wunsch, 1998).

But Wunsch (1998) finds that much of the work done by the wind comes from the strong zonal winds that race across the Southern Ocean. He notes that it is unclear what fraction of this energy is dissipated locally, what fraction is available for cross-isopycnal mixing, and what fraction is exported elsewhere. He concludes by suggesting that much of the mixing done by the wind could occur primarily in the Southern Ocean. We run two additional experiments to test such a case.

In the two runs presented here, mixing is confined to latitudes south of 30°S, the latitudes south of the model's Cape of Good Hope (see figure 4-1). In the first experiment, the results of which are shown in figure 4-10, κ takes a value of 0.5 cm^2/s in the Southern Ocean and 0.05 cm^2/s elsewhere. Here we see an even weaker circulation than in the extratropical mixing case presented in figure 4-9 and a substantially weaker circulation than in the control run, which was shown in figure 4-7. While a circulation forced by Southern Ocean winds remains in the Atlantic, the deep Pacific is calm; the heat fluxes change little from the extratropical mixing case (see figure 4-9c), suggesting what remains is governed principally by the surface wind stress rather than the Southern Ocean mixing. Note that regardless of where mixing is placed in the extratropics, the weaker circulations that result by shutting off tropical mixing carry far less heat than in the simulation with globally uniform mixing.

If the value of mixing is amplified in the Southern Ocean to 2.0 cm^2/s, the circulation changes little (results not shown). The overturning in the North Atlantic increases to 17 Sv; Scott (2000) found that mixing in subtropical latitudes (to about 40°) can still have an effect on the circulation, albeit a smaller one than mixing in the deep tropics. The abyssal circulation is largely dead, and the Deacon Cell remains unchanged with the elevated Southern Ocean mixing.

Mixing here appears to have a minimal effect. This material has reconfirmed the findings of Scott (2000) and Bugnion (2001), and shows that the overturning circulation is most sensitive to mixing in the tropical oceans. In the next section, we build on these results by examining the contribution of mixing in tropical latitudes of different basins.

4.4 Basin dependence

Many idealized studies have used single-hemisphere or single-basin models to advance the conceptual understanding of the meridional overturning circulation in the Atlantic Ocean (e.g., Toggweiler and Samuels, 1995; Scott and Marotzke, 2002). This is not without good reason, of course, as a principal goal of pioneering work is to capture

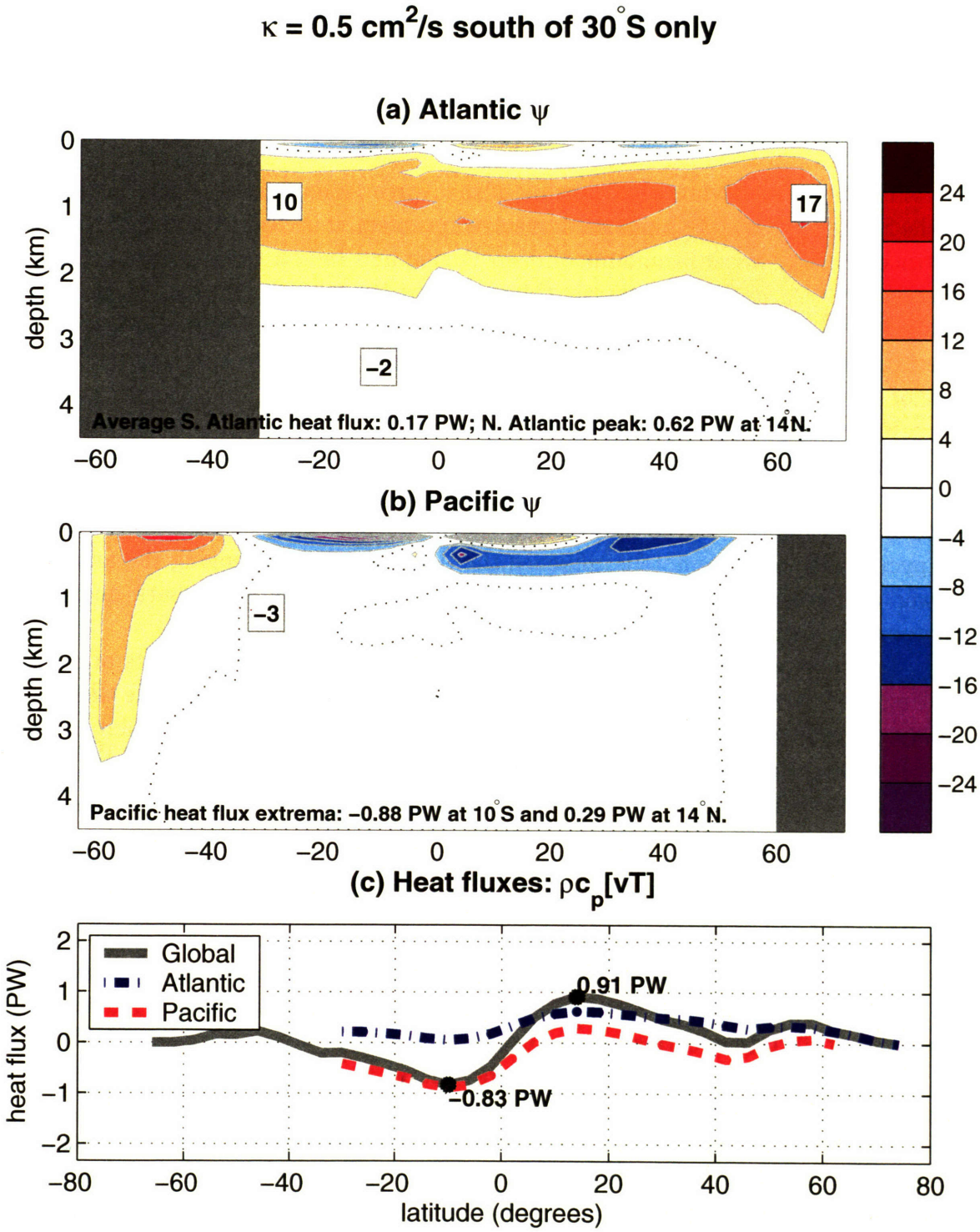

Figure 4-10: As in figure 4-4, but for a run in which κ is $0.5\,\mathrm{cm^2 s^{-1}}$ south of 30°S only; elsewhere, it is $0.05\,\mathrm{cm^2 s^{-1}}$. (a) Meridional overturning in the Atlantic (Sv). (b) Meridional overturning in the Pacific (north of 30°S) and in the entire Southern Ocean (south of 30°S). (c) Atlantic, Pacific, and global heat fluxes; extrema in global flux are noted.

the salient physics in the simplest possible representation. Nevertheless, the focus on the Atlantic has largely ignored the role of mixing deep waters to the surface in the Pacific and Indian Oceans. For example, the Toggweiler and Samuels (1995) idea is silent on the role of the Pacific. Were Southern Ocean winds exclusively responsible for forcing an overturning circulation in the North Atlantic, the Pacific could be left quiescent.

Though quantifying what portion of the North Atlantic Deep Water is upwelled in the Southern Ocean remains an unresolved problem, it is clear from the distribution of tracers that a notable amount of deep Pacific and Indian Ocean water originates from sinking in the North Atlantic (Mantyla and Reid, 1983; Broecker et al., 1998). While the response of the Atlantic circulation to the Southern Ocean wind stress has been extensively documented in the last decade, scant attention has been paid to the role of mixing in the Pacific and Indian Oceans.

Furue and Endoh (2005) and Tsujino et al. (2000) have recently addressed some issues related to Pacific upwelling, but their studies focus largely on the role of the layered circulation in the Pacific and the role of mixing between 1000 and 2000 meters depth. Furue and Endoh (2005) do note that changes in the Pacific diapycnal diffusivity remotely influence the Atlantic cell by changing the amount of power available to return deep waters to the surface; here we embark on a more thorough investigation.

In the experiments presented in this section, we examine the effects of concentrating mixing in either the tropical Atlantic or the tropical Pacific. While there is no reason to believe that such a separation occurs in the real world, the point of these simulations is to isolate the effects that mixing in a particular basin can have on the global circulation.

4.4.1 Conserving a tropical area-weighted κ

Mindful of the results presented in section 4.3, we confine our present analysis to mixing that occurs in the tropics. We take our control run to be the simulation in which a diffusivity of 0.5 cm^2/s is imposed in the tropics, with only 0.05 cm^2/s poleward of 30° latitude; this run was discussed in section 4.3 and presented in figure 4-8. We begin by supposing that all of the mixing that occurs in our control run is actually concentrated in the tropical Atlantic, as diagrammed in figure 4-11a.

We conserve the area-weighted average of κ, thus giving a locally enhanced value of mixing in the tropical Atlantic of 1.40 cm^2/s and 0.05 cm^2/s everywhere else, including the entire Pacific. The results of this experiment are presented in figure 4-12.

Note that a robust circulation is maintained in the Atlantic, modestly increasing from 20 Sv in the control to 22 Sv here, but the cell is entirely recirculated in the Atlantic alone. This result looks quite similar to that found in a single-hemisphere model, such as that used by Scott and Marotzke (2002). Here deep water is formed

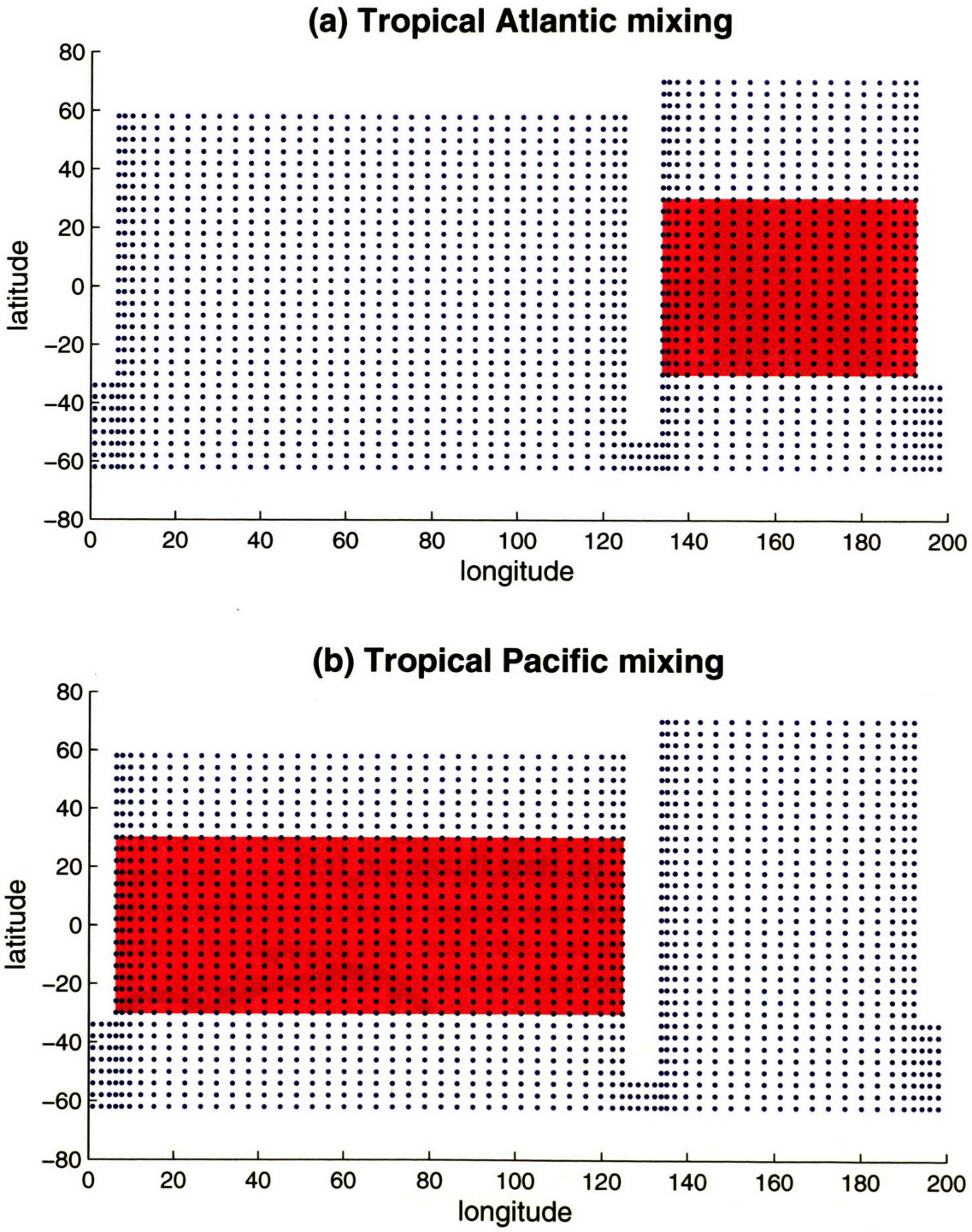

Figure 4-11: A map of where mixing is concentrated in the runs presented in this section. When mixing is high in the tropical Atlantic, values are elevated in the orange box shown in panel (a). When mixing is high in the tropical Pacific, values are elevated in the orange box shown in panel (b). Elsewhere, a pelagic value of 0.05 cm^2/s is applied.

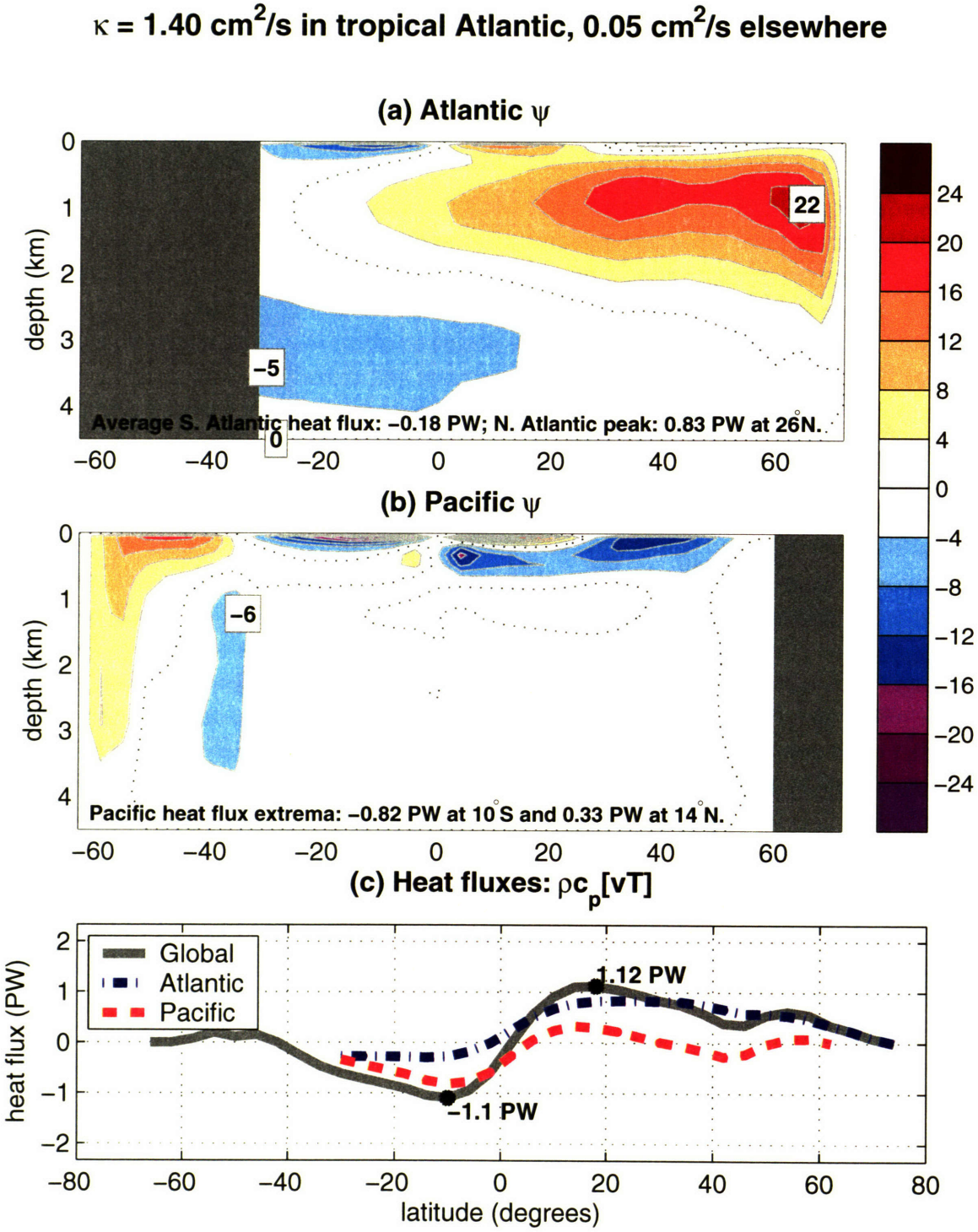

Figure 4-12: As in figure 4-8, but for a run in which κ is concentrated in the tropical Atlantic. The area-weighted average is conserved, so κ is $1.40\,\mathrm{cm^2 s^{-1}}$ equatorward of 30° in the Atlantic; elsewhere, it is $0.05\,\mathrm{cm^2 s^{-1}}$. (a) Meridional overturning in the Atlantic (Sv). (b) Meridional overturning in the Pacific (north of 30°S) and in the entire Southern Ocean (south of 30°S). (c) Atlantic, Pacific, and global heat fluxes.

at high latitudes and is upwelled by low latitude mixing. Interestingly the global heat flux seems little affected by this change; though the poleward heat flux in the South Pacific has decreased with the weakened deep circulation there, this is offset by a reversal in the sign of the South Atlantic flux. While the South Atlantic is unique among ocean basins in that it transports heat equatorward, here there is no longer any mid-level inflow of waters from the Southern Ocean or Pacific.

The global circulation produced by such a simulation is clearly unrealistic, as tracers indicate North Atlantic Deep Water travels into the Pacific (Mantyla and Reid, 1983; Broecker et al., 1998), and techniques that estimate the oceans' heat transport without explicit knowledge of the oceans' circulation show an equatorward flux in the South Atlantic (Trenberth and Caron, 2001). However, this simulation does illustrate that upwelling in the Atlantic affects only a local component of the circulation. For example, the deep Pacific is quiescent here, as it is in cases with uniformly weak diffusivity. (Compare with figure 4-4b, where the diffusivity was 0.1 cm^2/s everywhere, which is twice the value used in the Pacific here.)

By contrast, when mixing is concentrated in the tropical Pacific, as in figure 4-11b, the global circulation retains a shape similar to the control run. Though the circulation in the South Pacific is slightly higher owing to the locally enhanced mixing, what is most surprising is the resilience of the circulation in the Atlantic. The 19 Sv circulation is remarkably similar in magnitude to the 20 Sv in the control run. Little of this circulation is upwelled in the Atlantic (where mixing is now weak), and 12 Sv flow across 30°S at the southern end of the Atlantic. Interestingly, the equatorward heat flux is stronger here than in the control run, and is in closest agreement with estimates from observations (Peixoto and Oort, 1992; Trenberth and Caron, 2001).

In these simulations it appears that the amount of mixing, rather than the basin in which it occurs, governs the strength of the overturning in the Atlantic. If deep waters are upwelled, other parcels must sink somewhere to compensate. We force the sinking locations to be in the North Atlantic and Antarctic by our imposed surface density structure (recall figure 4-2), but if the real world is buoyantly forced in the same manner, these findings have interesting implications for the ability of remote mixing to affect the global circulation. The Atlantic clearly seems to be sensitive to upwelling in the Pacific and Indian Ocean basins.

4.4.2 Higher values of κ

In this section we continue our analysis of the role of mixing in different basins, but present additional experiments in which the value of the diffusion coefficient is further elevated. We will again concentrate mixing in the tropics of one basin at a time, but rather than conserving the area-weighted average of κ in the tropics alone, we conserve the global area-weighted average. For comparison, we take our control run to be a run with a uniform κ of 0.5 cm^2/s everywhere, as shown in figure 4-7. By concentrating all of this mixing in the tropics, we move mixing from regions of

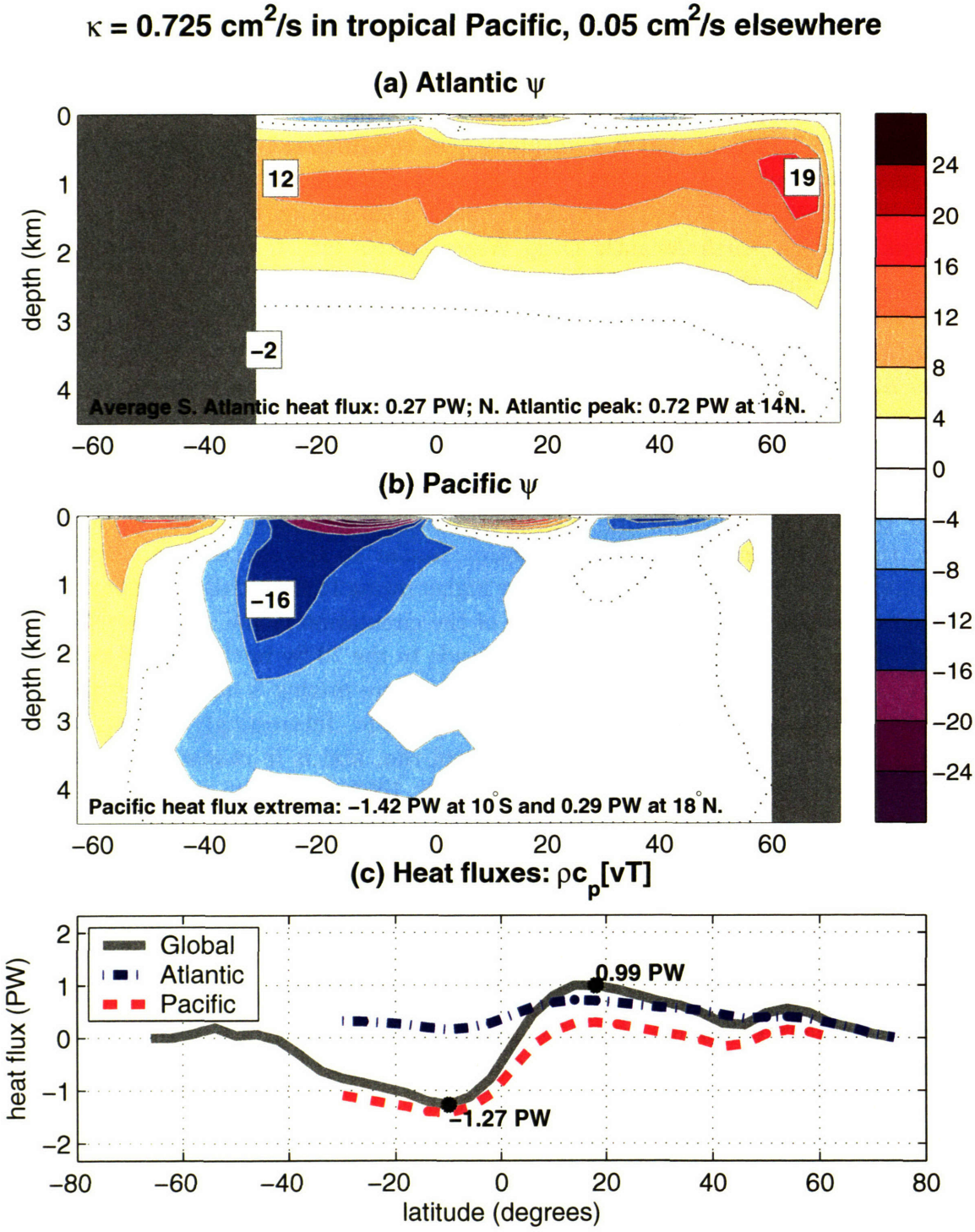

Figure 4-13: As in figure 4-7, but for a run in which κ is concentrated in the tropical Pacific. The area-weighted average is conserved, so κ is $0.725\,\mathrm{cm^2 s^{-1}}$ equatorward of 30° in the Pacific; elsewhere, it is $0.05\,\mathrm{cm^2 s^{-1}}$. (a) Meridional overturning in the Atlantic (Sv). (b) Meridional overturning in the Pacific (north of 30°S) and in the entire Southern Ocean (south of 30°S). (c) Atlantic, Pacific, and global heat fluxes.

the globe where mixing matters little to a region in which the overturning circulation is highly sensitive to the magnitude of κ (Bugnion, 2001). By comparing these runs with those presented in the last subsection, we will see how an increase in tropical mixing in either the Atlantic or the Pacific can affect the global circulation.

We begin by concentrating mixing in the tropical Atlantic, as in figure 4-11a. Conserving the globally area-weighted average of κ from the control run (figure 4-7) produces a value of 2.37 cm^2/s in the tropical Atlantic, again leaving a pelagic value of 0.05 cm^2/s for numeric stability elsewhere. The results of this experiment are presented in figure 4-14.

The circulation in the Atlantic has intensified with the elevated mixing. (Compare this with the earlier simulation in which mixing was also isolated in the tropical Atlantic; see figure 4-12.) This is a direct consequence of the enhanced upwelling in the low latitudes of the Atlantic; the sinking must increase to replenish the recirculation in the tropics. Again, however, note that the deep Pacific is unaffected by the enhanced mixing in the Atlantic. The global heat flux has increased over the control run (figure 4-7) in the North Atlantic owing to the stronger circulation, but the heat flux in the Southern Hemisphere remains nearly constant. Though the South Pacific is transporting nearly 0.5 PW less heat than in the control run, the reversal of the South Atlantic heat flux compensates.

When mixing is concentrated in the tropical Pacific, κ is 1.21 cm^2/s equatorward of 30° there, and 0.05 cm^2/s everywhere else in the globe. Note that both the local upwelling in the Pacific and the sinking in the North Atlantic respond to the higher Pacific mixing. The Residual Atlantic, taken to be the amount upwelled locally, is just 7 Sv, as it was in the last subsection (figure 4-13a), which is not surprising given the weak mixing throughout the Atlantic.

What is remarkable is that the maximum in the North Atlantic responds directly to elevated mixing in the tropical Pacific. The circulation is stronger still if mixing in the Pacific is pushed higher. In figure 4-16, results from a simulation in which tropical Pacific mixing is set to 2 cm^2/s are presented. The heat fluxes increase everywhere with higher Pacific mixing, and the South Atlantic heat flux produces an equatorward flow of heat at nearly 0.5 PW (this is not outside the range of estimates in the real ocean [e.g., Peixoto and Oort, 1992]).

Clearly mixing in the tropical Pacific can play a strong role in the global ocean circulation. Not only is there enhancement of the upwelling in the South Pacific, but the sinking in the North Atlantic is remotely forced as well. It seems not to matter where upwelling occurs (be it locally in the Atlantic or remotely in the Pacific). The most realistic heat flux in the South Atlantic was produced in the simulations forced with isolated Pacific mixing. This has a number of implications for mixing induced by tropical cyclones. About 85% of the tropical cyclones that form globally occur in the Pacific and Indian Oceans; the North Atlantic is highly variable, but mostly because it has such a small share of the global total. If the cumulative mixing from tropical cyclones, most of which are located in the Pacific and Indian Oceans, was

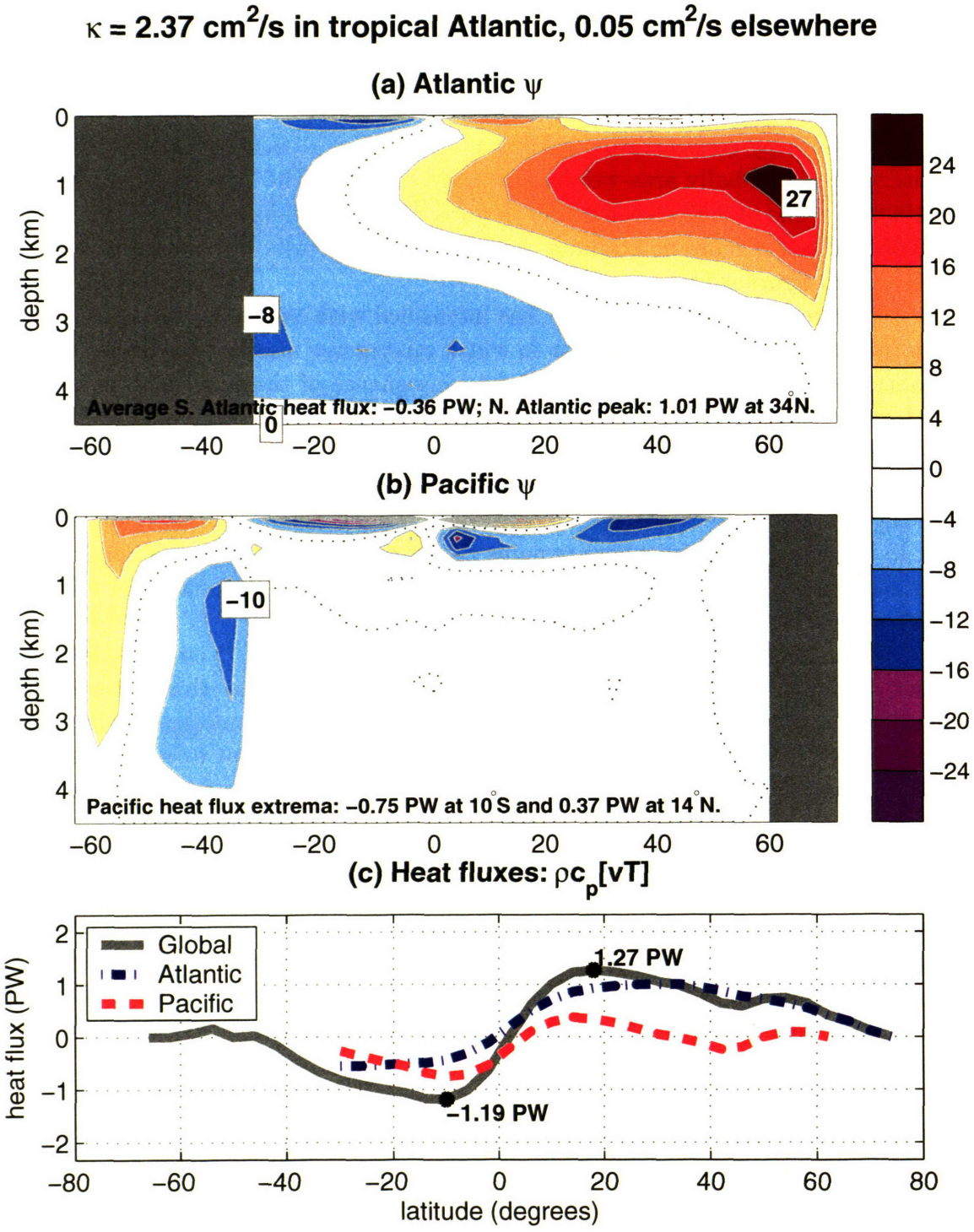

Figure 4-14: As in figure 4-7, but for a run in which κ is concentrated in the tropical Atlantic. The area-weighted average is conserved, so κ is $2.37\,\mathrm{cm^2 s^{-1}}$ equatorward of 30° in the Atlantic; elsewhere, it is $0.05\,\mathrm{cm^2 s^{-1}}$. (a) Meridional overturning in the Atlantic (Sv). (b) Meridional overturning in the Pacific (north of 30°S) and in the entire Southern Ocean (south of 30°S). (c) Atlantic, Pacific, and global heat fluxes.

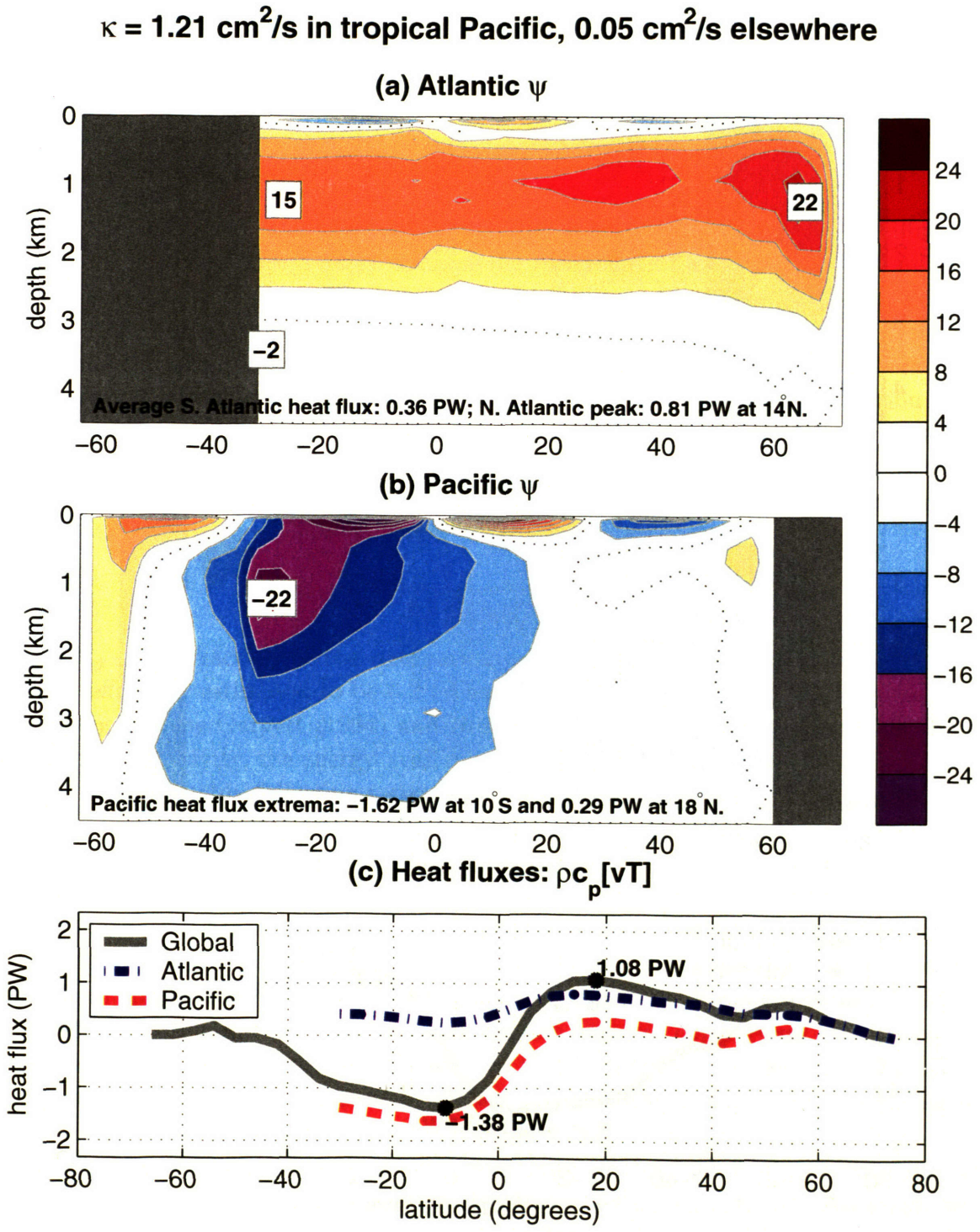

Figure 4-15: As in figure 4-8, but for a run in which κ is concentrated in the tropical Pacific. The area-weighted average is conserved, so κ is $1.21\,\mathrm{cm^2 s^{-1}}$ equatorward of 30° in the Pacific; elsewhere, it is $0.05\,\mathrm{cm^2 s^{-1}}$. (a) Meridional overturning in the Atlantic (Sv). (b) Meridional overturning in the Pacific (north of 30°S) and in the entire Southern Ocean (south of 30°S). (c) Atlantic, Pacific, and global heat fluxes.

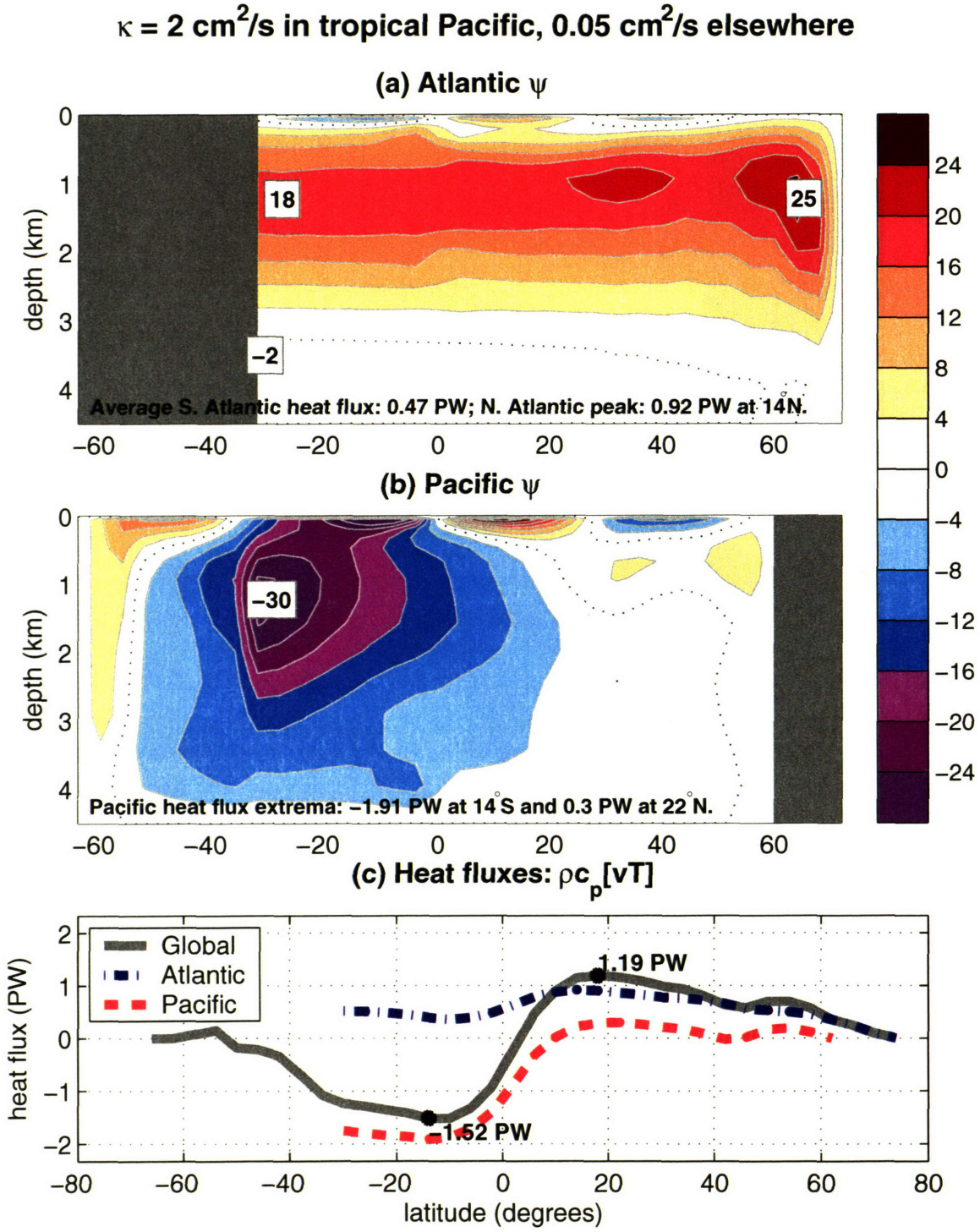

Figure 4-16: As in figure 4-8, but for a run in which κ is concentrated in the tropical Pacific. The mixing is elevated to $2\,\mathrm{cm^2 s^{-1}}$ equatorward of 30° in the Pacific; elsewhere, it is $0.05\,\mathrm{cm^2 s^{-1}}$. (a) Meridional overturning in the Atlantic (Sv). (b) Meridional overturning in the Pacific (north of 30°S) and in the entire Southern Ocean (south of 30°S). (c) Atlantic, Pacific, and global heat fluxes.

different in a past climate, the global circulation could have responded. Of course, this requires a sensitivity to mixing in the upper most ocean rather than throughout the depth column. We take up this issue in the next section.

4.5 Vertical dependence

Observations suggest that the use of a spatially and vertically invariant diffusion coefficient is an inaccurate description of the complexities and variability of mixing (contrast spatially uniform diffusivities with the findings of Ledwell et al., 1993; Polzin et al., 1997; and Ledwell et al., 2000). More physically based parameterizations of diapycnal diffusivity can be formulated in terms of the turbulent dissipation rate, ε (Nilsson et al., 2003). In these formulations, diffusivity is related to dissipation and the buoyancy frequency (Osborne, 1980; Gargett, 1984). Wunsch and Ferrari (2004) note in their review that much of the turbulent kinetic energy is dissipated by viscous friction, but a fraction, Γ, is used to vertically mix density and raise the potential energy; the relationship between κ and dissipation, ε, is:

$$\varepsilon_p = \Gamma\varepsilon = \kappa N^2, \tag{4.3}$$

where ε_p is the fraction of the dissipation available to mix the fluid, and Γ is the mixing efficiency estimated to be 0.2 (Wunsch and Ferrari, 2004). Parameterizations of mixing used by Gargett (1984) and Nilsson et al. (2003) assume that rather than a constant diffusivity, the energy available for mixing should be fixed.

Profiles roughly following a stratification dependence have been used since the work of Bryan and Lewis (1979). In their formulation, the values of κ are specified rather than an interactive function of stratification, but the imposed diffusivities rise an order of magnitude from the pycnocline to the deep, comparatively unstratified ocean. Scott and Marotzke (2002) have noted that enhanced deep mixing can drive a stronger abyssal circulation, but that the heat flux is not affected by mixing below the thermocline; this point has been illustrated nicely by Boccaletti et al. (2005). Bugnion (2001) found that the strength of the Atlantic overturning circulation is most sensitive to values of the diffusivity in the deep tropics in the top 500 meters (cf. figures 3.3 and 3.9 of Bugnion, 2001). At these depths, the greatest stratification and density gradients in the tropical ocean are found.

In this section we investigate the sensitivity of the heat flux and overturning strength to elevated mixing at various depths in the ocean column. Although we impose the diffusion coefficient here, its value will be different at different depths. We shall investigate interactive mixing parameterizations, like those discussed above, in Chapter 5.

We begin by reviewing two simulations in which κ is assigned a uniform value, both horizontally and vertically. The results from the experiment in which κ equals 0.3 cm^2/s are shown in figure 4-17, and the results when κ equals 1.5 cm^2/s are

presented in figure 4-18. As expected, the meridional overturning circulation and heat fluxes scale up with the increase in diapycnal diffusion. In this section, our goal is to identify the levels at which elevated mixing is most important. We consider the questions of sensitivity of the heat fluxes and of the overturning circulation to higher mixing separately, as there is growing evidence that these are different issues (Cummins et al., 1990; Scott and Marotzke, 2002; Boccaletti et al., 2005).

4.5.1 Elevating mixing from the top down

In this section, we examine the response to increasing the diffusion coefficient one model level at a time. In the first simulation, the vertical profile is uniformly 0.3 cm^2/s. We begin to test the influence of upper ocean mixing by elevating this to 1.5 cm^2/s, one level at a time. That is, the deep ocean will maintain a weak abyssal mixing of 0.3 cm^2/s, while consecutive runs increase the depth to which the elevated κ penetrates. The real ocean, of course, does not behave this way, and there is no basis for believing that an upper ocean source of mixing could penetrate through the entire depth of the strongly stratified thermocline. The point of these experiments is to identify the depth at which the heat flux and meridional overturning circulation are most sensitive to elevated upper ocean mixing, regardless of whether or not a real mechanism exists to diffuse heat in this manner. For the more extreme of these simulations, where mixing is elevated through the entire thermocline but not at depth, a real mechanism almost certainly does not exist.

Figure 4-19 summarizes the results in the Atlantic. In panel (a), the maximum value of ψ in the North Atlantic overturning circulation is plotted for each of ten runs. Each point corresponds to a run in which κ is increased from 0.3 to 1.5 cm^2/s *at and above* the depth at which it is plotted on the y-axis; κ remains 0.3 cm^2/s everywhere below. For example, at the top most point, plotted at a depth of 50 meters, κ has a value of 1.5 cm^2/s, but 0.3 cm^2/s everywhere deeper. The second point, at a depth of 85 meters is from a run in which κ is 1.5 cm^2/s at and above 85 m.

The addition of this mixing in the top most level has no effect on the abyssal circulation; the maximum overturning remains 19 Sv, just as in the case with uniform mixing of 0.3 cm^2/s, as shown in figure 4-17. Indeed, extending the depth of this elevated mixing down into the upper thermocline has a minimal impact on the strength of the deep circulation; the abyssal circulation remains less than 20 Sv even when κ increases down to 260 meters depth (the fourth model level, counting down from the top). This underscores the point that in order to affect the abyssal circulation, upper ocean mixing must be able to pass down to deeper levels. Bugnion (2001) also looked at the sensitivity of the overturning circulation to the depth at which mixing occurs, and found a strong sensitivity to mixing in the upper 200 m of the ocean.

Below 300 meters, elevating mixing at greater depths continues to influence the abyssal circulation. Figure 4-19c shows the relative impact of additional mixing at each level. The magnitude of the gain in intensity rises when mixing is allowed

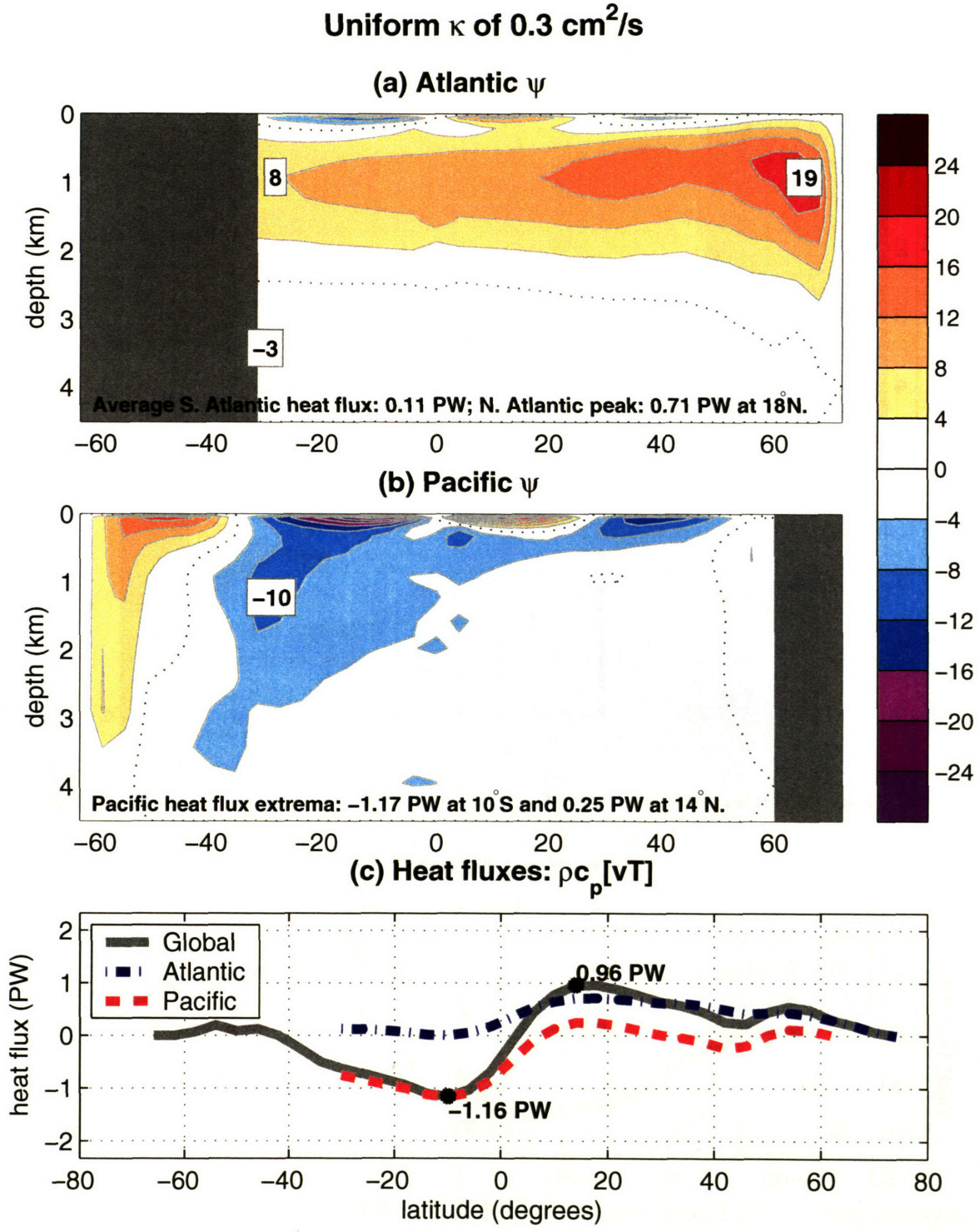

Figure 4-17: Overturning strength and heat fluxes when κ has a spatially uniform value of $0.3\,\mathrm{cm^2 s^{-1}}$. (a) Meridional overturning in the Atlantic (Sv). (b) Meridional overturning in the Pacific (north of 30°S) and in the entire Southern Ocean (south of 30°S). (c) Atlantic, Pacific, and global heat fluxes; extrema in global flux are noted.

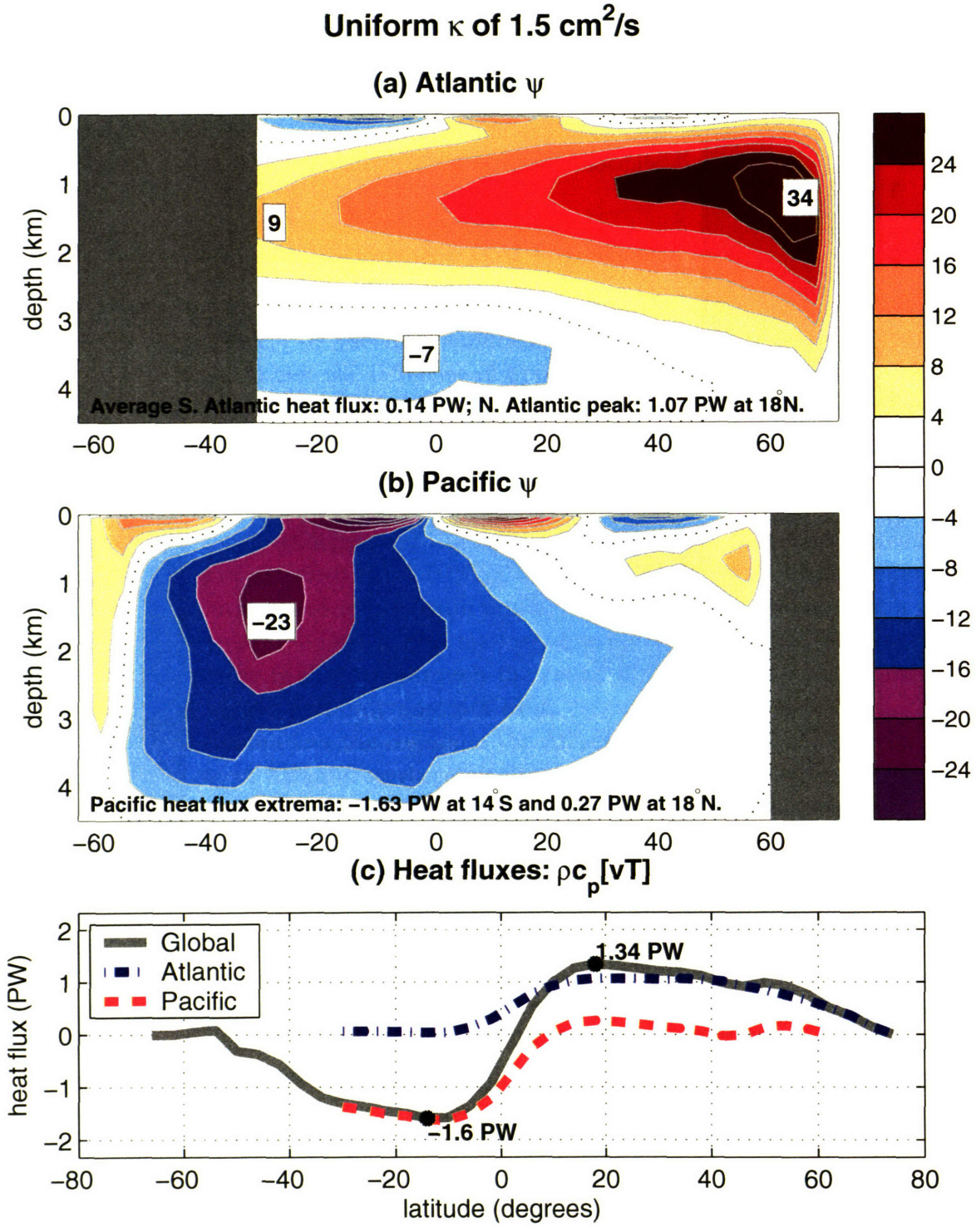

Figure 4-18: Overturning strength and heat fluxes when κ has a spatially uniform value of $1.5\,\mathrm{cm^2 s^{-1}}$. (a) Meridional overturning in the Atlantic (Sv). (b) Meridional overturning in the Pacific (north of 30°S) and in the entire Southern Ocean (south of 30°S). (c) Atlantic, Pacific, and global heat fluxes; extrema in global flux are noted.

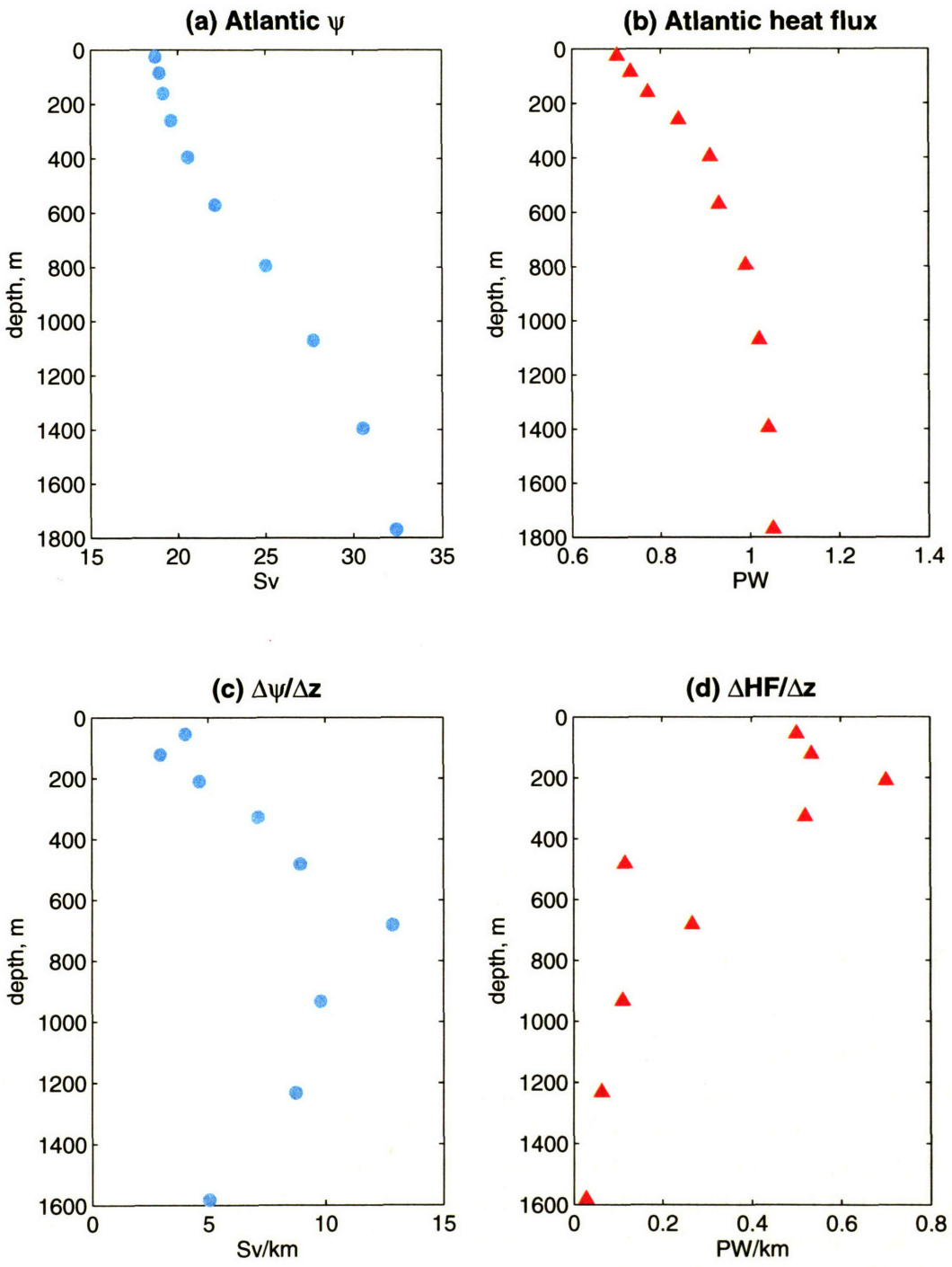

Figure 4-19: (a) Maximum ψ in North Atlantic from simulations in which κ was increased from 0.3 to $1.5\,\mathrm{cm^2 s^{-1}}$ at and above the depth shown on the y-axis (at all depths below the level on the y-axis, κ remains $0.3\,\mathrm{cm^2 s^{-1}}$. (b) Peak North Atlantic heat flux given by increasing κ from 0.3 to $1.5\,\mathrm{cm^2 s^{-1}}$ at and above the depth shown on the y-axis. (c) Finite-difference derivative of results in (a) with depth. (d) Finite-difference derivative of results in (b) with depth.

to penetrate an additional level until about 700 meters, roughly corresponding with the depth of the internal thermocline in the subtropics (Samelson and Vallis, 1997). Below this level, adding mixing continues to influence the intensity of the abyssal circulation, albeit at a weaker pace.

By contrast, upper ocean mixing need not penetrate deeply at all in order to affect the poleward flux of heat. Panel (b) shows the poleward heat flux associated with elevated upper ocean mixing. Panel (d) shows the relative impact on the heat flux of increasing mixing at each level. Note that the greatest gain comes from adding mixing in the top 400 meters. Adding mixing below this level has little additional impact, as seen by the small values in panel (d) below 400 m and by the vertical alignment of the points in the lower portion of panel (b). This point underscores the importance of upper ocean processes in affecting the poleward heat flux. The heat function discussed in Boccaletti et al. (2005) shows this too.

In addition to elevating the peak heat flux, thermocline mixing also increases the latitude range over which the oceans' heat flux is significant. In figure 4-20, profiles for the Atlantic, Pacific, and global totals are shown. Note that in the standard case, which has uniform mixing of 0.3 cm^2/s everywhere, the heat flux peaks around 18°N, and then begins a steady decline in the subtropics. By contrast, elevated thermocline mixing sustains a heat flux near the peak value to higher latitudes. This effect increases as mixing penetrates more deeply into the thermocline. (Contrast the poleward extent of the near-peak Atlantic heat flux when elevated mixing penetrates to a depth of 160 m with the poleward extent when elevated mixing penetrates to 570 m; there is a slight poleward shift.) In these runs, the elevated upper ocean mixing was imposed at all latitudes, but even when it is confined equatorward of 30°, the rise in subtropical fluxes persists (results of these experiments not shown).

4.5.2 Elevating mixing from the bottom up

In this section, our experiments follow the reverse logic of those in the previous one: what affect does elevating mixing from the bottom of the ocean up have on the circulations and heat flux? This question has little physical relevance, as it is difficult to imagine a source of abyssal mixing that would penetrate into the thermocline (though perhaps interaction with topographic features could affect lower thermocline mixing), but I again emphasize that this is a study of model sensitivity. In conjunction with the experiments in the previous subsection, the results of these tests will elucidate the depths at which enhanced mixing makes an appreciable difference to the poleward heat flux and overturning strength.

As before, the changes in the Atlantic overturning and heat flux are shown in figure 4-21, but here each point symbolizes a run in which mixing is elevated to 1.5 cm^2/s at the depth shown on the y-axis *and below*; above this depth, mixing remains 0.3 cm^2/s. Note that increasing mixing has a growing impact on the overturning circulation through the lower thermocline (the maximum gain per unit depth

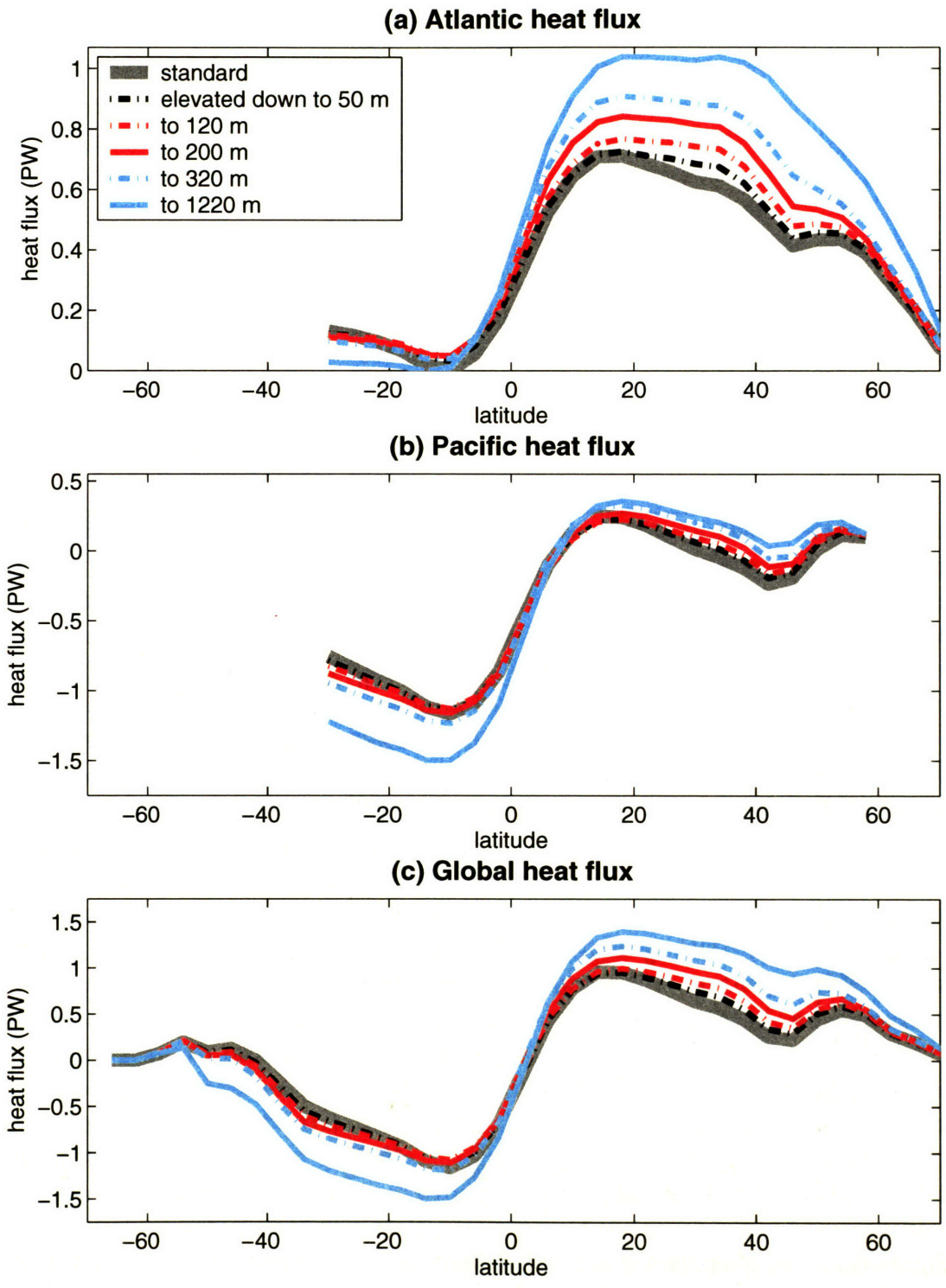

Figure 4-20: Heat fluxes in (a) the Atlantic, (b) the Pacific, and (c) globally from experiments in which elevated mixing was gradually lowered through the water column. The standard case (heavy gray line) has a uniform diffusivity of $0.3\,\mathrm{cm^2 s^{-1}}$, and the other nine cases have a diffusivity of $1.5\,\mathrm{cm^2 s^{-1}}$ down to the depth listed and $0.3\,\mathrm{cm^2 s^{-1}}$ below.

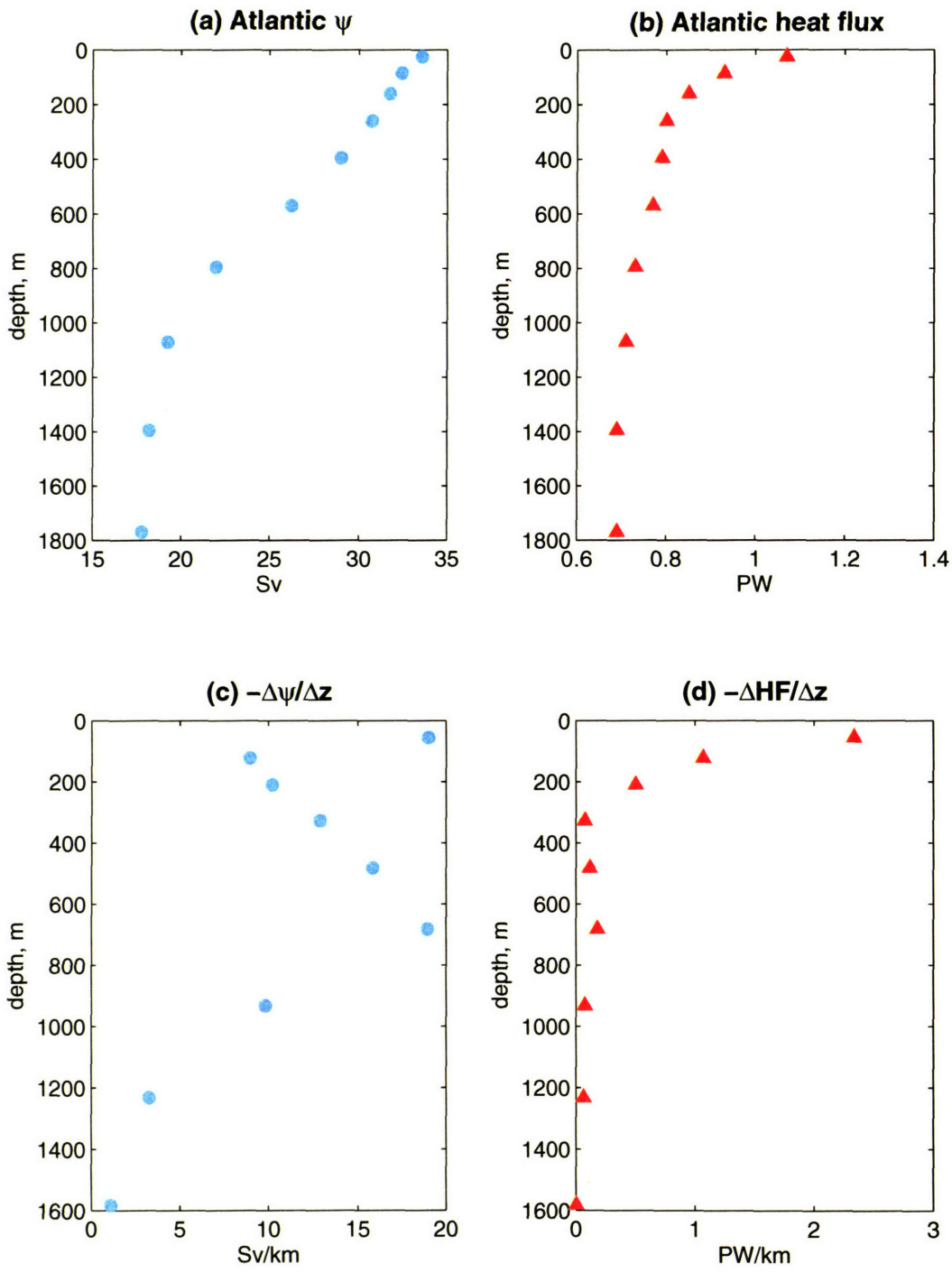

Figure 4-21: (a) Maximum ψ in North Atlantic from simulations in which κ was increased from 0.3 to $1.5\,\mathrm{cm^2 s^{-1}}$ at and below the depth shown on the y-axis (at all depths above the level on the y-axis, κ remains $0.3\,\mathrm{cm^2 s^{-1}}$. (b) Peak North Atlantic heat flux given by increasing κ from 0.3 to $1.5\,\mathrm{cm^2 s^{-1}}$ at and below the depth shown on the y-axis. (c) Finite-difference derivative of results in (a) with depth. (d) Finite-difference derivative of results in (b) with depth.

occurs at 700 m, as seen in figure 4-21c), and the increases continue as mixing is pushed higher into the stratified upper ocean, albeit at a smaller pace.

But the heat flux does not respond until mixing reaches the uppermost 200 m of the ocean (see figure 4-21d). The largest gain comes when the topmost layer is made more diffusive. This is also clear from the results presented in figure 4-22. This is not to suggest that the upper 50 m are important in isolation; we saw in the previous subsection that elevated mixing at this top level alone made little difference. Rather, there must be a connection between the surface mixed-layer and the thermocline below, an argument that dates to Jeffreys (1925). Once there is a mechanism to mix heat down from the top of the ocean, upper thermocline mixing can raise the heat flux.

4.6 Wind forcing

Toggweiler and Samuels (1995) hypothesized that upwelling of North Atlantic Deep Water in the Southern Ocean controls the intensity of the overturning circulation in the Atlantic. Given the zonally unobstructed fetch of ocean south of Cape Horn, strong westerlies race around the latitudes surrounding the Drake Passage. Ekman transport is convergent near 40°S and divergent south of 50°S; this pattern induces the Deacon cell. Though eddy transports cancel much of the Deacon cell, they do not suppress it entirely (Danabasoglu and McWilliams, 1995).

Although this concept is silent on the role of the Pacific and Indian Oceans in the global circulation, it has attracted considerable attention in the last decade. Model sensitivity to the strength of Southern Ocean wind stress is strong when the surface density is constrained by rapid restoration, as it was in Toggweiler and Samuels (1995) original study, but the sensitivity is abated in the presence of less restrictive boundary conditions and in coupled models (Rahmstorf and England, 1997; Bugnion, 2001).

Samelson and Vallis (1997) and Vallis (2000) argue that, in the presence of weak diffusion, wind alters the classic Welander (1986) scaling behavior of the overturning circulation. The two processes also commingle to produce a ventilated thermocline in the upper subtropical ocean (Luyten et al., 1983) with a diffusively driven internal thermocline beneath it, affecting the stratification of the upper ocean (Samelson and Vallis, 1997).

Clearly the wind stress exerts a strong influence on the circulation in the fluid beneath. In this section, we begin an investigation of the sensitivity of our results to changes in the amplitude of the wind forcing; the sensitivity will be particularly strong in these simulations, as densities are held nearly fixed. This section lies largely beyond the original scope of my thesis, and it is even tangential to the issues principally raised in the rest of this chapter. However, given the excitement the Toggweiler and Samuels (1995) mechanism generated in the oceanography community, it is worth investigating what role the wind plays in our own simulations. Given the complexity

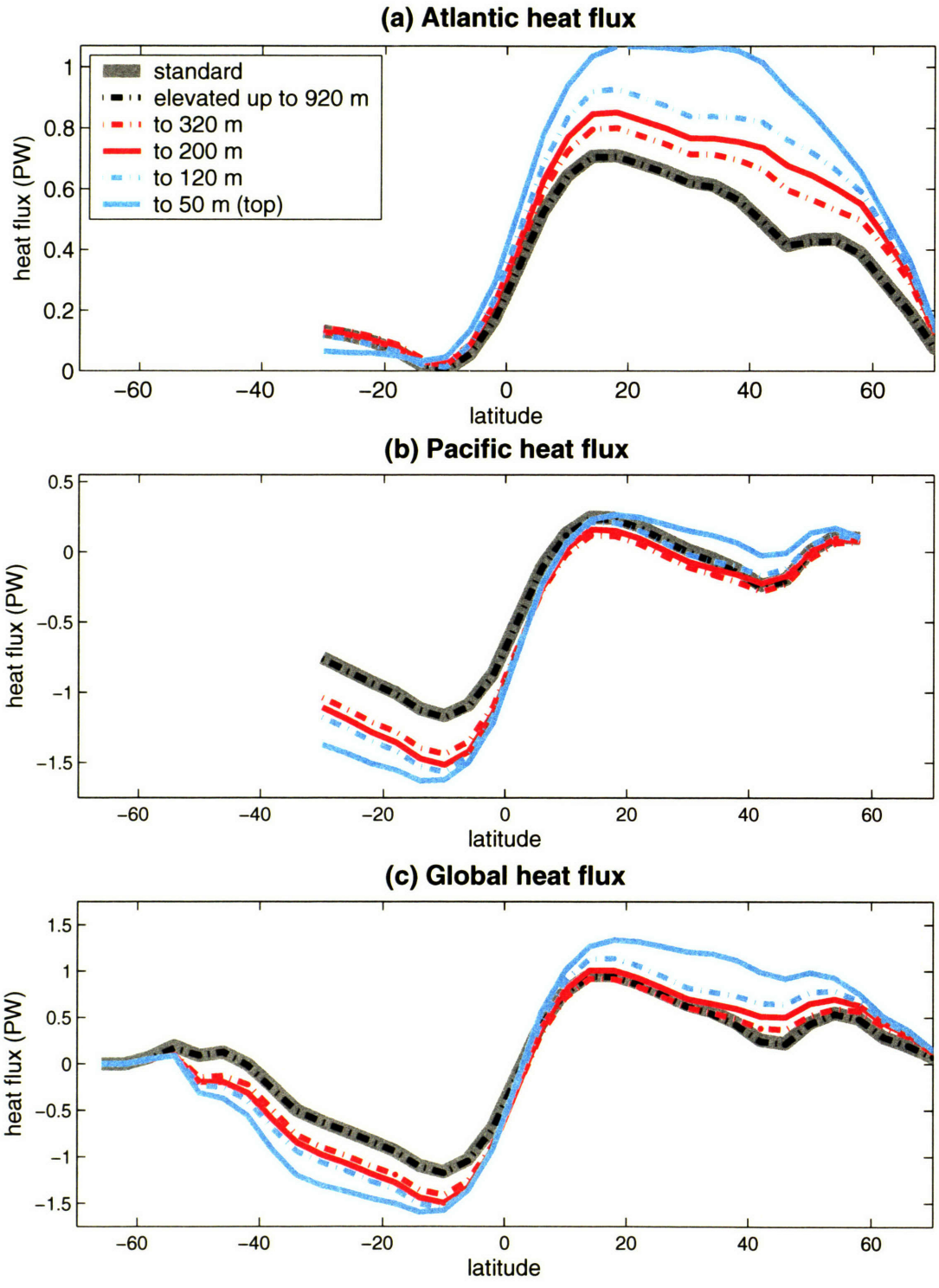

Figure 4-22: Heat fluxes in (a) the Atlantic, (b) the Pacific, and (c) globally from experiments in which elevated mixing was gradually raised through the water column. The standard case (heavy gray line) has a uniform diffusivity of $0.3\,\mathrm{cm^2 s^{-1}}$, and the other nine cases have a diffusivity of $1.5\,\mathrm{cm^2 s^{-1}}$ from the ocean bottom up to the depth listed and $0.3\,\mathrm{cm^2 s^{-1}}$ above.

of the interaction, and the difficulty of separating the effect of winds and mixing, this work provides only a cursory overview of the problem.

In this section, I present the results from simulations identical to those discussed earlier (again forced with uniform, static values of κ and rapid restoration of surface density), except that the amplitude of the wind forcing shown in figure 4-3 has been varied. We shall consider three cases: one in which the wind profile is half as strong, one in which it is twice as strong, and one in which the wind is absent all together.

4.6.1 Weak wind stress

First, let us examine the response to a weaker wind stress. Figure 4-23 shows the response to the weak amplitude wind stress (half the magnitude shown in figure 4-3) when κ is 0.1 cm^2/s; this may be compared to the standard case shown in figure 4-4 in section 4.2. Note that the circulation is weaker throughout the Atlantic, and in the surface Ekman cells everywhere. The latter is a direct result of the lower wind stress, as Ekman transport has been reduced in the surface gyre circulations. The deep circulation in the Pacific is largely unaffected, with weak upwelling of abyssal waters occurring in low latitudes. The heat fluxes are considerably diminished, as the transport by the surface Ekman cells dominates the ocean heat flux (Haidvogel and Bryan, 1992); this underscores the importance of processes in the upper ocean to the oceans' poleward heat transport.

The portion of the North Atlantic circulation that upwells in low latitudes of the Atlantic is not affected by the diminished winds; the difference between $\psi_{\max}$ in the North Atlantic and the outflow across 30°S remains about 7 Sv. This is not surprising, as mixing dominates the upwelling of abyssal parcels in the tropics, but it does suggest that the magnitude of the wind stress in low latitudes has little direct impact on amount of abyssal upwelling that occurs here.

In figure 4-24, the response to the weak wind is shown when the diapycnal diffusivity is a larger 0.9 cm^2/s; this should be compared to figure 4-5, which shows the results with the standard wind stress and a uniform value of κ of 0.9 cm^2/s. With the weaker winds, the deep circulation is slightly weaker in the North Atlantic, and the amount that flows into the southern boundary of the Atlantic has decreased by a similar amount (about 2 Sv). Otherwise, however, the abyssal circulations look remarkably similar, suggesting only a weak role for the intensity of the wind. Note that the heat fluxes diminish significantly when the wind stress decreases, emphasizing the importance of near-surface transport to the oceans' total heat flux.

The maximum strength of the overturning circulation scales with the diffusion coefficient as shown in figure 4-25. As in figure 4-6, the offset in equation (estimate), ψ_0, is zero for the solid, colored lines and found for the least squares solution, which is shown in dashed gray. The Atlantic scales more weakly than predicted by Welander (1986), which was also noted by Dalan (2003), who studied the response in a coupled model with idealized global geometry. The Pacific scales more weakly than Welander

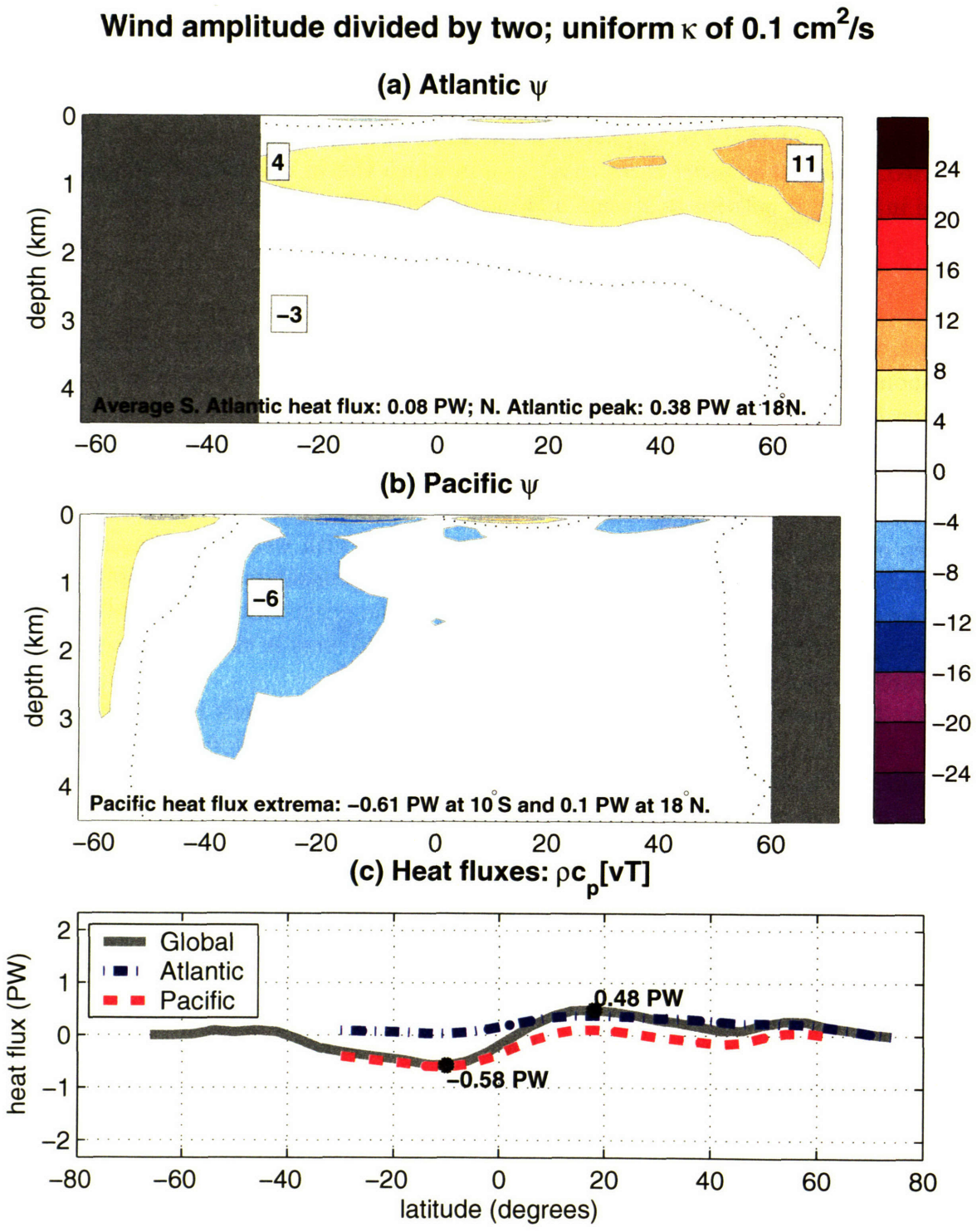

Figure 4-23: As in figure 4-4, but for a spatially uniform κ of 0.1 $cm^2 s^{-1}$ using a wind profile with half the surface stress. (a) Meridional overturning in the Atlantic (Sv). (b) Meridional overturning in the Pacific (north of 30°S) and in the entire Southern Ocean (south of 30°S). (c) Atlantic, Pacific, and global heat fluxes; extrema in global flux are noted.

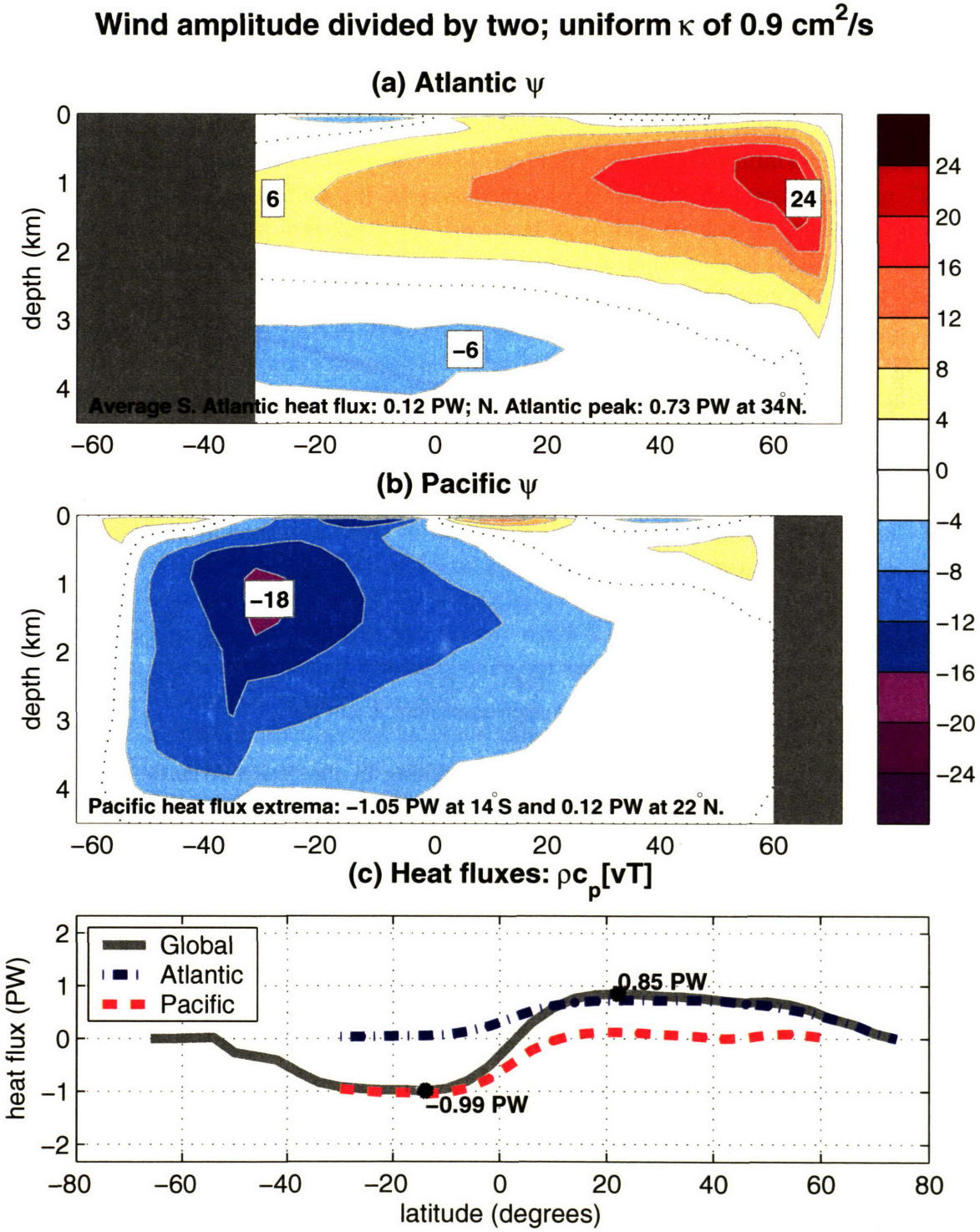

Figure 4-24: As in figure 4-4, but for a spatially uniform κ of $0.9\,\mathrm{cm^2 s^{-1}}$ using a wind profile with half the surface stress. (a) Meridional overturning in the Atlantic (Sv). (b) Meridional overturning in the Pacific (north of 30°S) and in the entire Southern Ocean (south of 30°S). (c) Atlantic, Pacific, and global heat fluxes; extrema in global flux are noted.

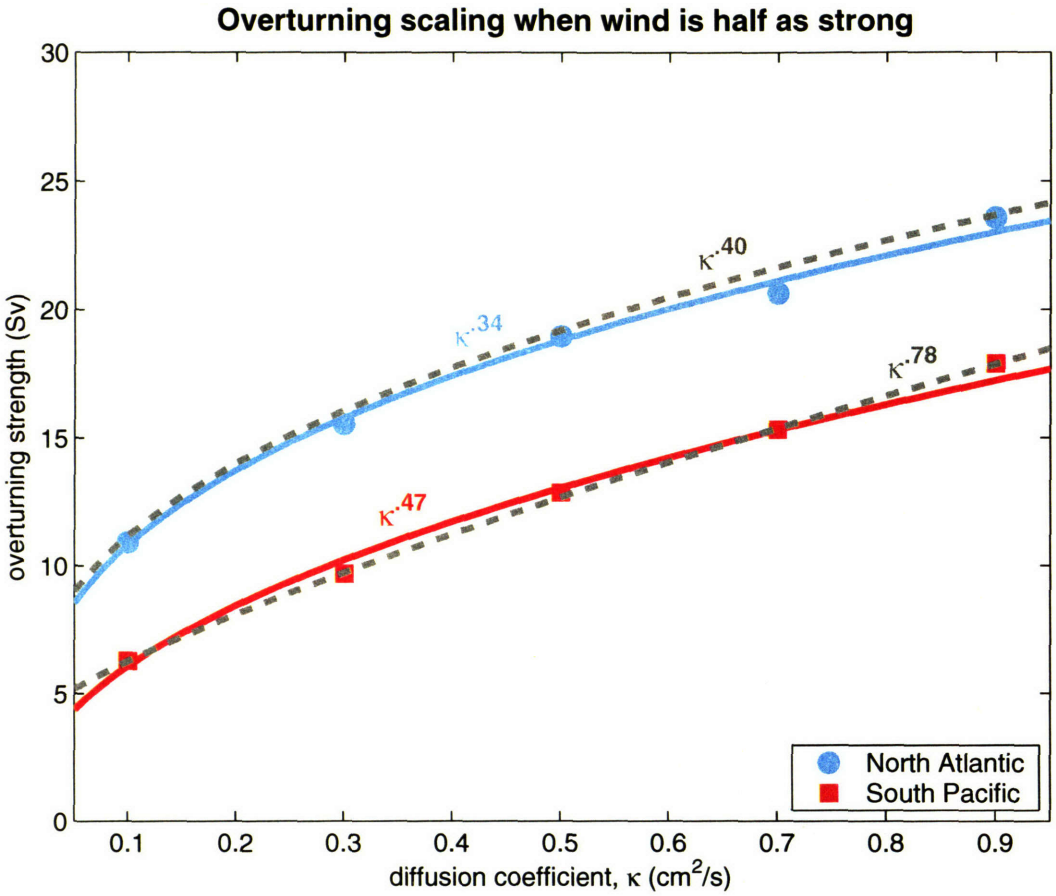

Figure 4-25: Maximum strength of the overturning in the North Atlantic (blue circles) and South Pacific (orange squares) across a decade of variation in κ, the diapycnal diffusion coefficient. The best fit curve estimated by equation (4.2) is shown running through the data with ψ_0 zero (solid, colored) and ψ_0 chosen so that the sum of the least squares is a minimum (dashed, gray).

when forced to pass through zero, but when the offset is chosen to minimize the mean-squares misfit, the behavior scales with a stronger power of κ.

4.6.2 Doubled wind stress

We now examine the response to a strong forcing by the wind. The wind stress imposed here is stronger than observations at all latitudes. The results from a simulation with weak diffusion and strong (doubled) wind stress are shown in figure 4-26; compare this with the results from the standard wind profile displayed in figure 4-4 and with the simulation using weak winds (see figure 4-23). With stronger wind forcing, the Atlantic circulation has increased substantially, and the portion upwelling in the tropical Atlantic has increased by a modest 2 Sv (from 7 Sv in figures 4-4 and 4-23 to approximately 9 Sv here). The wind has no effect on the abyssal circulation in

the Pacific; with weak diffusion it is nearly quiescent in all cases. The heat flux, by contrast, is strongly affected by the magnitude of the wind, as the surface Ekman transport changes directly with the magnitude of the wind.

When diffusion is stronger, the Atlantic circulation and heat transports in both basins increase; figure 4-27 shows the results from a simulation in which κ is 0.9 cm^2/s. Like the weak diffusion case, the portion of the North Atlantic circulation upwelling in the tropical Atlantic exhibits a modest increase with the stronger wind forcing. This suggests that Ekman upwelling along the equator, forced by a divergence in Ekman transport, is enhancing the strong mixing in tropical latitudes. The Residual Atlantic increases from 18 Sv when forced with a weak or standard wind stress to 21 Sv here. The abyssal Pacific circulation exhibits little change, though stronger surface cells penetrate more deeply into the ocean. The heat flux is strongly regulated by the intensity of the wind stress, confirming that processes in the upper ocean dominate this quantity (Haidvogel and Bryan, 1992; Boccaletti et al., 2005).

The scaling for these runs is shown in figure 4-28. Note the agreement between the scaling of the Pacific cell with the classic Welander (1986) dependence. Forcing the offset ψ_0 in equation (4.2) to be zero is also the least squares solution. The Atlantic scales quite weakly with κ when ψ_0 is forced to be zero, but it scales with the classic Welander scaling when ψ_0 is chosen to minimize the mean-squares misfit. This is interesting, as it suggests the strong wind forcing is responsible for a background circulation upon which a mixing-induced component, which scales according to Welander's relations, is superimposed.[7]

There is considerable spread in the scaling estimates seen in figures 4-6, 4-25, and 4-28. The Atlantic scales, on average, with the 0.47 power of κ when the offset is allowed to be nonzero. The Pacific cell, on average, scales with the 0.67 power of κ when the offset is allowed to be nonzero. This $\kappa^{1/2}$ dependence in the Atlantic and $\kappa^{2/3}$ dependence in the Pacific was also found by Dalan (2003).

4.6.3 No wind

Thus far, we have examined runs in which the surface density is rapidly restored. As noted, this allows for an arbitrarily large role for the wind forcing. If the wind is shut off in these simulations, the scaling with horizontally and vertically uniform diffusivities agrees with a $\kappa^{1/2}$ dependence in the Atlantic; these results are shown in figure 4-29. This is exactly the average value found in the earlier cases with wind forcing. The Pacific cell scales with a stronger power of κ regardless of the wind forcing. On average, it agrees well with the classic Welander scaling, though there is considerable spread.

[7]This is not exactly true, of course, as the system is not linear. Assuming ψ_0 takes a constant background value upon which a mixing-driven component can be superimposed is valid only if the system is linear. My point here is that assuming ψ_0 is nonzero is no worse than forcing it be zero, which is clearly not correct when wind forcing is present.

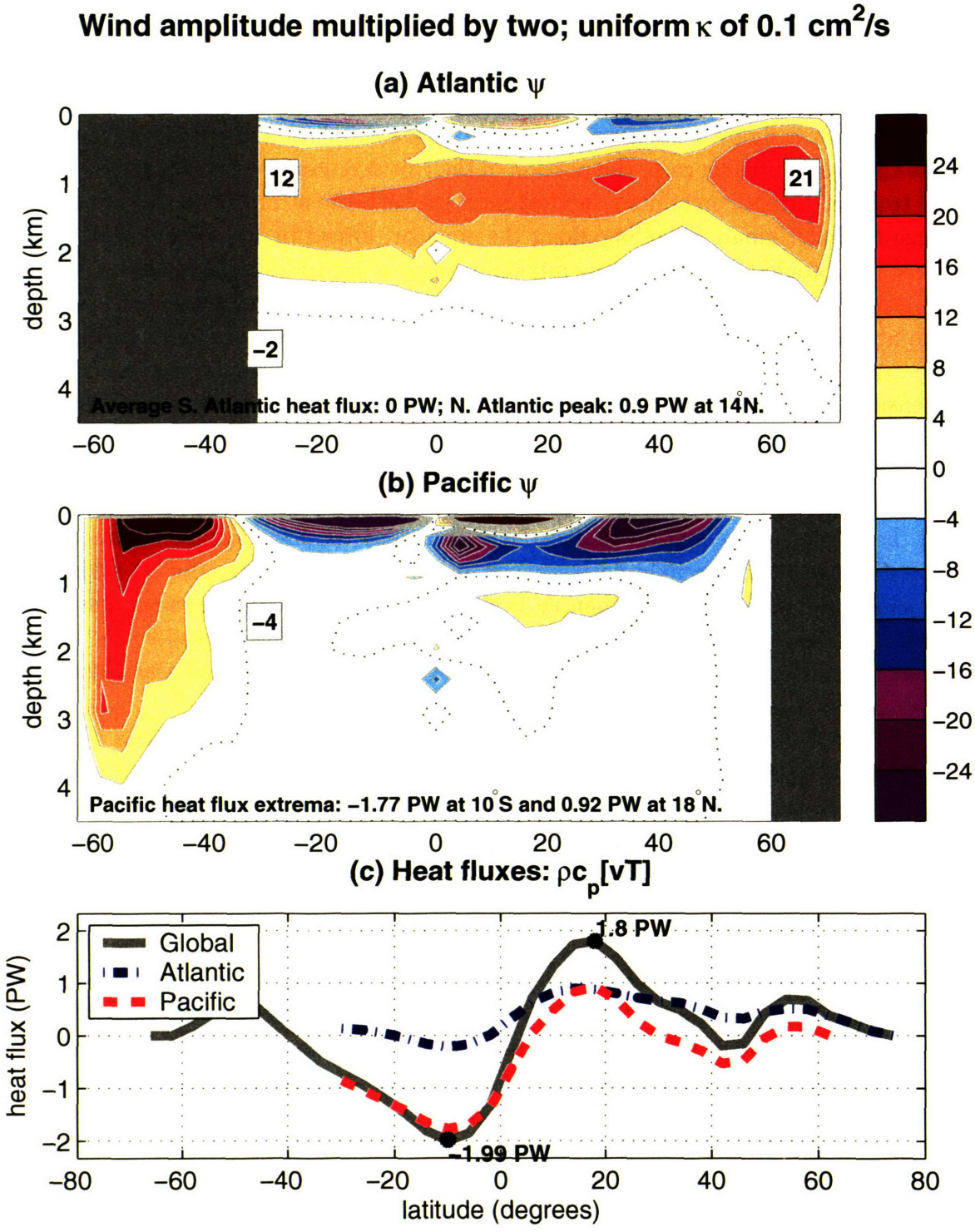

Figure 4-26: As in figure 4-4, but for a spatially uniform κ of 0.1 $cm^2 s^{-1}$ using a wind profile with twice the surface stress. (a) Meridional overturning in the Atlantic (Sv). (b) Meridional overturning in the Pacific (north of 30°S) and in the entire Southern Ocean (south of 30°S). (c) Atlantic, Pacific, and global heat fluxes; extrema in global flux are noted.

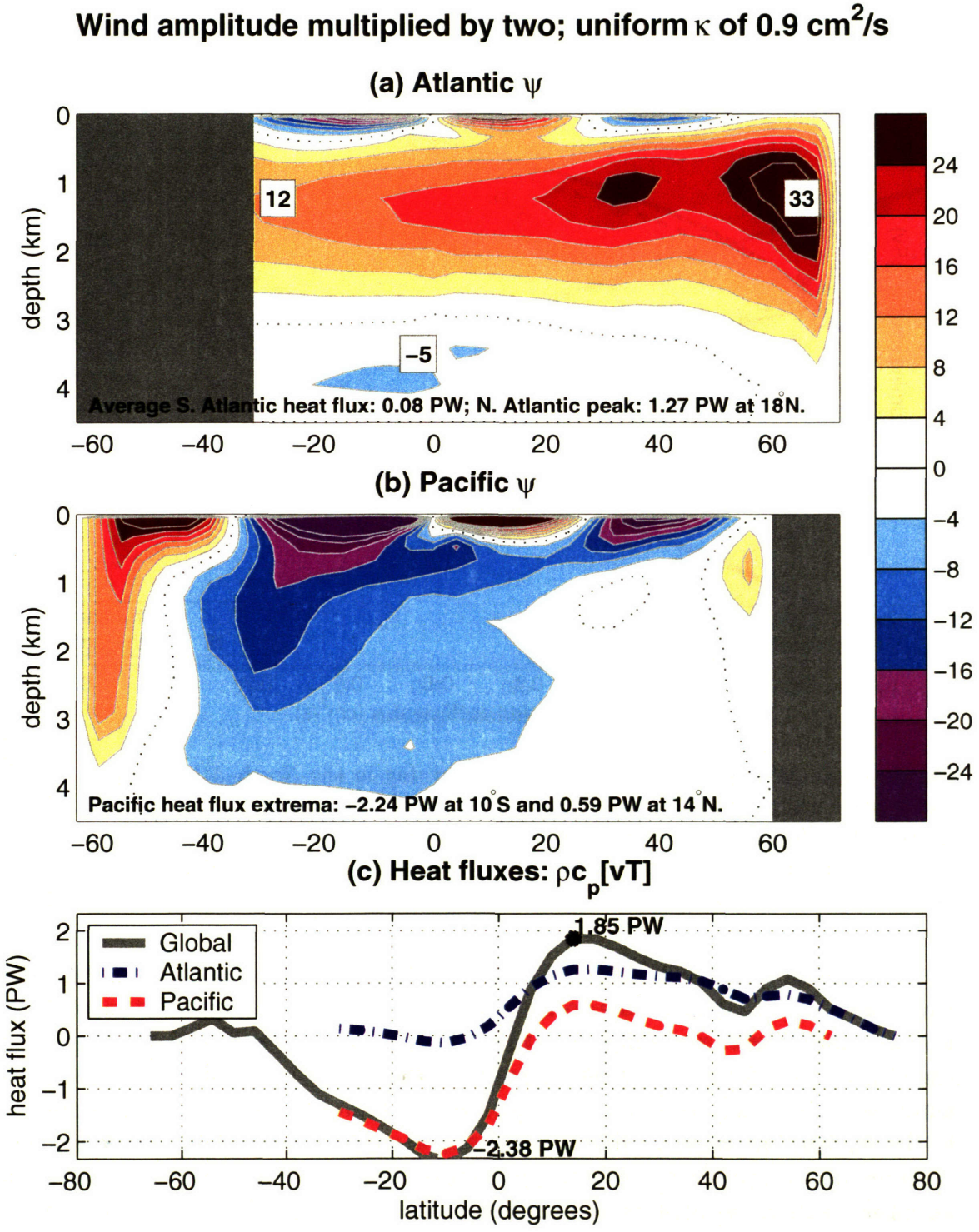

Figure 4-27: As in figure 4-4, but for a spatially uniform κ of 0.9 $cm^2 s^{-1}$ using a wind profile with twice the surface stress. (a) Meridional overturning in the Atlantic (Sv). (b) Meridional overturning in the Pacific (north of 30°S) and in the entire Southern Ocean (south of 30°S). (c) Atlantic, Pacific, and global heat fluxes; extrema in global flux are noted.

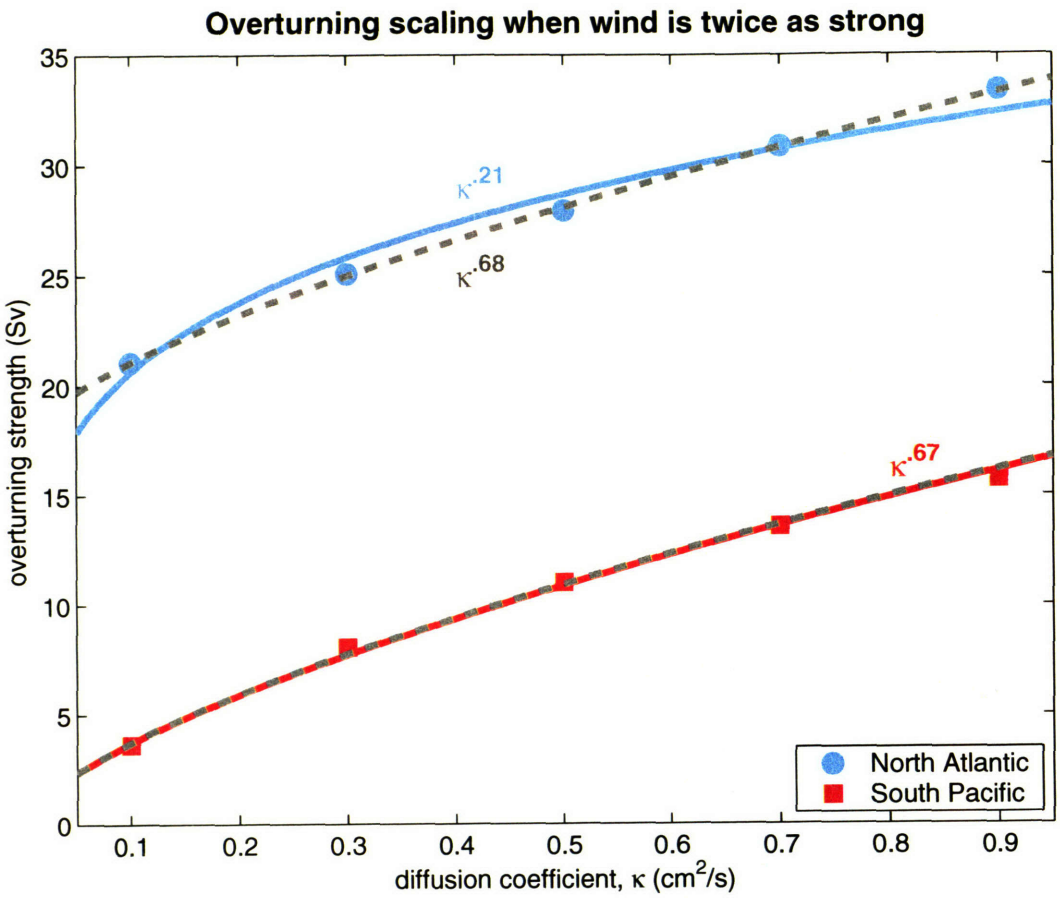

Figure 4-28: Maximum strength of the overturning in the North Atlantic (blue circles) and South Pacific (orange squares) across a decade of variation in κ, the diapycnal diffusion coefficient. The best fit curve estimated by equation (4.2) is shown running through the data with ψ_0 zero (solid, colored) and ψ_0 chosen so that the sum of the least squares is a minimum (dashed, gray).

Samelson and Vallis (1997) and Vallis (2000) argued that, in the presence of wind, the relevant length scale to be used in the advective-diffusive estimate of the horizontal temperature gradient is not that of the gyre, but the lateral distance across the sloping thermocline. This distance scales with the wind, and in the limit of no wind collapses back to the basin-wide gyre scale. Our results show considerable spread in the scaling, but there we find no evidence to suggest that the scaling depends on the presence of the wind. In fact, the average dependence on κ from the three sets of experiments with different wind forcings is the same as the dependence found in the case with no wind. Though there is considerable spread, the Atlantic overturning follows $\sim\kappa^{1/2}$ while the Pacific overturning scales with a higher power of κ, on average very nearly with the predicted $\kappa^{2/3}$. Note that ψ_0 is zero in the Atlantic when the wind is turned off, and highest when the wind is strongest, showing that the wind driven portion of the circulation increases with the strength of the wind.

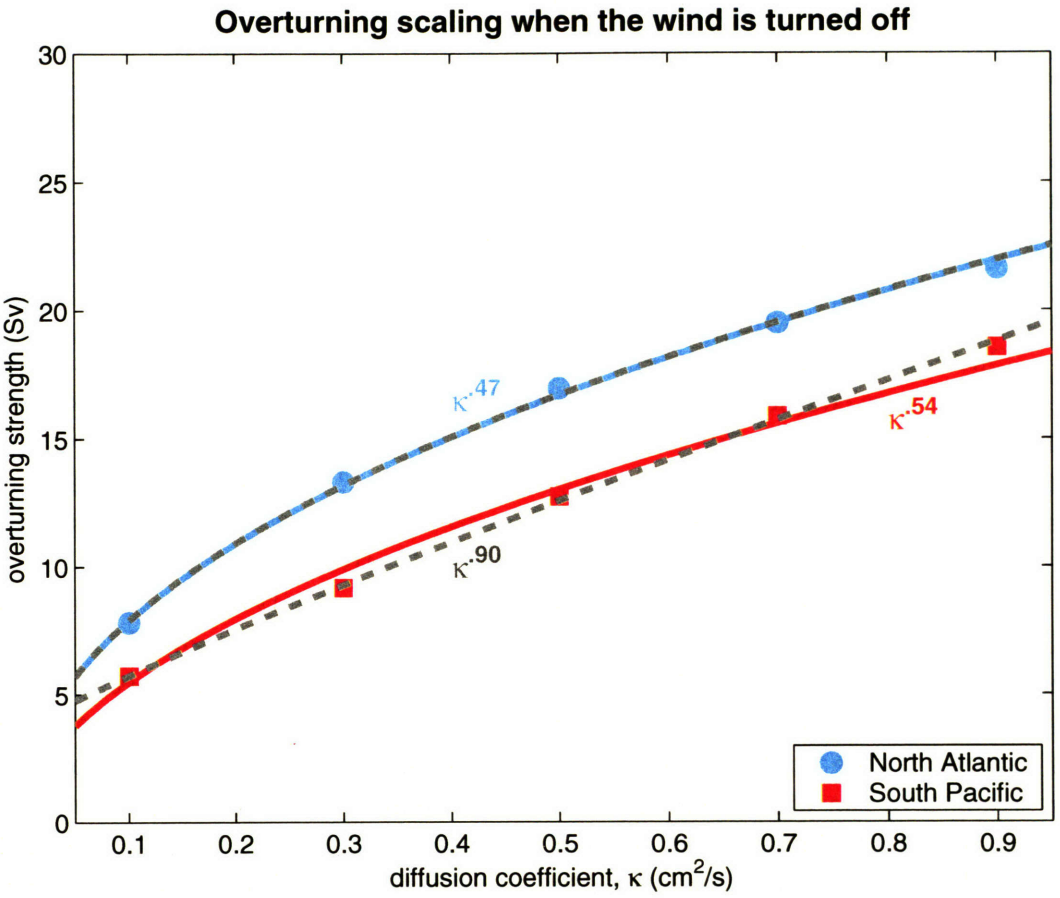

Figure 4-29: Maximum strength of the overturning in the North Atlantic (blue circles) and South Pacific (orange squares) across a decade of variation in κ, the diapycnal diffusion coefficient. The best fit curve estimated by equation (4.2) is shown running through the data with ψ_0 zero (solid, colored) and ψ_0 chosen so that the sum of the least squares is a minimum (dashed, gray).

While the amplitude of the wind stress clearly has an impact on the intensity of the heat flux, its effects on the abyssal circulation are more complicated. Given the rapidity with which surface density is restored, there is no thermal feedback to quash an anomalous circulation (see footnote 3). Rahmstorf and England (1997) and Bugnion (2001) have already noted that much of the sensitivity presented in this section is merely an artifact of the boundary conditions; coupled models are far less sensitive to the amplitude of the Southern Ocean winds.

We raise the issue of wind forcing here to demonstrate the strong effect that the surface cells have on the peak in the oceans' heat flux. While the Pacific abyssal circulation was largely unaffected by the strength of the winds, the heat flux carried poleward in the South Pacific varied by nearly 1.5 PW, regardless of the value of the diffusion coefficient. Upper ocean processes affect the oceans' heat transport (Boccaletti et al., 2005), and they play an important role in our results too.

4.7 Other boundary conditions

Coupled models have far less sensitivity to Southern Ocean winds than do ocean-only runs in which the surface density is rapidly restored or prescribed (Rahmstorf and England, 1997; Bugnion, 2001). Here we briefly discuss how some of these findings vary with different surface boundary conditions. Many of these experiments lie beyond the scope of this thesis, and are not presented here. We shall confine our present focus to the lessened influence of the wind and on the influences of different boundary conditions on the heat flux.

One can approximate the effects of a coupled model by forcing the ocean model as though it were coupled to an energy balance model. We constructed an exaggerated temperature (density) profile to which temperatures were restored on a 300 day timescale, similar to the construction used by Xiaoli Wang (1997) in her thesis. This allows the surface conditions to evolve much more freely than in the simulations discussed in earlier sections, where surface densities were effectively prescribed.

The main effect of this change is to kill the sensitivity of the overturning circulation to the strength of the wind. Regardless of the magnitude of the wind, the strength of the deep circulations is controlled by the amount of specified mixing. This remains true even if no wind forcing is used at all. (The strength of the Deacon cell, which fills the Southern Ocean in the Eulerian mean, is naturally dependent on the strength of the winds over the Southern Ocean.) The heat flux, however, varies considerably with the intensity of the wind, which underscores the importance of the near surface motions in transporting heat (Haidvogel and Bryan, 1992; Boccaletti et al., 2005).

The central findings presented in this chapter, however, are not affected by the choice of boundary conditions used at the surface. Tropical mixing in both the Pacific and Atlantic affects the North Atlantic overturning, and mixing in the upper ocean has the strongest impact on the strength of the heat flux.

4.8 Summary of the main findings

The results of this chapter have shown that mixing in the upper tropical oceans can have a powerful impact on the heat flux carried poleward. We confirmed that the intensity of mixing in low latitudes matters most to both the heat flux and overturning circulation. Mixing in both the Atlantic and Pacific affected the strength of the overturning in the North Atlantic. To the overturning circulation, the amount of mixing at all depths in the thermocline is important; to the heat flux, which is our principal concern, mixing in the upper 400 m of the ocean mattered most.

While it is clear that mixing is highly variable in much of the deep ocean, estimates from the upper ocean have found it to be uniformly weak there (e.g., Ledwell et al., 1993). Theories that presume mixing processes to be unimportant in the upper ocean have enjoyed success: the Luyten et al. (1983) ventilated thermocline

theory presumes that mixing is weak in the upper ocean. But what if some process contributed to mixing the upper tropical oceans, perhaps forcefully but in isolation? The results of this chapter show that the effects on the poleward heat flux could be substantial; for the deep circulation to increase, there must be some mechanism to carry this energy to deeper levels (perhaps internal waves).

Tropical cyclones vigorously mix this part of the ocean by turbulently entraining thermocline water into the surface mixed-layer. If these storms were stronger or more frequent during warm climates, it is possible that the oceans' heat flux and circulation could have been stronger. We take up these questions in the next chapter.

Chapter 5

Mixing from tropical cyclones

In the last chapter we saw that the oceans' heat flux is sensitive to mixing in the tropics, in the upper ocean, and to upwelling in both the Pacific and Atlantic basins. Many measurements taken in the tropical thermocline have revealed that little mixing occurs there in the present climate (e.g., Gregg, 1987; Polzin et al., 1997), but more recent measurements have found that mixing may be nearly nonexistent when the wind stress is too weak to push the local Richardson number below a critical value (Raymond et al., 2004). This suggests that mixing in the tropical thermocline is a highly transient event, and it leaves open the possibility that more mixing occurs here (episodically) than has been observed directly.[1] Even if one remains convinced that there is little mixing in the tropical thermocline today, what if mixing were not always weak? In this final chapter of results, we explore a more speculative problem: how might a change in tropical cyclone activity affect the global climate?

Barron and Washington (1985) showed that elevating carbon dioxide to high levels warmed high latitudes, but it produced tropical temperatures that were too warm when compared with evidence from proxy data. The gap between simulations and proxies of paleo-temperatures has narrowed somewhat in recent years (J. Kiehl, personal communication), though much of this has come from an upward revision of the estimates of tropical temperatures (e.g., Pearson et al., 2001). If the warm periods that dominated the early Cenozoic era had substantially more carbon dioxide than our present atmosphere (Pearson and Palmer, 2000), the proper question to ask is why were tropical temperatures not substantially warmer than they are today.

Emanuel (2001) has shown that the heating required to balance tropical cyclone

[1] Tracer studies removed most lingering doubt about the representativeness of microstructure measurements, which are a snapshot in space and time. Ledwell et al. (1998) studied the evolution of a dye injected in the eastern subtropical Atlantic over the course of two years (1992–1994), by which point it spread west to 55°W; they inferred that mixing was $O(10^{-5})$ m^2/s in the upper ocean. Note that there were no tropical cyclones during 1992–1994 in this region of the Atlantic, and none has formed in the Brazil Basin, where they released dye in a separate experiment (Ledwell et al., 2000). There have been no studies on the evolution of a tracer in regions of the world subjected to regular tropical cyclone mixing, such as the eastern or western tropical Pacific.

wakes is large. In the time-mean, this heating must be exported out of the tropics; the turbulent mixing along the paths of tropical cyclones could contribute substantially to the oceans' heat flux, which dominates the climate system's poleward transport of enthalpy equatorward of 20° latitude (Peixoto and Oort, 1992). Lyle (1997) and Nilsson et al. (2003) have considered the effects of a stratification-dependent mixing parameterization, and have demonstrated that the ocean circulation will strengthen when the buoyancy gradient weakens if the energy available to mixing, rather than mixing itself, is held fixed.

Tropical cyclones vigorously mix the upper tropical oceans, but the strong stratification in the thermocline limits the depth to which this mixing penetrates (Schade, 1994). The stratification of the Eocene oceans is not known, and this creates considerable uncertainty for studies that attempt to model the general circulation. There is some reason to suspect that the thermocline may have been more diffusive during warm climates. Scott (2000) showed that a decrease in the planetary temperature gradient produced a deeper thermocline in experiments with fixed mixing. In separate experiments in which the buoyancy gradient was fixed but κ increased, Scott (2000) showed that stronger mixing diffuses heat downward and creates a more diffusive thermocline. If the stratification of the ocean was weaker during the Eocene epoch, which would not be inconsistent with proxy evidence of mild bottom waters, the depth to which tropical cyclone mixing penetrated may have increased as well. This is a potentially powerful feedback, and we comment on the implications of a parameterization incorporating this dependence at the end of this chapter.

Our goal is to present evidence that mixing from tropical cyclones could make a substantial contribution to the poleward transport of enthalpy during warm climates. We begin by reviewing the coupled model of intermediate complexity used in this study. In section 5.2 we examine our control cases, which use fixed mixing; one experiment is run for the present climate, and another is run for a climate with a high load of carbon dioxide (a factor of ten larger than in the present climate). We discuss a parameterization of mixing in section 5.3 that ties the amount of mixing to the potential intensity of tropical cyclones. In section 5.5, we explore the effects of both stratification and tropical cyclones on ocean mixing. Finally, we consider the direct upper ocean mixing in isolation, without making assumptions about changes in the abyssal ocean.

5.1 Coupled model

To explore these issues, we use the coupled model described by Dutkiewicz et al. (2005); an earlier version was described by Kamenkovich et al. (2002). This model couples a three-dimensional ocean model with a two-dimensional, statistical-dynamical atmosphere. The older version described by Kamenkovich et al. (2002) used the modular ocean model from the Geophysical Fluid Dynamics Laboratory, but here the

ocean model has been replaced with the MIT general circulation model (Marshall et al., 1997a; Marshall et al., 1997b).

By using a zonal mean atmosphere, this coupled model can run efficiently while using an ocean model detailed enough to examine mechanisms and feedbacks that are essential for understanding changes in the ocean circulation. Thus, we were able to run a modest number of experiments to equilibrium in order to test various parameterizations of interactive ocean mixing.

A deficiency of this model is the need to use flux adjustments or anomaly coupling. While some of the most recent climate models no longer use such adjustments (e.g., Collins et al., 2004), they still have slow drifts in the deep ocean temperature; often, these are slow enough to ignore for global warming experiments. Many others models cannot simulate present-day conditions without adjustments (e.g., Opsteegh et al., 1998; Goose et al., 2000). The principal problem in coupling atmosphere and ocean general circulation models has been the mismatch between oceanic heat transport before and after the coupling (e.g., Weaver and Hughes, 1996). In other words, ocean models are often unable to produce a heat flux strong enough to sustain the modern sea surface temperature field; when such models are coupled to an atmosphere without adjustments, they exhibit a tendency to drift to cold climates (e.g., Manabe and Stouffer, 1988).

5.1.1 Atmosphere

The two-dimensional zonally averaged atmospheric model is described in detail by Sokolov and Stone (1998); it is a modified, zonally average version of the GISS general circulation model (Hansen et al., 1983). The model solves the zonally averaged primitive equations in latitude-pressure coordinates; it has variable resolution, but here we use forty-six evenly spaced points along the meridian and eleven vertical levels (concentrated in the boundary layer and near the tropopause, with less resolution in the middle troposphere). The model includes parameterizations of heat, moisture, and momentum transports by large-scale eddies (Stone and Yao, 1987; Stone and Yao, 1990). Thus, even though the model is two-dimensional, it includes a representation of the transport by three-dimensional eddies.

The model's numerics, physics, and parameterizations closely parallel the parent GISS model, and the radiation code includes several greenhouse gases (e.g., CO_2, CH_4, N_2O, etc.) and different aerosols. Each zonal band can consist of four different types of surfaces in the same grid-cell: open ocean, sea-ice, land, and land-ice. Surface characteristics, as well as turbulent and radiative fluxes and their derivatives, are calculated separately for each kind of surface, while the atmosphere above is assumed to be well-mixed zonally (Dalan et al., 2005). The atmospheric model uses a realistic land-ocean ratio for each latitude band. Additional detail can be found in Sokolov and Stone (1998) and Prinn et al. (1999).

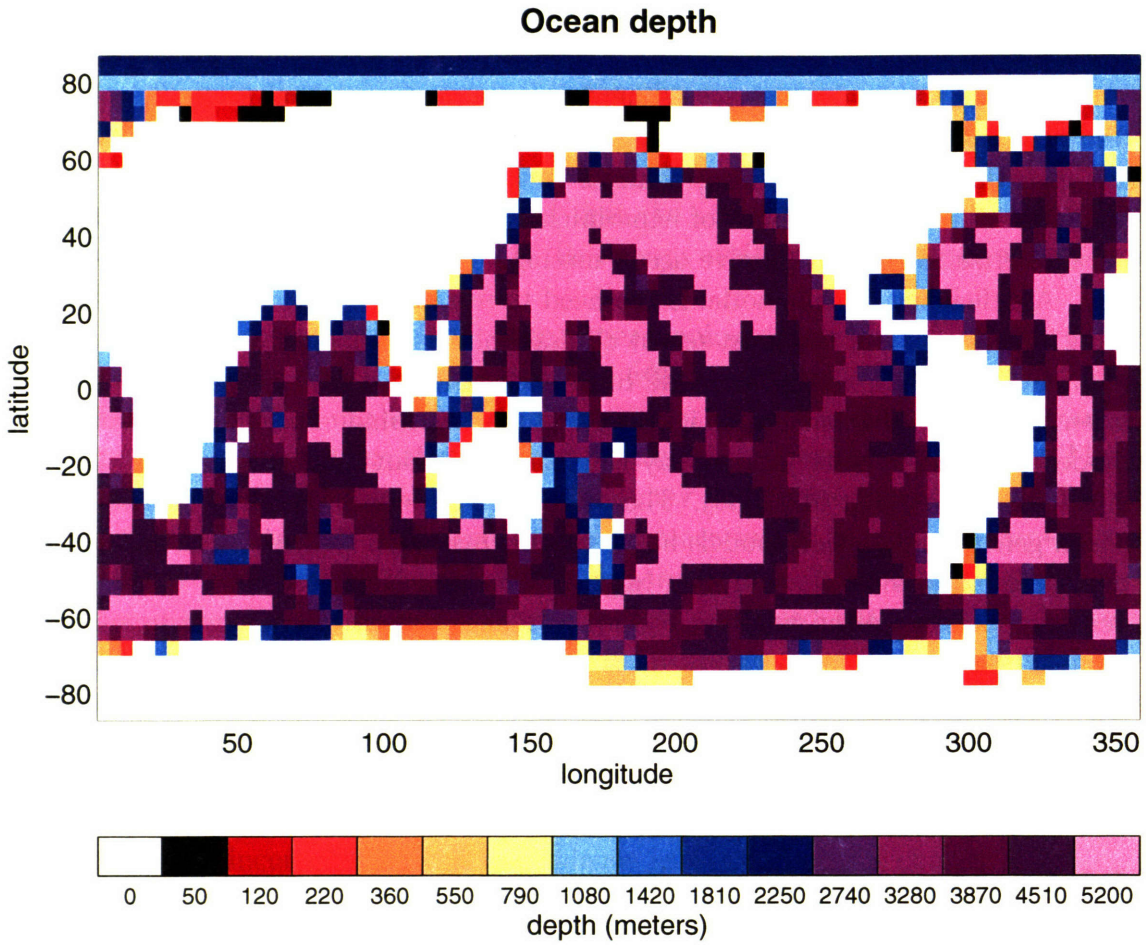

Figure 5-1: The topography of the MIT general circulation model used for the results presented in this chapter. The depth of the ocean at each point is plotted in color (land is shown in white). There are fifteen irregularly spaced vertical levels in the model.

5.1.2 Ocean

The ocean component of the coupled model is the MIT general circulation model, which was used to produce the results in Chapter 4. In contrast with those simulations, however, we use realistic, contemporary topography as shown in figure 5-1. There are fifteen levels in the vertical; the thickness of each layer increases monotonically from 50 m at the surface to 690 m in the bottom layer. The depth at each point is shown in figure 5-1. Model points are spaced four degrees apart in latitude from 82°S to 82°N, with two additional points at 87°S and 87°N. In the zonal direction, points are evenly spaced every 4° longitude. Unlike the experiments presented in the last chapter, the effects of salinity on the equation of state are considered; the full, nonlinear equation of state is used for all experiments in this chapter.

The model solves the primitive equations for momentum and the advection and diffusion of temperature and salt; it makes both hydrostatic and Boussinesq

assumptions. No-slip boundary conditions are used for horizontal velocities at lateral walls, while free-slip boundary conditions are applied to the bottom. The coarse horizontal resolution limits the model's ability to capture the mixing induced by eddy motions; therefore, the model uses the Gent-McWilliams (Gent and McWilliams, 1990) scheme, which introduces eddy-induced transport velocities. The main effect of these velocities is to homogenize isopycnal thicknesses with strong tendencies to flatten isopycnal surfaces, which effectively reduces the available potential energy. Additional detail can be found in Marshall et al. (1997a), Marshall et al. (1997b), and Dutkiewicz et al. (2005).

5.1.3 Coupling

Coupling takes place once daily. The ocean model supplies the atmosphere with zonally averaged sea surface and ice surface temperatures, the fraction of ocean covered by sea ice, and air-sea carbon dioxide fluxes. The atmospheric model calculates a daily mean value of the heat and fresh-water fluxes over the open ocean, their derivatives with respect to sea surface temperature, the heat flux through the bottom of the ice, and the wind stress. It also passes fresh water runoff from the land, mean sea level pressure, incident shortwave radiation, and atmospheric carbon dioxide content. These quantities are linearly interpolated to the ocean grid. The ocean model, after being forced and integrated for twelve model hours, passes the atmosphere a zonal mean sea surface temperature, sea-ice thickness, and sea-ice concentration.

The atmosphere's forcing fields are zonally averaged, and must be interpolated when passed to the ocean. As described by Kamenkovich et al. (2002), fluxes of heat (Q) and evaporation (E) can be expressed as functions of longitude (x) and latitude (y) by:

$$Q(x,y) = Q_z(y) + \left(\frac{\partial Q}{\partial T}\right)_z [T_s(x,y) - T_z(y)] \tag{5.1}$$

$$E(x,y) = E_z(y) + \left(\frac{\partial E}{\partial T}\right)_z [T_s(x,y) - T_z(y)], \tag{5.2}$$

where the subscript z denotes a zonal value provided by the atmosphere and the subscript s refers to surface values (either open ocean or sea ice).

The surface representation of the zonal mean wind stress given by the atmosphere model is too poor to use directly, particularly at middle and high latitudes (Dutkiewicz et al., 2005). Therefore anomaly coupling is employed. In this technique, the wind stress is taken from observations, but its strength is modified by the atmospheric model. For a wind stress, τ:

$$\tau(x,y) = \left[\tau_z(y) - \overline{\tau_z(y)}^t\right] + \tau_{obs}(x,y). \tag{5.3}$$

The two-dimensional field provided to the ocean, $\tau(x, y)$, is produced by subtracting the climatological averaged zonal wind stress, $\overline{\tau_z(y)}^t$, from the instantaneous value, $\tau_z(y)$, and adding the observed mean, $\tau_{obs}(x, y)$; the procedure to calculate $\overline{\tau_z(y)}^t$ will be discussed in the next section. The term in square brackets of equation (5.3) is the anomaly produced by the atmospheric model. Note that the longitudinal structure of the wind field is always confined by the observations.

As noted earlier, this model requires flux adjustments to reproduce the present climate. Fluxes of heat (Q) and fresh water (F) can be modified by adding an additional term that brings the surface fields back to consistency with observations. The problem with using such a formulation in climates different from the present (or in modeling climate change) is that the "observed" conditions to which the model should be relaxed is unknown (in many problems such a field is the solution one is after). Therefore, the model is spun up using a relaxation term to reproduce the present sea surface temperature distribution, and a temporal average of the needed relaxation is calculated to form a "fixed flux adjustment." This procedure is described in the next section; further details may be found in Dalan et al. (2005) and Dutkiewicz et al. (2005).

5.1.4 Procedures

The model is spun up with concentrations of carbon dioxide and other greenhouse gasses from 1980; CO_2 was 337.9 ppm. During this phase, the wind stresses, heat flux, and fresh water fluxes used to force the model are taken from observations:

$$\tau_x(x, y) = \tau_{x_{obs}}(x, y) \tag{5.4}$$
$$\tau_y(x, y) = \tau_{y_{obs}}(x, y) \tag{5.5}$$
$$Q(x, y) = Q_o(x, y) - Q_r(x, y) \tag{5.6}$$
$$F(x, y) = F_{obs}(x, y), \tag{5.7}$$

where $Q_r(x, y)$ is the adjustment that corrects back to observed values:

$$Q_r(x, y) = \frac{1}{\lambda}\left[T(x, y) - T_{obs}(x, y)\right] \tag{5.8}$$

The values of Q_o are determined by equations (5.1). The relaxation time scale, λ, was sixty days. The observed wind stresses are derived from the analysis of Trenberth et al. (1989), and the observed fresh water field is taken from Jiang et al. (1999).

While the model runs in the spin-up mode, the atmospheric model calculates the wind field and precipitation, evaporation, and river runoff for fresh water forcing; if it were coupled, these fields would be passed to the ocean. At this point, however, these quantities are not passed, but they are stored for diagnostic purposes at the end of the spin-up. At the conclusion of the spin-up (generally 1500 model years),

the heat flux adjustment, Q_r, and wind stresses are averaged over the final century to produce $\overline{Q_r}$, $\overline{\tau_{x_z}(y)}^t$, and $\overline{\tau_{y_z}(y)}^t$. Similarly, the evaporation and precipitation are averaged over the last century.

Henceforth, with the model now fully coupled, the wind stresses are computed using equation (5.3), and the value of Q_r in equation (5.8) is fixed to $\overline{Q_r}$. The adjustment Q_r can be thought of as model deficiency; this correction must be applied to reproduce the current climate.

After verifying that the model is stable (i.e., running for at least 500 years with no drift in circulation, temperatures, or salinities), it can be used to explore the changes that develop when radiative forcing becomes stronger. From the conclusion of the coupled simulation of the present climate, carbon dioxide jumps to 3379 ppm, a factor of ten larger. We run this experiment to equilibrium and assess how the model behaves with high carbon dioxide. Note that the same values of Q_r are added to the elevated carbon dioxide experiments that were used in the control case for the same mixing parameterization; this is called "fixed flux adjustments" in Dutkiewicz et al. (2005).

5.1.5 Experiments

We examine how various parameterizations of mixing that depend on tropical cyclone activity and stratification are able to modify the results. For each new parameterization of mixing, the procedure described above was repeated: first a spin-up with the new mixing scheme was run for 1500 years, after which average values were calculated for the anomaly coupling and flux adjustments. Mixing schemes affect the circulation, and thus require a different flux adjustment to reproduce the present climate in each experiment. Often, these changes are small or subtle, but this step is necessary in order to produce an accurate present climate.

For each mixing parameterization, we then run a coupled experiment to verify that the present climate is faithfully reproduced. At its conclusion, another experiment with high carbon dioxide (a factor of ten larger) is run to compare with its companion simulation of the present climate. In this way, we can quantify how much the circulations and heat fluxes increase or decrease in a high carbon dioxide climate for each mixing scheme tested.

5.2 Control: changing CO_2 alone

Later in this chapter we shall explore physically based parameterizations of mixing, but first we review our control case. In figure 5-2, the results from a simulation forced with contemporary amounts of carbon dioxide (338 ppm) and uniform diapycnal diffusivity (κ is 0.3 cm^2/s) are presented. (These data are an average over the final century of the fully coupled simulations.) Note that a vigorous deep circulation

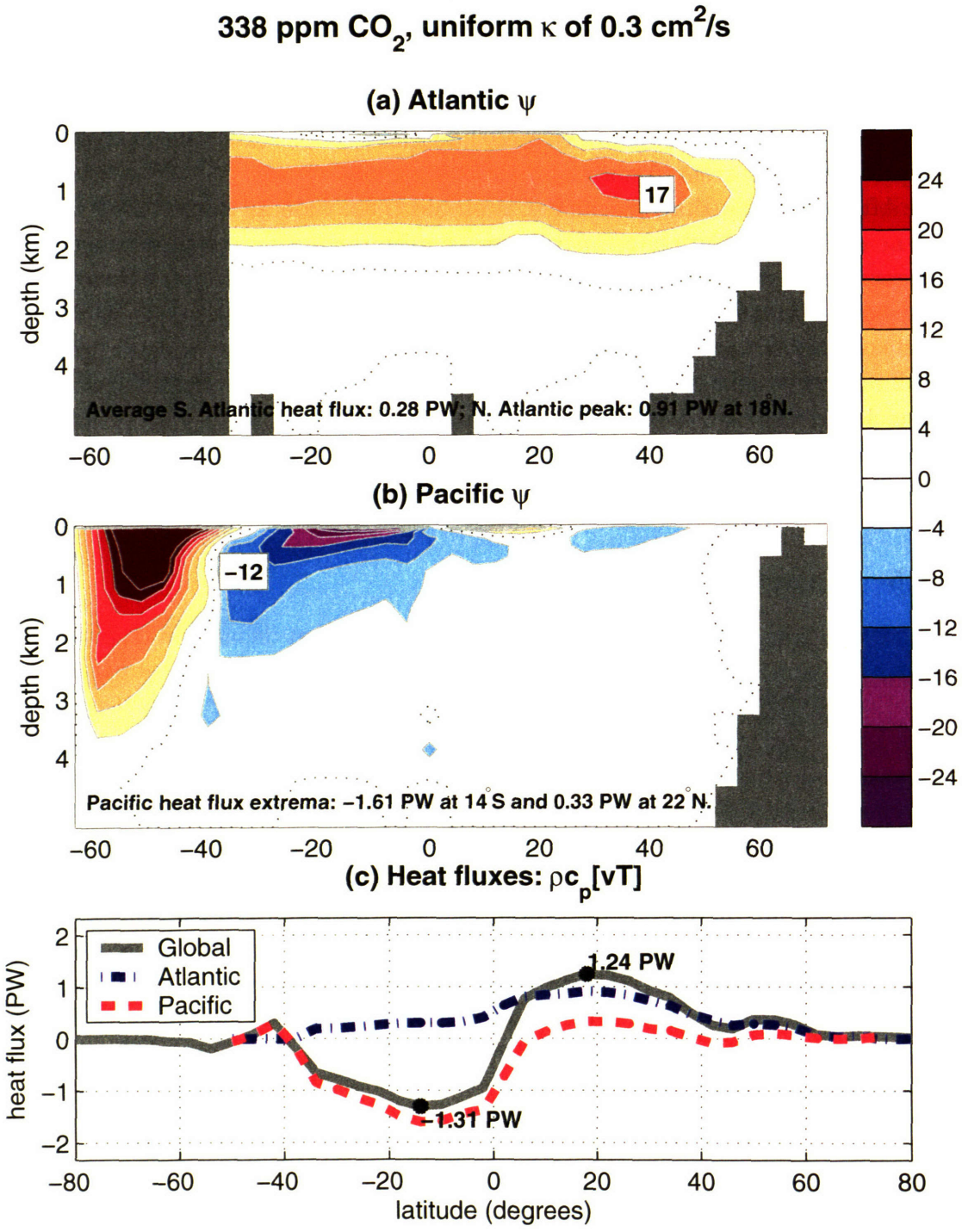

Figure 5-2: The overturning circulation and heat fluxes from a simulation with contemporary levels of carbon dioxide (338 ppm) and specified, fixed mixing. The value of the diffusion coefficient, κ, is 0.3 cm^2/s everywhere.

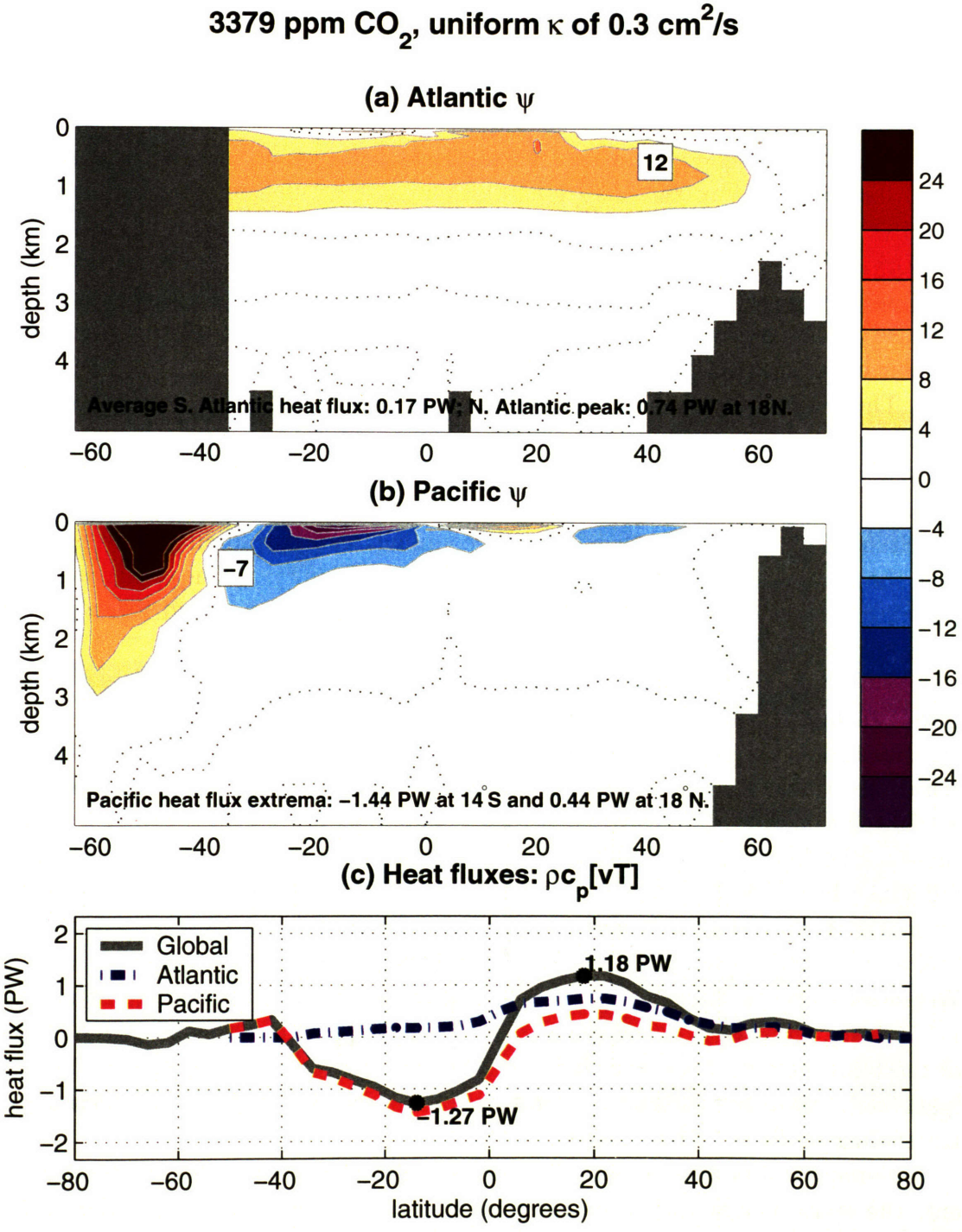

Figure 5-3: The overturning circulation and heat fluxes from a simulation with high carbon dioxide (3379 ppm) and specified, fixed mixing. The value of the diffusion coefficient, κ, is 0.3 cm^2/s everywhere.

travels northward in the upper kilometer of the Atlantic Ocean, sinks, and returns southward at depth. Some of this deep water is upwelled in the Atlantic, but most flows out to return to the surface in the Pacific, Indian, or Southern Ocean. Note the surface Ekman cells confined to the upper ocean; this part of the circulation is wind-driven and is responsible for a substantial fraction of the oceans' poleward heat flux (Haidvogel and Bryan, 1992).

When the coupled model is loaded with ten times more carbon dioxide (3379 ppm), temperatures warm at all latitudes and the circulation weakens. Huber and Sloan (2001) obtained a similar result with the NCAR coupled model, but Manabe and Bryan (1985) found circulations of roughly equal intensity as carbon dioxide was increased by a factor of eight; they found that the density gradient changed little because of the nonlinearity of the equation of state. With fixed mixing, the intensity of their circulations did not vary.

These simulations show a reduced pole-to-equator density gradient decreases when carbon dioxide increases; high latitude waters in the North Atlantic are both warmer and fresher (see figure 5-4). With constant mixing and a reduced buoyancy gradient, the classic scaling (Welander, 1986) predicts a reduction in the intensity of the circulation. Because we use anomaly coupling, the wind forcing is largely similar (not shown, but the maximum change is only 0.01 N/m^2); the heat flux weakens in the high carbon dioxide experiment, but the strength of the wind forcing keeps it from decreasing further.

This high load of carbon dioxide produces much warmer sea surface temperatures. In figure 5-4a, note that while temperatures are 8-10°C warmer in northern high latitudes, temperatures in the tropics are now 6-7°C warmer as well. (Temperatures show less change along the Antarctic coast, where seasonal sea ice persists even in the high carbon dioxide experiment; the presence of ice confines temperatures to the freezing point of ocean water, which is about −2°C.) While the density difference between the tropics and high latitudes does decrease, it does not decrease by much. For example, the difference between Atlantic zonally averaged density at 2°N and 62°N decreases by about 10% from the present to ten-times CO_2 run. The Welander scaling predicts a fairly weak dependence on the buoyancy gradient (to the 1/3 power), but Scott (2000) found the overturning strength followed a 2/3 power of the buoyancy gradient in a single hemisphere model. In any event, the North Atlantic overturning circulation changes by −8 Sv, which is a far larger decrease than the scaling predicts (−1 Sv only).

Some authors have argued that rather than the equator-to-pole density gradient, the steric height difference between the southern and northern Atlantic is the more relevant quantity on which to focus in climate change experiments (Hughes and Weaver, 1994; Rahmstorf, 1996; Wiebe and Weaver, 1999; Scott et al., 1999; Thorpe et al., 2001). In this view, the relevant buoyancy gradient has weakened more, though uncertainties remain in how and where to measure the steric height in a topographically accurate model (J. Scott, personal communication).

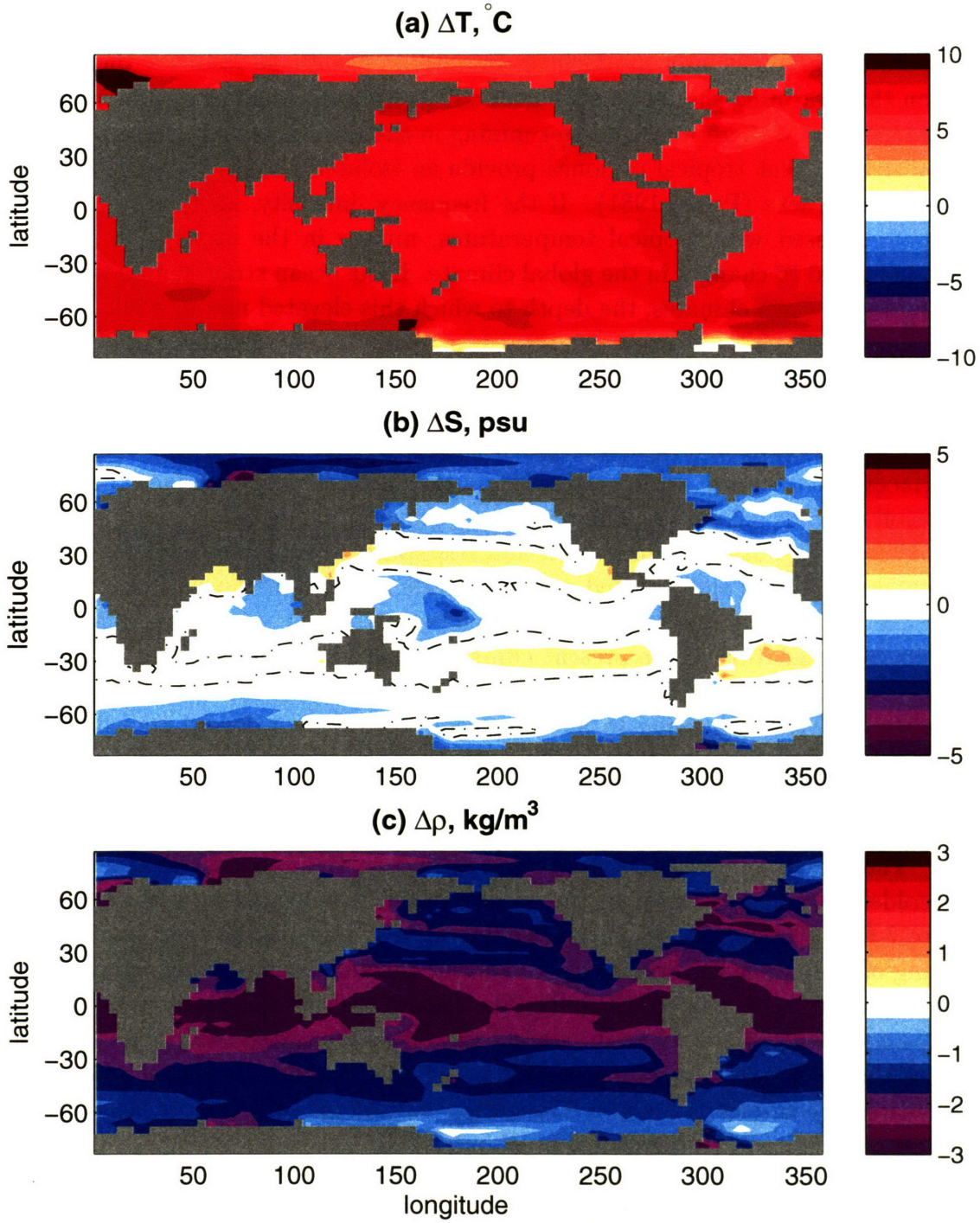

Figure 5-4: Differences in (a) sea surface temperatures, (b) sea surface salinities, and (c) surface densities between a simulation with 3379 ppm carbon dioxide and one with 338 ppm; both simulations used a uniform diffusivity (0.3 cm^2/s). Note that the 338 ppm simulation was subtracted from the 3379 ppm one, showing a warming, freshening, and lightening of most of the ocean surface when carbon dioxide is elevated. Zero contour lines are plotted in dash-dotted black.

Can the pole-to-equator temperature gradient be weakened further? It seems clear from numerous studies that elevated carbon dioxide can reduce the planetary temperature gradient only so much, as beyond an ice-albedo feedback there is little reason that warming should be stronger at high latitudes than at low latitudes.

But what if there were stronger mixing in the tropics during warm climates? It is well known that tropical cyclones provide an isolated but intense blast of mixing along their tracks (Price, 1981). If the frequency, intensity, and duration of these storms increased with tropical temperatures, mixing in the upper tropical oceans would respond to changes in the global climate. If the ocean stratification was weaker during these warm climates, the depth to which this elevated mixing could penetrate might also increase.

To illustrate the potential power of this idea, we ran another experiment with 3379 ppm carbon dioxide and specified mixing, but the diffusion coefficient was elevated by an order of magnitude (to 3 cm^2/s) at the 50, 120, and 220 m model interfaces equatorward of 30° latitude; at the next deepest interface (360 m) the diffusion remains 0.3 cm^2/s. The results are shown in figure 5-5.

Note that both the circulation and heat flux increase over the case with uniformly weak mixing and elevated carbon dioxide (which was shown in figure 5-3). In fact, the global heat flux is now 25% stronger in the Northern Hemisphere than it was in the simulation of the present climate; much of this comes from an enhanced poleward heat transport in the North Pacific. There is a 29% rise in the Southern Hemisphere, partially owing to an enhancement of the southward transport in the Ekman cell of the South Atlantic. This offsets the northward transport by the overturning circulation and allows the southward transport in the Pacific to control the Southern Hemisphere flux.

The principal effect of the elevated mixing in the upper tropical oceans is to lift colder thermocline water to the surface where it is heated by surface fluxes. In figure 5-6, the change in sea surface temperatures[2] that results from more vigorous mixing of the upper tropical oceans is shown; the simulations being compared both have high carbon dioxide (3379 ppm). The control case has uniformly weak mixing (κ is 0.3 cm^2/s everywhere) while the second test raised the vertical diffusion to 3.0 cm^2/s across the three top interfaces equatorward of 30° latitude. Note that when mixing is elevated the tropics cool and a stronger circulation transports more heat poleward, raising high latitude temperatures by about 1-2°C.

The increased heat transport comes by diffusing heat down through the upper tropical ocean. This produces a stronger meridional temperature gradient beneath the surface, which in turn generates stronger zonal flows. As described by Scott

[2]The observant reader might note that the area-integrated SST change is not zero. While much of the tropics do cool about 0.5-1°C, higher latitudes warm more. The global mean ocean temperature is about 0.4°C warmer in the simulation with elevated tropical mixing than in the control case. The strong mixing lowers surface temperatures, which are quickly heated by radiation, and leaves a warm anomaly below.

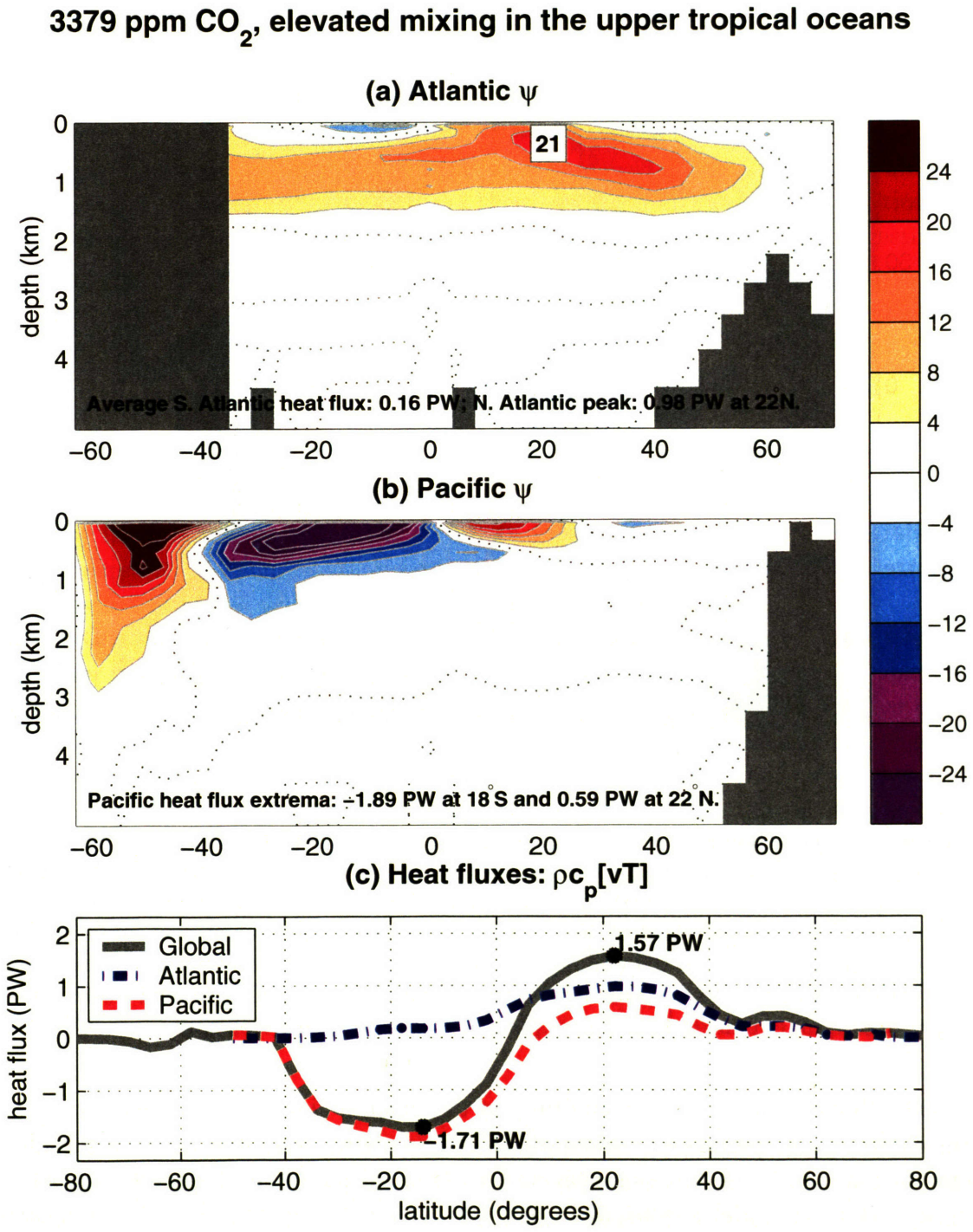

Figure 5-5: The overturning circulation and heat fluxes from a simulation with high carbon dioxide (3379 ppm) and specified, fixed mixing. The value of the diffusion coefficient, κ, is 0.3 cm^2/s everywhere except in the upper tropical oceans, where equatorward of 30° latitude and at the top three interfaces (50, 120, and 220 m), the diffusion coefficient is 3.0 cm^2/s.

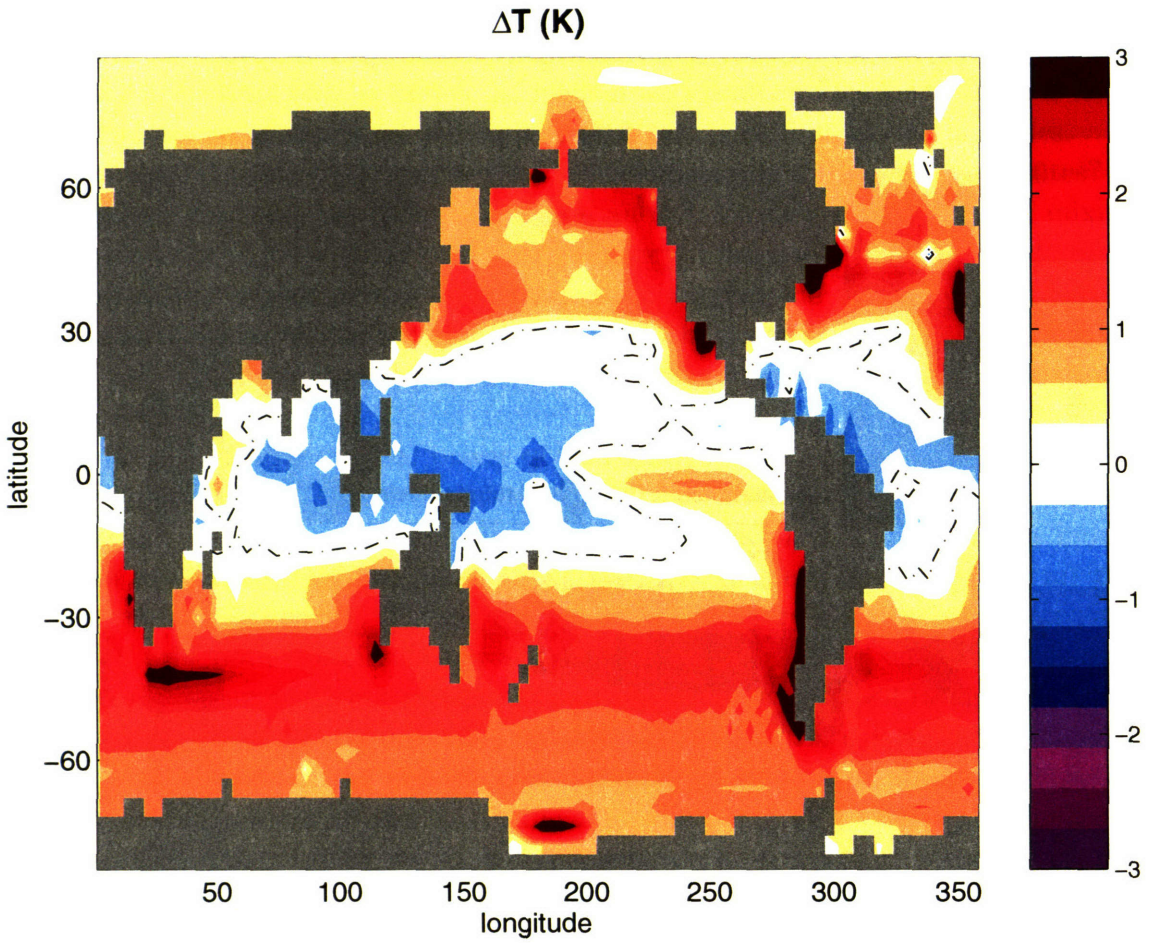

Figure 5-6: The change in sea surface temperatures that results from elevating mixing in the upper tropical ocean. The two simulations compared were both forced with high carbon dioxide (3379 ppm), but one had strong diffusion of heat (3.0 cm^2/s) across the 50, 120, and 220 m interfaces equatorward of 30° latitude. The other case, which had uniformly weak mixing with a diffusion of 0.3 cm^2/s, was subtracted from the one with elevated mixing. The strong mixing cools tropical sea surface temperatures by mixing heat down into the upper ocean; an enhanced heat flux exports the heat to higher latitudes.

(2000), this increases the downwelling on the eastern side of the basins, strengthens the east-west temperature gradient at depth and supports a more vigorous meridional circulation. Qualitatively, this near-surface tropical mixing narrows the gap between proxy data and model results: if the atmosphere was loaded with high levels of carbon dioxide and tropical mixing increased, the ocean can sustain a stronger poleward heat flux, which holds tropical temperatures down.

Could changes in global tropical cyclone activity account for a change in mixing that is this large? We shall investigate this question in this chapter. We first investigate a parameterization of mixing that is vertically invariant, assuming that mixing at all depths scales with the power put into the ocean surface by tropical cyclones.

5.3 Interactive mixing

Returning deep, dense parcels to the surface of the ocean requires that work be done against gravity and a stable stratification. Mixing is necessary to maintain a realistic vertical structure; without it, the ocean would become a stagnant pool of cold, salty water [this follows from Sandström (1908); see Munk and Wunsch (1998)]. Munk and Wunsch (1998) argue that the strength of the meridional overturning circulation and its associated heat flux are determined by the power available to return deep fluid parcels to the surface layers, rather than by high-latitude buoyancy forcing.

The rate of work (power) done against gravity in a stably stratified fluid is:

$$\varepsilon_p = \Gamma\varepsilon = \kappa\left(-\frac{g}{\rho}\frac{d\rho}{dz}\right) = \kappa N^2, \tag{5.9}$$

where ε_p is the portion of the dissipation of energy (ε) that goes into the production of potential energy; Γ is the mixing efficiency, commonly believed to be about 0.2 (Osborn, 1980; Munk and Wunsch, 1998). In warm climates, if energy available for mixing increases, the stratification decreases, or both occur, mixing will be stronger than it is in the present climate.

In this section, we assume that the diffusion coefficient scales with the cumulative power put into the oceans by tropical cyclones. In the tropics, such an assumption may not be as far-fetched as it sounds; Raymond et al. (2004) report that upper ocean mixing is a highly nonlinear process that appears to respond most vigorously to the strongest atmospheric disturbances. Nilsson (1995) calculated the energy flux from hurricanes to the oceanic internal wave field, and found that these storms might make an important contribution in tropical oceans, though they contribute only a small amount to the global internal wave field. Emanuel (2001) has demonstrated that the power put into the oceans by the passage of tropical cyclones scales with the third power of the potential intensity, which is the theoretical maximum intensity that a storm can achieve (Emanuel, 1988a; Bister and Emanuel, 1998). The rate at which the wind does work on the ocean may be calculated by:

$$W = \tau \cdot \mathbf{v}, \tag{5.10}$$

where τ is the surface wind stress and $\mathbf{v}$ are the surface currents [Wunsch (1998) used the geostrophic part of the surface currents, $\mathbf{v}_g$, as an approximation]. Note that τ increases with the square of the wind, so if one assumes that the surface currents scale linearly with the wind, W will scale with the third power of potential intensity.

Before proceeding with a parameterization of mixing dependent on forcing by tropical cyclones, we first review the theory governing the strength of tropical cyclone winds. Emanuel showed that hurricanes can be regarded as a Carnot heat engine (see Emanuel, 1986; Emanuel, 1988a; Emanuel, 1988c; and Bister and Emanuel, 1998). The maximum potential intensity of tropical cyclones is a function of the thermody-

namic efficiency of the Carnot heat engine, surface and outflow temperatures, and ambient relative humidity, which measures the degree of thermodynamic disequilibrium between the ocean and the atmosphere (Emanuel, 1988c). The maximum wind speed that a storm can achieve is:

$$\mathrm{PI} = V_{max} = \sqrt{\frac{T_s - T_o}{T_s}\left(\frac{T_s}{T_o}\frac{C_k}{C_D}\right)(k_o^* - k)}, \tag{5.11}$$

where $(T_s - T_o)/T_s$ is the thermodynamic efficiency of a Carnot heat engine, C_k/C_D is the ratio of the surface exchange coefficients for enthalpy and drag, and $(k_o^* - k)$ is the difference between saturation enthalpy at the ocean surface and the enthalpy of the overlying atmosphere (e.g., Emanuel, 1986). This thermodynamic disequilibrium is what drives a hurricane. The ratio of surface to outflow temperatures multiplying the ratio C_k/C_D results from the inclusion of dissipative heating (see Bister and Emanuel, 1998). Note that equation (5.11) was derived on energy principles alone; this is the maximum achievable intensity, but it says nothing about how close real storms may come. However, Emanuel (2000) has demonstrated that there is a strong statistical relationship between observed intensities and potential intensity. Thus potential intensity can be used as a surrogate for actual storm intensity.[3]

The cumulative power put into the oceans will also increase with the frequency of events. Emanuel and Nolan (2004) showed that the genesis rate of tropical cyclones is highly sensitive to climate. They found that the frequency of disturbances scales with the third power of potential intensity, but this might be conservative if temperatures warm to sufficiently high levels. Emanuel and Nolan (2004) postulate that while tropical cyclones can be viewed as a finite-amplitude instability in the present climate, they may spontaneously form over high sea surface temperatures. It is not clear at what point such a transition would occur in the climate system, nor even whether such a bifurcation exists in nature (K. Emanuel, personal communication).

Combining the genesis dependence on climate [PI^3; see Emanuel and Nolan (2004)] with the power put into the tropical oceans by these storms [PI^3; see Emanuel (2001)], we scale the diffusion coefficient with the sixth power of potential intensity. The vertical diffusivity is parameterized by:

$$\kappa(x, y) = a \cdot [\mathrm{PI}(x, y)]^6, \tag{5.12}$$

where $\mathrm{PI}(x, y)$ is the potential intensity [given by equation (5.11); its units are m/s]

[3]Note that nothing in equation (5.11) prohibits hurricanes along the equator, where f goes to zero. Again, this expression is based on energetic considerations alone. Equatorward of 5° latitude, no storms form; within this equatorial belt all later parameterizations of mixing that are based on potential intensity will be too large. I have done some experiments with the ocean model described in Chapter 4, and found that there is no difference in the circulations between a run having tropical mixing equatorward of 30° latitude and a run with mixing between 8° and 30° latitude alone, provided that the area-averaged value of the diffusivity is conserved.

at longitude x and latitude y and a is a constant. The value of a was chosen so that the average diffusivity in the deep tropics is about 0.3 cm^2/s in the simulation of the present climate. As the results of the last chapter showed, ocean models are most sensitive to the value of the diffusion coefficient in the tropics, so we chose to normalize a here. The potential intensity along the equator[4] was diagnosed to have an average value of about 75 m/s. Allowing a to be $1.6856 \times 10^{-16}\ s^6/m^6$ reproduces a value of κ equal to $3 \times 10^{-5}\ m^2/s$ wherever the potential intensity equals 75 m/s. The value of κ was prohibited from falling below 0.05 cm^2/s for numerical stability. Of course if storms remain at their peak intensity longer (Emanuel, 2005), or if more of them reach their peak intensity, this parameterization might prove to be conservative.

Note that this parametrization is vertically invariant and applied at all latitudes. Here we assume that mixing scales at all depths with the power (and frequency) of the strong blasts of wind provided by these transient events. This is not realistic, particularly outside of the tropics, but as we saw in the last chapter, mixing in middle and high latitudes is unimportant to the oceans' heat flux. The purpose of this experiment is to investigate the behavior of the coupled interaction; we discuss more realistic vertical parameterizations in section 5.5.

After completing a spin-up with the new parameterization of mixing given by equation (5.12), we ran two coupled experiments using this interactive mixing scheme. The first one redoes the present climate and the other was forced with 3379 ppm carbon dioxide (ten times the present amount). Figure 5-7 shows the zonally averaged values of κ from these two runs. The values shown were averaged over the last 100 years of each simulation; by this time, the runs had reached equilibrium. Note that the diffusion coefficient is 0.2-0.4 cm^2/s in the tropics in the simulation of the present climate, but poleward of 30° values fall off to the prescribed minimum. Poleward of about 40°, sea surface temperatures are too cool to support tropical cyclones, and the potential intensity falls to zero.

A time-series of the data is presented in figure 5-8. This shows the zonally averaged values of κ over the last ten years of the present climate simulation. The range of values shown is typical of the full time-series. Note that there is a strong seasonal cycle: when sea surface temperatures are highest, the potential intensity is as well, and equation (5.12) produces stronger diffusion. Boos et al. (2004) demonstrated that mixing can be episodic; the time-mean value is important to the model.

When the model is forced with ten times more carbon dioxide, the sea surface temperatures warm and the potential intensity increases. The potential intensity was, on average, about 20% stronger in the high carbon dioxide case, which produces diffusivities that are about three times as large.[5] The latitudinal structure has changed little, however, as temperatures poleward of 40° remain too cold to support tropical cyclones.

[4] Again, no real storms will form at the equator, but the potential intensity here is representative of the average value throughout the deep tropics.

[5] N.B. $(1.2)^6 \approx 3$.

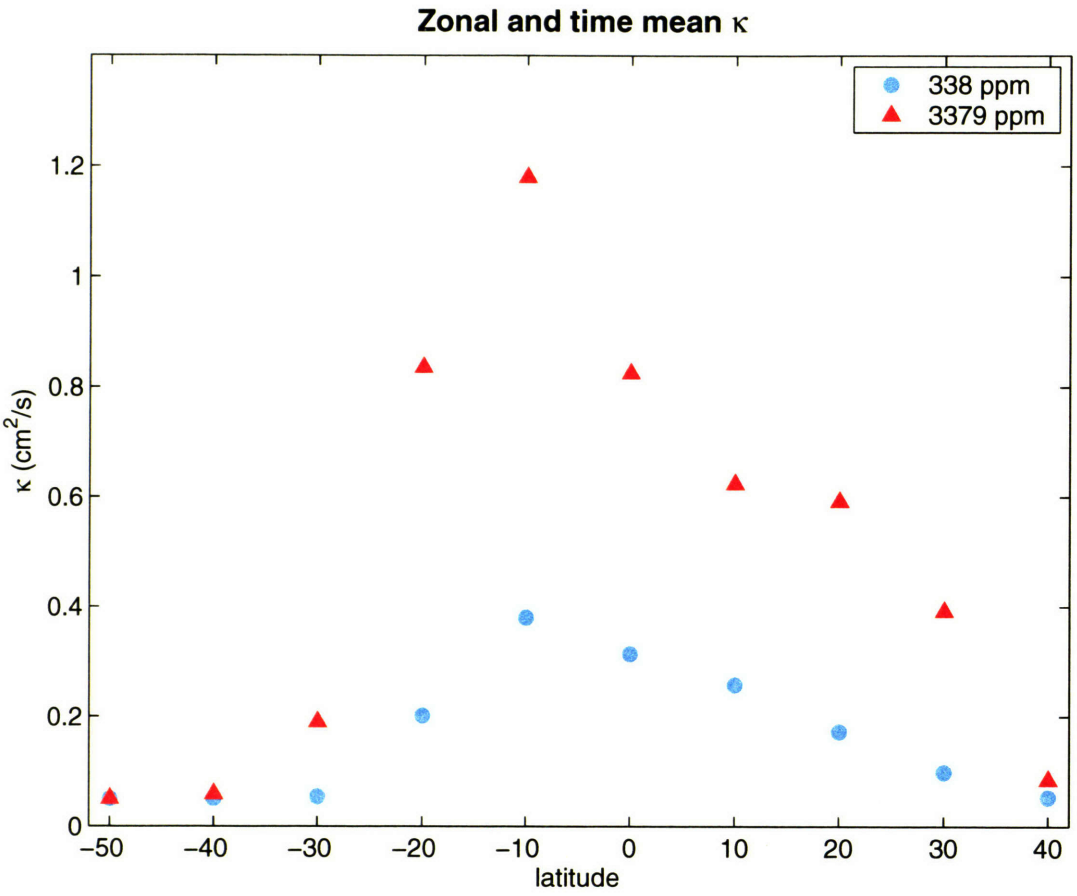

Figure 5-7: Vertical diffusion coefficients for $1\times CO_2$ (blue circles) and $10\times CO_2$ (red triangles). The diffusion coefficient takes the same value at all depths, but it varies horizontally according to the relation: $\kappa = a(\mathrm{PI})^6$, where PI is the potential intensity of tropical cyclones determined from a sounding and the sea surface temperature. The coefficient a was selected so that the the simulation of the present climate returned an average value of κ of about 0.3 cm^2/s along the equator. Because the potential intensity increases by about 20% in the elevated carbon dioxide experiment, the amplitude of the diffusion coefficients increase by a factor of 3.

The circulations and heat fluxes are shown in figure 5-9 for the present climate and in figure 5-10 for the high carbon dioxide experiment. [Recall that the value of a in equation (5.12) was chosen to reproduce the present climate control case (with uniform diffusion of 0.3 cm^2/s) by tuning κ to be 0.3 cm^2/s in the deep tropics.] In the high carbon dioxide experiment, the stronger mixing produces a more vigorous circulation, as expected. With it, the peak values of the global heat flux are approximately 25% stronger than they are in the simulation of the present climate.

One consequence of this enhanced upwelling is a reduction in tropical sea surface temperatures. Figure 5-11 shows the difference between two simulations forced with 3379 ppm carbon dioxide. For this plot, the control had uniform vertical diffusion of

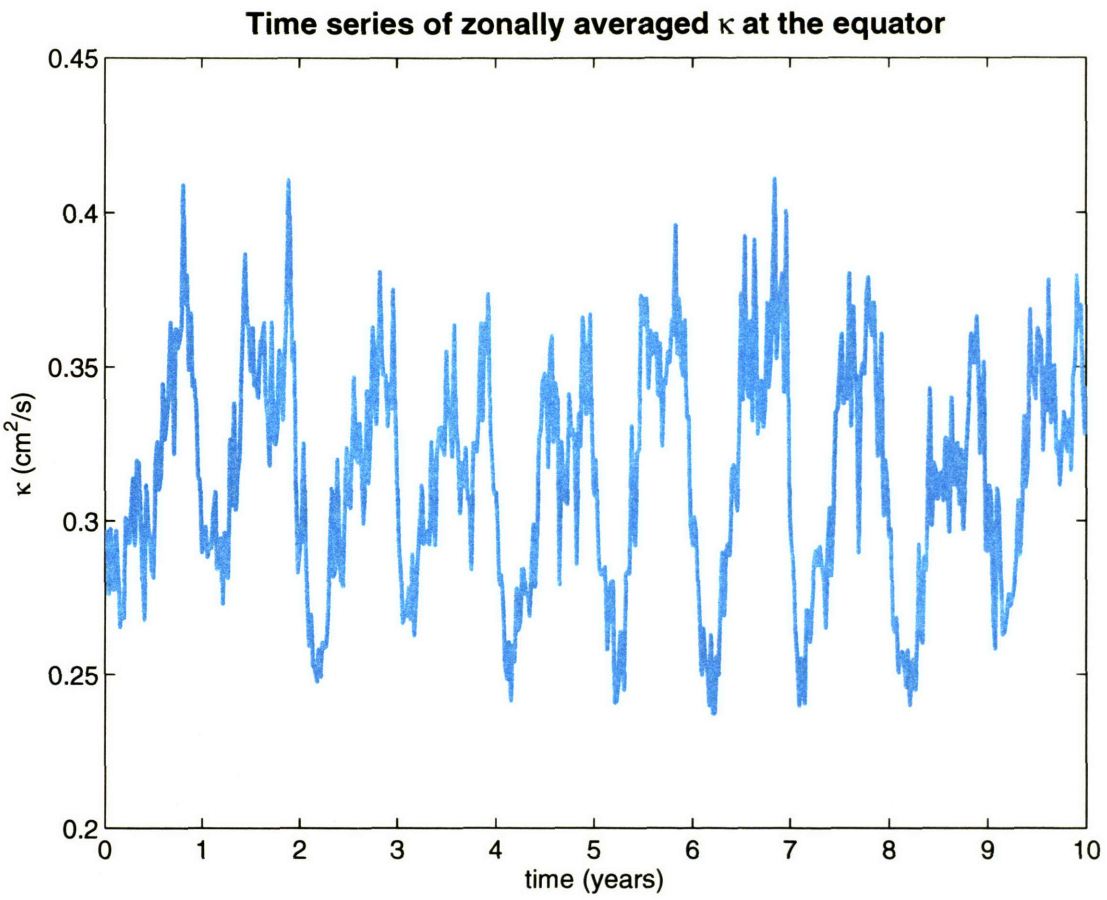

Figure 5-8: Zonally averaged κ at the equator from experiment with contemporary CO_2 (338 ppm). This series is lifted from the last decade of the coupled experiment, but the range is typical of the longer series. Note that values reach a seasonal minimum shortly after January and grow with sea surface temperatures.

0.3 cm^2/s; the circulation from this experiment was shown in figure 5-3. The other experiment had interactive mixing given by equation (5.12). Note that the main impact of the interactive mixing has been to reduce the pole-to-equator temperature gradient: the tropics are now about a degree cooler while higher latitudes are warmer. The reader is cautioned that the two simulations are not strictly comparable, as they use slightly different flux adjustments. (Differences are, however, small.) Nevertheless, the response to interactive mixing is encouraging: stronger mixing can narrow the gap between proxy data and model simulations. The sea surface temperatures peak at 36°C in the simulation with fixed mixing, but are never higher than 34°C in the one with interactive mixing. Still, this combination of elevated carbon dioxide and interactive mixing parameterization falls short of an equable climate. But what if the mixing were to respond to changes in stratification as well?

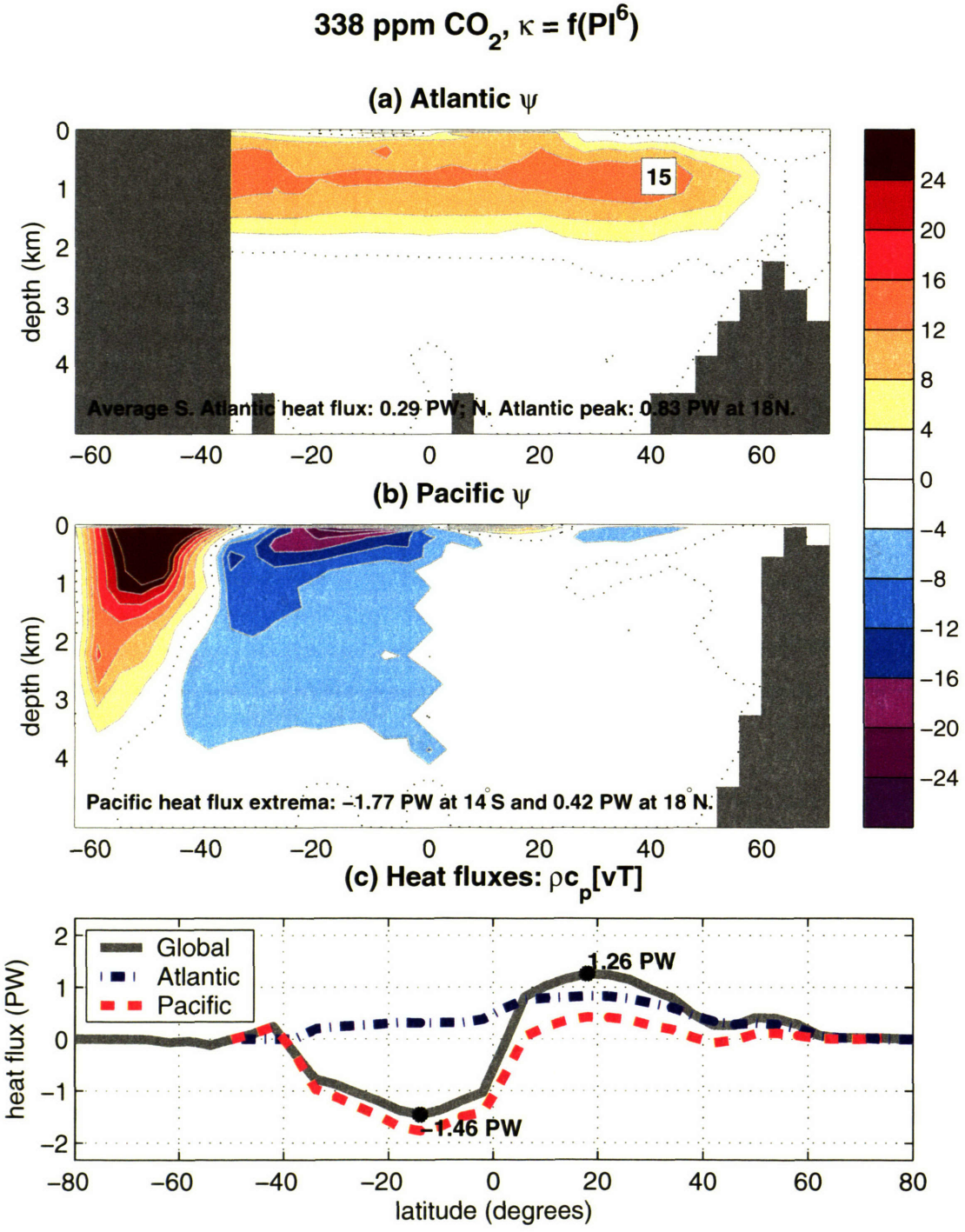

Figure 5-9: The overturning circulation and heat fluxes from a simulation with present carbon dioxide (338 ppm) and variable, interactive mixing. The value of the diffusion coefficient, κ, is a function of the sixth power of the potential intensity of tropical cyclones at each point in latitude and longitude (see text for discussion). The diffusion coefficient takes the same value from the surface to the ocean bottom.

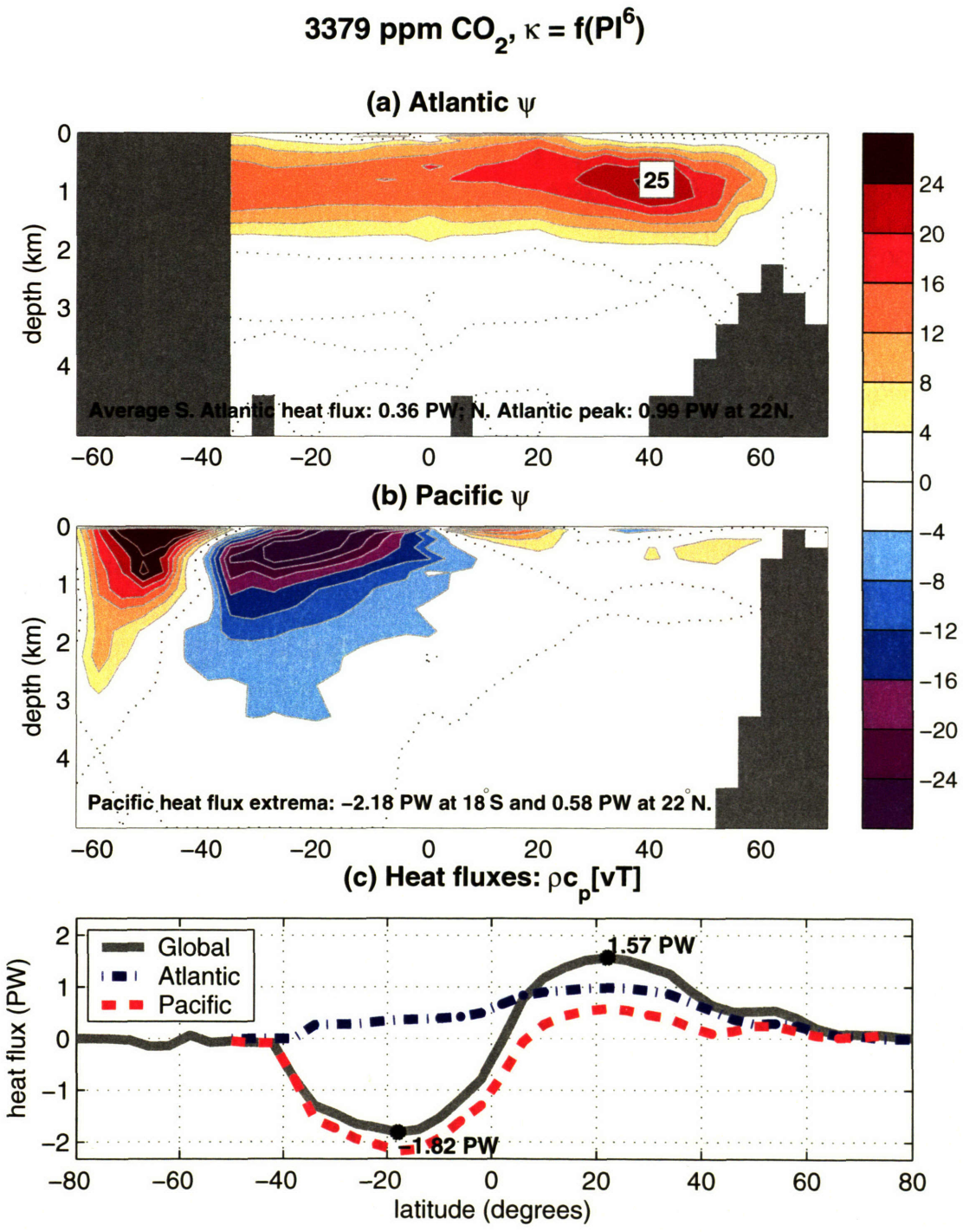

Figure 5-10: The overturning circulation and heat fluxes from a simulation with high carbon dioxide (3379 ppm) and variable, interactive mixing. The value of the diffusion coefficient, κ, is a function of the sixth power of the potential intensity of tropical cyclones at each point in latitude and longitude (see text for discussion). The diffusion coefficient takes the same value from the surface to the ocean bottom.

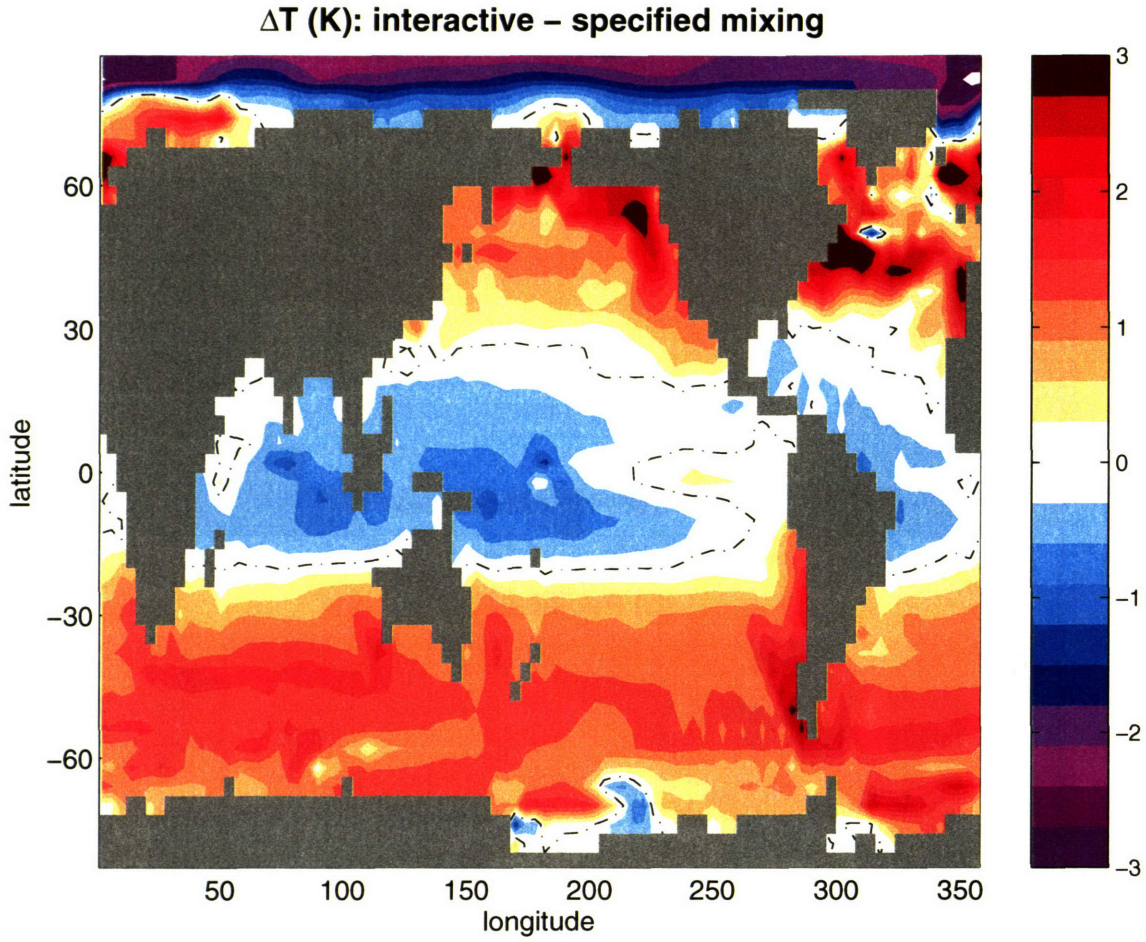

Figure 5-11: Change in sea surface temperatures between two simulations forced with 3379 ppm carbon dioxide. One (the control) had imposed, uniform mixing, and the circulation was presented in figure 5-3. The other had mixing scale with the sixth power of potential intensity; its circulation was shown in figure 5-10. Note that the tropical temperatures are cooler and high latitudes warmer when mixing is made interactive. The Arctic, which is largely isolated from the ocean general circulation to its south, is several degrees cooler in the interactive run. Seasonal sea ice persists longer in the interactive run, which holds the annual mean temperatures down.

5.4 Including a stratification feedback

Recent work by Lyle (1997) and Nilsson et al. (2003) examined the consequences of applying a stratification-dependent mixing scheme to an ocean with a weak surface buoyancy gradient. To the extent that the vertical buoyancy gradient also weakens, this allows stronger mixing and a stronger circulation, as it is the energy available for mixing, rather than the mixing itself, that is held constant in these parameterizations. It is not clear *a priori* that a warmer climate will generate a weaker buoyancy gradient. Manabe and Bryan (1985) found that the surface density gradient changed little over

experiments in which carbon dioxide was varied by a factor of eight, owing to the nonlinearity of the equation of state. They found Atlantic overturning circulations of roughly equal intensity in each experiment, as the imposed mixing was held constant.

And even though a stratification-dependent mixing scheme can produce a stronger circulation with a weaker density gradient, the heat flux will not generally be stronger. To see this, consider the following. Classic scaling (Welander, 1986) predicts that if mixing is constant, the overturning circulation will scale with $\Delta\rho^{1/3}$ and the heat flux with $\Delta\rho^{4/3}$, as $F \sim \psi \cdot \Delta T$. But as Nilsson et al. (2003) pointed out, if the energy available for mixing is fixed, rather than the mixing itself, then

$$\psi \sim \Delta\rho^{-1/3}\varepsilon^{2/3} \tag{5.13}$$

as $\varepsilon \sim \kappa/\Delta\rho$. Given this constraint, a decrease in the pole-to-equator temperature gradient will reduce the pole-to-equator density difference, which in turn should increase the overturning circulation.[6] Note however, that even though mixing increases with warm climates if the energy available for mixing is held constant, the heat flux will not increase with the density gradient because it scales with $\psi \cdot \Delta T$; if the temperature gradient alone affects the density gradient (ignoring salt variations), then the relation given by equation (5.13) yields:

$$\begin{aligned} F &\sim \psi \cdot \Delta T \\ &\sim \Delta\rho^{2/3}\varepsilon^{2/3}; \end{aligned} \tag{5.14}$$

weaker density gradients will still lead to weaker heat fluxes. (A strong heat flux requires a strong circulation and a strong temperature contrast; the circulation cannot increase enough to compensate for the decreased temperature contrast without an increase in the energy available to mixing.)

In this section, we add a stratification dependence to the mixing scheme tested in the last section. Gargett (1984) introduced a parameterization that varies inversely with the local buoyancy frequency:

$$\kappa(x, y, z) = \frac{a}{N(x, y, z)}; \tag{5.15}$$

Nilsson et al. (2003) recently applied this parameterization to a study with buoyancy gradients applicable to a wide variety of climate states. We adopt the following mod-

[6]This somewhat counterintuitive result follows directly from the assumption of fixed energy available for mixing. Lifting a parcel of water from the deep ocean adiabatically (against the stratification) requires work as the potential energy of the parcel increases. This work is performed by small-scale vertical mixing, which heats the rising cold water at a rate that keeps its buoyancy neutral (Nilsson et al., 2003). If the energy supply to the small-scale vertical mixing is fixed, a weaker stratification will allow for stronger upwelling. Energetically, this small-scale mixing and the associated production of potential energy should be viewed as the driving agent of the upwelling (Munk and Wunsch, 1998; Nilsson et al., 2003).

ification: the coefficient a will vary with the potential intensity of tropical cyclones equatorward of 30°. Implicitly, this assumes that the internal wave energy varies with the power put into the oceans by tropical cyclones [see section 2 of Nilsson et al. (2003) for a discussion and derivation of the energetics of various stratification-dependent mixing schemes]. We impose a parameterization of mixing that combines the stratification dependence with equation (5.12) in the tropics, but uses a $1/N$ dependence at higher latitudes; that is,

$$\kappa(x,y,z) = \begin{cases} b \cdot [\mathrm{PI}(x,y)]^6 / N(x,y,z) & \phi < 30° \\ c/N(x,y,z) & \phi > 30° \end{cases} \tag{5.16}$$

where b was chosen such that the diffusion coefficient was 0.3 cm^2/s at 100 m in the tropical Pacific; its value is $1.6855 \times 10^{-18}\,\mathrm{s}^5/\mathrm{m}^6$. The value of c was chosen in a similar manner from an earlier experiment in which the c/N dependence was imposed at all latitudes; these experiments are not shown, but the value of c was selected to be 3×10^{-7} s to give a diffusivity of about 0.3 cm^2/s in the upper tropical ocean. [For comparison, note that Nilsson et al. (2003) implemented equation (5.15) and chose the coefficient to be 7×10^{-7} s, but their model was a single hemisphere only.]

After running a spin-up with the new parameterization given by equation (5.16), two coupled experiments were run. The circulations for the present and high carbon dioxide experiments are shown in figures 5-12 and 5-13, respectively. With warm sea surface temperatures, the high carbon dioxide experiment produces vigorous tropical mixing owing to the PI^6 dependence in equation (5.16) equatorward of 30°. As shown in figures 5-14 and 5-15, the zonally averaged diffusivities increase by a factor of two or three throughout the tropics with the higher sea surface temperatures, but now there is a modification by the $1/N$ dependence. Note that diffusivities increase in the abyssal ocean in both simulations, owing to the weak stratifications found at these depths. As noted by several authors, this has little impact on the heat flux, but can affect the abyssal circulations (Cummins et al., 1990; Scott and Marotzke, 2002).

With the stratification-dependence included, mixing is strong in the weakly stratified abyss. Note that the increase in PI with higher carbon dioxide ramps up the energy available for mixing. The stronger diffusivities create a stronger circulation, which in turn supports a much stronger heat flux. Compared to the present climate, the peak oceanic heat flux increases by 27% in the Northern Hemisphere and by 40% in the Southern Hemisphere when carbon dioxide is high and mixing is dependent on both stratification and energy from tropical cyclones. This combination of dependencies produces a spectacular response in the sea surface temperature fields.

In figure 5-16, the difference in sea surface temperatures between two runs with high carbon dioxide are shown. The run in this section, in which mixing depends on both stratification and potential intensity according to equation (5.16), is compared with the run in which mixing was specified to be 0.3 cm^2/s everywhere. Note that the upwelling of abyssal waters and strong heat flux out of the tropics leaves temperatures

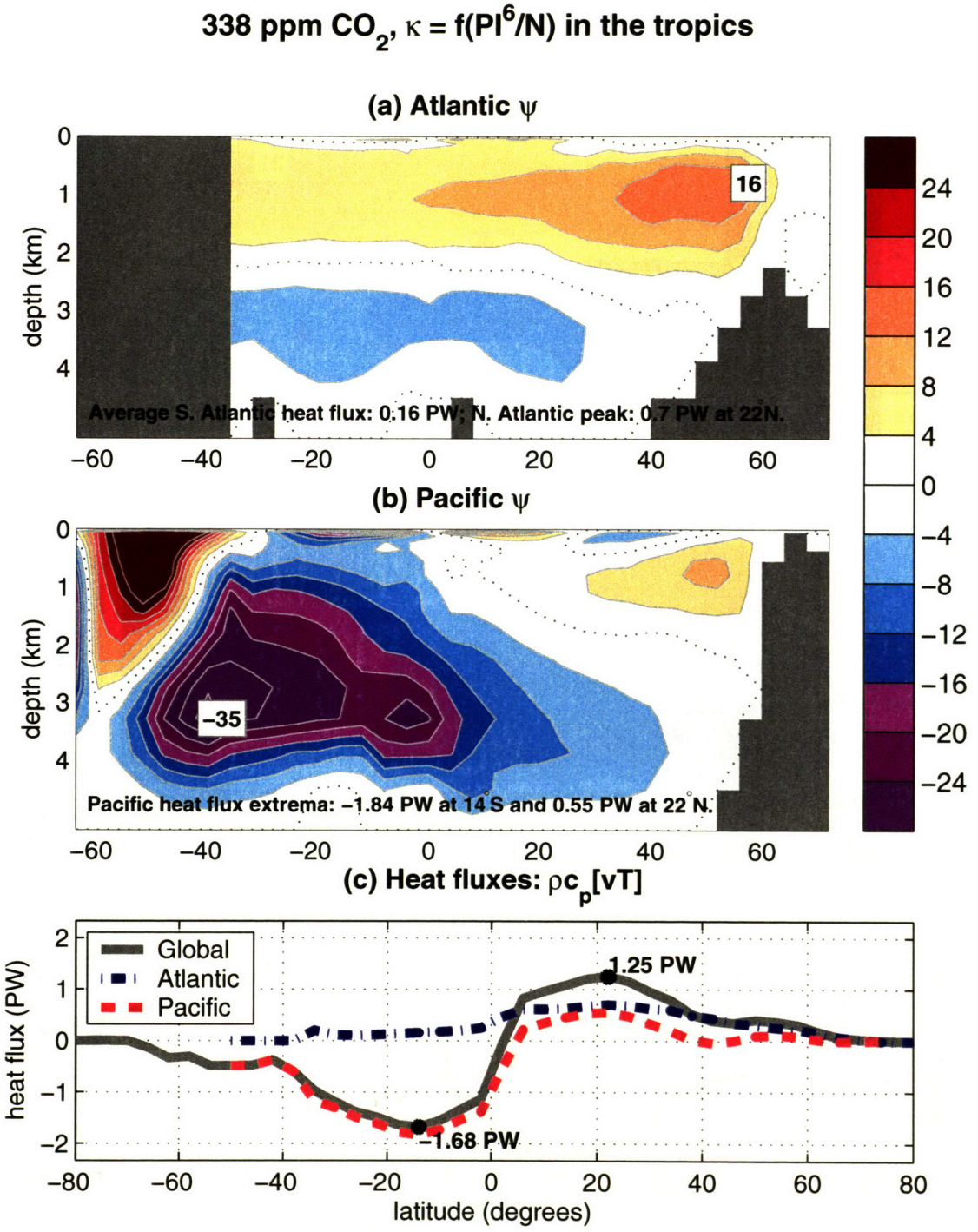

Figure 5-12: The overturning circulation and heat fluxes from a simulation with present carbon dioxide (337.9 ppm) and variable, interactive mixing. Equatorward of 30° latitude, the value of the diffusion coefficient, κ, is a function of the sixth power of the potential intensity of tropical cyclones and the inverse of the buoyancy frequency, N. Poleward of 30° latitude, κ varies as N^{-1} only. At each point in the ocean, κ is determined from the local stratification; the amplitude through the water column is multiplied in the tropics as a function of the potential intensity (see text for more details).

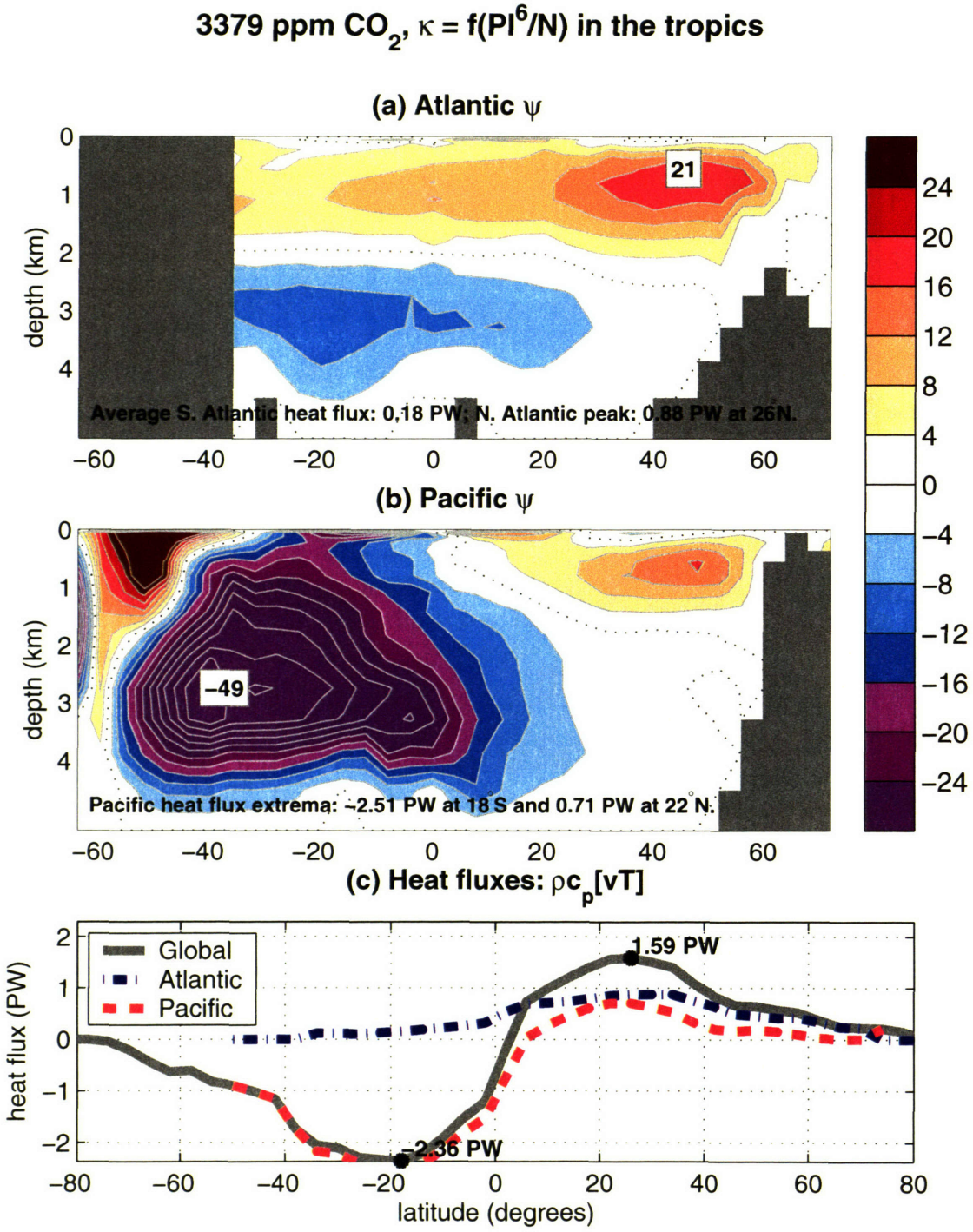

Figure 5-13: The overturning circulation and heat fluxes from a simulation with high carbon dioxide (3379 ppm) and variable, interactive mixing. Equatorward of 30° latitude, the value of the diffusion coefficient, κ, is a function of the sixth power of the potential intensity of tropical cyclones and the inverse of the buoyancy frequency, N. Poleward of 30° latitude, κ varies as N^{-1} only. At each point in the ocean, κ is determined from the local stratification; the amplitude through the water column is multiplied in the tropics as a function of the potential intensity (see text for more details).

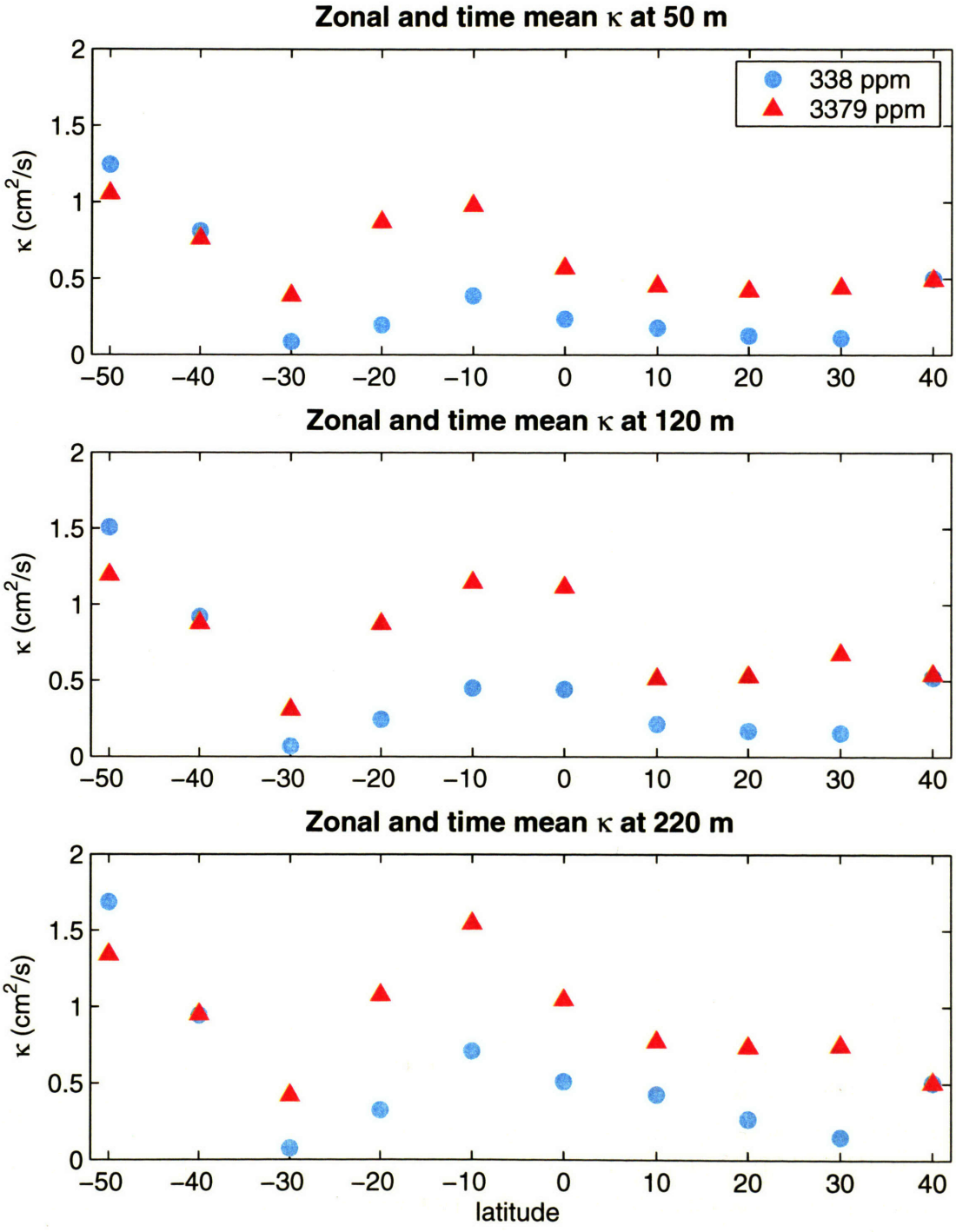

Figure 5-14: The value of the zonally and temporally averaged (over the last century of each simulation) diffusion coefficients at 50, 120, and 220 m for simulations implementing the mixing scheme given by equation (5.16). The present climate is shown with blue circles, and one with ten times more carbon dioxide is shown in red triangles.

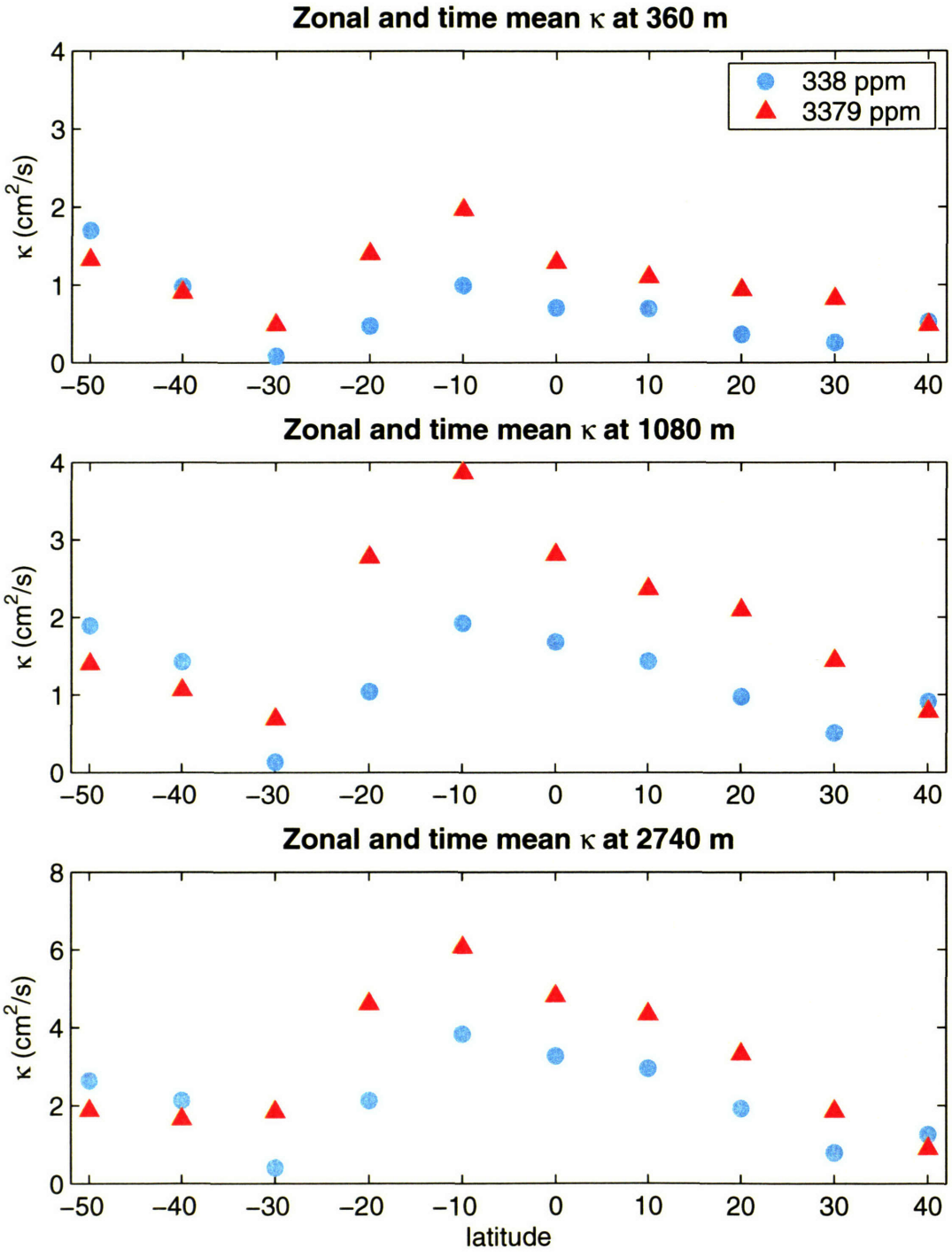

Figure 5-15: The value of the zonally and temporally averaged (over the last century of each simulation) diffusion coefficients at 360, 1080, and 2740 m for simulations implementing the mixing scheme given by equation (5.16). The present climate is shown with blue circles, and one with ten times more carbon dioxide is shown in red triangles.

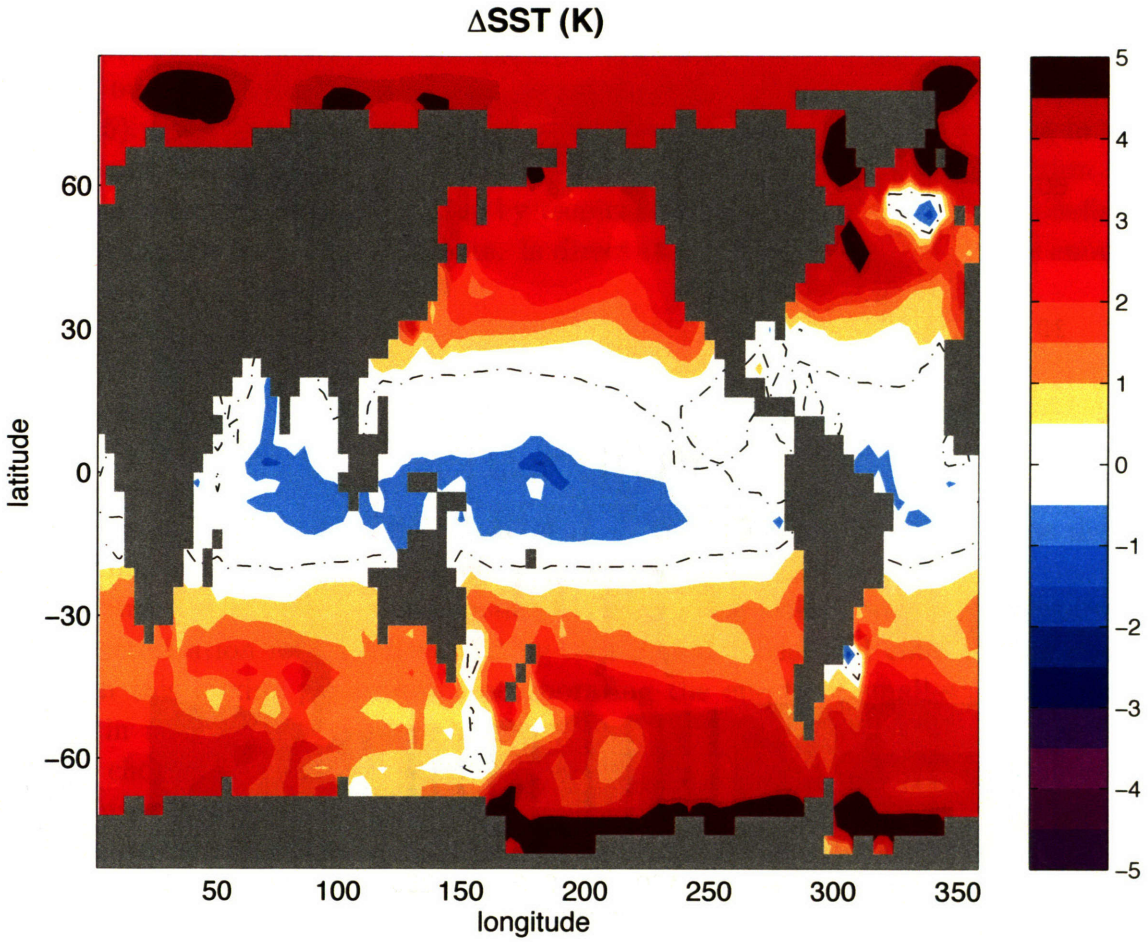

Figure 5-16: Change in sea surface temperatures between two simulations forced with 3379 ppm carbon dioxide. One (the control) had imposed, uniform mixing, and the circulation was presented in figure 5-3. The other had interactive mixing given by equation (5.16); its circulation was shown in figure 5-13. Note that the tropical temperatures are cooler and high latitudes warmer when mixing is made interactive.

about a degree cooler in low latitudes, and the strong heat flux warms the extratropics by several degrees.

In fact, the combination of high carbon dioxide and the parameterization given by equation (5.16) come closer to producing an equable climate than any previous modeling study. The predicted sea surface temperature distribution moves to within striking distance of replicating the warm climate states common in the early Cenozoic. Sea surface temperatures from this experiment are shown in figure 5-17. Note that temperatures in the Arctic and along the Antarctic coast are well above freezing, while tropical temperatures remain a few degrees warmer than recent proxy estimates (e.g., Pearson et al., 2001).

There remain a few outstanding issues with the stratification dependence, which

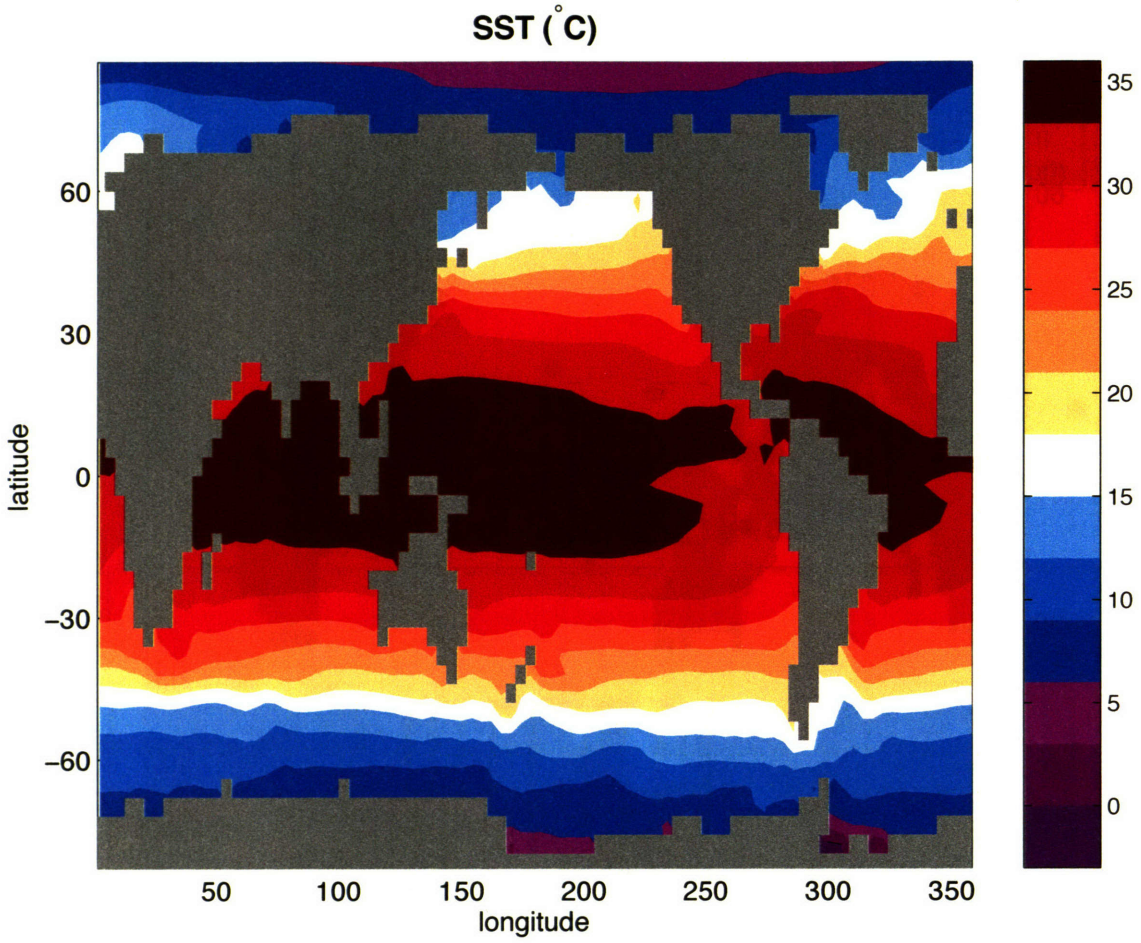

Figure 5-17: Sea surface temperatures from a run with high carbon dioxide (3379 ppm) and a mixing parameterization given by equation (5.16). This produces sea surface temperatures that are closer to an equable climate: tropical temperatures are 33-36°C, a bit higher than suggested by recent estimates (Pearson et al., 2001), while polar temperatures are above freezing.

merit further examination. In many of the experiments I did, the response was sensitive to the exact formulation of the mixing parameterization and the values chosen for the normalizing coefficients. Often, the high load of carbon dioxide would force the ocean mixed-layer to warm quickly, but the abyssal ocean beneath it remained cold. This creates a strong stratification at their interface, and if the coefficient was not large enough to produce sufficient mixing, the hot surface waters became isolated from the cold, deep ocean below.

Another concern is that the experiments shown in this and the previous section assume that mixing at all depths will scale with the potential intensity of tropical cyclones. While tropical cyclones do contribute to the internal wave field of the ocean (Nilsson, 1995), it is not clear what fraction of this energy is consumed by mixing

processes at depth. At the conclusion of the last chapter, we saw that mixing in the upper ocean is more important to the heat flux than is mixing at depth. This has been pointed out by Cummins et al. (1990), Scott and Marotzke (2002), and Boccaletti et al. (2005). This finding is confirmed by the simulation with elevated mixing in the upper tropical oceans alone that was presented in section 5.2. In the next section, we consider the impact of direct mixing by tropical cyclones, which is generally confined to the upper 200 meters of the ocean. Is direct tropical cyclone mixing alone enough to retain a strong impact?

5.5 Direct hurricane mixing

We now relax the assumption that abyssal mixing scales with the potential intensity. In this section, tropical cyclones will affect the upper ocean only, down the depth that turbulent entrainment penetrates. Does this kill the strong affect of interactive mixing that we saw in the last section? Before proceeding, we must first derive a parameterization for turbulent mixing in a global model and consider the depth to which this mixing penetrates. Incorporating the effects of small-scale turbulent mixing in a global model presents several immediate challenges. First, what is a sensible choice for the diffusion coefficient? To what depth does this mixing penetrate? What impact does it have on the heat fluxes and global circulation in a global model? We consider these issues in the sections that follow.

5.5.1 A sensible choice for the diffusion coefficient

Price and Sundermeyer (1999) investigated stratified Ekman layers and estimate that, in fair weather conditions, a sensible choice for the diffusion coefficient in the surface mixed-layer is on the order of 1000 cm^2/s. This is confined to the well-mixed region at the top of the ocean; the vigorous mixing there creates a nearly isothermal temperature profile from the sea surface to the top of the thermocline. Beneath this layer, mixing nearly disappears in the strongly stratified thermocline (e.g., Gregg, 1987; Raymond et al., 2004). Given the nearly nonexistent mixing at these depths, some thermocline theories assume it is absent all together, such as Luyten et al. (1983).

Estimates of mixing inferred from measurements taken in the tropical thermocline show that the diffusion coefficient is $O(10^{-5})$ m^2/s (Gregg, 1987; Wunsch and Ferrari, 2004). Our view, however, is that these measurements have largely captured the quiescent background. Recently, Raymond et al. (2004) presented data suggesting that rather than a slow, steady mixing, the thermocline is mixed only when the winds are strong enough to drive the local Richardson number below a critical threshold, creating a shear instability. They conclude that mixing is a highly transient event, and that only the strongest atmospheric disturbances are likely to account for most of what mixing occurs in the thermocline.

In low latitudes, tropical cyclones vigorously mix the upper ocean and cool the warm surface layer by entraining cold thermocline water. It is probably impossible to accurately characterize the turbulent entrainment that occurs below a tropical cyclone with a simple diffusion coefficient. Nevertheless, we are only after the cumulative effects of such mixing, which simplifies the problem considerably.

Measurements from within a hurricane are obviously difficult to secure. We know that an initial thermal profile in the undisturbed ocean is radically altered by the passage of a storm. Data collected from the ocean in advance of a storm often show a shallow surface-layer (anywhere from 25-200 m deep, depending on the region and time of year) in which temperatures are nearly uniform. Beneath this layer temperatures drop quickly, at a rate of about 8°C/100 m in the upper most ocean [see Schade (1994) and references therein]. When a storm passes over an ocean column, cold water from the upper thermocline is entrained into the surface-layer. The depth of the mixed-layer increases owing to the entrainment of thermocline parcels from below, and it oscillates in the wake owing to inertia-gravity waves. After a storm passes, temperatures are nearly uniform to a greater depth, but surface temperatures are now cooler because mixing stirred cooler waters to the surface. This transition is diagrammed in figure 5-18.

Given that the initial and final profiles are known, and given that mixing occurs only on a time-scale similar to that of the storm's passage, we can find the value of κ during the storm's passage. The initial profile shown in blue in figure 5-18 relaxes to the final one shown in red by the time direct mixing from the tropical cyclone has ceased. This process can be represented by diffusion using the heat conduction equation:

$$\frac{\partial T}{\partial t} = \kappa \frac{\partial^2 T}{\partial z^2}. \tag{5.17}$$

If no flux boundary conditions[7] are imposed and an initial profile is specified, then it is straight-forward to show that

$$T(z,t) = \sum_{n=1}^{\infty} c_n \cos\left(\frac{n\pi z}{L}\right) e^{-\kappa(n\pi/L)^2 t}, \tag{5.18}$$

where

$$c_n = \frac{2}{L}\int_0^L \cos\left(\frac{n\pi z}{L}\right) \left.\frac{\partial T(z,0)}{\partial z}\right|_{t=0} dz. \tag{5.19}$$

Here $T(z,0)$ is the initial profile, and L is the length over which the mixing occurs (h_f in figure 5-18). If the initial profile is represented by a single cosine wave, then κ can be estimated by specifying an e-folding time-scale for t, and substituting h_f into L. Given that a typical storm may induce intense mixing over a lateral distance of roughly 200 km, and that a typical translation speed is roughly 5 m/s, the initial

[7]These are reasonable given the rapidity of the mixing.

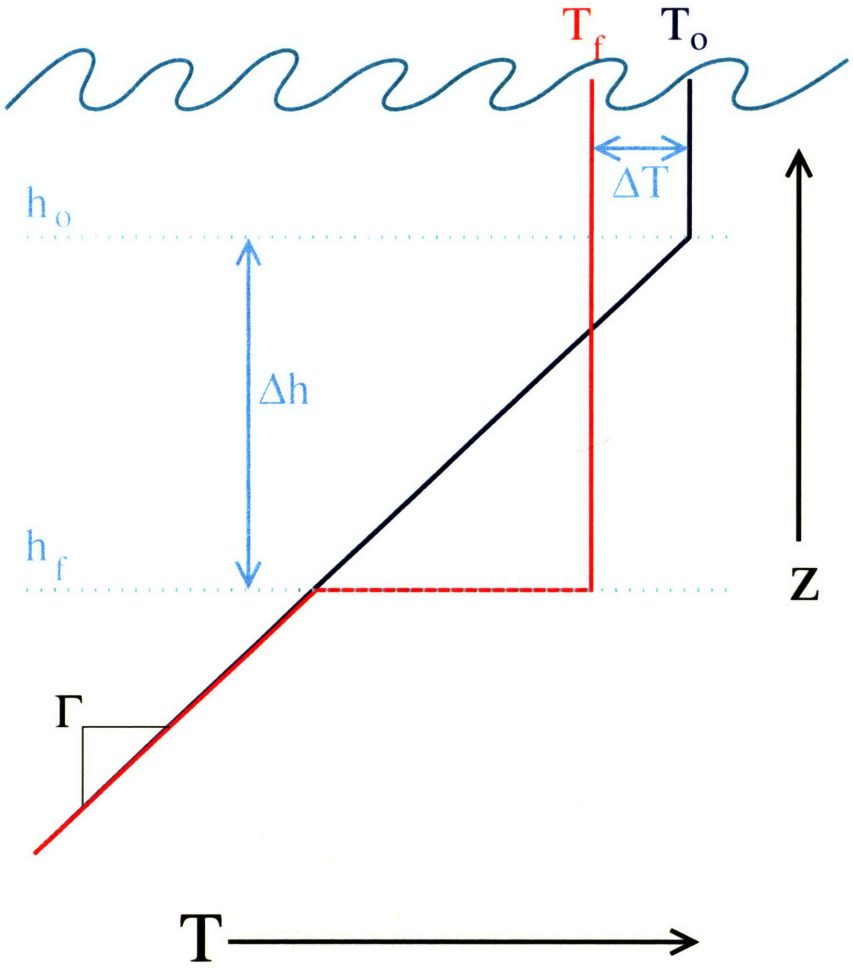

Figure 5-18: Temperature structure of the upper ocean before and after the passage of a hurricane. Initially, the surface layer has a uniform temperature of T_o to a depth of h_o; after vigorous mixing, colder thermocline waters are entrained into the surface layer and the temperature is mixed to a value of T_f to a depth of h_f. Below this level, the temperature profile is undisturbed.

profile must adjust to the final one within twelve hours, as intense mixing does not occur away from the core of the storm. To go through at least two e-foldings (to get to a nearly isothermal profile with depth), κ must be about 2000 cm^2/s.

Using a value of κ equal to 2000 cm^2/s, the initial profile shown in figure 5-19 is adjusted to the final one after twelve hours of mixing; this is the duration of intense mixing for a typical storm that spans 200 km and moves at 5 m/s. Note that the profile has yet to completely mix to become isothermal; this would require a diffusion coefficient 50-100% larger in magnitude. Nevertheless, setting κ equal to 2000 cm^2/s produces a reasonable final profile, with surface cooling of about 4°C.

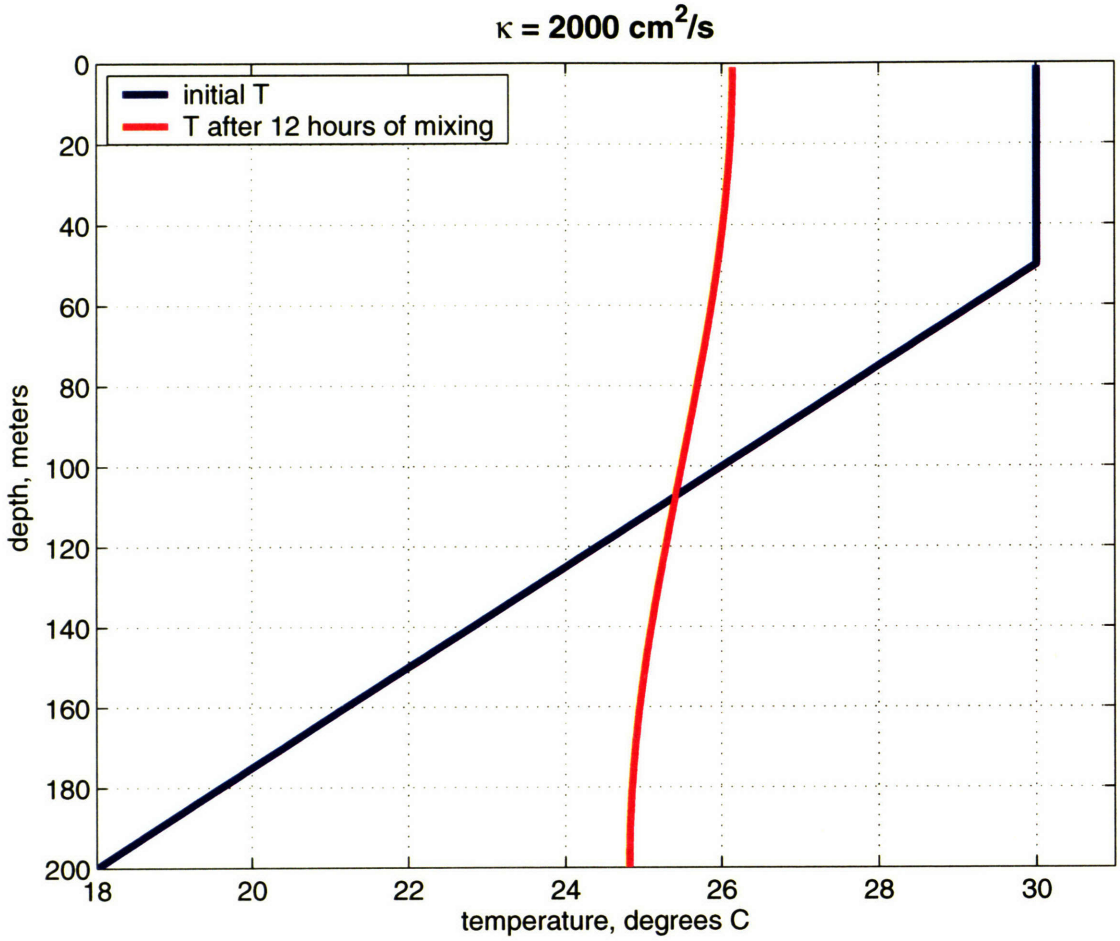

Figure 5-19: Before a hurricane induces mixing in the upper ocean, the initial profile (blue) consists of a well-mixed surface layer (isothermal to 50 m depth), and a stratified upper thermocline. Temperatures decrease at a rate of 8°C/100 m. After twelve hours of mixing with a diffusion coefficient of 2000 cm^2/s, the vertical temperature profile adjusts to the final one (red).

5.5.2 Depth to which the mixing penetrates

Changes in sea surface temperatures and the depth of the mixed-layer are directly related to the amount of thermocline water entrained into the surface layer. The fundamental premise behind the mixing closure developed by Price (1979) and used by Schade (1994) and Emanuel et al. (2004) is the constancy of the bulk Richardson number, which is defined:

$$Ri \equiv \frac{gh\Delta\rho}{\rho u^2} \tag{5.20}$$

where u and h are the mixed-layer velocity and depth, respectively. If the density jump is just what results from eroding a constant background stratification, N, down

to a depth h, equation (5.20) becomes

$$Ri \equiv \frac{1}{2}\frac{h^2 N^2}{u^2} \tag{5.21}$$

or simply

$$Nh = R^\star u, \tag{5.22}$$

where $R^\star \equiv \sqrt{2Ri}$. The Price formulation assumes that $R^\star$ is always at a critical value, here around 1.

Given the rapidity with which this entrainment occurs, the turning by the Coriolis force can be neglected (Schade, 1994), and the mixed-layer momentum budget may be written:

$$\frac{\partial\left(\rho_w u h\right)}{\partial t} = \rho_a u_*^2, \tag{5.23}$$

where $\rho_a u_*^2$ is the surface stress; u_* is the friction velocity.[8] By combining equations (5.22) and (5.23), we obtain:

$$\frac{\partial h^2}{\partial t} = R^\star \frac{\rho_a}{\rho_w}\frac{u_*^2}{N}. \tag{5.24}$$

Integrating equation (5.24) over the time it takes for the storm to pass over each ocean column, we get an expression for the depth to which the mixing penetrates:

$$h^2 = h_o^2 + R^\star \frac{\rho_a}{\rho_w}\frac{u_*^2}{N}\tau, \tag{5.25}$$

where τ is duration of the storm's wind forcing in seconds. The right-hand-side of equation (5.24) can be regarded as the effective diffusion coefficient on dimensional grounds. This is the rate at which the square of the mixed-layer changes owing to turbulent entrainment. Sensible choices for the parameters are $R^\star \sim \mathrm{O}(1)$, $\rho_a \sim \mathrm{O}(1)$, $\rho_w \sim \mathrm{O}(10^3)$, $u_*^2 \sim \mathrm{O}(1)$, and $N \sim \mathrm{O}(10^{-2})$, giving a diffusion coefficient of $\mathrm{O}(10^{-1})$ m^2/s, which is what we found in the last section. Equation (5.25) shows that the depth to which the mixing penetrates will increase linearly with the wind speed and as $1/\sqrt{N}$. A slightly more detailed derivation is presented in Appendix E.

We shall model the depth to which mixing penetrates based on the derivation in Appendix E; it agrees with the dependence found by Schade (1994). The depth to which the mixing penetrates depends on the strength of the storms (potential intensity) and thermocline stratification:

$$h_o + \Delta h = h_o + h_\star \left(\frac{u}{u_\star}\right)^{1.2}\left(\frac{\Gamma}{\Gamma_\star}\right)^{-.3}. \tag{5.26}$$

[8]N.B. The friction velocity, u_*, is defined: $u_*^2 = C_D u^2$, where u is the ten meter wind speed and C_D is the drag coefficient, typically about 0.001.

With the model-calculated potential intensity [u in equation (5.26)] and stratification (Γ), the depth may be explicitly calculated once normalizing factors are specified. We take $h_\star$ to be 94.05 m, $u_\star$ to be 75 m/s, and $\Gamma_\star$ to be 8°C/100 m; h_o, the background mixed-layer depth, is 50 m. Several regions of the tropical oceans have mixed-layers deeper than 50 m, but few are shallower than this. These choices are based on the present climate, and we allow the model to evolve with higher carbon dioxide.[9]

5.5.3 Temporal and spatial average of κ

Now that we have a sensible estimate for the diffusion coefficient in the presence of intense mixing, what is a temporally and spatially averaged value? We rely heavily on the earlier work of Scott and Marotzke (2002), who showed that mixing can be concentrated in space, and of Boos et al. (2004), who showed that mixing can be isolated in time. Their work showed that changes in the ocean's circulation were dependent on variations in the spatially and temporally averaged mixing value, and that concentrating mixing in infrequent or localized bursts can produce circulations that behave as though the mixing were spread uniformly over space and in time. The spatial averaging is a bit trickier because mixing is more important in some locations than in others. For example, as we saw again in the last chapter, mixing at tropical latitudes is far more important than mixing at high latitudes in driving the meridional overturning circulation (Scott, 2000; Bugnion, 2001). Because we are interested in an average value of mixing in regions affected by tropical cyclones, we confine the area of interest to those latitudes equatorward of 30°.

We assume the background value of κ is 0.3 cm^2/s in the upper ocean below the mixed-layer (Bryan and Lewis, 1979). This is the value of mixing to which the upper ocean is subjected most of the time; it is nearly quiescent. But as discussed above, the upper most tropical ocean is subjected to intense and localized blasts when a tropical cyclone passes by. Here we wish to average this blast over space and time.

Consider the area mixed by a single storm shown in figure 5-20. The swath of ocean subjected to mixing by a tropical cyclone will scale with a cross-track length scale, L_y, multiplied by the length of the track, $U_T \cdot \tau$, where U_T is the translation speed and τ is the duration of the storm. The total area of the world's oceans exposed to mixing in a given year will be

$$A_m = N \cdot L_y \cdot U_T \cdot \tau, \tag{5.27}$$

where N is the number of storms that occur globally. The spatial average of κ is then:

$$[\kappa] = \kappa_{tc} \cdot \frac{A_m}{A_t} + \kappa_b \cdot \frac{A_t - A_m}{A_t}, \tag{5.28}$$

[9]The small discrepancy between the exponents used in equation (5.26) and equation (5.25) is discussed in Appendix E. They are quite similar, but the expression given by equation (5.26) more nearly replicates the behavior of a coupled hurricane-ocean model found by Schade (1994).

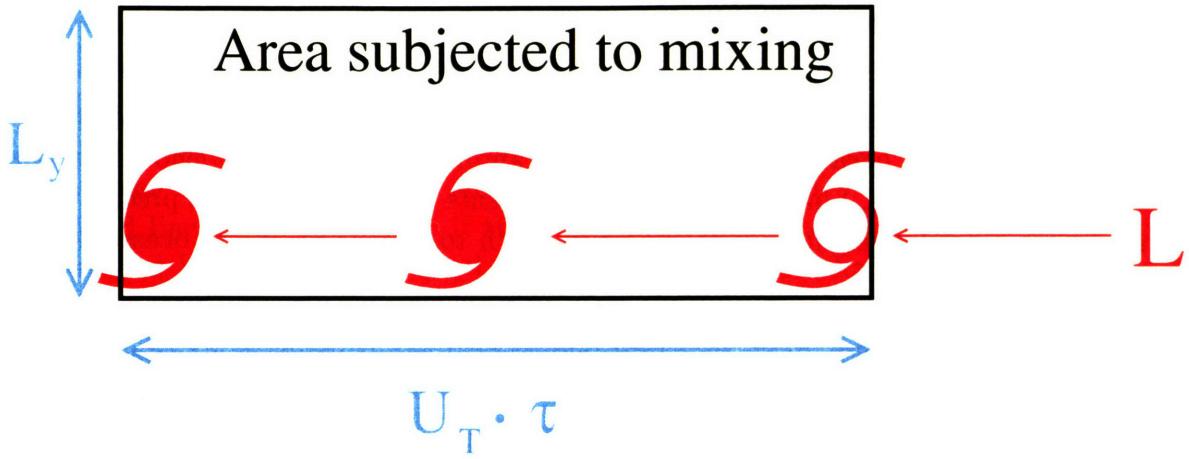

Figure 5-20: The area of the tropical ocean subjected to intense mixing by a hurricane. At any point perpendicular to the storm's motion, parallel to L_y, mixing occurs for a period of L_x/U_T, where L_x is a characteristic scale over which intense mixing occurs.

where κ_{tc} is the value of κ in the presence of a tropical cyclone (2000 cm^2/s based on the arguments made in section 5.5.1), A_t is the area of the tropical oceans (approximately $0.7 * 2\pi R_e^2$, where $2\pi R_e^2$ is the surface area of the Earth equatorward of 30°, and 0.7 is the fraction of that region that is ocean), κ_b is the background value of mixing (0.3 cm^2/s), and A_m is determined by equation (5.27).

It remains then to average this value in time. Each point visited by a tropical cyclone is exposed to mixing for L_x/U_T seconds, where L_x must be the along-track distance over which intense mixing occurs within a storm, a value that will scale with the radius of maximum winds. Then

$$\begin{aligned}
[\overline{\kappa}] &= \kappa_{tc} \cdot \frac{A_m}{A_t} \cdot \frac{L_x/U_T}{s_y} + \kappa_b \cdot \frac{s_y - L_x/U_T}{s_y} \cdot \frac{A_t - A_m}{A_t} \\
&= \kappa_{tc} \cdot \frac{N L_y L_x \tau}{s_y A_t} + \kappa_b \cdot \frac{s_y - L_x/U_T}{s_y} \cdot \frac{A_t - A_m}{A_t} \\
&\approx \kappa_{tc} \cdot \frac{N L_y L_x \tau}{s_y A_t} + \kappa_b \\
&\approx \{\kappa_{tc}\} + \kappa_b. \qquad (5.29)
\end{aligned}$$

Because s_y is the number of seconds in a year, the value of $[\overline{\kappa}]$ given by equation (5.29) is the annual and tropical spatial average of κ. We used the facts that $A_m \ll A_t$ and $L_x/U_T \ll s_y$ to approximate equation (5.29). The notation $\{\kappa_{tc}\}$ is shorthand for the product $\kappa_{tc} N L_y L_x \tau / (s_y A_t)$.

It is interesting that in the current climate, $N \cdot \tau / s_y$ is approximately 1, though this has grown to a slightly larger value in the last decade owing to an increase in τ (Emanuel, 2005). This is equivalent to having one continuous tropical cyclone somewhere in the world at all moments in a given year. Substituting values of $L_y =$

$L_x = 200$ km, one finds that

$$[\overline{\kappa}] \approx 0.8 \text{ cm}^2\text{s}^{-1}. \tag{5.30}$$

This is significantly higher than the background value of 0.3 cm^2/s, but applies only to the upper most ocean. Though the exact amplitude is highly dependent on the choices of parameters, I have done some experiments and found that the precise value chosen for $[\overline{\kappa}]$ is less significant than is the depth to which this upper ocean mixing penetrates.

5.5.4 Model results

To test whether tropical cyclones do enough mixing of the upper tropical oceans to weaken the meridional temperature gradient (without appealing to enhanced mixing through the entire water column), we constructed an experiment incorporating the dependencies derived in the previous sections. We allow the amplitude of the diffusion coefficient in the upper ocean to vary with both tropical cyclone genesis and entrainment intensity.

Based upon the findings of Emanuel and Nolan (2004), we believe the number of tropical cyclones will vary with the third power of the potential intensity of tropical cyclones. As seen in section 5.5.2, both storm intensity and thermocline stratification govern the strength of the turbulent entrainment. Strong storms deposit large amounts of momentum into the surface layer, which generates a shear across the base of the mixed-layer. Thermocline stratification impedes the progress of turbulent entrainment by creating a density jump between the well-mixed layer and the colder waters below. This dependence was shown in equation (5.25), and combined with the genesis rate, we expect the strength of the mixing to vary with the fifth power of potential intensity and inversely with N.

We implement a parameterization of tropical cyclone mixing as follows:

$$\{\kappa_{tc}(x,y)\} = 5.0 \times 10^{-5} \left[\frac{\text{PI}(x,y)}{75}\right]^5 \left[\frac{dT(x,y)/dz}{0.08}\right]^{-1/2}, \tag{5.31}$$

where PI is the potential intensity (in m/s) and dT/dz is the vertical derivative of temperature (in °C/m), which is proportional to N^2 when salinity variations are ignored. The averaged potential intensity and thermocline stratification in the deep tropics were diagnosed in the experiment with present amounts of carbon dioxide and uniform mixing; these were taken to be the normalizing factors in equation (5.31) so that the cumulative, average mixing from tropical cyclones, $\{\kappa_{tc}\}$, will have a value of $O(10^{-5})$ m^2/s in the present climate (as was estimated in section 5.5.3). The justification for these specific choices can be made only crudely, but the principal goal of this experiment is to examine the qualitative behavior with this type of dependence. Equation (5.31) was added to a background value of 0.3 cm^2/s down to a depth given by equation (5.26). Below this depth, the diffusion coefficient remains 0.3 cm^2/s.

Given that this model has discrete and coarsely spaced interfaces at which vertical diffusion is applied, we incorporate the depth dependence as follows. The top model box is 50 m deep, and is assumed to be well-mixed. The second model box extends from 50-120 m; the third from 120-220 m. If the depth given by equation (5.26) is between 50 and 120 m, the amplitude of $\{\kappa_{tc}\}$ applied to the 50 m interface is adjusted linearly; for example, if the mixing penetrates to 85 m, half way through the second box, the value of $\{\kappa_{tc}\}$ at the 50 m interface is half that given by equation (5.31). If the depth exceeds 120 m (but not 220 m), then the full value of equation (5.31) is added to the background profile at 50 m, and the diffusion applied at the 120 m interface is adjusted accordingly.

We ran two experiments: one to replicate the present climate, and another with ten times the present amount of carbon dioxide. In the latter experiment, sea surface temperatures are considerably warmer, and stronger storms produce more vigorous mixing of the upper tropical oceans. The circulation for the present climate is shown in figure 5-21, and the simulation with ten times more carbon dioxide is presented in figure 5-22.

A comparison of the two runs shows that the Atlantic circulation is largely unchanged, as are the heat fluxes. The abyssal circulations are weaker in the high carbon dioxide experiment, though these do not have a strong affect on the heat flux (Cummins et al., 1990; Scott and Marotzke, 2002; Boccaletti et al., 2005). Otherwise, however, the circulations are remarkably similar.

The mixing in the upper oceans does increase with the higher sea surface temperatures and potential intensity of tropical cyclones. Figure 5-23 shows the zonally averaged diffusivities at the top three model interfaces (the data have been averaged over the last century of each integration). Throughout the tropics, the diffusivities have increased by a factor of two to three, consistent with the approximately 20% increase in potential intensity. Note, however, that the values at 220 m are almost always confined to the background value of 0.3 cm^2/s in both simulations. As can be seen in figure 5-24, the depth to which these storms penetrates increases in the high carbon dioxide climate, but the increase is not large enough to push through the next model level. The result of this is to create a strongly mixed ocean across the top three model boxes (from the surface to 220 m), but the weak background diffusion applied at 220 m and all levels below isolates thermocline waters.

While the direct mixing accounts for some impressive changes over the static mixing case shown in figure 5-3, it does not penetrate deeply enough to produce changes as large as seen in figure 5-11, where elevated mixing penetrated through the water column. Adding mixing at the 220 m interface has a strong impact, as was seen in figure 5-5, where mixing was imposed down to that interface. As was seen in figure 4-19 in the last chapter, the heat flux is sensitive to mixing at depths from the surface to 400 m; direct mixing, as implemented here, taps only the upper half of this region of sensitivity. These findings will motivate some future work, with higher resolution in the upper ocean.

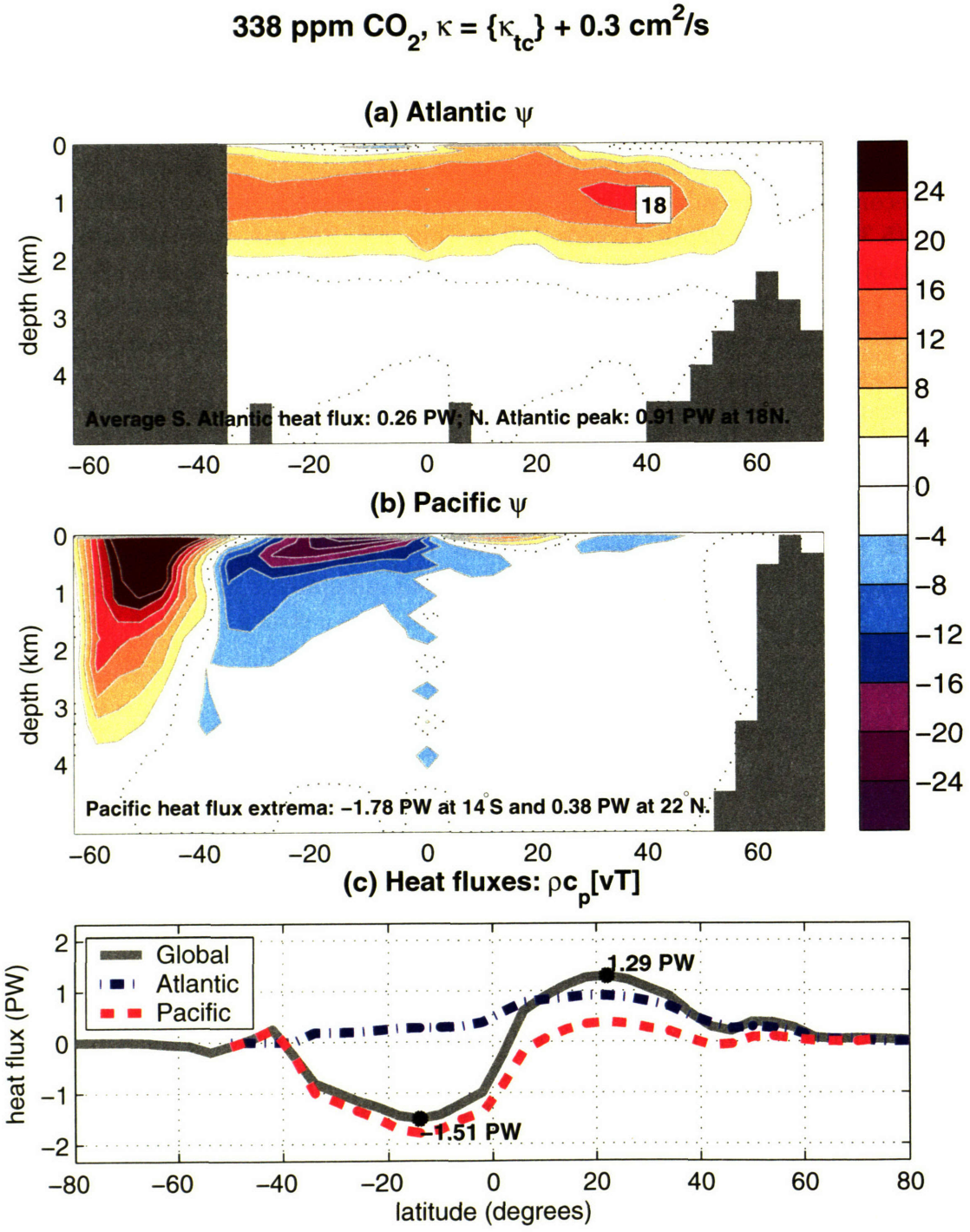

Figure 5-21: The overturning circulation and heat fluxes from a simulation with contemporary levels of carbon dioxide (337.9 ppm); the diffusion coefficient is 0.3 cm^2/s everywhere except in the upper most tropical oceans, where it is increased by an amount that scales with tropical cyclone intensity and frequency [see equation (5.31)] down to a depth given by equation (5.26).

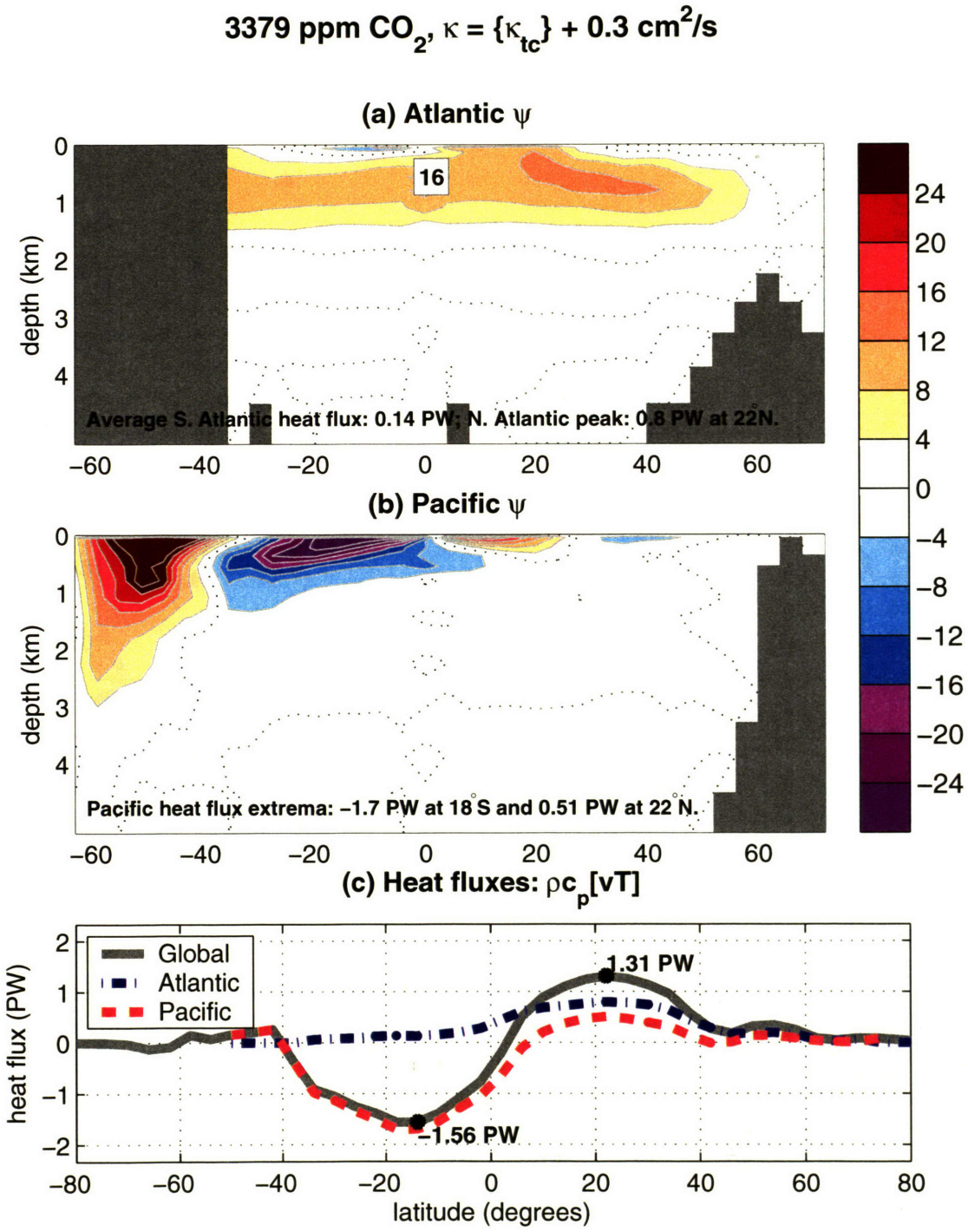

Figure 5-22: As in figure 5-21, but from a simulation with high levels of carbon dioxide (3379 ppm); the diffusion coefficient is 0.3 cm^2/s everywhere except in the upper most tropical oceans, where it is increased by an amount that scales with tropical cyclone intensity and frequency [see equation (5.31)] down to a depth given by equation (5.26).

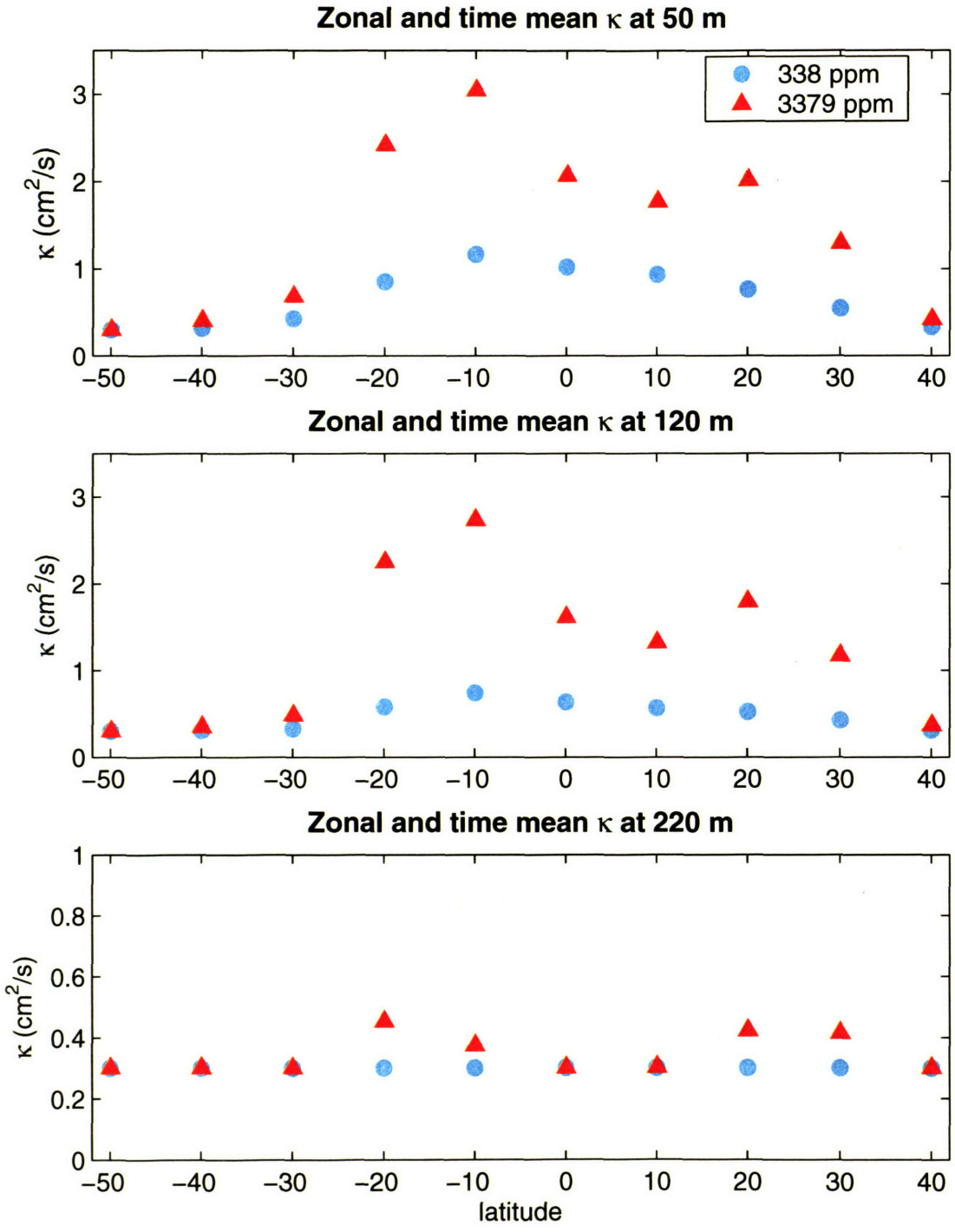

Figure 5-23: Vertical diffusion coefficient, κ at three top model interfaces. The intensity of the mixing was determined by equation (5.31), and the depth to which the mixing penetrates was calculated using equation (5.26). While both the amplitude and depth increase in the high carbon dioxide experiment, the storms rarely mix down to the 220 m interface assuming an initial mixed-layer depth of 50 m.

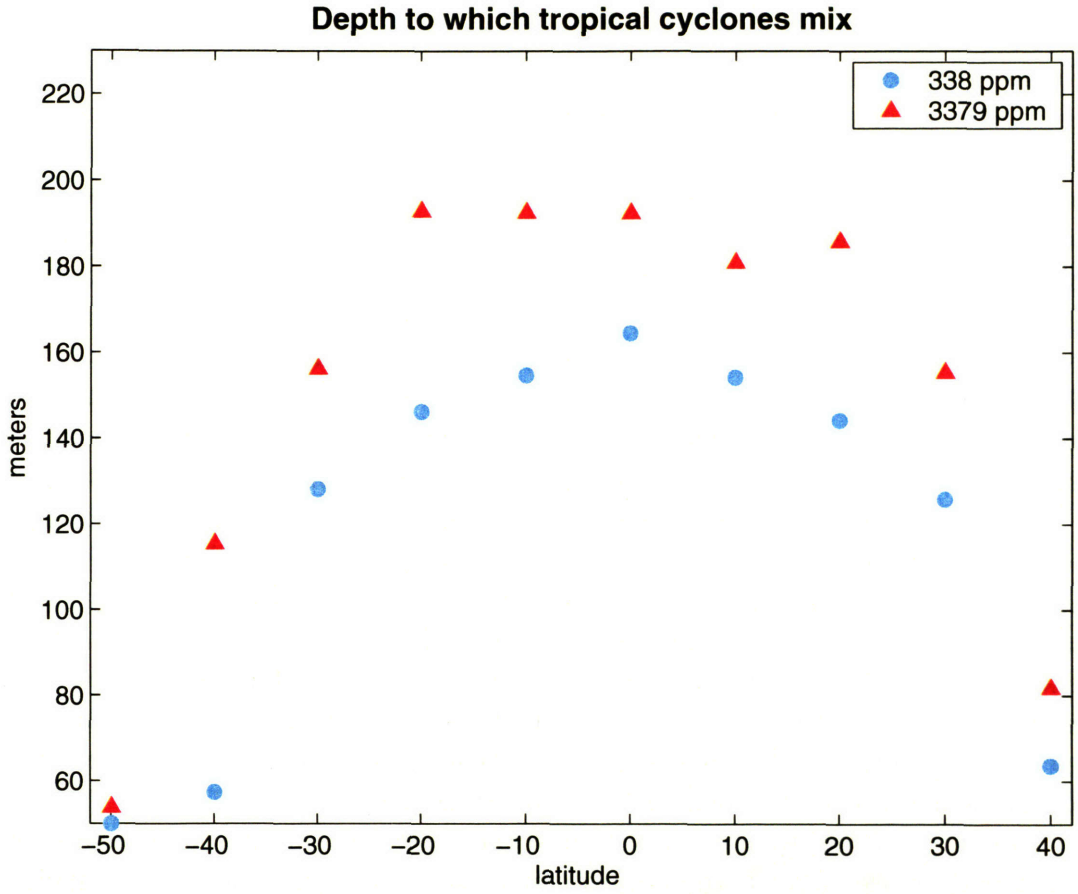

Figure 5-24: Zonal and time averaged depth to which tropical cyclones mix, as predicted by equation (5.26). Higher sea surface temperatures and stronger storms mix more vigorously in the high carbon dioxide climate, but storms rarely mix down to the 220 m interface assuming an initial mixed-layer depth of 50 m.

Obviously if hurricanes contribute more energy to the internal wave field of the ocean during warm climates (Nilsson, 1995), deeper mixing may increase as well. But perhaps there is another way that the direct mixing can be more significant. Schade (1994) showed that strong thermocline stratification impedes turbulent entrainment beneath a storm. If the ocean had a weaker vertical buoyancy gradient during warm climates, the weaker stratification would provide less resistance to turbulent entrainment, which would allow it to penetrate to a greater depth. Additionally, if temperatures just below the mixed-layer were not as cold as they are today, a negative feedback on storm intensity would be suppressed. [The mixing of thermocline parcels to the surface diminishes the surface fluxes beneath a hurricane, reducing the storm's intensity (Schade, 1994).] This would support stronger storms, which in turn would deposit more momentum into the surface layer, supporting more vigorous mixing. We discuss this potentially powerful feedback in the sections that follow.

5.6 Final remarks

We have just begun to explore the richness of this problem. As many of these experiments have revealed, the results are quite sensitive to the intensity of the mixing, the depths at which it is applied, and the thermal structure of the ocean. Each of these runs produces a slightly different thermocline structure. Figure 5-25 shows average temperature profiles in the tropics; the average was constructed by multiplying the volume of each grid box by its temperature, summing over all points equatorward of 30°, then dividing by the total volume of water equatorward of 30° at that vertical level. The coefficients for the PI^6 parameterization discussed in section 5.3 and the PI^6/N parameterization discussed in section 5.4 were chosen to replicate the specified diffusivity in the uniform case. Thus, they were all normalized to produce tropical diffusivities of about 0.3 cm^2/s, and the profiles are similar for the present climate.

When applied to the warm climate experiments with high levels of carbon dioxide, some notable differences emerge. The stronger mixing makes the thermocline more diffusive, showing a gentler decent through the upper 500 m of the ocean. The stronger mixing blends temperatures between grid boxes, cooling the upper ones while heating below. The inclusion of tropical cyclone mixing, which is stronger with the warmer sea surface temperatures in the high carbon dioxide experiment, mixes heat downward into the upper thermocline. Note, however, that only when the stratification dependence is included do bottom waters begin to warm.

In this chapter, we have seen that without stronger mixing the predicted ocean heat flux decreases when carbon dioxide increases. Stronger upper ocean mixing (e.g., direct mixing from tropical cyclones) with high carbon dioxide is sufficient to return the strength of the heat flux to values calculated for the present climate, but a large increase beyond the present climate can occur when mixing increases throughout the water column and carbon dioxide is high. This suggests an avenue for future research: how do the circulation and heat flux respond to direct tropical cyclone mixing when the background diffusivities evolve with a stratification-dependence?

We lack information about the thermocline structure from the Eocene and Cretaceous oceans, but a diffusive thermocline could have at least two feedbacks on the results discussed in this chapter. First, stratification-dependent mixing schemes will produce stronger mixing when the stratification weakens. This provides a positive feedback, because stronger mixing diffuses surface heat through the thermocline more efficiently, thus further weakening the stratification. Additionally, tropical cyclones are greatly affected by the entrainment of cold thermocline waters that choke off the surface fluxes of enthalpy that feed the storm. If the thermocline were less stratified, the sea surface temperatures would not cool as precipitously (the waters mixed to the surface are now warmer), and the average intensity of tropical cyclones could increase. There are many exciting problems remaining to be explored, particularly involving the interaction of direct tropical cyclone mixing with stratification-dependent mixing schemes. Some ideas of these ideas are discussed in the next chapter.

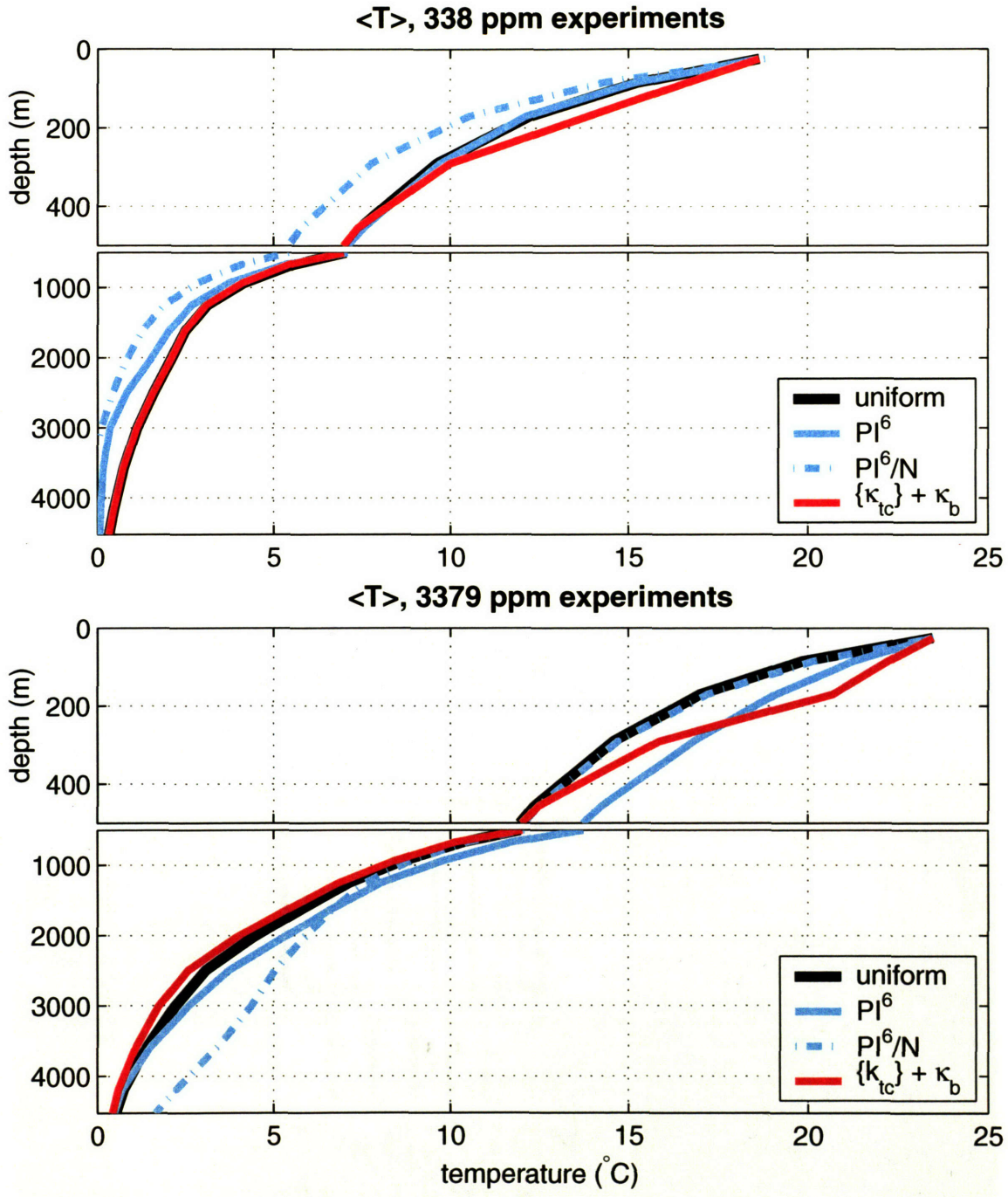

Figure 5-25: Average vertical profiles between 30°S and 30°N. The average was constructed by multiplying the volume of each grid box by its temperature, summing over all points equatorward of 30°, then dividing by the total volume of water equatorward of 30° at that vertical level.

Chapter 6

Conclusions

Evidence of crocodiles in Greenland, palms in Wyoming, and flourishing fauna on the Arctic coast lead one naturally to ask how high latitudes during the Eocene or Cretaceous were so warm (e.g., see figure 6-1). But perhaps a better question is this: why were the tropics so cool? In this thesis, we reviewed existing theory regarding the dynamics of warm climate states, and made progress on a novel view of the problem. We now summarize the main findings and discuss avenues for related future work.

Figure 6-1: Fossilized remains of an ancient forest along the Arctic coast. Across northern Canada, Greenland, Patagonia, and Antarctica, evidence of early Cenozoic high-latitude warmth lies scattered across the barren landscape. Picture courtesy of Kirk Johnson, curator of the Denver Museum of Nature and Science.

6.1 Chapter summaries

We introduced the warm climate problem by reviewing the challenges posed by earlier modeling studies of paleoclimates with a weak temperature gradient. Over the last decade, several papers have investigated the possibility that polar stratospheric clouds played a role in maintaining the mild conditions over polar latitudes. We examined stratospheric dynamics in the first part of the thesis.

In Chapter 2, we used a two-dimensional model to explore the $(\Delta T, \tau_m)$ phase space, where ΔT is the pole-to-equator temperature difference and τ_m is the momentum damping applied at the model top, a surrogate for wave damping in the real atmosphere. We found that polar stratospheric temperatures would cool below the frost point of water only if a large feedback between the strength of the stratosphere's residual mean circulation and the surface temperature gradient exists. A rise in the height of the polar tropopause forced by convection increased the size of the necessary feedback. This model has no parameterization of eddies, so convective and radiative processes set the tropopause height.

But in Chapter 3 we saw that no such feedback exists in the Community Atmosphere Model. In fact, winter stratospheric temperatures were remarkably stable even when the surface gradient varied substantially. Here too the polar tropopause rises and tropospheric stratification is convectively neutralized at all latitudes. With weak meridional temperature gradients extending through the depth of the troposphere, the tropospheric jets weaken. Though tropospheric eddy kinetic energy decreases in the warm climate states, there is an increase in the activity vertically propagating into the stratosphere; the weak jet permits wavenumbers one, two, and three to regularly pass into the winter stratosphere. Stratospheric convergence of the Eliassen-Palm flux intensifies, and the residual circulation strengthens during warm climates. This prohibits temperatures from falling below present levels, though increased longwave cooling to space could create significant deviations in the upper stratosphere. Still, absent a very large chemical source of water vapor, it seems unlikely that conditions were ripe for widespread polar stratospheric cloud formation.

At the conclusion of Chapter 3, we saw that the atmosphere's poleward transport of enthalpy falls off markedly during warm climates, principally because of the decrease in transient eddies, which are the dominant mechanism for transporting heat in middle latitudes. The implied ocean heat transport increases in magnitude, and the ocean must make a sizable contribution over a larger range of latitudes. We examined ocean heat transport in the second half of the thesis.

In Chapter 4, the sensitivity of the oceans' meridional overturning circulation and heat transport to variations in the location and strength of diapycnal mixing was explored. We confirmed that the intensity of mixing in low latitudes matters most, as both the heat flux and overturning circulation are quite sensitive to the value of the diffusion coefficient there. We noted that this sensitivity extends beyond the equator itself, where Bugnion (2001) found a peak in sensitivity; mixing can be concentrated in

tropical latitude bands between 8° and 30° and produce the same circulation provided that the area-weighted average of κ is conserved. We also found that mixing in the Pacific basin can affect the intensity of the overturning circulation, and thus the heat transport, in the Atlantic basin [Bugnion's (2001) linear study identified sensitivity to mixing in this basin as well]. The vertical structure of mixing is also important. The overturning circulation is sensitive to mixing from the base of the mixed-layer into the abyss, but the heat flux is sensitive to mixing only in the upper 400 m of the ocean. Cummins et al. (1990) and Scott and Marotzke (2002) noted that abyssal mixing does not affect the heat flux, and Boccaletti et al. (2005) constructed a diagnostic that illustrates the oceans' heat flux is carried in the top 500 m of the ocean. Taken together, processes that vigorously mix the upper tropical oceans in both the Pacific and Atlantic can have a large impact on the oceans' poleward heat transport.

Chapter 5 contains our work using a coupled model. Without elevated mixing, higher loads of carbon dioxide warm temperatures and melt high latitude ice, which combine to produce a sluggish circulation and weak heat flux. We showed, however, that strong mixing of the upper tropical oceans can reduce the pole-to-equator temperature gradient by several degrees, and that tropical cyclones can produce more vigorous mixing in the upper ocean in warmer climates. We derived a parameterization for the direct affects of tropical cyclone mixing, including the depth to which entrainment occurs. We also discussed some possible interactions with stratification-dependent mixing schemes; ideas for additional work on this potentially powerful feedback is discussed further in section 6.3.

6.2 Thesis summary

The results of this thesis cast some doubt on the viability of the polar stratospheric cloud hypothesis advanced by Kirk-Davidoff et al. (2002). There appears to be little connection between the surface temperature gradient and the stratosphere's residual mean circulation. Though eddy energy decreases substantially with a weak surface temperature gradient, the longest planetary waves propagate uninhibited into the lower stratosphere. Indeed there is some compensation as the weaker jets, in balance with the weak meridional temperature gradients, allow some energy in shorter waves (e.g., wavenumber three) to propagate into the stratosphere. While chemical oxidation of methane could provide an abundant source of water vapor for polar stratospheric cloud formation, as suggested originally by Sloan et al. (1992), there are lingering questions regarding the feasibility of building an optically thick cloud at such altitudes. There must be a replenishing source of water vapor to compensate for the settling of ice crystals. There are also radiative feedbacks that could limit the growth of stratospheric clouds (e.g., Rosenfield, 1992).

Instead, we prefer to revive the early question investigated by Barron and Washington (1985): could high levels of carbon dioxide explain Cretaceous and Eocene

warmth? Pearson and Palmer (2000) used boron isotopes to show that carbon dioxide concentrations exceeded 2000 ppm during the early Cenozoic (during the Paleocene and early Eocene epochs, from 65 Ma to the thermal maximum at 52 Ma). While there has been growing acceptance that carbon dioxide levels were higher during the early Cenozoic (Sloan and Rea, 1995; Shellito et al., 2003), they cannot be the full story as proxies place an upper bound on tropical temperatures (Schrag, 1999; Pearson, 2001).

If mixing in the upper ocean increases with the cumulative power put into the ocean by tropical cyclones, stronger mixing can increase the oceans' heat transport. To be effective, this mixing must be vigorous and located in the upper tropical oceans. We showed model simulations in which the tropics cool, on average, by 1°C while high latitudes warm 2°C (compared to simulations with static mixing) when such a parameterization is employed. While not enough to close the gap between proxies and modeling studies, the results are encouraging. We discuss other interactions and areas for future research in the last section.

6.3 Future research

We demonstrated the ability of mixing directly attributable to tropical cyclones to increase the oceans' poleward heat transport during warm climates over simulations using fixed mixing. If the stratification of the ocean were weaker, the results of Nilsson et al. (2003) suggest that diffusion at depth could be higher as well. Consider the following: if storms were stronger, and stratification in the upper ocean weaker, the direct mixing could penetrate to a greater depth during warm climates. We demonstrated that the depth to which tropical cyclones mix is dependent on the background stratification in equation (5.26). If the ideas of Nilsson et al. (2003) are combined with our parameterization, the impact of direct mixing from tropical cyclones could amplify. Should the initial stratification of the oceans be weak, hurricanes could mix heat down through the upper thermocline, where stronger background diffusivities (owing to the weak stratification) could then mix the heat further down. This could produce a self-sustaining, vigorous circulation. More work with higher upper ocean resolution must be done, perhaps combining a mixed-layer model to more accurately represent the upper ocean physics. Continuing work along these lines is producing some promising results.

In the first half of this thesis, we saw the tropopause height in middle and high latitudes rises in both the two-dimensional model used in Chapter 2 and in the Community Atmosphere Model used in Chapter 3. At the conclusion of the first part of the thesis, we reviewed a number of soundings showing convectively neutral stratification, even at high latitude continental locations. This suggests an intriguing line of future research, which is briefly motivated below.

In recent decades, winter temperatures at northern high latitudes have warmed

significantly more than have tropical temperatures. While some portion of this sensitivity might be attributed to feedbacks such as the ice-albedo one, general circulation models also suggest that the stable stratification in the extratropics enhances the surface response to changes in radiative forcing (e.g., Wetherald and Manabe, 1975). If the way in which extratropical stratification is maintained varies with climate, this feedback may be modified, leading to a change in climate sensitivity.

Since the work of Stone (1978a), evidence has grown that the extratropical atmosphere is equilibrated by eddies toward a state neutral to the further growth of baroclinic waves (Lindzen and Farrell, 1980; Stone and Nemet, 1996). Recently, Schneider (2004) derived a dynamical constraint on the tropospheric lapse rate of a dry atmosphere by relating the tropopause and surface potential temperatures through a diffusive closure of baroclinic eddy fluxes.

But Emanuel (1988b) produced evidence that slantwise moist convection occurs in the extratropical atmosphere, and he identifies extensive regions along angular momentum surfaces where lapse rates follow a moist adiabat. Juckes (2000) argues

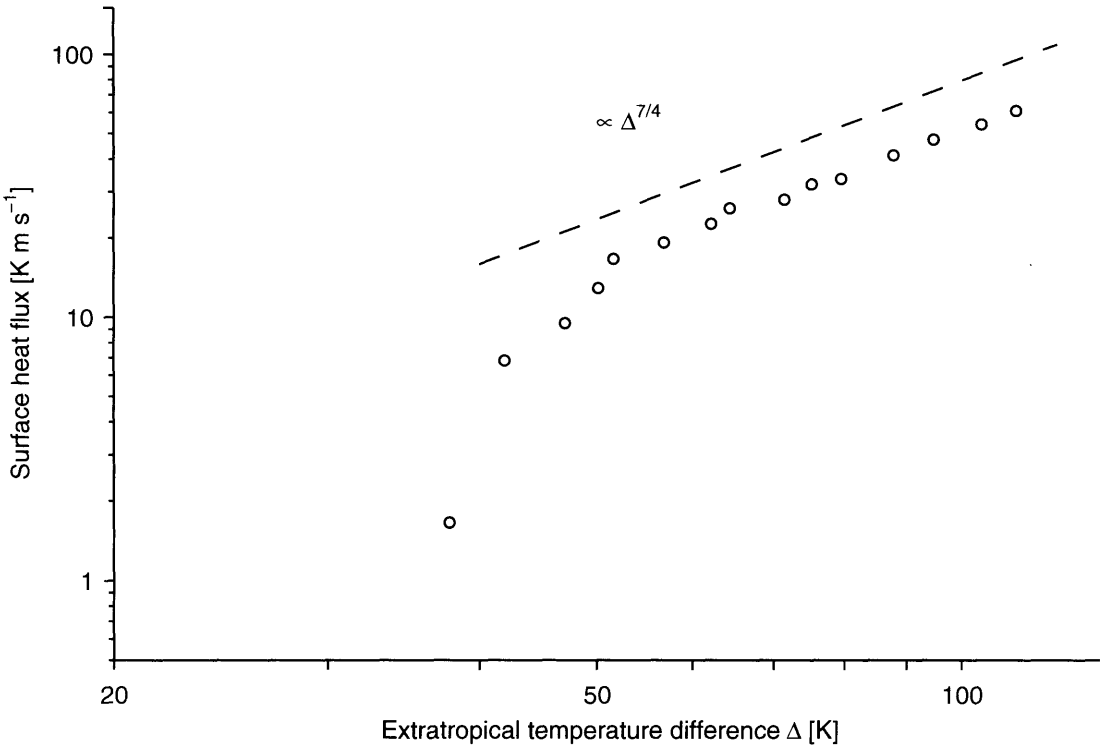

Figure 6-2: The meridional eddy flux of surface potential temperature $(\overline{v'\theta'_s})$ as a function of the difference in θ_s between the tropics and polar latitudes in an idealized general circulation model with a dry variant of a quasi-equilibrium convection scheme. Baroclinic eddies carry a strong flux of enthalpy poleward when $\partial_y \theta_s$ is strong, but the scaling becomes different as convection sets the stratification in climates with a weaker gradient. Figure courtesy of Tapio Schneider.

that the sporadic moist convection in the warm sectors of surface cyclones acts as a central determiner of the tropospheric stratification and that eddies provide the variance.

There is some evidence that the physics controlling extratropical stratification may be different in various climates, and this has implications for the strength of the meridional heat flux. Tapio Schneider (personal communication) has found a phase transition from convective to baroclinic regimes in an idealized general circulation model. When the surface temperature gradient is strong, baroclinic eddies carry a significant meridional flux of enthalpy poleward, but in climates with a weaker surface temperature gradient, such as the Eocene or Cretaceous, the scaling becomes quite different as convection sets the extratropical stratification. This divide is shown in figure 6-2; the present climate appears to lie near the transition. While it is difficult to imagine that convection could ever control the horizontal heat flux in the atmosphere, it could greatly influence the baroclinic eddies that do so through its effect on the stratification.

If the simulations shown in figure 6-2 are representative of the dynamical range of the Earth's atmosphere, the present climate may lie near a transition, perhaps giving an explanation for the apparent success of both the baroclinic adjustment (Stone and Nemet, 1996) and slantwise convective adjustment (Emanuel, 1988b) techniques for assessing extratropical stratification. I plan to investigate how much of the present extratropical atmosphere exists in a state neutralized by slantwise moist convection by using reanalysis data to calculate thermodynamic soundings along surfaces of angular momentum. Slantwise moist convection confines values of saturation potential vorticity, q^*, to be near zero. By calculating this quantity from reanalysis data, I intend to create a climatology, which should help identify the extent to which slantwise moist convection makes an important contribution to the stratification of the present atmosphere.

If the results shown in figure 6-2 are representative of the behavior in different climates, the importance of ocean heat transport during warm climates cannot be overemphasized. The atmosphere is simply ineffective at transporting heat in the presence of a weak temperature gradient.

Appendix A

Poleward energy transport

In this appendix we calculate the poleward flux of enthalpy in the presence of various temperature gradients. In the course of this derivation, we make several assumptions and approximations, but this problem is meant to be illustrative only.

Because the Earth receives and absorbs more solar radiation in the tropics than high latitudes, the highest surface temperatures are found here. But the Earth receives and absorbs so much more radiation at low latitudes than in polar ones that the planetary temperature gradient should be about twice what is observed in the present climate (Farrel, 1990). The tropics emit less radiation than they absorb, and high latitudes emit much more than they receive. This implies a redistribution of enthalpy; the temperature gradient established by local radiation and convection alone is unstable to baroclinic eddies, and these eddies are principally responsible for carrying heat poleward. Trenberth and Caron (2001) have recently reviewed satellite data, and they estimate that the climate system has a peak heat flux between 5.5 and 5.75 PW in middle latitudes.

The amount of solar radiation incident at each point on the globe is a complex function of the orbital and planetary geometry. It is a function of the sun's zenith angle, the time of year, the time of day, the latitude, the distance between the sun and Earth, the solar constant, and the solar declination (Iqbal, 1983; Peixoto and Oort, 1992). The incident radiation, Q, may be written:

$$Q = \frac{S \cos z_{\odot}}{l^2}, \tag{A.1}$$

where S is the solar constant, $z_{\odot}$ is the solar zenith angle, and l is the distance to the sun, which is not constant over the course of a year. The zenith angle depends on latitude, time of day, and solar declination. Because we are concerned with the annually averaged transport of energy, which simplifies the calculation considerably.

North (1975) showed that because Q may be determined from astronomical calculations, it may be developed in a Fourier-Legendre series with known coefficients.

That is,

$$\begin{aligned} \overline{Q} &= C \sum_{n=0,2,4,...} A_n P_n(x) \\ &= \frac{S}{4} \left[1 + S_2 P_2(x) + S_4 P_4(x) + ...\right], \end{aligned} \tag{A.2}$$

where $\overline{Q}$ is the annual average of Q, x is the sine of the latitude, S_n are coefficients, and P_n are the Legendre polynomials. North (1975) found that truncating the infinite series in equation A.2 after the second term resulted in less than a 2% error compared with tabulated data. This will be good enough for our purposes here. As in North (1975), S_2 equals -0.482. Note that all odd coefficients are identically zero, as $\overline{Q}$ is symmetric about the equator.

Next we must find the fraction of the solar radiation that is received at each latitude. We make the approximation that a zonal mean albedo is adequate, and that this can be estimated from the geometry and ice-line alone. Following Wang and Stone (1980), the albedo is parameterized by:

$$\alpha = \alpha_0 + \alpha_2 P_2(x) + \delta u(x - x_s) \tag{A.3}$$

where x_s is the ice-line and

$$u = \begin{cases} 1, & x > x_s \\ 0, & x < x_s. \end{cases} \tag{A.4}$$

As in Wang and Stone (1980), the coefficients α_0 and α_2 are taken to be 0.316 and 0.146, respectively. Note that the first coefficient dominates the global mean, and the second term corrects the latitudinal dependence. That is, the albedo is low in the tropics but it increases poleward owing to the zenith angle dependence. The coefficient δ is taken to be 0.186, and it is applied for the present climate only. As in Wang and Stone (1980), x_s is taken to be 0.95 (corresponding to about 72° latitude); this will be used in the calculation of the albedo for the present climate (in which polar ice is present). For the warmer climates, the ice-free albedo will be used, and x_s is taken to be greater than 1.

By multiplying equation (A.2) with one minus equation (A.3), the latitudinal dependence of the absorbed solar radiation is obtained. Next, we find the emitted longwave radiation.

This is a bit trickier, because the outgoing longwave radiation is a strong function of temperature and the gaseous constituents of the atmosphere. Sellers (1969) and North (1975) parameterized the thermal longwave radiation as:

$$I = A + B \cdot \overline{T_s}, \tag{A.5}$$

where A and B were chosen to approximate the distribution in the present climate. The coefficients would almost certainly change values in a different climate, and it is

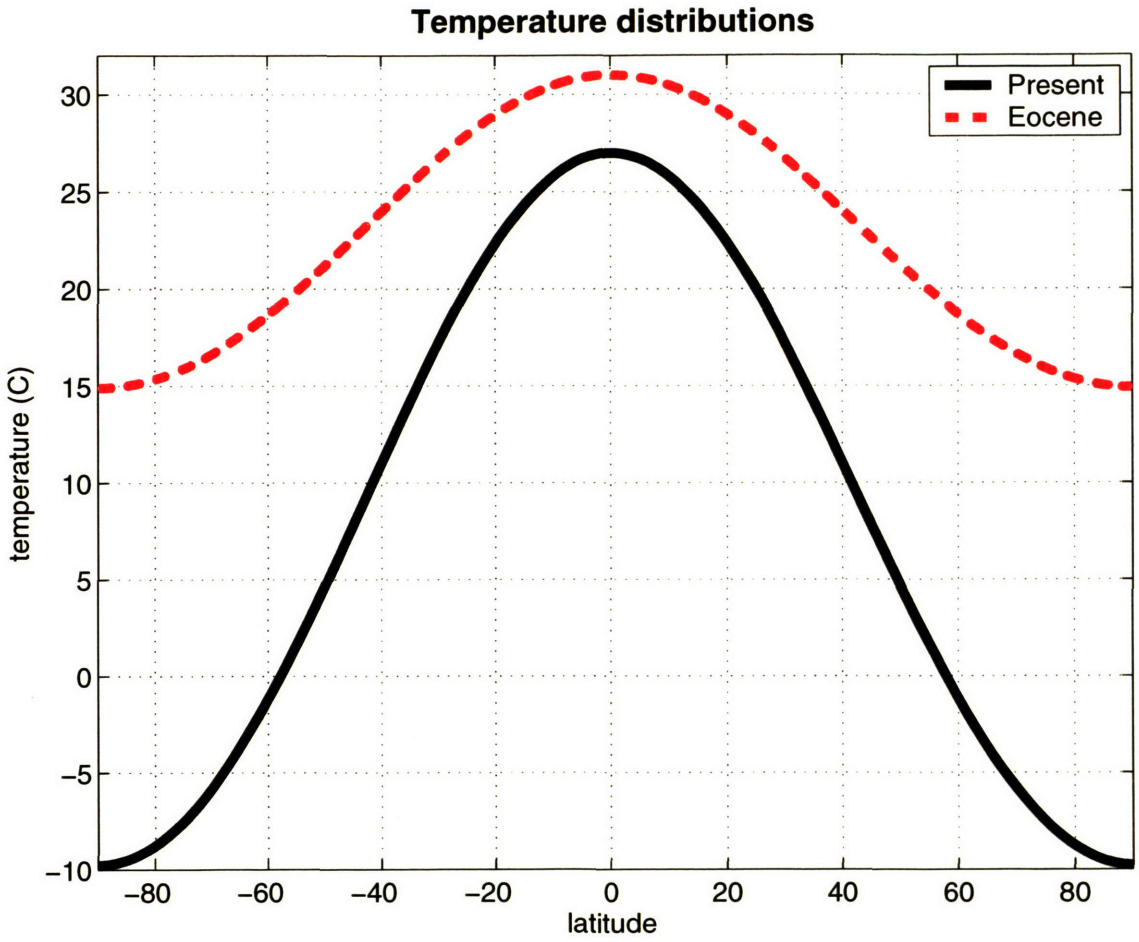

Figure A-1: Temperature distributions expressed by equations (A.7)–(A.8).

difficult to represent equation (A.5) more generally. I shall retain the value of B used by North (1975), which is 1.55 W/m^2, and choose A such that the globally integrated net radiation at the top of the atmosphere balances to zero. That is,

$$\begin{aligned} \int \overline{Q(1-\alpha)}\, dA &= \int I\, dA \\ &= \int \left(A + B \cdot \overline{T_s}\right)\, dA \\ \Longrightarrow A &= \left(\int \overline{Q(1-\alpha)}\, dA - \int B \cdot \overline{T_s}\, dA\right) \div \int dA, \end{aligned} \tag{A.6}$$

where dA is the area of each latitude band. The value of B used by Sellers (1969) and North (1975) is truly applicable only to the present atmosphere; were the chemical composition very different during the last equable climate, the value of B would likely be different as well. However, B is already empirical, and we have no reason-

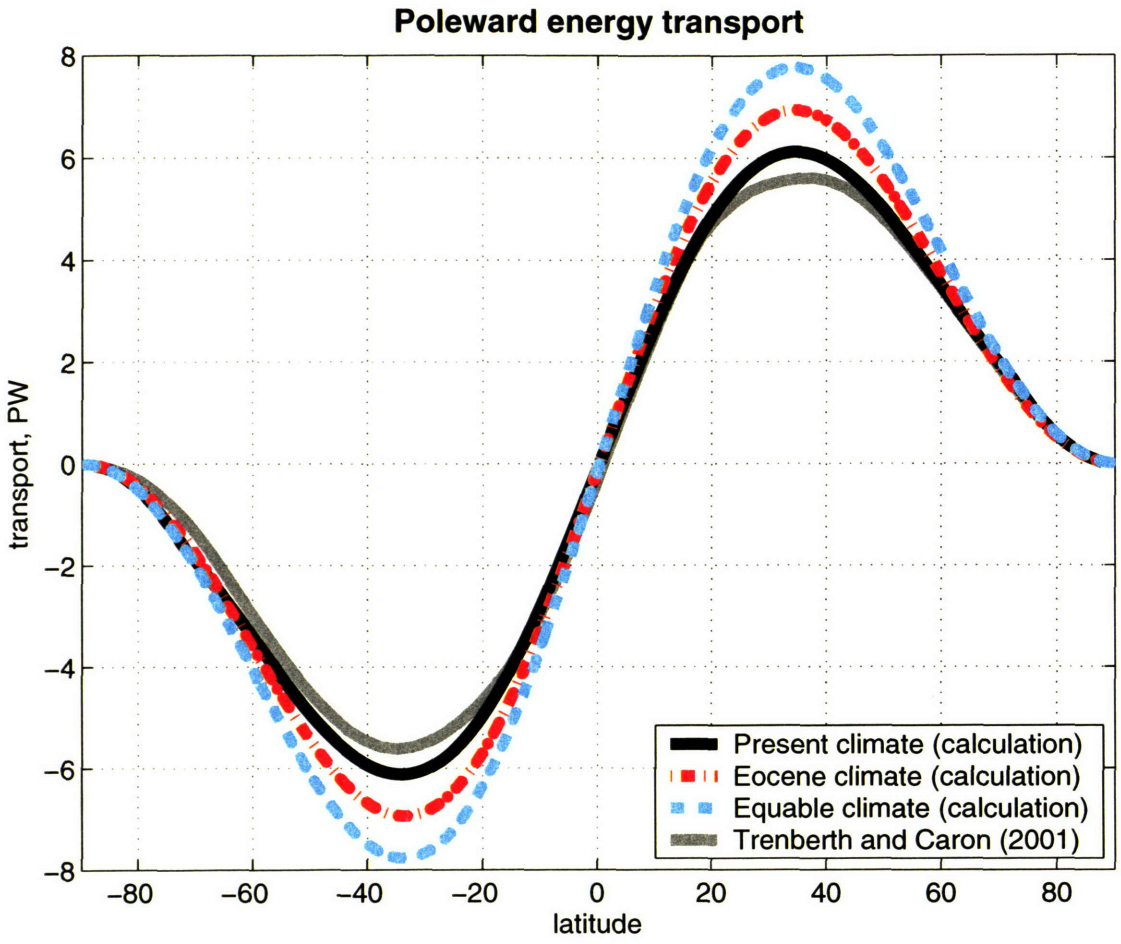

Figure A-2: Poleward flux of energy by methods calculated in this section for a Present (solid black), Eocene (red dash-dotted), and equable (light-blue dashed) temperature distribution.

able way to estimate a sensible choice for an equable climate, so the value from the contemporary atmosphere is retained in these calculations.

Three temperature distributions are studied. The first represents the present climate; it is termed T_p. The second represents the Eocene, and is labeled T_{eoc}. Finally, we consider a temperature distribution that is isothermal, truly an equable climate, T_{eq}. The distributions for the present and Eocene are:

$$T_p = -53 + 80 \cdot \cos(\sin\phi) \tag{A.7}$$

$$T_{eoc} = -4 + 35 \cdot \cos(\sin\phi)\,; \tag{A.8}$$

these are plotted in figure A-1. With the definition of A specified by equation (A.6),

there is no unique value for T_{eq}; it follows from equation (A.5) that

$$T_{eq} = \frac{\int \overline{Q(1-\alpha)}\, dA}{B \int dA} - \frac{A}{B}, \tag{A.9}$$

so there is a unique value for T_{eq} only when A is specified. [If the value of A is taken to be 211.2 W/m^2 as in North (1975), then T_{eq} would be 17.99°C on an ice-free planet.]

The net absorbed solar radiation at the top of the atmosphere, $\overline{Q(1-\alpha)}$, may be calculated at each point from equations (A.2) and (A.3). The net longwave radiation at each latitude can be computed by substituting the temperature distribution [equations (A.7)–(A.9)] into equation (A.5), along with the value of A from equation (A.6). The difference between the net solar radiation and net longwave radiation at the top of the atmosphere is F_{TA}. This quantity can be integrated from each latitude, ϕ, to the North Pole to find the total amount of energy that the climate system must transport to correct the radiative imbalances at the top of the atmosphere:

$$T_A + T_O = -\int_{\phi}^{\pi/2} F_{TA} 2\pi R_e^2 \cos\phi' d\phi'. \tag{A.10}$$

This total poleward flux is shown for the three temperature distributions in figure A-2. Note that this says nothing about how the heat flux is partitioned between the atmosphere and oceans.

Appendix B

Radiative equilibrium calculations

In this appendix, I document the algebra for three radiative equilibrium calculations. The first and simplest problem treats a one-layer atmosphere; the second problem treats a two-layer atmosphere. Both of these are standard problems. The third problem extends the two-layer solution by allowing some solar radiation to be absorbed at the top layer in addition to the surface.

B.1 One-layer atmosphere

The one-layer problem is constructed by assuming that all solar radiation that is not reflected is absorbed at the surface; the atmospheric layer is therefore transparent to shortwave radiation and absorbs and emits longwave radiation with an emissivity ε_1. This construction is diagrammed in figure B-1.

At the surface,

$$\sigma T_s^4 = \sigma T_e^4 + \varepsilon_1 \sigma T_1^4, \tag{B.1}$$

where σ is the Stefan-Boltzmann constant, T_s is the temperature of the surface, T_1 is the temperature of the atmospheric level, and T_e is the effective emissions temperature. Note that σT_e^4 is equivalent to $S_o(1-\alpha)/4$, where S_o is the solar constant and α is the planetary albedo. Using values of 1370 W m^{-2} for S_o and 0.3 for α, T_e is 255 K. The balance at the atmospheric level is:

$$2\varepsilon_1 \sigma T_1^4 = \varepsilon_1 \sigma T_s^4; \tag{B.2}$$

this balance is between radiation absorbed from the surface and radiation emitted both up and down (the bi-directional emission is responsible for the factor of two). At the top of the atmosphere, outgoing longwave radiation must equal what comes into the system:

$$\sigma T_e^4 = (1-\varepsilon_1)\sigma T_s^4 + \varepsilon_1 \sigma T_1^4. \tag{B.3}$$

Note that a value of $\varepsilon_1 < 1$ causes some of the radiation emitted by the surface to

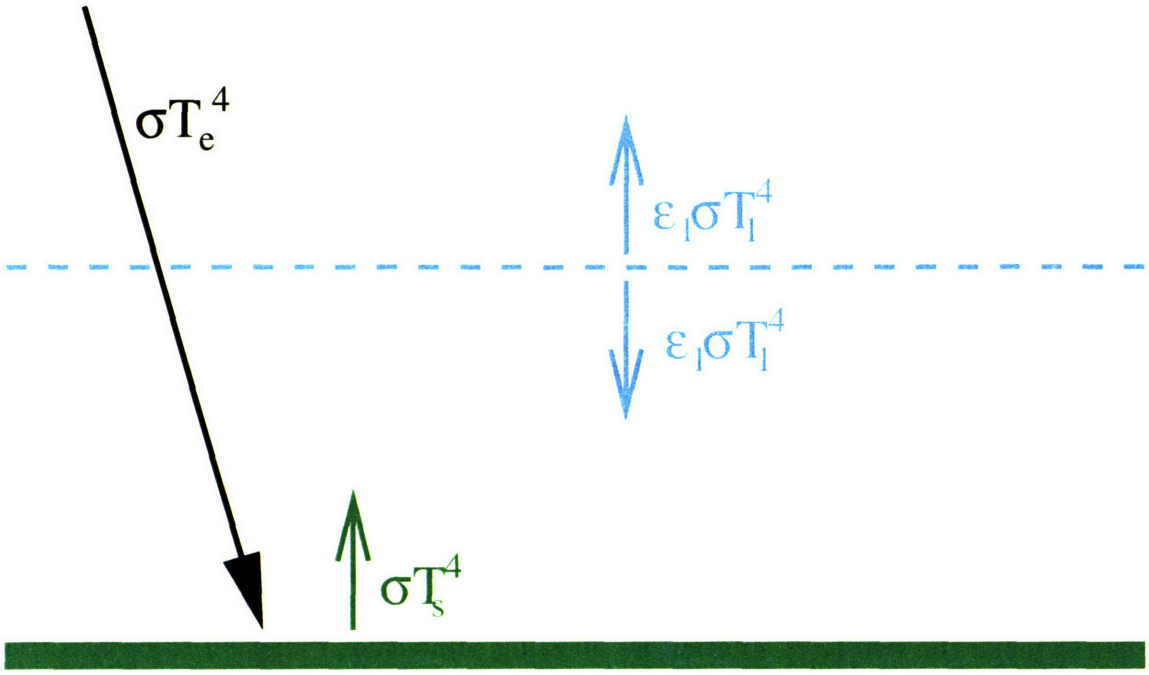

Figure B-1: A one-layer model in which the incoming solar radiation is absorbed at the surface and a longwave emissivity of ε_1 governs the fraction of absorption and emissions at the atmospheric level.

escape directly to space; this represents a longwave "window" to space.

Substituting equation (B.2) into equation (B.1) gives relates the surface temperature with the known equivalent emission temperature:

$$T_s = \left(\sqrt[4]{\frac{2}{2-\varepsilon_1}} \right) T_e. \tag{B.4}$$

With this expression, T_1 may now be expressed as a function of T_e:

$$T_1 = \left(\sqrt[4]{\frac{1}{2-\varepsilon_1}} \right) T_e. \tag{B.5}$$

These expressions can be inserted into equation (B.3) to verify the algebra.

Note that the warmest temperatures at both the surface and atmospheric layer are found in the blackbody limit when $\varepsilon_1 = 1$; in this limit, T_s is 303 K and T_1 is 255 K. As $\varepsilon \to 0$, $T_s \to 255$ K and $T_1 \to 214.4$ K. (When $\varepsilon_1 = 0$ there is no atmospheric layer, so defining a temperature there becomes ill posed.) Whenever $\varepsilon_1 < 1$ some radiation leaks to space, and the top of the atmosphere will be colder than the effective emissions temperature.

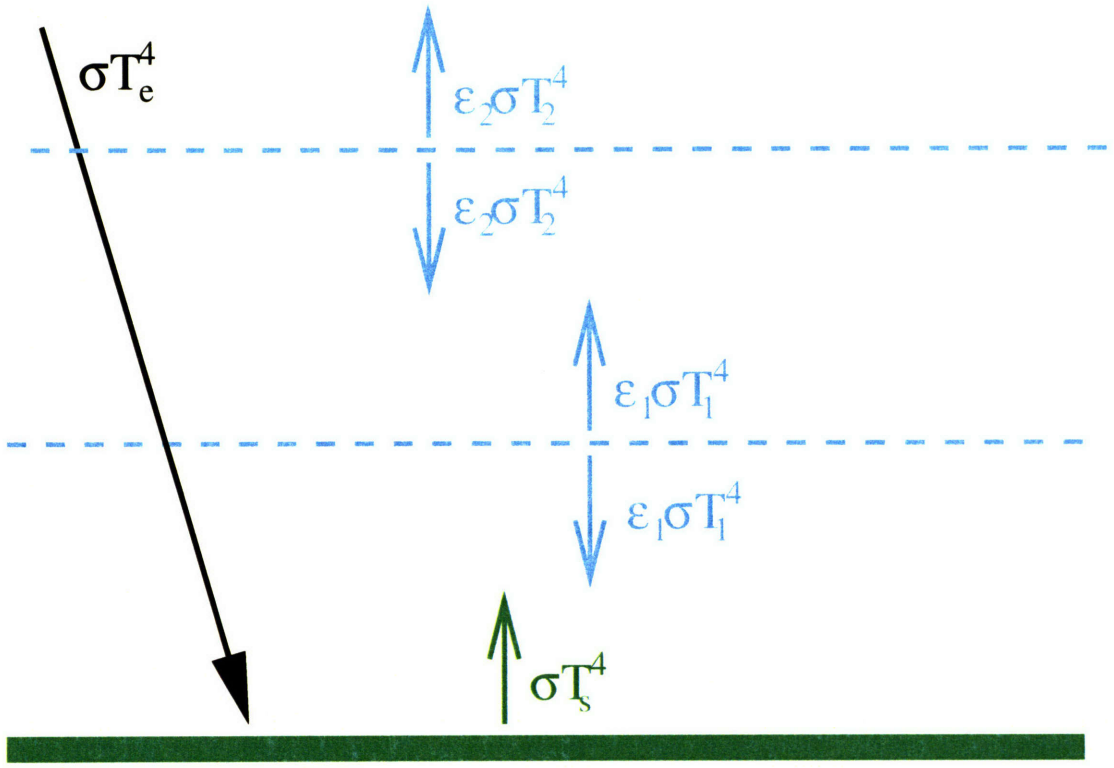

Figure B-2: A two-layer model in which the incoming solar radiation is absorbed at the surface and a longwave emissivity of ε_1 and ε_2 govern the fraction of absorption and emissions at the atmospheric levels.

B.2 Two-layer atmosphere

Adding additional layers quickly makes the algebra increasingly tedious. I have solved the variations of this problem that follow for both two and three atmospheric layers, but since the physics I wish to highlight can be seen in a two-layer problem just as easily as a multi-layer one, I limit the algebra by presenting only the two-layer calculations. Figure B-2 shows the construction of a two-layer problem.

The balances at the surface, first layer, and second layer are:

$$T_s^4 = T_e^4 + \varepsilon_1 T_1^4 + \varepsilon_2(1-\varepsilon_1)T_2^4 \quad \text{(B.6)}$$

$$2\varepsilon_1 T_1^4 = \varepsilon_1 T_s^4 + \varepsilon_2\varepsilon_1 T_2^4 \quad \text{(B.7)}$$

$$2\varepsilon_2 T_2^4 = \varepsilon_2\varepsilon_1 T_1^4 + \varepsilon_2(1-\varepsilon_1)T_s^4. \quad \text{(B.8)}$$

Note that all terms have been divided by σ. These equations constitute the system to be solved. The balance at the top of the atmosphere is:

$$T_e^4 = \varepsilon_2 T_2^4 + (1-\varepsilon_2)\varepsilon_1 T_1^4 + (1-\varepsilon_2)(1-\varepsilon_1)T_s^4; \quad \text{(B.9)}$$

I shall use this to check my solutions later. Note in the blackbody limit $T_2 = T_e$, showing again that emissivities smaller than one cause the atmosphere to lose radiation to space and cause the effective emissions level to fall from the top of the atmosphere into the interior. Rewriting equations (B.6)-(B.8),

$$\begin{aligned} T_s^4 - \varepsilon_1 T_1^4 - (1-\varepsilon_1)\varepsilon_2 T_2^4 &= T_e^4 && \text{(B.10)} \\ T_s^4 - 2T_1^4 + \varepsilon_2 T_2^4 &= 0 && \text{(B.11)} \\ (1-\varepsilon_1)T_s^4 + \varepsilon_1 T_1^4 - 2T_2^4 &= 0. && \text{(B.12)} \end{aligned}$$

Add equation (B.12) to equation (B.10) for an equation relating T_s and T_2 to T_e:

$$(2-\varepsilon_1)T_s^4 + (\varepsilon_1\varepsilon_2 - \varepsilon_2 - 2)T_2^4 = T_e^4. \qquad \text{(B.13)}$$

Subtracting equation (B.11) from equation (B.10) gives:

$$(2-\varepsilon_1)T_1^4 - \varepsilon_2(2-\varepsilon_1)T_2^4 = T_e^4, \qquad \text{(B.14)}$$

an equation relating T_1 and T_2 to T_e. Multiplying equation (B.11) by $-\varepsilon_1$ and adding it to two times equation (B.10) gives a second equation relating T_s and T_2 to T_e:

$$(2-\varepsilon_1)T_s^4 - \varepsilon_2(2-\varepsilon_1)T_2^4 = 2T_e^4. \qquad \text{(B.15)}$$

Eliminating T_s between equations (B.13) and (B.15) solves for T_2:

$$(2-\varepsilon_2)T_2^4 = T_e^4. \qquad \text{(B.16)}$$

Note that if $\varepsilon_2 = 1$, $T_2 = T_e$; T_2 is independent of the emissivity at lower levels, showing that if the top layer is a blackbody, the manner in which radiation is redistributed through the lower levels of the system is immaterial to setting the effective emissions level. By substituting equation (B.16) into (B.14), I can solve for T_1:

$$(2-\varepsilon_1)T_1^4 = \left[1 + \frac{\varepsilon_2(2-\varepsilon_1)}{2-\varepsilon_2}\right] T_e^4. \qquad \text{(B.17)}$$

Substituting equation (B.16) into (B.13) solves for T_s. After rearranging,

$$(2-\varepsilon_1)T_s^4 = \left[2 + \frac{\varepsilon_2(2-\varepsilon_1)}{2-\varepsilon_2}\right] T_e^4. \qquad \text{(B.18)}$$

Note that if $\varepsilon_1 = \varepsilon_2 = 1$, $T_1^4 = 2\,T_e^4$ and $T_s^4 = 3\,T_e^4$, as in the blackbody problem.

These solutions [equations (B.16), (B.17), and (B.18)] can be plugged into the top of the atmosphere balance [equation (B.9)]. The algebra is tedious and not particularly illustrative, so I have elected not to show it here, but the solutions do verify.

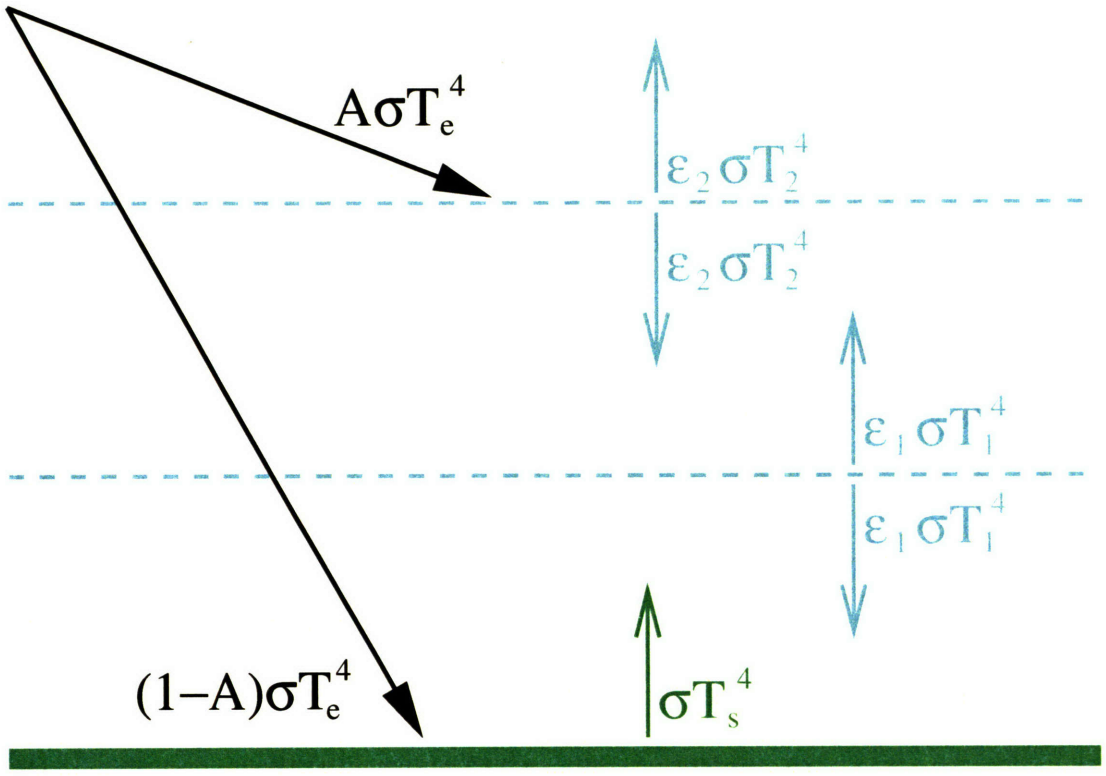

Figure B-3: A copy of figure 2-2. A two layer model in which a fraction (A) of the incoming solar radiation is absorbed at the top layer. Longwave emissivities of ε_1 and ε_2 govern the fraction of absorption and emissions at the two atmospheric levels.

B.3 Interactive ozone heating

In section 2.3.1 I reviewed the standard problem in which the two-layer problem is treated as a thin layer with small amounts of ozone heating and a small emissivity that can be ignored at the surface and lower atmospheric layer. This is really a variation of the one-layer problem, since the surface and first atmospheric layer are completely ignorant about the existence of a second layer above them. In this section, I detail the algebra for a two-layer problem in which the fraction of solar heating and outgoing longwave radiation need not (but can be) small. I repeat the diagram shown in figure 2-2 in figure B-3.

Balances at the surface, first layer, and second layer are:

$$T_s^4 = (1-A)T_e^4 + \varepsilon_1 T_1^4 + \varepsilon_2(1-\varepsilon_1)T_2^4 \quad \text{(B.19)}$$

$$2\varepsilon_1 T_1^4 = \varepsilon_1 T_s^4 + \varepsilon_2\varepsilon_1 T_2^4 \quad \text{(B.20)}$$

$$2\varepsilon_2 T_2^4 = AT_e^4 + \varepsilon_2\varepsilon_1 T_1^4 + \varepsilon_2(1-\varepsilon_1)T_s^4. \quad \text{(B.21)}$$

Note that all terms have been divided by σ. These equations constitute the system

to be solved. The balance at the top of the atmosphere is:

$$T_e^4 = \varepsilon_2 T_2^4 + (1-\varepsilon_2)\varepsilon_1 T_1^4 + (1-\varepsilon_2)(1-\varepsilon_1)T_s^4; \tag{B.22}$$

this can be used to check my solutions later. Rewriting equations (B.19)-(B.21),

$$\begin{aligned} T_s^4 - \varepsilon_1 T_1^4 + \varepsilon_2(1-\varepsilon_1)T_2^4 &= (1-A)T_e^4 && \text{(B.23)} \\ T_s^4 - 2T_1^4 + \varepsilon_2 T_2^4 &= 0 && \text{(B.24)} \\ -\varepsilon_2(1-\varepsilon_1)T_s^4 - \varepsilon_1\varepsilon_2 T_1^4 + 2\varepsilon_2 T_2^4 &= AT_e^4. && \text{(B.25)} \end{aligned}$$

Subtracting equation (B.24) from (B.23) relates T_1 and T_2 with T_e:

$$(2-\varepsilon_1)\left(T_1^4 - \varepsilon_2 T_2^4\right) = (1-A)T_e^4. \tag{B.26}$$

Multiplying equation (B.23) by ε_2 and subtracting (B.25) from it relates T_s and T_2 to T_e:

$$\varepsilon_2(2-\varepsilon_1)T_s^4 + \varepsilon_2(\varepsilon_1\varepsilon_2 - \varepsilon_2 - 2)T_2^4 = \left[\varepsilon_2 - A(\varepsilon_2+1)\right]T_e^4. \tag{B.27}$$

Eliminating T_1 between equations (B.23) and (B.24) yields:

$$(2-\varepsilon_1)T_s^4 - \varepsilon_2(2-\varepsilon_1)T_2^4 = 2(1-A)T_e^4. \tag{B.28}$$

Note that all layers must emit. It is not necessary that they absorb in all wavelengths, but if the do exist, then they must emit if they have a temperature. Thus $\varepsilon \neq 0$: $0 < \varepsilon_2 \leq 1$. Given this, equation (B.27) can be rewritten by dividing through by ε_2:

$$(2-\varepsilon_1)T_s^4 + (\varepsilon_1\varepsilon_2 - \varepsilon_2 - 2)\,T_2^4 = \left[1 - A\left(1 + \frac{1}{\varepsilon_2}\right)\right]T_e^4. \tag{B.29}$$

Subtracting equation (B.28) from (B.29) solves T_2 in terms of the known T_e:

$$(2-\varepsilon_2)\,T_2^4 = \left[1 - A\left(1 - \frac{1}{\varepsilon_2}\right)\right]T_e^4. \tag{B.30}$$

Substituting (B.30) into (B.26) gives:

$$(2-\varepsilon_1)\,T_1^4 = \left\{1 + \frac{\varepsilon_2\,(2-\varepsilon_1)}{(2-\varepsilon_2)} - A\left[1 + \frac{(2-\varepsilon_1)\,(\varepsilon_2-1)}{(2-\varepsilon_2)}\right]\right\}T_e^4. \tag{B.31}$$

Finally, substitute (B.30) into (B.28) to solve for T_s:

$$(2-\varepsilon_1)T_s^4 = \left\{2 + \frac{\varepsilon_2\,(2-\varepsilon_1)}{(2-\varepsilon_2)} - A\left[2 + \frac{(\varepsilon_2-1)\,(2-\varepsilon_1)}{(2-\varepsilon_2)}\right]\right\}T_e^4. \tag{B.32}$$

These solutions can be plugged into the top of the atmosphere balance to verify them.

I have done this, but since the algebra is long, I will not copy it here. A plot of the solution to T_2 shown in equation (B.30) can be found in figure (2-3).

The solution for the temperature at the first layer is a function of three variables: the emissivity at that layer, the fraction of solar radiation absorbed above it, and the emissivity of the layer above it. Two slices of the solution are presented in figure B-4. The highest temperatures are achieved in the blackbody limit when $\varepsilon_1 = \varepsilon_2 = 1$ and when the bulk of the shortwave radiation is absorbed at the surface. When more shortwave radiation is absorbed at the top of the atmosphere, the surface and first layer cool because half of the radiation emitted by the top layer is returned directly to space.

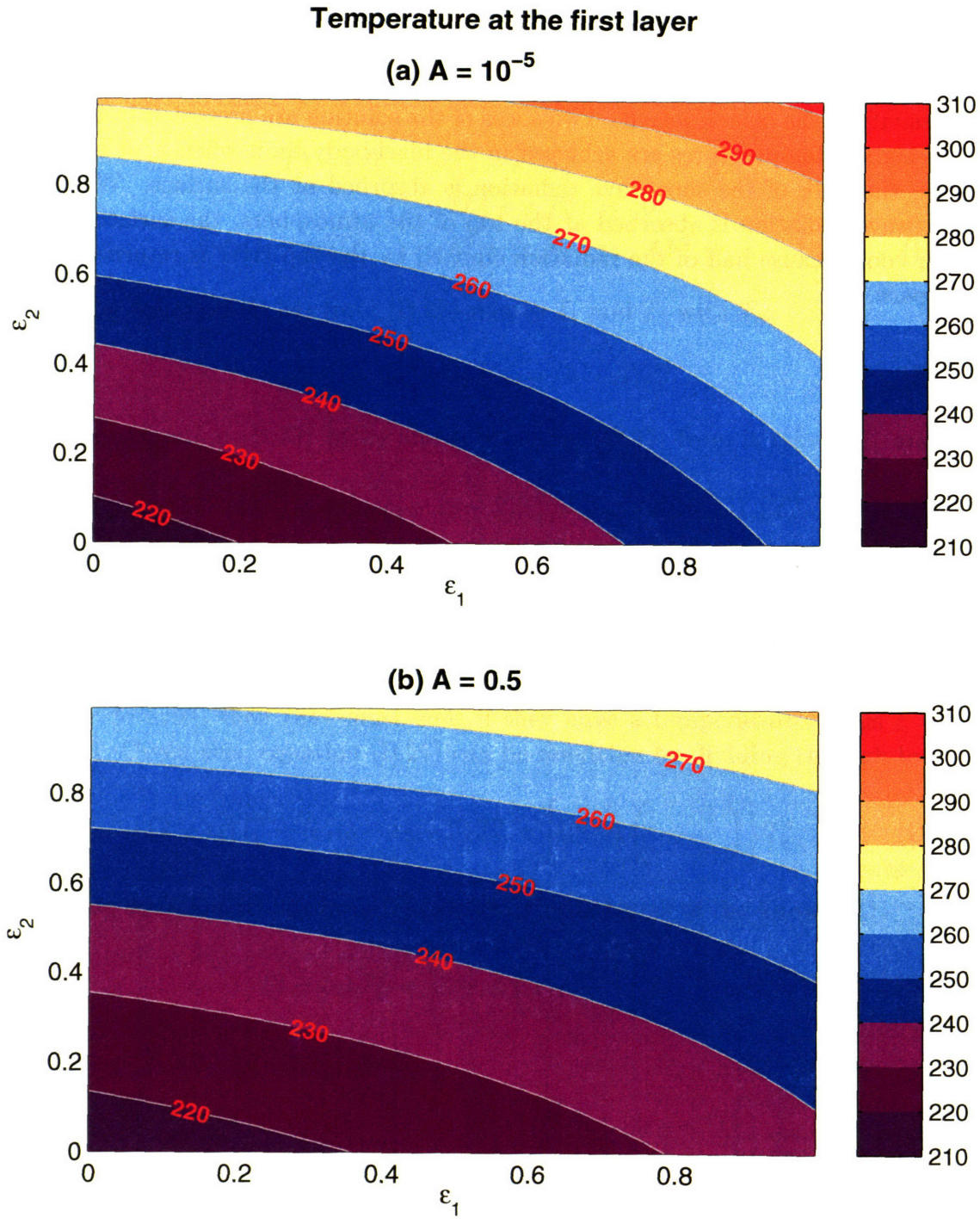

Figure B-4: Temperatures at the first level when the values of A and ε_2 are permitted to influence the temperatures below and when the fraction of shortwave radiation absorbed at the top level is small (panel a) and significant (panel b). In all cases, the temperature is warmest at the blackbody limit, when $\varepsilon_1 = \varepsilon_2 = 1$.

Appendix C

Stratospheric solutions

In Chapter 2 we examined some results from a two-dimensional model. The model is essentially a collection of column models oriented along a north-south axis, stretching from pole to pole. In the meridional plane of the real atmosphere, there is an overturning circulation in the winter stratosphere. This circulation is driven by breaking planetary-scale waves, which are absent in a two dimensional model. How then can the stratospheric overturning shown in figure C-1 be explained?

In this appendix we shall see that the momentum damping (provided by a sponge at the model top) coupled with the cold-core anticyclone at the tropopause (forced by the Hadley cell) forces overturning in the stratosphere. The mechanism of damping is different than in the real stratosphere, but nevertheless provides a needed body force to drive a residual mean circulation.

Consider the quasi-geostrophic response to geopotential forcing of the tropopause with a rigid lid as the upper boundary condition. The response to a rigid lid along which all wind perturbations are forced to zero is mathematically different than the response to a sponge boundary condition in which such perturbations are damped, but the point I am trying to make is merely qualitative: damping in the top of a two-dimensional model will force a stratospheric overturning circulation when coupled with a tropical temperature perturbation.

C.1 Geopotential forcing of the tropopause

Here we consider a zonally averaged fluid in a single hemisphere. The problem is phrased on a sphere ranging in latitude from $\phi = 0$ northward to $\phi = \pi/2$ and from $p = p_t$, the pressure at which the tropopause occurs, to $p = 0$. The Coriolis parameter is approximated by a constant, mid-latitude value f_o.

The top is a rigid lid along which all streamfunction perturbations are zero, and lateral boundary conditions allow a symmetric solution along $\phi = 0$. Note that v_g is zero as $[\partial_x \phi']$ is zero by definition of the zonal averages; thus, there is no flow through the lateral walls. A function of geopotential is specified along the lower boundary;

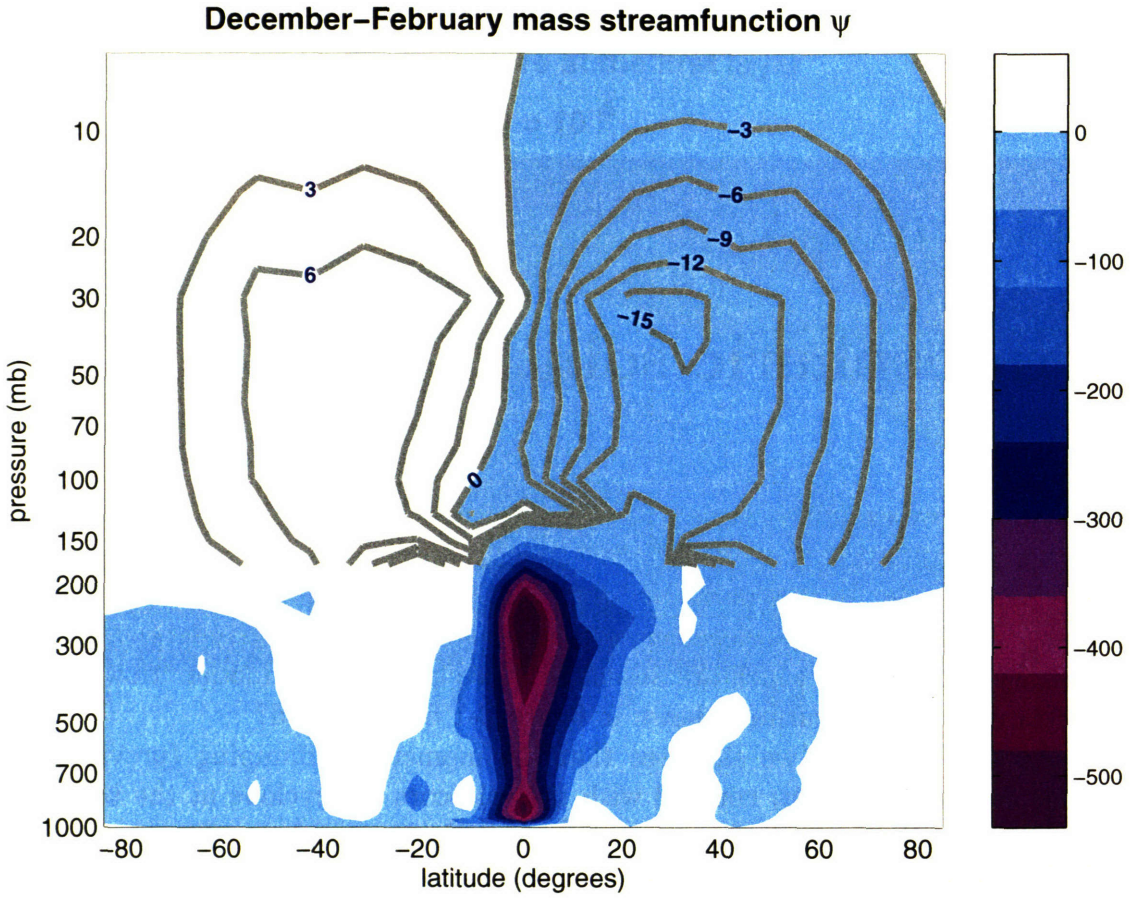

Figure C-1: Mass streamfunction in the two dimensional model discussed in sections 2.4 and 2.5. Streamfunction values (in 10^9 kg/s) of the colored contours are shown in the colorbar; smaller values are drawn in gray above 150 mb. Negative streamfunction lines rotate clockwise in the figure. The Hadley cell dominates the overturning in the troposphere, with sharp ascent in low-latitudes of the summer hemisphere and a broader descent in the tropical latitudes of the winter hemisphere. Overturning in the stratosphere rises in the equatorial latitudes and sinks at high-latitudes.

this forces the response in the fluid above it.

On the interior, the quasi-geostrophic potential vorticity perturbations are zero:

$$\begin{aligned} q &= 0 \\ q &= \nabla^2 \psi \\ &= \frac{1}{a^2 f_o \cos\phi} \frac{\partial}{\partial \phi} \left(\cos\phi \frac{\partial \psi}{\partial \phi} \right) + \frac{f_o}{S} \frac{\partial^2 \psi'}{\partial p^2} \end{aligned}$$

here S has been taken to be constant and not a function of p. To facilitate the mathematics, the coordinates are converted from the (ϕ, p) plane to the (x, p) plane,

where $x = \sin\phi$. With this definition,

$$\frac{\partial\psi}{\partial\phi} = \frac{\partial\psi}{\partial x}\frac{\partial x}{\partial\phi} = \cos\phi\frac{\partial\psi}{\partial x},$$

and

$$\begin{aligned}
\frac{1}{a^2\cos\phi}\frac{\partial}{\partial\phi}\left(\cos^2\phi\frac{\partial\psi}{\partial x}\right) + \frac{f_o^2}{S}\frac{\partial^2\psi}{\partial p^2} &= 0 \\
\frac{\cos\phi}{a^2}\frac{\partial^2\psi}{\partial\phi\partial x} - \frac{2\cos\phi\sin\phi}{a^2\cos\phi}\frac{\partial\psi}{\partial x} + \frac{f_o}{S}\frac{\partial^2\psi}{\partial p^2} &= 0 \\
-\frac{2}{a^2}\sin\phi\frac{\partial\psi}{\partial x} + \frac{\cos\phi}{a^2}\frac{\partial^2\psi}{\partial x^2}\frac{\partial x}{\partial\phi} + \frac{f_o^2}{S}\frac{\partial^2\psi}{\partial p^2} &= 0 \\
\cos^2\phi\frac{\partial^2\psi}{\partial x^2} - 2\sin\phi\frac{\partial\psi}{\partial x} + \frac{f_o^2a^2}{S}\frac{\partial^2\psi}{\partial p^2} &= 0,
\end{aligned}$$

but because $x = \sin\phi$, $\cos^2\phi = 1 - x^2$; therefore

$$\left(1-x^2\right)\frac{\partial^2\psi}{\partial x^2} - 2x\frac{\partial\psi}{\partial x} + \frac{f_o^2a^2}{S}\frac{\partial^2\psi}{\partial p^2} = 0 \tag{C.1}$$

is the governing equation subject to four boundary conditions. These are:

$$\psi = 0 \quad \text{at} \quad p = 0, \tag{C.2}$$

$$\psi = f(x) = 2x^4 - 4x^2 + 1 \quad \text{at} \quad p = p_t, \tag{C.3}$$

$$u' = 0 \Rightarrow \frac{\partial\psi}{\partial x} \quad \text{at} \quad x = 0, \tag{C.4}$$

$$\psi \quad \text{be finite} \quad \text{at} \quad x = 1. \tag{C.5}$$

The form specified in equation (C.3) is a polynomial roughly mimicking the latitudinal gradient in tropopause height. To solve this equation, assume separable solutions of the form

$$\psi = A \cdot Y(x) \cdot Z(p).$$

Plugging this into equation (C.1),

$$\begin{aligned}
A\cdot Z\left[\left(1-x^2\right)\frac{d^2Y}{dx^2} - 2x\frac{dY}{dx}\right] + A\cdot Y\cdot\frac{f_o^2a^2}{S}\frac{d^2Z}{dp^2} &= 0 \\
-\frac{1}{Y}\left[\left(1-x^2\right)\frac{d^2Y}{dx^2} - 2x\frac{dY}{dx}\right] = \frac{1}{Z}\frac{f_o^2a^2}{S}\frac{d^2Z}{dp^2} &= \lambda^2 \\
\left(1-x^2\right)\frac{d^2Y}{dx^2} - 2x\frac{dY}{dx} + \lambda^2Y &= 0 \qquad \text{(C.6)} \\
\frac{d^2Z}{dp^2} - r^2Z &= 0, \qquad \text{(C.7)}
\end{aligned}$$

where $r \equiv \lambda\sqrt{S}/(f_o a)$. The solution to equation (C.7) is

$$Z(p) = C_1 \cosh rp + C_2 \sinh rp;$$

to satisfy the top boundary condition (C.2), $C_1 = 0$ so

$$Z(p) = C \sinh\left(\frac{\lambda\sqrt{S}}{f_o a} p\right). \tag{C.8}$$

Note that equation (C.6) is a Strum-Liouville problem of the form

$$\frac{d}{dx}\left[p(x)\frac{dy}{dx}\right] + [q(x) + \lambda r(x)]\, y = 0$$

where

$$\begin{aligned} p(x) &= 1 - x^2 \\ q(x) &= 0 \\ r(x) &= 1. \end{aligned}$$

This is Legendre's equation, with solution

$$Y(x) = B_1 P_p(x) + B_2 Q_p(x),$$

where $P_p(x)$ are Legendre polynomials of order p and $Q_p(x)$ are Legendre polynomials of the second kind of order p. It can be shown that the solution to Legendre's equation of order p whose derivative vanishes when $x = 0$, which satisfies (C.4), must be a multiple of

$$\begin{aligned} u_p(x) &= 1 - \frac{p(p+1)}{2!}x^2 + \frac{p(p-2)(p+1)(p+3)}{4!}x^4 \\ &\quad - \frac{p(p-2)(p-4)(p+1)(p+3)(p+5)}{6!}x^6 + \ldots \end{aligned}$$

At $x = 1$, $u_p(x)$ is only finite if p is an even integer. Because ψ is finite at $x = 1$ (C.5), $B_2 = 0$ as $Q_p(x)$ is divergent at $x = 1$. Thus,

$$Y_n(x) = C_n P_{2n}(x) \tag{C.9}$$

and $\lambda_n = 2n(2n+1)$. Thus,

$$\psi(x,p) = \sum_{n=0}^{\infty} C_n P_{2n}(x) \sinh\left[\frac{\sqrt{S}}{f_o a}\left(4n^2 + 2n\right) p\right],\ n = 0, 1, 2, \ldots$$

or, writing $m = 2n$,

$$\psi(x,p) = \sum_{m=0}^{\infty} C_m P_m(x) \sinh\left[\frac{\sqrt{S}}{f_o a}\left(m^2+m\right)p\right],\ m = 0,2,4,... \tag{C.10}$$

This is the general solution, and all that now remains is to determine the coefficients C_m is such a way that the fourth boundary condition is satisfied.

C.2 Determine coefficients

In order to determine the values of C_m in equation (C.10), a Legendre-Fourier series using the bottom boundary condition (C.3) must be constructed. Note from (C.3),

$$\sinh\left[\frac{\sqrt{S}}{f_o a}\left(m^2+m\right)p_t\right] C_m \equiv A_m = \begin{cases} 0 & m \text{ odd} \\ (2m+1)\int_0^1 f(x)P_m(x)dx & m \text{ even.} \end{cases}$$

From (C.3), $f(x)$ is a polynomial of degree four. All derivatives of order n vanish identically when $n > 4$. Since it can be shown that

$$\begin{aligned} A_n &= \frac{2n+1}{2}\int_{-1}^{1} f(x)P_n(x)dx \\ &= \frac{2n+1}{2^{n+1}n!}\int_{-1}^{1}\left(1-x^2\right)^n \frac{d^n f(x)}{dx^n}dx, \end{aligned}$$

it follows that $A_n = 0$ when $n > 4$. Only A_0, A_2, and A_4 must be calculated to solve the problem.

C.2.1 Calculate A_0

Since $P_0(x) = 1$,

$$\begin{aligned} A_0 &= 1\int_0^1 f(x)P_0(x)dx \\ &= \int_0^1 \left(2x^4 - 4x^2 + 1\right)dx = \frac{2x^5}{5} - \frac{4x^3}{3} + x\Big|_0^1 \\ A_0 &= \frac{1}{15} \end{aligned} \tag{C.11}$$

C.2.2 Calculate A_2

The second order Legendre polynomial is $P_2(x) = \frac{1}{2}(3x^2 - 1)$ so

$$\begin{aligned} A_2 &= 5\int_0^1 \left(2x^4 - 4x^2 + 1\right)\frac{(3x^2-1)}{2}dx \\ &= \frac{5}{2}\int_0^1 6x^6 - 14x^4 + 7x^2 - 1dx \\ &= \frac{5}{2}\left(\frac{6x^6}{7} - \frac{14x^5}{5} + \frac{7x^3}{3} - x\right)\Big|_0^1 \\ A_2 &= -\frac{32}{21}. \end{aligned} \tag{C.12}$$

C.2.3 Calculate A_4

Since $P_4 = \frac{1}{8}(35x^4 - 30x^2 + 3)$,

$$\begin{aligned} A_4 &= 9\int_0^1 \left(2x^4 - 4x^2 + 1\right)\frac{(35x^4 - 30x^2 + 3)}{8}dx \\ &= \frac{9}{8}\int_0^1 70x^8 - 200x^6 + 161x^4 - 42x^2 + 3dx \\ &= \frac{9}{8}\left(\frac{70}{9}x^9 - \frac{200}{7}x^7 + \frac{161}{5}x^5 - 14x^3 + 3x\right)\Big|_0^1 \\ A_4 &= \frac{16}{35}. \end{aligned} \tag{C.13}$$

C.3 Solution

With the results from the proceeding sections, equation (C.10) may be written in its final form. The geopotential perturbation, ψ, in the stratosphere takes the form:

$$\psi(x,p) = \frac{1}{15} - \frac{48x^2 - 16}{21}\frac{\sinh\left(\frac{6\sqrt{S}}{f_o a}p\right)}{\sinh\left(\frac{6\sqrt{S}}{f_o a}p_t\right)} + \frac{70x^4 - 60x^2 + 6}{35}\frac{\sinh\left(\frac{20\sqrt{S}}{f_o a}p\right)}{\sinh\left(\frac{20\sqrt{S}}{f_o a}p_t\right)}, \tag{C.14}$$

where $x = \sin(\phi)$. The solution is plotted in figure C-2.

The perturbation wind field is proportional to $-\partial_y\psi$; the perturbation temperature field is proportional to $\partial_p\psi$. Given the distribution of ψ along the tropopause, temperatures will be anomalously cold in the tropics and warm at higher latitudes. Now if radiation relaxes these anomalies back to their unperturbed value, the thermodynamic equation is forced with a diabatic heating term. This thermal forcing, coupled with the frictional drag at the top of the stratosphere drive an overturning circulation even in a two-dimensional model. The stronger the drag, the stronger the

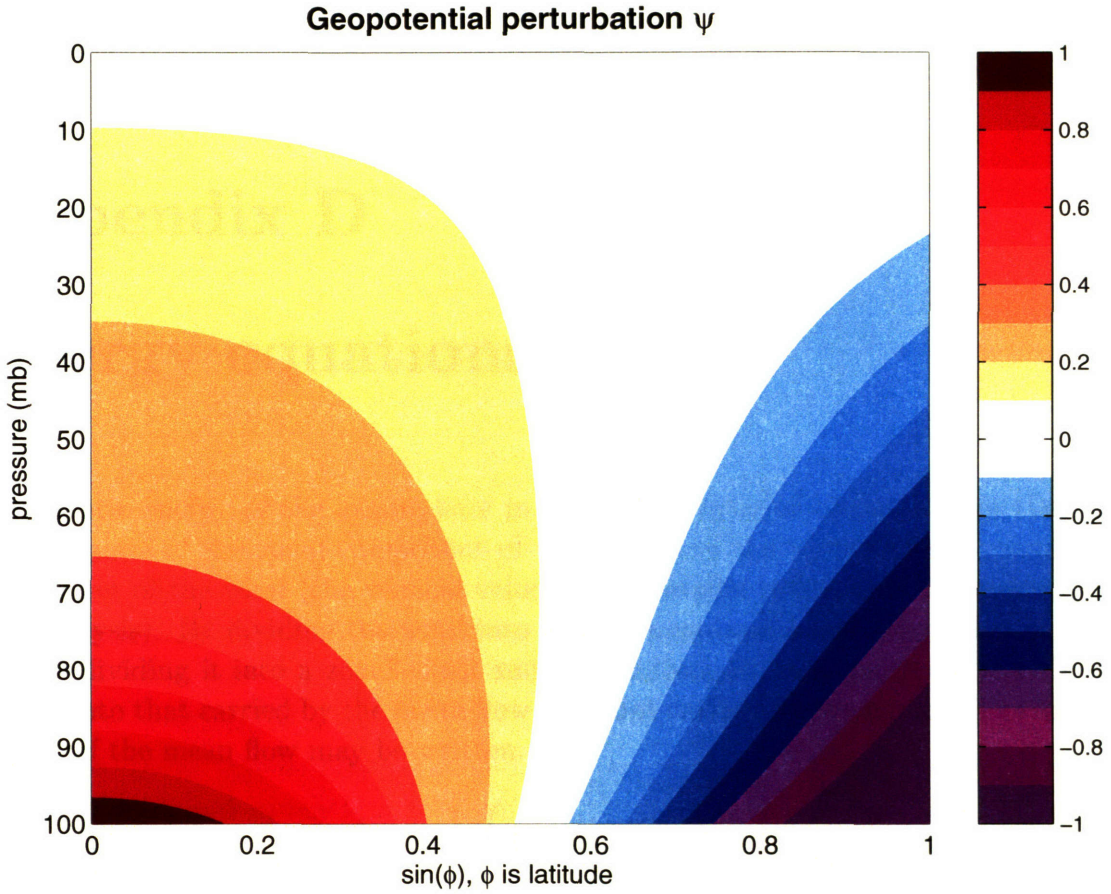

Figure C-2: Plot of equation (C.14). The geopotential function specified along 100 mb decays upward as it must go to zero along the upper boundary. The solution is symmetric about the equator, showing an anticyclone in the lower tropical stratosphere that decays in intensity poleward. Note that the amplitude of the specified forcing in equation (C.3) has been normalized to one; a different amplitude will magnify the field plotted above.

circulation.

Plumb and Eluszkiewicz (1999) note that upwelling in the real stratosphere occurs in equatorial latitudes, while wave drag is confined to the extratropics. In view of downward control, upwelling should not occur equatorward of the imposed drag, as the flow would be required to cross contours of angular momentum. But as discussed by Plumb and Eluszkiewicz (1999), model viscosity provides a forcing in tropical latitudes, and the principle of downward control is violated *if the principle of downward control is restricted to large-scale drag.* (Strictly, the model viscosity provides a drag, and the flow can not extend above the altitude at which it is imposed.) They find that tropospheric thermal forcing might make a contribution to lower-stratosphere upwelling, but it remains unclear how important such a forcing might be in practice.

Appendix D

Energy equations

The kinetic energy of the atmosphere is simply the integral of one-half of the sum of the square of the zonal component of the wind and the square of the meridional component of the wind (the vertical velocity is a smaller order, and we neglect it in this analysis). By dividing the wind into a time-mean and a deviation from it, then further dividing it into a zonal-mean and a deviation, we may partition the kinetic energy into that carried by the mean flow and that carried by the eddies. The kinetic energy of the mean flow may be written:

$$\mathrm{K_M} = \frac{1}{2} \int \left([\overline{u}]^2 + [\overline{v}]^2 \right) \, dm, \tag{D.1}$$

where the overbar denotes a time average, the square brackets denote a zonal average, and dm is a mass element equal to $dx\,dy\,dp/g$. The kinetic energy of the eddies may be further broken down into transient and stationary components:

$$\begin{aligned} \mathrm{K_E} &= \mathrm{K_{TE}} + \mathrm{K_{SE}} \\ &= \frac{1}{2} \int \left(\left[\overline{u'^2} + \overline{v'^2} \right] + \left[\overline{u}^{*2} + \overline{v}^{*2} \right] \right) \, dm, \end{aligned} \tag{D.2}$$

where primes denote a departure from the time-mean and asterisks denote a departure from the zonal-mean.

The potential energy of the atmosphere is much larger than the kinetic energy, and not all of it accessible to the flow. To circumvent this difficulty, Lorenz (1955) defined the available potential energy as the difference between the observed state of the atmosphere and a reference state in which an isentropic redistribution of mass results in horizontal isentropic surfaces. (Note that dynamics may not exist to redistribute the atmospheric mass in such a way.) Lorenz (1955) derived the available potential energy in isentropic coordinates; an approximation of his result (e.g., Peixoto and

Oort, 1992) for the available potential energy of the mean flow may be written:

$$\mathrm{P_M} = \frac{c_p}{2} \int \gamma \left(\left[\overline{T} \right]^2 - \widetilde{\overline{T}}^2 \right) \, dm, \tag{D.3}$$

where the tildes represent departures from an isobaric mean and γ is an inverse measure of the gross global mean static stability:

$$\begin{aligned} \gamma &= -\frac{\kappa\theta}{pT} \left(\frac{\partial \widetilde{\theta}}{\partial p} \right)^{-1} \\ &= \frac{\Gamma_d}{\widetilde{T}} \frac{1}{\Gamma_d - \widetilde{\Gamma}}, \end{aligned} \tag{D.4}$$

where Γ_d is the dry adiabatic lapse rate and Γ is the environmental lapse rate. The available potential energy of the transient and stationary eddies may be written:

$$\begin{aligned} \mathrm{P_E} &= \mathrm{P_{TE}} + \mathrm{P_{SE}} \\ &= \frac{c_p}{2} \int \gamma \left(\left[\overline{T'^2} \right] + \left[\overline{T}^{*2} \right] \right) \, dm. \end{aligned} \tag{D.5}$$

The time rate of change of the mean flow's kinetic energy, $\partial_t \mathrm{K_M}$, consists of several terms, which in symbolic form may be written (Peixoto and Oort, 1974):

$$\frac{\partial}{\partial t} \mathrm{K_M} = \mathrm{C}\left(\mathrm{P_M}, \mathrm{K_M}\right) + \mathrm{C}\left(\mathrm{K_E}, \mathrm{K_M}\right) - \mathrm{D}\left(\mathrm{K_M}\right). \tag{D.6}$$

The first two terms in equation (D.6) represent the conversion of available potential energy to kinetic energy. The derivation, which is detailed in Peixoto and Oort (1992), consists of multiplying the zonal momentum equation by $[u]$, the meridional momentum equation by $[v]$, adding and finally integrating over the entire atmosphere.

The first term, $\mathrm{C}\left(\mathrm{P_M}, \mathrm{K_M}\right)$, shows that kinetic energy in the zonal mean flow can be generated by horizontal cross isobaric flow down the north-south pressure gradient or by the rising of light air and sinking of dense air in zonally symmetric meridional overturning. These two forms, called the $v\nabla z$ and the $\omega\alpha$ formulations, may be written:

$$\mathrm{C}\left(\mathrm{P_M}, \mathrm{K_M}\right) = -\int g \frac{[\overline{v}]}{a} \frac{\partial \left[\overline{\Phi} \right]}{\partial \phi} \, dm \tag{D.7}$$

$$\mathrm{C}\left(\mathrm{P_M}, \mathrm{K_M}\right) = -\int [\overline{\omega}]'' \, [\overline{\alpha}]'' \, dm; \tag{D.8}$$

where Φ is geopotential, ω is the vertical velocity in pressure coordinates, α is the specific volume (ρ^{-1}), and a is the radius of the Earth. The rate of conversion between mean potential and mean kinetic energy can be written in either of the two

forms above; provided that global integrals are considered, the two formulations are equivalent:

$$\begin{aligned} -\vec{v}\cdot\nabla\Phi &= -\nabla\cdot\vec{v}\Phi + \Phi\nabla\cdot\vec{v} \\ &= -\nabla\cdot\vec{v}\Phi - \Phi\frac{\partial\omega}{\partial p} \\ &= -\nabla\cdot\vec{v}\Phi - \frac{\partial\omega\Phi}{\partial p} - \frac{\omega\alpha}{g}. \end{aligned}$$

Thus,

$$-\int g\vec{v}\cdot\nabla\Phi\ dm = -\int \omega\alpha\ dm.$$

The second term in equation (D.6), $\mathrm{C}(\mathrm{K_E}, \mathrm{K_M})$, represents the conversion from eddy into mean kinetic energy. This conversion will occur (i.e., be positive) so long as the north-south and up-down transports of momentum by eddies are up the gradient of the mean zonal wind (Starr referred to this phenomenon as "negative viscosity"). It may be broken into contributions from both transient and stationary eddies:

$$\begin{aligned} \mathrm{C}(\mathrm{K_E}, \mathrm{K_M}) &= \int \left[\overline{v'u'} + \overline{v}^*\overline{u}^*\right] \frac{\cos\phi}{a}\frac{\partial}{\partial\phi}\left(\frac{[\overline{u}]}{\cos\phi}\right) dm \\ &+ \int \left[\overline{v'^2} + \overline{v}^{*2}\right] \frac{1}{a}\frac{\partial[\overline{v}]}{\partial\phi}\ dm \\ &+ \int \left[\overline{\omega'u'} + \overline{\omega}^*\overline{u}^*\right] \frac{\partial[\overline{u}]}{\partial p}\ dm \\ &+ \int \left[\overline{\omega'v'} + \overline{\omega}^*\overline{v}^*\right] \frac{\partial[\overline{v}]}{\partial p}\ dm \\ &- \int [\overline{v}]\left(\left[\overline{u'^2} + \overline{u}^{*2}\right]\right) \frac{\tan\phi}{a}\ dm. \end{aligned} \tag{D.9}$$

Though we do not calculate it in our budgets, the dissipation term is the final sink for kinetic energy of the mean flow; it is the product of the horizontal components of the wind and frictional forces:

$$\mathrm{D}(\mathrm{K_M}) = -\int \left([u][\mathcal{F}_x] + [v][\mathcal{F}_y]\right)\ dm.$$

In a similar manner, the time rate of change of eddy kinetic energy can be obtained; in place of multiplying the momentum equations by the zonally averaged wind, they should be multiplied by the deviations, added, then integrated over the whole atmosphere. This yields:

$$\frac{\partial}{\partial t}\mathrm{K_E} = \mathrm{C}(\mathrm{P_E}, \mathrm{K_E}) - \mathrm{C}(\mathrm{K_E}, \mathrm{K_M}) - \mathrm{D}(\mathrm{K_E}). \tag{D.10}$$

The second term was discussed above (and, naturally, takes the opposite sign here). The first term in equation (D.10) represents the conversion between eddy potential energy and eddy kinetic energy, and may be written in either the $v\nabla\Phi$ or $\omega\alpha$ formulation:

$$\begin{aligned} \mathrm{C}\left(\mathrm{P_E}, \mathrm{K_E}\right) &= \mathrm{C}\left(\mathrm{P_{TE}}, \mathrm{K_{TE}}\right) + \mathrm{C}\left(\mathrm{P_{SE}}, \mathrm{K_{SE}}\right) \\ &= -\int g \left[\overline{\frac{u'}{a\cos\phi}\frac{\partial\Phi'}{\partial\lambda}} + \overline{\frac{v'}{a}\frac{\partial\Phi'}{\partial\phi}} \right] dm \\ &\quad -\int g \left[\frac{\overline{u}^*}{a\cos\phi}\frac{\partial\overline{\Phi}^*}{\partial\lambda} + \frac{\overline{v}^*}{a}\frac{\partial\overline{\Phi}^*}{\partial\phi} \right] dm \end{aligned} \tag{D.11}$$

$$\mathrm{C}\left(\mathrm{P_E}, \mathrm{K_E}\right) = -\int \left[\overline{\omega'\alpha'} + \overline{\omega}^*\overline{\alpha}^* \right] dm. \tag{D.12}$$

Note that unlike Peixoto and Oort (1992), we have broken this term into conversion of transient and stationary eddies separately.

A balance equation for the mean and eddy available potential energy in the atmosphere may be derived as follows. Multiply the first law of thermodynamics by $c_p\Gamma\left([T]-\widetilde{T}\right)$, where $\left([T]-\widetilde{T}\right)$ is the departure of the zonal average temperature from its isobaric mean. Next integrate the product over the entire atmosphere.[1] This yields:

$$\frac{\partial}{\partial t}\mathrm{P_M} = \mathrm{G}\left(\mathrm{P_M}\right) - \mathrm{C}\left(\mathrm{P_M}, \mathrm{P_E}\right) - \mathrm{C}\left(\mathrm{P_M}, \mathrm{K_M}\right). \tag{D.13}$$

Here

$$\mathrm{G}\left(\mathrm{P_M}\right) = \int \gamma \left[\overline{T}\right]'' \left[\overline{Q}\right]'' \, dm \tag{D.14}$$

represents the generation of available potential energy of the mean flow through heating of relatively warm air at low latitudes and cooling of relatively cold air at high latitudes. Given that this term represents the covariance of temperature and heating, it is difficult to estimate from real atmospheric data (Peixoto and Oort, 1992), and we do not estimate it in our budgets either.

The second term in equation (D.13) can be written:

$$\begin{aligned} \mathrm{C}\left(\mathrm{P_M}, \mathrm{P_E}\right) &= -c_p \int \gamma \left[\overline{v'T'} + \overline{v}^*\overline{T}^* \right] \frac{1}{a}\frac{\partial\left[\overline{T}\right]}{\partial\phi} \, dm \\ &\quad -c_p \int p^{-\kappa} \left[\overline{\omega'T'} + \overline{\omega}^*\overline{T}^* \right] \frac{\partial}{\partial p}\left(\gamma p^{\kappa} \left[\overline{T}\right]'' \right) \, dm, \end{aligned} \tag{D.15}$$

which indicates the rate of conversion from mean to eddy available potential energy through poleward or upward eddy heat transports down the gradient of the mean zonal temperature. (Note that κ is the ratio of the gas constant for the dry atmo-

[1] Or over a subdomain, but this will leave boundary terms.

sphere, R_d, to the heat capacity of dry air, c_p.)

Finally, using the same methodology, the balance equation for the time rate of change of eddy available potential energy can be derived:

$$\frac{\partial}{\partial t}\mathrm{P_E} = \mathrm{G}\left(\mathrm{P_E}\right) + \mathrm{C}\left(\mathrm{P_M}, \mathrm{P_E}\right) - \mathrm{C}\left(\mathrm{P_E}, \mathrm{K_E}\right); \tag{D.16}$$

the only new term is the rate of generation of $\mathrm{P_E}$:

$$\mathrm{G}\left(\mathrm{P_E}\right) = \int \gamma \left[\overline{T'Q'} + \overline{T}^*\overline{Q}^*\right] \, dm. \tag{D.17}$$

The stationary component of this term represents heating of warm air anomalies and cooling of cold air anomalies along each latitude circle, which increases the east-west variance of temperature and $\mathrm{P_E}$. The transient component represents heating of warm air anomalies and cooling of cold air anomalies, where an anomaly refers to the departure from a time-mean.

Thus far, we have considered the energy budget of the entire atmosphere, but these equations may also be applied to a subset of the volume. For example, early work was hampered by a limited volume of data, particularly in the Southern Hemisphere; Oort (1964) restricted his analysis to the Northern Hemisphere, which required boundary terms to be calculated at the equator. Muench (1965) considered the energy budget of the winter stratosphere, which prompted the need for boundary terms across an isobaric surface. Starr (1960) first suggested that the lower stratosphere might be dependent on energy brought in from the troposphere rather than energy generated internally. The subsequent developments of Charney and Drazin (1961) and analyses of Oort (1964), Muench (1965), and Dopplick (1971) largely confirmed this idea.

Because our principal interest is the evolution of the stratosphere, we shall consider a budget of this layer separately. By isolating the volume above 100 mb, we can compare similarities and differences between the simulations in both the full atmosphere and in the stratosphere alone. A budget of this volume requires the development of boundary terms at the 100 mb surface.

The lower boundary term at 100 mb must represent the flux of energy into the stratosphere from the troposphere. The boundary terms for the eddy kinetic energy, $\mathrm{B}\left(\mathrm{K_E}\right)$, include the advection of eddy kinetic energy, the work performed on the layer by pressure forces at 100 mb, and the work performed on the layer by the measured

eddy stresses (Oort, 1964). These terms may be added together to form:

$$\begin{aligned} \mathrm{B}(\mathrm{K_E}) &= -\frac{1}{2g} \iint\limits_{100\ \mathrm{mb}} [\overline{\omega}] \left\{ \left[\overline{u'u'} \right] + [\overline{u}^*\overline{u}^*] + \left[\overline{v'v'} \right] + [\overline{v}^*\overline{v}^*] \right\} dx\, dy \\ &\quad - \iint\limits_{100\ \mathrm{mb}} \left[\overline{\omega'\phi'} \right] + \left[\overline{\omega}^*\overline{\phi}^* \right] dx\, dy \\ &\quad - \iint\limits_{100\ \mathrm{mb}} \left[\overline{u}^*\overline{u'\omega'}^* \right] + \left[\overline{v}^*\overline{v'\omega'} \right] + \frac{1}{2} \left[\overline{\omega}^* \left(\overline{u'u'}^* + \overline{v'v'}^* \right) \right] \frac{dx\, dy}{g}. \end{aligned} \tag{D.18}$$

Note that the second of these terms (the work performed on the layer by pressure forces) dominates the magnitude of $\mathrm{B}(\mathrm{K_E})$ (cf. figure 6 of Muench, 1965). In a similar manner, the boundary term for the kinetic energy of the mean flow can be written:

$$\begin{aligned} \mathrm{B}(\mathrm{K_M}) &= -\frac{1}{2} \iint\limits_{100\ \mathrm{mb}} [\overline{\omega}] \left([\overline{u}^2] + [\overline{v}^2] \right) \frac{dx\, dy}{g} \\ &\quad - \iint\limits_{100\ \mathrm{mb}} [\overline{u}] \left(\left[\overline{u'\omega'} \right] + [\overline{u}^*\overline{\omega}^*] \right) \frac{dx\, dy}{g} \\ &\quad - \iint\limits_{100\ \mathrm{mb}} [\overline{v}] \left(\left[\overline{v'\omega'} \right] + [\overline{v}^*\overline{\omega}^*] \right) \frac{dx\, dy}{g} \\ &\quad - \iint\limits_{100\ \mathrm{mb}} [\overline{\omega}]'' \left[\overline{\phi} \right]'' dx\, dy; \end{aligned} \tag{D.19}$$

this represents the sum of contributions from the advection of mean kinetic energy, the work performed by eddy stresses on the 100 mb surface, and work performed by pressure forces (Oort, 1964; Muench, 1965; Dopplick, 1971). At the top of the stratosphere, around 1 mb, these boundary terms will all take the opposite sign; an upward flux of energy across the stratopause represents a loss of energy to the stratosphere.

These integrals were calculated for the Present, Eocene, and Greenhouse simulations for data from the last five Decembers, Januaries, and Februaries; for last five Junes, Julys, and Augusts; and for the last five years of each simulation. In order to compare changes in the entire domain with changes that occur in the stratosphere alone, the analysis was performed separately for the two volumes. The terms were calculated and presented in section 3.4.

Appendix E

The depth to which tropical cyclones mix

E.1 Temperature profiles

The profiles shown in figure 5-18 show that the increase in mixed-layer depth, Δh, must be related to the degree of surface cooling, ΔT, assuming that the final profile is well mixed. The initial temperature structure, T_i, is defined by the background profile, and we evaluate:

$$T_i(h_f) = T_o - \Gamma \Delta h \tag{E.1}$$

$$T_i(h_o) = T_o, \tag{E.2}$$

where Γ is the lapse rate in the thermocline. For simplicity, Γ is assumed to be linear in this region, and from this it follows that the initial, vertically averaged temperature in the region between h_o and h_f is

$$\overline{T_i}(h_o \rightarrow h_f) = T_o - \frac{1}{2}\Gamma \Delta h, \tag{E.3}$$

which is equal to the initial temperature evaluated at $h_o + \Delta h/2$. The final temperature is simply the weighted average of two quantities: the initial mixed-layer temperature, which occupies a depth of h_o, and the initial average thermocline temperature given by equation (E.3), which occupies a depth of Δh. It follows that the final profile T_f, which extends to a depth of $h_f = h_o + \Delta h$ is

$$T_f = \frac{T_o \cdot h_o + \left(T_o - \frac{1}{2}\Gamma \Delta h\right) \cdot \Delta h}{h_o + \Delta h}. \tag{E.4}$$

Continuing with the algebra, and noting that $T_f = T_o - \Delta T$, we can find an expression relating the degree of surface cooling, ΔT, to the depth to which mixing penetrates,

Δh:

$$\begin{aligned}
T_f \cdot h_f &= T_o \cdot h_o + T_o \Delta h - \frac{1}{2}\Gamma (\Delta h)^2 \\
(T_o - \Delta T)(h_o + \Delta h) &= T_o \cdot h_o + T_o \Delta h - \frac{1}{2}\Gamma (\Delta h)^2 \\
T_o \cdot h_o + T_o \cdot \Delta h - \Delta T \cdot h_o - \Delta T \Delta h &= T_o \cdot h_o + T_o \cdot \Delta h - \frac{\Gamma}{2}(\Delta h)^2 \\
\Delta \cdot h_o + \Delta T \Delta h &= \frac{\Gamma}{2}(\Delta h)^2 \\
\Delta T (h_o + \Delta h) &= \frac{\Gamma}{2}(\Delta h)^2 \\
\Delta T &= \frac{\Gamma}{2}\frac{(\Delta h)^2}{h_o + \Delta h}. \qquad \text{(E.5)}
\end{aligned}$$

To be more precise, the effect of salinity variations on the density must be included; using density in lieu of temperature, a parallel derivation of equation (E.5) results in the relation:

$$\Delta \rho = \frac{\Gamma}{2}\frac{(\Delta h)^2}{h_o + \Delta h}, \qquad \text{(E.6)}$$

where Γ is understood to be $d\rho/dz$.

E.2 Relating penetration depth to entrainment

The depth to which mixing penetrates is a direct function of the rate of entrainment:

$$\int_{h_o}^{h_f} dh = \int_0^{\tau} w_e dt, \qquad \text{(E.7)}$$

where w_e is the rate of entrainment and τ is the duration of the intense mixing ($\tau = L/U_T$). How should one parameterize entrainment? There is an extensive literature on this subject, but here I take the formulation developed by Price (1979), Thompson (1979), and Kranenburg (1984); see Schade (1994) for a more thorough discussion of the development. These authors found that the ratio of w_e/u_* is proportional to the square-root of the inverse of the bulk-Richardson number, R_{b*}, which is:

$$R_{b*} = \frac{g(\delta\rho/\rho_o)\, h}{u_*^2}, \qquad \text{(E.8)}$$

where u_*^2 is the square of the friction velocity. It follows that

$$w_e = \frac{n \cdot u_*^2}{\sqrt{g\frac{\delta\rho}{\rho_o}h}}, \qquad \text{(E.9)}$$

where n is a constant of proportionality.

Neglecting salinity variations, $\delta\rho$ may be replaced with δT, the jump in temperature across the base of the mixed-layer. This will evolve in time, but for any depth h, the temperature approaching this depth from above will be:

$$T(h^+) = T_{ml}, \tag{E.10}$$

where T_{ml} is the adjusted temperature of the mixed-layer (see below); the temperature approaching h from below is the undisturbed temperature at this level:

$$T(h^-) = T_o - \Gamma\,(h - h_o)\,. \tag{E.11}$$

Subtracting equation (E.11) from (E.10) yields:

$$\delta T = T_{ml} - T_o + \Gamma\,(h - h_o)\,. \tag{E.12}$$

The adjusted temperature in the mixed-layer may be related to the amount of entrained water *assuming here that the drop in temperature occurs instantaneously.* Proceeding as above, one finds that $T_{ml} = T_o - dT_{ml}$, where

$$dT_{ml} = \frac{\Gamma}{2h}\,(h - h_o)^2 \tag{E.13}$$

in direct analogy to equation (E.5).

It follows from equation (E.7) that

$$\Delta h = \overline{w_e} \cdot \tau, \tag{E.14}$$

provided that w_e can be represented by a temporal average. Note from the formulation in equation (E.9) that the rate of entrainment will decrease when the mixed-layer is deeper and the jump in density (or temperature) across its base increases. Both of these effects have physical interpretations. As the mixed-layer deepens, the surface stress goes into currents over a greater depth, lessening the shear across the base of the mixed-layer. As the temperature or density jump increases, it takes a more powerful shear to overcome the resistance given by the jump in stratification.

To place a lower bound on $\overline{w_e}$, I take the temporal average value of the entrainment coefficient to be its smallest value: the value as the mixed-layer reaches h_f, just prior to the cessation of mixing when the density jump is largest. With this choice, it follows from (E.9) that

$$w_e^2 = \frac{n \cdot u_*^4}{g\alpha h_f \delta T}, \tag{E.15}$$

where α is the specific volume of the base-state, equal to $1/\rho_o$. From (E.12) we have

$$\delta T = -\Delta T + \Gamma\delta h = -\Delta T + \Gamma\,(h_f - h_o) \tag{E.16}$$

when we take w_e to be its value at h_f. Using this and substituting into equation (E.14), we find

$$(\Delta h)^4 + 2h_o(\Delta h)^3 = \frac{2n\tau u_*^4}{g\alpha\Gamma}. \tag{E.17}$$

This is a quartic equation, and though it has an analytic solution, the algebra needed to arrive at a closed expression for Δh is voluminous. A good estimate of the behavior of the exact solution is:

$$\Delta h \sim u^{1.2}\Gamma^{-0.3}. \tag{E.18}$$

This is quite similar to the scaling found by Schade (1994), who related the degree of cooling to parameters including the storm's intensity and thermocline stratification through more than a thousand coupled hurricane-ocean experiments. This shows that the depth to which mixing penetrates will increase slightly faster than linearly with the strength of the storm; weaker stratification in the thermocline will also increase the depth to which mixing penetrates, though this effect is somewhat weaker.

From the work of Schade (1994), we can propose a formulation for the depth to which mixing should penetrate. Let

$$\Delta h = h_\star \left(\frac{u}{u_\star}\right)^{1.2} \left(\frac{\Gamma}{\Gamma_\star}\right)^{-.3}, \tag{E.19}$$

where $h_\star$ is 94.05 m, $u_\star$ is 75 m/s, and $\Gamma_\star$ is 8°C/100 m. We shall take u to be the potential intensity calculated from the sea surface data and atmospheric sounding, given our choice for $u_\star$. With these values, mixing easily penetrates to 150 m in present climate, and this depth will increase with increasing storm intensity and gentler thermocline stratification.

The choice of $h_\star$ to be $O(10^2)$ m may seem high, given that few storms reach their potential intensity. This derivation, however, is only a scaling analysis, not a thorough prediction of the depth to which mixing penetrates. Results from the coupled hurricane-ocean model used by Schade (1994) and Emanuel et al. (2004), which includes detailed turbulent entrainment schemes, reveal that minimal hurricanes ($u \sim 35$m/s) are capable of mixing to this depth when contemporary initial profiles are specified. Real storms do frequently mix down to 150 m (J. Price, personal communication) in the present climate. We expect the depth to vary with storm intensity and thermocline stratification, and typical values may have been quite different in warm climates.

Bibliography

Andrews, D. G., J. R. Holton, and C. B. Leovy: 1987, *Middle Atmosphere Dynamics*. Academic Press, 489 pp.

Andrews, D. G. and M. E. McIntyre: 1976, Planetary waves in horizontal and vertical shear: the generalized Eliassen-Palm relation and the mean zonal acceleration. *Journal of the Atmospheric Sciences*, **33**, 2031–2048.

Archibald, J. D.: 1991, Comment on "'Equable' climates during Earth history?" *Geology*, **19**, 539.

Barron, E. J.: 1983, A warm, equable Cretaceous: The nature of the problem. *Earth Science Review*, **19**, 305–338.

Barron, E. J. and W. M. Washington: 1982, Cretaceous climate: A comparison of atmospheric simulations with the geologic record. *Palaeogeography, Paleoclimatology, Paleoecology*, **40**, 103–133.

——— 1985, Warm Cretaceous climates: high atmospheric CO_2 as a plausible mechanism. *The Carbon Cycle and Atmospheric CO_2: Natural Variations Archean to Present, Geophys. Monogr.*, **32**, 546–553, American Geophysical Union.

Berggren, W. A. and C. D. Hollister: 1974, Palaeogeography, paleobiogeography and the history of circulation in the Atlantic Ocean. *Soc. Econ. Paleontol. Min. Spec.*, **20**, 126–186.

Bister, M. and K. A. Emanuel: 1998, Dissipative heating and hurricane intensity. *Meteorology and Atmospheric Physics*, **52**, 233–240.

Boccaletti, G., R. Ferrari, A. Adcroft, D. Ferreira, and J. Marshall: 2005, The vertical structure of ocean heat transport. *Geophysical Research Letters*, accepted.

Bony, S. and K. A. Emanuel: 2001, A parameterization of the cloudiness associated with cumulus convection: evaluation using TOGA COARE data. *Journal of the Atmospheric Sciences*, **58**, 3158–3183.

Boos, W. R., J. R. Scott, and K. A. Emanuel: 2004, Transient diapycnal mixing and the meridional overturning circulation. *Journal of Physical Oceanography*, **34**, 334–341.

Boville, B. A.: 1986, Wave-mean flow interactions in a general circulation model of the troposphere and stratosphere. *Journal of the Atmospheric Sciences*, **43**, 1711–1725.

Brewer, A. W.: 1949, Evidence for a world circulation provided by the measurements of helium and water vapor distribution in the stratosphere. *Quarterly Journal of the Royal Meteorological Society*, **95**, 351–363.

Broecker, W. S., S. L. Peacock, S. Walker, R. Weiss, E. Fahrbach, M. Schroeder, U. Mikolajewicz, C. Heinze, R. Key, T.-H. Peng, and S. Rubin: 1998, How much deep water is formed in the Southern Ocean? *Journal of Geophysical Research*, **103**, 15833–15843.

Bryan, K. and L. J. Lewis: 1979, A water mass model of the World Ocean. *Journal of Geophysical Research*, **84**, 2503–2517.

Bugnion, V.: 2001, *Driving the ocean's overturning: an adjoint sensitivity study*. Ph.D. thesis, Massachusetts Institute of Technology.

Carslaw, K. S., B. P. Luo, S. L. Clegg, T. Peter, P. Brimblecombe, and P. J. Crutzen: 1994, Stratospheric aerosol growth and HNO_3 gas phase depletion from coupled HNO_3 and water uptake by liquid particles. *Geophysical Research Letters*, **21**, 2479–2482.

Charney, J. G.: 1947, The dynamics of long waves in a baroclinic westerly current. *Journal of Meteorology*, **4**, 135–163.

Charney, J. G. and P. G. Drazin: 1961, Propagation of planetary-scale disturbances from the lower into the upper atmosphere. *Journal of Geophysical Research*, **66**, 83–109.

Charney, J. G. and J. Pedlosky: 1963, On the trapping of unstable planetary waves in the atmosphere. *Journal of Geophysical Research*, **68**, 6441–6442.

Collins, W. D., P. J. Rasch, B. A. Boville, J. J. Hack, J. R. McCaa, D. L. Williamson, J. T. Kiehl, B. Briegleb, C. Bitz, S.-J. Lin, M. Zhang, and Y. Dai: 2004, Description of the NCAR Community Atmosphere Model (CAM3). Technical report, National Center for Atmospheric Research, Boulder, Colorado, NCAR/TN-464+STR.

Cummins, P. F., G. Holloway, and A. E. Gargett: 1990, Sensitivity of the GFDL ocean general circulation model to a parameterization of vertical diffusion. *Journal of Physical Oceanography*, **20**, 817–830.

Dalan, F.: 2003, *Sensitivity of climate change to diapycnal diffusivity in the ocean.* Master's thesis, Massachusetts Institute of Technology.

Dalan, F., P. H. Stone, I. Kamenkovich, and J. Scott: 2005, Sensitivity of the ocean's climate to diapycnal diffusivity in an EMIC. Part I: equilibrium state. *Journal of Climate*, in press.

Danabasoglu, G. and J. C. McWilliams: 1995, Sensitivity of the global ocean circulation to parameterizations of mesoscale tracer transports. *Journal of Climate*, **8**, 2967–2987.

Dawson, M. R., R. M. West, W. Langston, and J. H. Hutchinson: 1976, Paleogene terrestrial vertebrates: Northernmost occurrence, Ellesmere Island, Canada. *Science*, **192**, 781–782.

Dobson, G. M. B.: 1956, Origin and distribution of the polyatomic molecules in the atmosphere. *Proc. R. Soc. London A*, **236**, 187–193.

Dopplick, T. G.: 1971, The energetics of the lower stratosphere including radiative effects. *Quarterly Journal of the Royal Meteorological Society*, **97**, 209–237.

Dunkerton, T. J.: 1978, On the mean meridional mass motions of the stratosphere and mesosphere. *Journal of the Atmospheric Sciences*, **35**, 2325–2333.

Dutkiewicz, S., A. Sokolov, J. Scott, and P. Stone: 2005, A three-dimensional ocean-seaice-carbon cycle model and its coupling to a two-dimensional atmospheric model: Uses in climate change studies. Technical report, Massachusetts Institute of Technology.

Eady, E. T.: 1949, Long waves and cyclone waves. *Tellus*, **1**, 33–52.

Eberle, J. J. and J. E. Storer: 1999, Northernmost record of Brontotheres, Axel Heiberg Island, Canada—Implications for age of the Buchanan Lake Formation and Brontothere paleobiology. *Journal of Paleontology*, **73**, 979–983.

Emanuel, K., C. DesAutels, C. Holloway, and R. Korty: 2004, Environmental control of tropical cyclone intensity. *Journal of the Atmospheric Sciences*, **61**, 843–858.

Emanuel, K. A.: 1986, An air-sea interaction theory for tropical cyclones. Part I: steady-state maintenance. *Journal of the Atmospheric Sciences*, **43**, 585–604.

——— 1988a, The maximum intensity of hurricanes. *Journal of the Atmospheric Sciences*, **45**, 1143–1155.

——— 1988b, Observational evidence of slantwise convective adjustment. *Monthly Weather Review*, **116**, 1805–1816.

——— 1988c, Toward a general theory of hurricanes. *American Scientist*, **76**, 370–379.

——— 1994, *Atmospheric Convection*. Oxford University Press, New York.

——— 2001, The contribution of tropical cyclones to the oceans' meridional heat transport. *Journal of Geophysical Research*, **106**, 14771–14781.

——— 2002, A simple model of multiple climate regimes. *Journal of Geophysical Research*, **107**, 10.1029/2001JD001002.

——— 2005, Variability and trends in global tropical cyclone activity. *Nature*, submitted.

Emanuel, K. A. and D. S. Nolan: 2004, Tropical cyclone activity and the global climate system. *26th AMS Conference on Hurricanes and Tropical Meteorology*, 240–241, Miami, Florida.

Emanuel, K. A. and M. Živković Rothman: 1999, Development and evaluation of a convection scheme for use in climate models. *Journal of the Atmospheric Sciences*, **56**, 1766–1782.

Farrell, B. F.: 1990, Equable climate dynamics. *Journal of the Atmospheric Sciences*, **47**, 2986–2995.

Fels, S. B.: 1985, Radiative-dynamical interactions in the middle atmosphere. *Advances in Geophysics*, **28A**, 277–300.

Fels, S. B., J. D. Mahlman, M. D. Schwarzkopf, and R. W. Sinclair: 1980, Stratospheric sensitivity to perturbations in ozone and carbon dioxide: radiative and dynamical response. *Journal of the Atmospheric Sciences*, **37**, 2265–2297.

Furue, R. and M. Endoh: 2005, Effects of the Pacific diapycnal upwelling on the global and Pacific meridional overturning circulation. *Journal of Physical Oceanography*, submitted.

Ganachaud, A. and C. Wunsch: 2000, Improved estimates of global ocean circulation, heat transport and mixing from hydrographic data-transport. *Nature*, **408**, 453–457.

Gargett, A. E.: 1984, Vertical eddy diffusivity in the ocean interior. *Journal of Marine Research*, **42**, 359–393.

Gent, P. R. and J. C. McWilliams: 1990, Isopycnal mixing in ocean circulation models. *Journal of Physical Oceanography*, **20**, 150–155.

Gnanadesikan, A.: 1999, A simple predictive model for the structure of the oceanic pycnocline. *Science*, **283**, 2077–2079.

Goose, H., F. M. Selten, R. J. Haarsma, and J. D. Opsteegh: 2000, Decadal variability in high northern latitudes as simulated by an intermediate-complexity climate model. *Ann. Glaciol.*.

Greenwood, D. R. and S. L. Wing: 1995, Eocene continental climates and latitudinal temperature gradients. *Geology*, **23**, 1044–1048.

Gregg, M. C.: 1987, Diapycnal mixing in the thermocline: A review. *Journal of Geophysical Research*, **92**, 5249–5286.

H. J. Edmon, J., B. J. Hoskins, and M. E. McIntyre: 1980, Eliassen-Palm cross sections for the troposphere. *Journal of the Atmospheric Sciences*, **37**, 2600–2616.

Haidvogel, D. B. and F. G. Bryan: 1992, *Climate System Modeling*, Cambridge University Press, chapter Ocean general circulation modeling. 371–412.

Hansen, J., G. Russell, D. Rind, P. Stone, A. Lacis, S. Lebedeff, R. Ruedy, and L. Travis: 1983, Efficient three dimensional global models for climate studies: models I and II. *Monthly Weather Review*, **111**, 609–662.

Hartmann, D. L.: 1985, Some aspects of stratospheric dynamics. *Advances in Geophysics*, **28A**, 219–247.

——— 1994, *Global Physical Climatology*. Academic Press, San Diego.

Haynes, P. H., C. J. Marks, M. E. McIntyre, T. G. Shepherd, and K. P. Shine: 1991, On the "downward control" of extratropical diabatic circulations by eddy-induced mean zonal forces. *Journal of the Atmospheric Sciences*, **48**, 651–678.

Held, I. M.: 2001, The partitioning of the poleward energy transport between the tropical ocean and atmosphere. *Journal of the Atmospheric Sciences*, **58**, 943–948.

Held, I. M. and B. J. Hoskins: 1985, Large-scale eddies and the general circulation of the troposphere. *Advances in Geophysics*, **28A**, 3–31.

Held, I. M., M. Ting, and H. Wang: 2002, Northern winter stationary waves: theory and modeling. *Journal of Climate*, **15**, 2125–2144.

Holton, J. R., P. H. Haynes, M. E. McIntyre, A. R. Douglass, R. B. Rood, and L. Pfister: 1995, Stratosphere-troposphere exchange. *Reviews of Geophysics*, **33**, 403–409.

Huber, B. T., K. G. Macleod, and S. L. Wing, eds.: 2000, *Warm climates in Earth History*. Cambridge University Press.

Huber, M. and L. C. Sloan: 2001, Heat transport, deep waters, and thermal gradients: coupled simulation of an Eocene greenhouse climate. *Geophysical Research Letters*, **28**, 3481–3484.

Hughes, T. M. C. and A. J. Weaver: 1994, Multiple equilibria of an asymmetric two-basin ocean model. *Journal of Physical Oceanography*, **24**, 619–637.

Iqbal, M.: 1983, *An Introduction to Solar Radiation*. Academic, New York.

Jeffreys, H.: 1925, On fluid motions produced by difference of temperature and humidity. *Quarterly Journal of the Royal Meteorological Society*, **51**, 347–356.

Jiang, S., P. Stone, and P. Malannotte-Rizzoli: 1999, An assessment of the Geophysical Fluid Dynamics Laboratory ocean model with coarse resolution: Annual-mean climatology. *Journal of Geophysical Research*, **104**, 25623–25645.

Juckes, M. N.: 2000, The static stability of the midlatitude troposphere: the relevance of moisture. *Journal of the Atmospheric Sciences*, **57**, 3050–3057.

Julian, P. R. and K. B. Labitzke: 1965, A study of atmospheric energetics during the January-February 1963 stratospheric warming. *Journal of the Atmospheric Sciences*, **22**, 597–610.

Kamenkovich, I. V., A. P. Sokolov, and P. H. Stone: 2002, An efficient climate model with a 3D ocean and statistical-dynamical atmosphere. *Climate Dynamics*, **19**, 585–598.

Kent, G. S., L. R. Poole, and M. P. McCormick: 1986, Characteristics of Arctic polar stratospheric clouds as measured by airborne lidar. *Journal of the Atmospheric Sciences*, **43**, 2149–2161.

Kiehl, J. T., B. A. Boville, and B. P. Briegleb: 1988, Response of a general circulation model to a prescribed Antarctic ozone hole. *Nature*, **322**, 501–504.

Kinne, S. and O. B. Toon: 1990, Radiative effects of polar stratospheric clouds. *Geophysical Research Letters*, **17**, 373–376.

Kirk-Davidoff, D. B., D. P. Schrag, and J. G. Anderson: 2002, On the feedback of stratospheric clouds on polar climate. *Geophysical Research Letters*, **29**, 10.1029/2002GL014659.

Kranenburg, C.: 1984, Wind-induced entrainment in a stably stratified fluid. *Journal of Fluid Mechanics*, **145**, 253–273.

Ledwell, J. R., E. T. Montgomery, K. L. Polzin, L. C. St. Laurent, R. W. Schmitt, and J. M. Toole: 2000, Evidence for enhanced mixing over rough topography in the abyssal ocean. *Nature*.

Ledwell, J. R., A. J. Watson, and C. S. Law: 1993, Evidence for slow mixing across the pycnocline from open-ocean tracer-release experiment. *Nature*, **364**, 701–703.

——— 1998, Mixing of a tracer in the pycnocline. *Journal of Geophysical Research*, **103**, 21499–21529.

Leovy, C. B.: 1964, Simple models of thermally driven mesospheric circulation. *Journal of the Atmospheric Sciences*, **21**, 327–341.

Lindzen, R. S.: 1990, *Dynamics in Atmospheric Physics*. Cambridge University Press.

Lindzen, R. S., M.-D. Chou, and A. Y. Hou: 2001, Does the Earth have an adaptive infrared iris? *Bulletin of the American Meteorological Society*, **82**, 417–432.

Lindzen, R. S. and B. Farrell: 1980, The role of the polar regions in global climate, and a new parameterization of global heat transport. *Monthly Weather Review*, **108**, 2064–2079.

Lindzen, R. S. and A. Y. Hou: 1988, Hadley circulation for zonally averaged heating centered off the equator. *Journal of the Atmospheric Sciences*, **45**, 2416–2427.

Lorenz, E. N.: 1955, Available potential energy and the maintenance of the general circulation. *Tellus*, **7**, 157–167.

Lucarini, V.: 2002, Thermohaline circulation stability. General exam paper, Program in Atmospheres, Oceans and Climate, Massachusetts Institute of Technology.

Luyten, J., J. Pedlosky, and H. Stommel: 1983, The ventilated thermocline. *Journal of Physical Oceanography*, **13**, 292–309.

Lyle, M.: 1997, Could early Cenozoic thermohaline circulation have warmed the poles? *Paleoceanography*, **12**, 161–167.

MacKenzie, A. R., M. Kulmala, A. Laaksonen, and T. Vesala: 1995, On the theories of type 1 polar stratospheric cloud formation. *Journal of Geophysical Research*, **100**, 11275–11288.

Manabe, S. and K. Bryan: 1985, CO_2-induced change in a coupled ocean-atmosphere model and its paleoclimatic implications. *Journal of Geophysical Research*, **90**, 11689–11708.

Manabe, S. and R. J. Stouffer: 1988, Two stable equilibria of a coupled ocean-atmosphere model. *Journal of Climate*, **1**, 841–866.

Mancini, E., G. Pitari, and G. Visconti: 1992, Dehydration in the Antarctic stratosphere: radiative effects. *Geophysical Research Letters*, **19**, 585–588.

Mantyla, A. and J. L. Reid: 1983, Abyssal characteristics of the World Ocean waters. *Deep-Sea Research*, **30**, 805–833.

Marotzke, J.: 1997, Boundary mixing and the dynamics of the three-dimensional thermohaline circulation. *Journal of Physical Oceanography*, **27**, 1713–1727.

Marshall, J., A. Adcroft, C. Hill, and L. Perelman: 1997a, Hydrostatic, quasi-hydrostatic and non-hydrostatic ocean modeling. *Journal of Geophysical Research*, **102**, 5733–5752.

Marshall, J., A. Adcroft, C. Hill, L. Perelman, and C. Heisey: 1997b, A finite-volume, incompressible Navier Stokes model for studies of the ocean on parallel computers. *Journal of Geophysical Research*, **102**, 5753–5766.

McKenna, M.: 1980, Eocene paleolatitude, climate, and mammals of Ellesmere Island. *Palaeogeography, Palaeoclimatology, Palaeoecology*, **30**, 349–362.

Miller, K. G., T. R. Janacek, M. E. Katz, and D. J. Keil: 1987, Abyssal circulation and benthic foraminiferal changes near the Paleocene/Eocene boundary. *Paleoceanography*, **2**, 741–761.

Molina, M. J. and F. S. Rowland: 1974, Stratospheric sink for chlorofluoromethanes: chlorine atomc-atalysed destruction of ozone. *Nature*, **249**, 810–812.

Molina, M. J., T.-L. Tso, L. T. Molina, and F. C.-Y. Wang: 1987, Antarctic stratospheric chemistry of chlorine nitrate, hydrogen chloride, and ice: release of active chlorine. *Science*, **238**, 1253–1257.

Morcrette, J.-J.: 1991, Radiation and cloud radiative properties in the European Centre Medium Range Weather Forecasts forecasting system. *Journal of Geophysical Research*, **96**, 9121–9132.

Muench, H. S.: 1965, On the dynamics of the wintertime stratospheric circulation. *Journal of the Atmospheric Sciences*, **22**, 349–360.

Munk, W.: 1966, Abyssal recipes. *Deep-Sea Research*, **13**, 707–730.

Munk, W. and C. Wunsch: 1998, Abyssal recipes II: Energetics of tidal and wind mixing. *Deep-Sea Research*, **45**, 1977–2010.

Murgatroyd, R. J. and R. M. Goody: 1958, Sources and sinks of radiative energy. *Quarterly Journal of the Royal Meteorological Society*, **84**, 225–234.

Murgatroyd, R. J. and F. Singleton: 1961, Possible meridional circulations in the stratosphere and mesosphere. *Quarterly Journal of the Royal Meteorological Society*, **87**, 125–135.

Nilsson, J.: 1995, Energy flux from traveling hurricanes to the oceanic internal wave field. *Journal of Physical Oceanography*, **25**, 558–573.

Nilsson, J., G. Brostrom, and G. Walin: 2003, The thermohaline circulation and vertical mixing: Does weaker density stratification give stronger overturning? *Journal of Physical Oceanography*, **33**, 2781–2795.

Nilsson, J. and K. A. Emanuel: 1999, Equilibrium atmospheres of a two-column radiative convective model. *Quarterly Journal of the Royal Meteorological Society*, **125**, 2239–2264.

North, G. R.: 1975, Analytical solution of a simple climate model with diffusive heat transport. *Journal of the Atmospheric Sciences*, **32**, 1301–1307.

Oort, A. H.: 1964, On the energetics of the mean and eddy circulations in the lower stratosphere. *Tellus*, **16**, 309–327.

Oort, A. H. and J. P. Peixoto: 1983, Global angular momentum and energy balance requirements from observations. *Advances in Geophysics*, **25**, 355–490.

Oort, A. H. and T. H. Vonder Haar: 1976, On the observed annual cycle in the ocean-atmosphere heat balance over the Northern Hemisphere. *Journal of Physical Oceanography*, **6**, 781–800.

Opsteegh, J. D., R. J. Haarsma, F. M. Selten, and A. Kattenberg: 1998, ECBILT: a dynamic alternative to mixed boundary conditions in ocean models. *Tellus*, **50A**, 348–367.

Osborne, T. R.: 1980, Estimates of the local rate of vertical diffusion from dissipation measurements. *Journal of Physical Oceanography*, **10**, 83–89.

Park, Y.-G. and K. Bryan: 2000, Comparison of thermally driven circulations from a depth coordinate model and an isopycnal layer model: Part I. A scaling law–sensitivity to vertical diffusivity. *Journal of Physical Oceanography*, **30**, 590–605.

Pearson, P. N., P. W. Ditchfield, J. Singano, K. G. Harcourt-Brown, C. J. Nicholas, R. K. Olsson, N. J. Shackleton, and M. A. Hall: 2001, Warm tropical sea surface temperatures in the Late Cretaceous and Eocene epochs. *Nature*, **413**, 481–487.

Pearson, P. N. and M. R. Palmer: 2000, Atmospheric carbon dioxide concentrations over the past 60 million years. *Nature*, **406**, 695–699.

Pedlosky, J.: 1996, *Ocean Circulation Theory*. Springer-Verlag, Heidelberg.

Peixoto, J. P.: 1974, The annual distribution of atmospheric energy on a planetary scale. *Journal of Geophysical Research*, **79**, 2149–2159.

Peixoto, J. P. and A. H. Oort: 1992, *Physics of Climate*. Springer-Verlag New York, Inc., New York, N.Y.

Pierrehumbert, R. T.: 2002, The hydrologic cycle in deep-time climate problems. *Nature*, **419**, 191–198.

Plumb, R. A. and J. Eluszkiewicz: 1999, The Brewer-Dobson circulation: dynamics of the tropical upwelling. *Journal of the Atmospheric Sciences*, **56**, 868–890.

Polzin, K. L., J. M. Toole, J. R. Ledwell, and R. W. Schmitt: 1997, Spatial variability of turbulent mixing in the abyssal ocean. *Science*, **276**, 93–96.

Price, J. F.: 1979, On the scaling of stress-driven entrainment experiments. *Journal of Fluid Mechanics*, **90**, 509–529.

——— 1981, Upper ocean response to a hurricane. *Journal of Physical Oceanography*, **11**, 153–175.

——— 1983, Internal wave wake of a moving storm, Part I: Scales, energy, budget, and observations. *Journal of Physical Oceanography*, **13**, 949–965.

Price, J. F. and M. A. Sundermeyer: 1999, Stratified Ekman layers. *Journal of Geophysical Research*, **104**, 20467–20494.

Prinn, R. G., H. D. Jacoby, A. P. Sokolov, C. Wang, X. Xiao, Z. L. Yang, R. S. Eckaus, P. H. Stone, A. D. Ellerman, J. M. Melillo, J. Fitzmaurice, D. W. Kicklighter, G. L. Holian, and Y. Liu: 1999, Integrated global system model for climate policy assessment: feedbacks and sensitivity studies. *Climate Change*, **41**, 469–546.

Rahmstorf, S.: 1996, On the freshwater forcing and transport of the Atlantic thermohaline circulation. *Climate Dynamics*, **12**, 799–811.

Rahmstorf, S. and M. H. England: 1997, Influence of Southern Hemisphere winds on North Atlantic Deep Water flow. *Journal of Physical Oceanography*, **27**, 2040–2054.

Raymond, D. J., S. K. Esbensen, C. Paulson, M. Gregg, C. S. Bretherton, W. A. Petersen, R. Cifelli, L. K. Shay, C. Ohlmann, and P. Zuidema: 2004, EPIC2001 and the coupled ocean-atmosphere system of the tropical east Pacific. *Bulletin of the American Meteorological Society*, **85**, 1341–1354.

Reed, R. J., J. L. Wolfe, and H. Nishimoto: 1963, A spectral analysis of the energetics of the stratospheric sudden warming of early 1957. *Journal of the Atmospheric Sciences*, **20**, 256–275.

Remsberg, E. E., J. M. Russell III, L. L. Gordley, J. C. Gille, and P. L. Baily: 1984, Implications of the stratospheric water vapor distribution as determined from the Nimbus 7 LIMS experiment. *Journal of the Atmospheric Sciences*, **41**, 2934–2945.

Rind, D., N. K. Balachandran, A. Lacis, and G. Russell: 1988a, The GISS global climate-middle atmosphere model. Part I: model structure and climatology. *Journal of the Atmospheric Sciences*, **45**, 329–370.

Rind, D., M. Chandler, P. Lonergan, and J. Lerner: 2001, Climate change and the middle atmosphere 5. Paleostratosphere in cold and warm climates. *Journal of Geophysical Research*, **106**, 20195–20212.

Rind, D., D. Shindell, P. Lonergan, and N. K. Balachandran: 1998, Climate change and the middle atmosphere. Part III: the doubled co_2 climate revisited. *Journal of Climate*, **11**, 876–894.

Rind, D., R. Suozzo, and N. K. Balachandran: 1988b, The GISS global climate-middle atmosphere model. Part II: model variability due to interactions between planetary waves, the mean circulation and gravity wave drag. *Journal of the Atmospheric Sciences*, **45**, 371–386.

Rind, D., R. Suozzo, N. K. Balachandran, and M. J. Prather: 1990, Climate change and the middle atmosphere. part I: the doubled co_2 climate. *Journal of the Atmospheric Sciences*, **47**, 475–494.

Rosenfield, J. E.: 1992, Radiative effects of polar stratospheric clouds during the Airborne Antarctic Ozone Experiment and the Airborne Arctic Stratospheric Expedition. *Journal of Geophysical Research*, 7841–7858.

——— 1993, Radiative feedback of polar stratospheric clouds on Antarctic temperatures. *Geophysical Research Letters*, **20**, 1195–1198.

Samelson, R. M. and G. K. Vallis: 1997, Large-scale circulation with small diapycnal diffusion: the two-thermocline limit. *Journal of Marine Research*, **55**, 223–275.

Sandström, J. W.: 1908, Dynamische Versuche mit Meerwasser. *Annals in Hydrodynamic Marine Meteorology*, **36**, 6–23.

Schade, L. R.: 1994, *The ocean's effect on hurricane intensity*. Ph.D. thesis, Massachusetts Institute of Technology.

Schade, L. R. and K. A. Emanuel: 1999, The ocean's effect on the intensity of tropical cyclones: Results from a simple coupled atmosphere-ocean model. *Journal of the Atmospheric Sciences*, **56**, 642–651.

Schmidt, G. A. and D. T. Shindell: 2003, Atmospheric composition, radiative forcing, and climate change as a consequence of a massive methane release from gas hydrates. *Paleoceanography*, **18**, 1004, doi:10.1029/2002PA000757.

Schneider, S. H., S. L. Thompson, and E. J. Barron: 1985, Mid-Cretaceous continental surface temperatures: are high carbon dioxide concentrations needed to simulate above freezing winter conditions? *The Carbon Cycle and Atmospheric CO_2: Natural Variations Archean to Present, Geophys. Monogr.*, **32**, 554–559, American Geophysical Union.

Schneider, T.: 2004, The tropopause and the thermal stratification in the extratropics of a dry atmosphere. *Journal of the Atmospheric Sciences*, **61**, 1317–1340.

Schrag, D. P.: 1999, Effects of diagenesis on the isotopic record of late Paleogene tropical sea surface temperatures. *Chemical Geology*, **161**, 215–224.

Schweitzer, H. J.: 1980, Environment and climate in the early Tertiary of Spitsbergen. *Palaeogeography, Palaeoclimatology, Palaeoecology*, **30**, 297–311.

Scott, J., J. Marotzke, and P. Stone: 1999, Interhemispheric thermohaline circulation in a coupled box model. *Journal of Physical Oceanography*, **29**, 351–365.

Scott, J. R.: 2000, *The roles of mixing, geothermal heating, and surface buoyancy forcing in ocean meridional overturning dynamics*. Ph.D. thesis, Massachusetts Institute of Technology.

Scott, J. R. and J. Marotzke: 2002, The location of diapycnal mixing and the meridional overturning circulation. *Journal of Physical Oceanography*, **32**, 3328–3345.

Seinfeld, J. H. and S. N. Pandis: 1991, *Atmospheric Chemistry and Physics*. John Wiley and Sons, Inc., New York, 1326 pages.

Sellers, W. D.: 1969, A climate model based on the energy balance of the earth-atmosphere system. *Journal of Applied Meteorology*, **8**, 392–400.

Semeniuk, K. and T. G. Shepherd: 2001, The middle-atmosphere Hadley circulation and equatorial inertial adjustment. *Journal of the Atmospheric Sciences*, **58**, 3077–3096.

Shackleton, N. J., M. A. Hall, and A. Boersma: 1984, Init. rep. deep sea drilling project. Technical report, Government Printing Office, Washington, D.C.

Shellito, C. J., L. C. Sloan, and M. Huber: 2003, Climate model sensitivity to atmospheric CO_2 levels in the Early-Middle Paleogene. *Palaeogeography, Palaeoclimatology, Palaeoecology*, **193**, 113–123.

Shepherd, T. G.: 2000, The middle atmosphere. *Journal of Atmospheric and Solar-Terrestrial Physics*, **62**, 1587–1601.

Sloan, L. C. and E. J. Barron: 1990, "Equable" climates during Earth history? *Geology*, **18**, 489–492.

——— 1991, Reply to comments on "'Equable' climates during Earth history?" *Geology*, **19**, 540–542.

——— 1992, A comparison of Eocene climate model results to quantified paleoclimatic interpretations. *Palaeogeography, Paleoclimatology, Paleoecology*, **93**, 183–202.

Sloan, L. C., M. Huber, and A. Ewing: 1999, *Reconstructing ocean history: a window into the future*, Plenum Publishers, chapter Polar stratospheric cloud forcing in a greenhouse world. 273–293.

Sloan, L. C. and D. Pollard: 1998, Polar stratospheric clouds: A high latitude warming mechanism in an ancient greenhouse world. *Geophysical Research Letters*, **25**, 3517–3520.

Sloan, L. C. and D. K. Rea: 1995, Atmospheric carbon dioxide and early Eocene climate: A general circulation modeling sensitivity study. *Palaeogeography, Palaeoclimatology, Palaeoecology*, **119**, 275–292.

Sloan, L. C., J. C. G. Walker, and T. C. Moore, Jr.: 1995, Possible role of oceanic heat transport in early Eocene climate. *Paleoceanography*, **10**, 347–356.

Sloan, L. C., J. C. G. Walker, T. C. Moore, Jr., D. K. Rea, and J. C. Zachos: 1992, Possible methane-induced polar warming in the early Eocene. *Nature*, **357**, 320–322.

Smith, A. K. and L. V. Lyjak: 1985, An observational estimate of gravity wave drag from the momentum balance of the middle atmosphere. *Journal of Geophysical Research*.

Sokolov, A. and P. Stone: 1998, A flexible climate model for use in integrated assessments. *Climate Dynamics*, **14**, 291–303.

Solomon, S., R. R. Garcia, F. S. Rowland, and D. J. Wuebbles: 1986, On the depletion of Antarctic ozone. *Nature*, **321**, 755–758.

Stanford, J. L. and J. S. Davis: 1974, A century of stratospheric cloud reports: 1870–1972. *Bulletin of the American Meteorological Society*, **55**, 213–219.

Starr, V. P.: 1948, An essay on the general circulation of the earth's atmosphere. *Journal of Meteorology*, **5**, 39–43.

——— 1960, Questions concerning the energy of stratospheric motions. *Archiv. für Met. Geophys. und Biokl., A.*, **12**, 1–7.

Stein, B., C. Wedekind, H. Wille, F. Immler, M. Müller, L. Wöste, M. del Guasta, M. Morandi, L. Stefanutti, A. Antonelli, P. Agostini, V. Rizi, G. Readelli, V. Mitev,

R. Matthey, R. Kivi, and E. Kyrö: 1999, Optical classification existence temperatures, and coexistence of different polar stratospheric cloud types. *Journal of Geophysical Research*, **104**, 23983–23993.

Stone, P. H.: 1978a, Baroclinic adjustment. *Journal of the Atmospheric Sciences*, **35**, 561–571.

——— 1978b, Constraints on dynamical transports of energy on a spherical planet. *Dynamics of Atmospheres and Oceans*, **2**, 123–139.

Stone, P. H. and B. Nemet: 1996, Baroclinic adjustment: a comparison between theory, observations, and models. *Journal of the Atmospheric Sciences*, **53**, 1663–1674.

Stone, P. H. and M.-S. Yao: 1987, Development of a two-dimensional zonally averaged statistical-dynamical model. Part II: the role of eddy momentum fluxes in the general circulation and their parameterization. *Journal of the Atmospheric Sciences*, **44**, 3769–3786.

——— 1990, Development of a two-dimensional zonally averaged statistical-dynamical model. Part III: the parameterization of the eddy fluxes of heat and moisture. *Journal of Climate*, **3**, 726–740.

Tabazadeh, A., E. J. Jensen, O. B. Toon, and M. R. Schoeberl: 2001, Role of the stratospheric polar freezing belt in denitrification. *Science*, **291**, 2591–2594.

Teisserenc de Bort, L. P.: 1902, Variations de la température de l'air libre dans la zone comprise entre 8 km et 13 km d'altitude. *C. R. Hebd. Seances Acad. Sci.*, **134**, 987–989.

Thompson, R.: 1979, A reinterpretation of the entrainment process in some laboratory experiments. *Journal of Fluid Mechanics*, **46**, 299–319.

Thorpe, R. B., J. M. Gregory, T. C. Johns, R. A. Wood, and J. F. B. Mitchell: 2001, Mechanisms determining the Atlantic thermohaline circulation response to greenhouse gas forcing in a non-flux-adjusted coupled climate model. *Journal of Climate*, **14**, 3102–3116.

Thuburn, J. and G. C. Craig: 1997, GCM tests of theories for the height of the tropopause. *Journal of the Atmospheric Sciences*, **54**, 869–882.

Toggweiler, J. R. and H. Bjornsson: 2000, Drake Passage and paleoclimate. *Journal of Quarternary Science*, **15**, 319–328.

Toggweiler, J. R. and B. Samuels: 1995, Effect of Drake Passage on the global thermohaline circulation. *Deep-Sea Research*, **42**, 477–500.

——— 1998, On the ocean's large-scale circulation near the limit of no vertical mixing. *Journal of Physical Oceanography*, **28**, 1832–1852.

Tolbert, M. A., M. J. Rossi, R. Malhotra, and D. M. Golden: 1987, Reaction of chlorine nitrate with hydrogen chloride and water at Antarctic stratospheric temperatures. *Science*, **238**, 1258–1260.

Toole, J. M., K. L. Polzin, and R. W. Schmitt: 1994, Estimates of diapycnal mixing in the abyssal ocean. *Science*, **264**, 1120–1123.

Trenberth, K., J. Olson, and W. Large: 1989, A global wind stress climatology based on ECMWF analyses. Technical report, National Center for Atmospheric Research, Technical Report NCAR/TN-338+STR.

Trenberth, K. E. and J. M. Caron: 2001, Estimates of meridional atmosphere and ocean heat transports. *Journal of Climate*, **14**, 3433–3443.

Tsujino, H., H. Hasumi, and N. Suginohara: 2000, Deep Pacific circulation controlled by vertical diffusivity at the lower thermocline depths. *Journal of Physical Oceanography*, **30**, 2853–2865.

Vallis, G. K.: 2000, Large-scale circulation and production of stratification: effects of wind, geometry, and diffusion. *Journal of Physical Oceanography*, **30**, 933–954.

Wang, W.-C. and P. H. Stone: 1980, Effect of ice-albedo feedback on global sensitivity in a one-dimensional radiative-convective climate model. *Journal of the Atmospheric Sciences*, **37**, 545–552.

Wang, X.: 1997, *Global thermohaline circulation and ocean-atmosphere coupling*. Ph.D. thesis, Massachusetts Institute of Technology.

Weaver, A. J. and T. M. C. Hughes: 1996, On the incompatibility of ocean and atmosphere models and the need for flux adjustments. *Climate Dynamics*, **12**, 141–170.

Welander, P.: 1986, Thermohaline effects in the ocean circulation and related simple models. *Large-Scale Transport Processes in Oceans and Atmosphere*, J. Willebrand and D. Anderson, eds., D. Reidel, 163–200.

Wiebe, E. C. and A. J. Weaver: 1999, On the sensitivity of global warming experiments to the parameterisation of sub-grid scale ocean mixing. *Climate Dynamics*, **15**, 875–893.

Wing, S. L.: 1991, Comment on "'Equable' climates during Earth history?" *Geology*, **19**, 539–540.

Wunsch, C.: 1998, The work done by the wind on the oceanic general circulation. *Journal of Physical Oceanography*, **28**, 2332–2340.

Wunsch, C. and R. Ferrari: 2004, Vertical mixing, energy, and the general circulation of the oceans. *Annual Reviews of Fluid Mechanics*, **36**, 281–314.

Xu, K.-M. and K. A. Emanuel: 1989, Is the tropical atmosphere conditionally unstable? *Journal of the Atmospheric Sciences*, **117**, 1471–1479.

Zachos, J. C., M. Pagani, L. Sloan, E. Thomas, and K. Billups: 2001, Trends, rhythms, and aberrations in global climate 65 Ma to Present. *Science*, **292**, 686.

Zachos, J. C., L. D. Stott, and K. C. Lohmann: 1994, Evolution of early Cenozoic marine temperatures. *Paleoceanography*, **9**, 353–387.